이학박사 학위논문

Dynamical invariants and measures on metric graphs and Applications in medical science

(거리그래프의 동역학적 불변량 및 측도와 의학 분야의 응용)

2023년 2월

서울대학교 대학원

수리과학부

박 재 민

Dynamical invariants and measures on metric graphs and Applications in medical science

(거리그래프의 동역학적 불변량 및 측도와 의학 분야의 응용)

지도교수 임 선 희

이 논문을 이학박사 학위논문으로 제출함

2022년 10월

서울대학교 대학원

수리과학부

박 재 민

박 재 민의 이학박사 학위논문을 인준함

2022년 12월

위 원 장	국웅	(인)
부 위 원 장	임선희	(인)
위 원	Otto van Koert	(인)
위 원	이계선	(인)
위 원	권상훈	(인)

Dynamical invariants and measures on metric graphs and Applications in medical science

A dissertation
submitted in partial fulfillment
of the requirements for the degree of
Doctor of Philosophy
to the faculty of the Graduate School of
Seoul National University

by

Jaemin Park

Dissertation Director : Professor Seonhee Lim

Department of Mathematical Sciences
Seoul National University

Fabruary 2023

Abstract

Dynamical invariants and measures on metric graphs and Applications in medical science

Jaemin Park
Department of Mathematical Sciences
The Graduate School
Seoul National University

The space of geodesics on a metric graph has three important invariant measures for geodesic flow that reflect the geometric, dynamical, and probabilistic properties of the metric graph. The measures are constructed by dynamical invariants and measure classes on the boundary of the universal covering tree. In this thesis, we focus on the structure of the metric graphs that determines the dynamical invariants and the boundary measure classes.

First, we formulate three boundary measure classes using potential functions analogous to the manifold cases: visibility measures, Patterson-Sullivan measures, and harmonic measures. We show that there is an edge length which is a necessary and sufficient condition to the equivalence of two of these measure classes (Theorem 3.4.2, Theorem 3.4.3, Theorem 3.4.4).

Next, we use the dynamical invariant and boundary measures to study the brain network. Regarding the brain network as a metric graph, we compute the volume entropy and Patterson-Sullivan measure numerically. Comparing the values between the tinnitus group and the non-tinnitus group, we strengthen the tinnitus cause interpretation based on the Bayesian hypothesis and the triple network model.

We also obtain a result of topological data analysis on medical science. Using the Mapper algorithm, we represent data space as a metric graph and propose a grouping method based on the structure of the metric graph. In this framework, we find the new subtype of Mitral regurgitation patients.

Finally, we improve a well-known result in the Diophantine approximation. We construct a fractal set contained in weighted singular vectors using tree structure and the shadowing property in homogeneous dynamics. By constructing the tree associated to lattice point counting, we obtain a nontrivial lower bound of Hausdorff dimension of weighted singular vectors (Theorem 1.5.1).

Key words: metric graph, dynamical invariant, invariant measure, brain network, topological data analysis, Diophantine approximation
Student Number: 2017-21999

Contents

Chapter 1

Introduction

A *graph* is a mathematical object consisting of vertices and edges. The vertex set is a discrete set, and edges are pairs of distinct vertices. Graph structures are widely used in many areas of mathematics, such as combinatorics, probability, group theory, etc. Moreover, real-world data often has a graph structure, so the graph theory has many applications to data analysis, such as brain networks, recommendation systems, deep neural networks, etc. In most of these studies, weighted graphs are considered, where edges adopt weights related to the similarity between vertices. In this thesis, we consider graphs as geometric objects, especially a hyperbolic metric space. We study the geometry of graphs (or their structure) mainly focusing on the dynamics of group actions on the metric graphs. In this thesis, we obtained the following results in the area of homogeneous dynamics and medical data analysis.

1. Equivalence of boundary measures;
2. Brain network analysis 1: Tinnitus on hearing loss patients [Son21];
3. Brain network analysis 2: Tinnitus on sudden sensorineural hearing loss patients [Lee22].

Moreover, we also obtained the two following results, which use graph structure of data networks and tree structure for a fractal set with the dynamical property of homogeneous space, respectively.

4. Topological data analysis: Mitral regurgitation [Cho22];
5. Lower bound of Hausdorff dimension of weighted singular vectors [KP22].

The studies 1 and 5 are related to homogeneous dynamics and the studies 2, 3 and 4 are related to medical data analysis.

1.1 Equivalence of boundary measures

Let M be a compact connected Riemannian manifold with pinched negative sectional curvature and $\widetilde{M}$ be the universal cover of M. In [Kai90], there are three natural invariant measures for the geodesic flow on the unit tangent bundle $T^1\widetilde{M}$: Lebesgue measure, the Bowen-Margulis measure, and harmonic invariant measure. All three measures are constructed via Hopf's parametrization $T^1\widetilde{M} \simeq \partial_\infty\widetilde{M} \times \partial_\infty\widetilde{M} \times \mathbb{R}$ using the suitable measure class $(m_x)_{x\in\widetilde{M}}$ on the boundary of the universal cover $\widetilde{M}$ (visibility measures, Patterson-Sullivan measures, and harmonic measures, respectively) and the corresponding kernel $\mathcal{K}$ as follows:

$$dm(\mathbf{v}) = \mathcal{K}(\mathbf{v}_+, \mathbf{v}_-, x)\; dm_x(\mathbf{v}_+)\; dm_x(\mathbf{v}_-)\; dt.$$

This construction has been used in [Pat76], [Pat87], [Sul76], and [Sul79]. Here, the boundary measures are Patterson densities associated to certain potential functions (geometric potential, zero potential, and harmonic potential, respectively). If two of the potential functions are cohomologous, then the associated boundary measures are equivalent, which implies that the Radon-Nikodym derivatives of measures are well-defined. Combining the Radon-Nikodym derivatives and kernels, it follows that the associated invariant measures coincide [PPS12]. Now, the question is when potential functions are cohomologous. Equivalently, when the boundary measures are equivalent or when the invariant measures coincide. Katok and Kaimanovich conjectured that any two of the invariant measures coincide if and only if $\widetilde{M}$ is locally symmetric. Many results [Kat82, Kat88, Led87, Led90, Ham] has been devoted to the conjecture.

Kaimanovich asked the analogous question for finite graphs. Lyons answered the question for combinatorial graphs [Lyo94] as follows. Let X be a finite connected simplicial graph, i.e. a graph with finite vertices and edges with all edge lengths equal to 1. Assume moreover that the degree of each vertex is at least 3. Lyons proved that if any two of the three boundary measures (visibility measure, Patterson-Sullivan measure, and harmonic measure) coincide, then X is regular or biregular.

Moreover, if each edge of X adopts an integer edge length (or a rational edge length after normalizing), then two of the three boundary measures coincide if and only if the edge length L is given in each case. However, the Lyons' results are proven combinatorially and their arguments can not be generalized naturally to real edge length case (in particular, rationally independent edge lengths). In this thesis, we proved analogous results for arbitrary metric graphs (Section 3.4) with new proofs by formulating the situation dynamically as follows.

Motivated by the manifold cases, we define potential functions and associated boundary measures as the Patterson density for the potential functions in Section 2.3.1. However, the unit tangent bundle of graphs is not appropriate for this situation, since there may be infinitely many geodesics on a graph starting from the given unit vector, which causes the geodesic flow to be not well defined. Thus we define a geodesic flow on the space of geodesics on a graph as in [BPP16]. Potential functions defined on the unit tangent bundle are naturally extended to functions on the space of geodesics by assigning the same function value on the unit tangent vector determined by the given geodesic. Hopf's parametrization also can be established for the space of geodesics so that invariant measures can be constructed similarly to the manifold cases (see Section 2.3.2).

The visibility measure λ_x for $x \in \widetilde{X}$ is the solid angle under which the boundary of $\widetilde{X}$ can be seen from x. In this sense, Lyons constructed the visibility measures for metric graphs as a Markov measure for cylinder sets of geodesic rays. On the other hand, Kaimanovich characterize the visibility measures for manifold cases by the Patterson density for the geometric potential function [Kai90]. The geometric potential function is the negative of the exponential growth rate of change of the volume on the strong unstable leaf under geodesic flow [PPS12]. For given geodesic segment of length t, the integration of the geometric potential function along the geodesic segment is the logarithm of change of the volume of a small ball in the strong unstable leaf by the geodesic flow φ_t [LS20]. We call this quantity the integrated geometric potential. In Section 3.1, we introduce an analog of the integrated geometric potential function for metric graphs. We define the integrated geometric potential and related measures on metric graphs analogous to the manifold cases. The Patterson density for integrated geometric potential is defined similarly to the manifold case and it is the family of visibility measures in our setting. We note that the visibility measures in this thesis are not equal to the Lyons'

construction but they are equivalent (see Remark 3.1.6).

We equip the boundary of $\widetilde{X}$ with the visual metric. For the visual metric, the Hausdorff dimension of the boundary of $\widetilde{X}$ is equal to the volume entropy of X [Bou95, BM96]. Lyons constructed the Patterson-Sullivan measures similar to the manifold cases and proved that they are equal to the Hausdorff measures on the boundary of $\widetilde{X}$ of dimension h_{vol}. The same situation arises for metric graphs. Moreover, [KN07] introduces an analog for metric graphs of the characterization of the Hausdorff measures in [Lyo94]. Using this characterization, we can easily compute the Patterson-Sullivan measure by matrix computation.

The harmonic measure ν_x for $x \in \widetilde{X}$ is the hitting measure on the boundary of $\widetilde{X}$ for the Brownian motion starting from x. Lyons interpreted the harmonic measure as a current flow [Lyo90] from x to infinity. That is, considering $\widetilde{X}$ as an electric network with the generator connecting x and $\partial\widetilde{X}$, the amount of electric current on a wire(edge) is the measurement by ν_x of boundary points(geodesic rays) passing through the edge. Lyons also introduced explicit formula for harmonic measure based on the series-parallel laws for electric networks. In the manifold case, the harmonic measures are characterized as the Patterson density for the harmonic potential function. The harmonic potential function is the negative of the exponential rate of change of Martin kernel under geodesic flow [Led88]. Martin kernel is given by the Radon-Nikodym derivative of the harmonic measures. In Section 3.3, we define an analog of the harmonic potential function for metric graphs. Similar to the geometric potential function, we define integrated harmonic potential along a geodesic. Even though the harmonic measures in this thesis are also different from Lyons' construction, they are equivalent (see Remark 3.3.8).

In Section 3.4, we introduce three main theorems for metric graphs with real edge lengths.

Theorem 1.1.1. *Let X be a metric graph with real edge lengths and $\widetilde{X}$ be the universal covering tree of X. Then*

1. *The visibility measure λ_x and the Patterson-Sullivan measure μ_x are equivalent for all $x \in \widetilde{X}$ if and only if for all $e \in EX$,*

$$L(e) = \frac{1}{h_{\mathrm{vol}}} \log(\deg(e^-) - 1)(\deg(e^+) - 1);$$

2. *The visibility measure λ_x and the harmonic measure ν_x are equivalent*

for all $x \in \widetilde{X}$ if and only if there exists $c > 0$ such that for all $e \in EX$,

$$L(e) = c\left(1 - \frac{1}{\deg(e^-)} - \frac{1}{\deg(e^+)}\right);$$

3. *The Patterson-Sullivan measure μ_x and the harmonic meausre ν_x are equivalent for all $x \in \widetilde{X}$ if and only if for all $e \in EX$,*

$$\frac{L(e)e^{h_{\mathrm{vol}}L(e)}}{e^{2h_{\mathrm{vol}}L(e)} - 1} = K(e^-)K(e^+),$$

where for $x \in VX$,

$$K(x)^2 = \frac{1 + \sum_{e^-=x} \frac{1}{e^{2h_{\mathrm{vol}}L(e)}-1}}{\sum_{e^-=x} \frac{1}{L(e)}}.$$

The key idea of proofs of the main theorems is the cohomological invariance of the invariant measures for geodesic flow. Proposition 2.3.6 implies that if two Patterson densities are equivalent, then the associated Gibbs measures coincide. From the observation, we compare the measure of some Bowen balls in the space of geodesics and hence obtain cohomologous relation of the potential functions (Theorem 3.4.2, Theorem 3.4.3, and Theorem 3.4.4). The overall proofs are motivated by Lyons' results.

1.2 Brain network analysis 1: Tinnitus on hearing loss patients

Non-pulsatile subjective tinnitus is a phantom auditory perception occurring in the absence of an external acoustic stimulus [Lee17]. The prevalence of tinnitus has been reported to be 6–22 [AR89, Gal15, Kim15, SCF10, Wu15] and increases with age [Oit15, Wu15]; tinnitus represents a social burden in aging societies.

Possible mechanisms suggested for the generation of tinnitus can be classified into three broad categories: (a) peripheral auditory deafferentation and central maladaptive plastic changes, (b) spontaneous auditory neuronal hyperactivity, and (c) increased cross-fiber synchrony among neurons [BMH13, ER12]. Previous studies have identified correlations between tinnitus pitch and the frequency of maximum hearing loss (HL) [STM, Sch12], suggesting that

tinnitus may be a "fill-in phenomenon" for missing auditory information due to HL. In animal studies, subsequent pathologic changes in the central auditory system linked HL to tinnitus [Lee17, NE05, Nor02]. Recent animal and human studies have also indicated that HL should be preceded by auditory experience to generate tinnitus [EK16, Lee17].

However, there are still a number of unanswered questions concerning the generation of tinnitus in subjects with HL. Although most cases of tinnitus are closely associated with HL or auditory deafferentation, not all individuals with HL develop tinnitus. This suggests that the filling in of missing auditory information does not occur in every individual with HL. Most commonly, HL originates from changes in the peripheral auditory system while tinnitus is generated in the brain. This suggests that different neural substrates may exist between hearing loss with tinnitus (HL-T) and hearing loss without the generation of tinnitus (HL-NT). Resting-state quantitative electroencephalography (rs-qEEG) may be able to identify the central mechanism that links HL to auditory phantom perception based on the fill-in phenomenon.

To determine if there were differences in resting-state cortical activity between the HL-T and HL-NT groups at the brain network level, we adopted the "volume entropy model" [LeeH19] and compared the groups with respect to information flow in the brain. The volume entropy of the brain network corresponds to the limit of asymptotic exponential growth rate of the number of paths in the network [LeeH19]. As a global measure of the brain network, volume entropy represents the global efficiency of the propagation of information throughout the brain network. Furthermore, we can obtain a local measure at each brain region based on the afferent node capacity, which is another marker of volume entropy. Afferent node capacity, which is associated with volume entropy, quantifies the contribution of each node to the spread of information.

Although the volume entropy model has not priory been adopted in tinnitus-related studies, based on precedent functional neuroimaging studies of the pathophysiology of tinnitus, our a priori hypothesis was that while the HL-T group may generate tinnitus by retrieving stored auditory memory [VD16] to fill in for the lost peripheral auditory input [DVF14], the HL-NT group may not develop unnecessary tinnitus in spite of peripherally decreased auditory input with the help of cortical areas involved in maintaining unfocused resting-state. In this regard, we hypothesized that the HL-T group would exhibit increased afferent node capacity in the cortical areas in charge of memory and Bayesian

inference, to reduce perceptual uncertainty by generating tinnitus in response to decreased peripheral auditory input [DJV14, DVF14]. Meanwhile, the HL-NT group was expected to show relatively increased afferent node capacity in areas involved in the maintenance of the task-free resting state of the brain, such as the default mode network (DMN) [Rai01, RS07], which are not affected by decreased auditory information. To test our hypotheses, we used the volume entropy model to compare the HL-T and HL-NT groups in terms of rs-qEEG data for cortical areas showing significantly different information flow, and discuss possible reasons for tinnitus generation in the HL-T group and non-generation in the HL-NT group.

1.3 Brain network analysis 2: Tinnitus on sudden sensorineural hearing loss patients

Tinnitus is a common otologic symptom characterized by the conscious perception of phantom sounds in the absence of corresponding external auditory signals [DeR21b]. The prevalence of tinnitus in the adult population is 10–15 [Hen05], and one in five people with the condition experience emotional distress [ER04]. Several mechanisms for the generation of tinnitus have been suggested at the microscopic, mesoscopic, and macroscopic levels [Egg15]. Two main types of tinnitus have been described: tinnitus based on deafferentation and tinnitus based on a noise cancelation deficiency [DeR14c]. However, the exact pathophysiology of the disorder remains elusive. Tinnitus has been described in terms of Bayesian brain processing [DeR14a, DeR21b, DeR15, DeR21a, Sed16, VD16, Lee17, Lee20, Moh18, DV21, Lee21, Son21]. The Bayesian brain can be conceptualized as a probability machine that constantly makes predictions about the world and updates them based on input from the senses [KP04, Fri10, DeR14b]. The goal of the Bayesian brain is to reduce environmental uncertainty [KP04, Fri10, DeR14b]. This model proposes that tinnitus resolves auditory uncertainty resulting from sensory deprivation [Fri14, VD16, Lee17]. In other words, the brain tries to "fill in" the missing auditory information from auditory memory when deprived of an external signal, resulting in the perception of phantom sounds that are not present in reality [NE05, Sch12, Lee17].

Recently, a "triple brain network" model was proposed to explain the psychopathology of certain cognitive and affective disorders [Men11]. The triple

network model proposes that neuropsychiatric disorders can be explained by abnormal interactions within and between three canonical brain networks: a self-representational default mode network (DMN) [Buc08], goal-oriented frontoparietal central executive network (CEN) [Vin08], and behavioral relevance-encoding salience network (SN) [See07]. The DMN is activated when individuals are internally oriented, exemplified by the "wandering mind" concept [Shu97, Mas07, Chr16], whereas the CEN, also known as the frontoparietal control system [Vin08, Col14]; is associated with externally directed cognitive behaviors. Normally, the DMN and CEN are anticorrelated [Men11]. The SN processes sensory, emotional, and cognitive information simultaneously and acts as a switch between the anticorrelated DMN and CEN; in this manner, it integrates and balances internal psychological processes with external stimulus–oriented cognitive and affective pathways [Fox05, Men11, Men18, Gou14]. However, when all components of the triple network are activated, the anticorrelation between the DMN and CEN is disrupted, and the SN erroneously ascribes meaning to unimportant external stimuli; this leads to neurophysiological dysfunction in the brain.

Sudden sensorineural hearing loss (SSNHL) is defined as an idiopathic acute hearing impairment (>30 dB loss) across three contiguous frequencies in a pure-tone audiogram occurring within 72 h [CP07, Cha10]. The development of tinnitus in subjects with SSNHL can be explained by the abovementioned Bayesian brain model; the brain attempts to compensate for prediction errors by retrieving previously stored auditory memories from the parahippocampal gyrus (PHC) after the sudden loss of auditory input [Lee20]. According to this perspective, prior auditory experience is necessary for the generation of tinnitus in patients with hearing loss; tinnitus is absent in patients with congenital single-sided deafness (SSD), while it is relatively frequent among those with acquired SSD [Lee17, LeeJ21].

A volume entropy model has been developed to statistically compare the quantity of information flow between hearing loss patients with and without tinnitus [Son21]. The volume entropy model calculates the exponential growth rate of network pathways by converting distributions of cortical activities derived from quantitative electroencephalography (qEEG) into mathematical information [Lim08]. Information inflow and outflow in certain brain cortical areas (i.e., nodes and vertices) are computed if the region is activated after the execution of certain behaviors. Specifically, the global and local efficiency of information flow is represented as volume entropy and afferent node capacity,

respectively [LeeH19, Son21].

In this study, we investigated the mechanism underlying the selective generation of tinnitus in patients with SSNHL and hypothesized that, in an SSNHL with tinnitus (T) group, tinnitus is caused by changes in the triple network. We further hypothesized that, in an SSNHL without tinnitus (NT) group, tinnitus does not occur due to the deactivation of areas associated with the generation of tinnitus and activation of cortical pathways involved in tinnitus suppression. In summary, a volume entropy model was applied to compare resting-state qEEG data among Brodmann areas (BAs) showing significant differences in information flow between T and NT groups and to elucidate the mechanisms underlying tinnitus generation and suppression.

1.4 Topological data analysis: Mitral regurgitation

Primary mitral regurgitation (MR) is a frequent surgical indication for valvular heart disease worldwide [Lun03, Nko06]. Despite recent advances in the understanding of clinical outcomes in MR patients, we still do not know comprehensively how the heart responds to chronic volume overload by MR [Bau17, Wri21]. Moreover, because several echocardiographic parameters commonly used for prognostication in primary MR are closely correlated with each other, there is a need to understand the structural and functional remodeling in an integrative fashion.

Topological data analysis (TDA) is a mathematical tool used to recognize the "shape" of data, and therefore, to gain insights from the conformation of the model constructed from the data [Lum13]. The fundamental goal of TDA is to apply a geometric approach to capture the complex connections and interactions by visualizing the conformation of high-dimensional data as the network [Lum13]. The network models of data connections are critical for a simple yet intuitive understanding of extensive complex data, and thus, new insights [PB18, LeeH17, Ha20]. Recent applications of TDA have provided an understanding of the phenotypic diversity of a disease based on the patient-patient similarity network [NLC11, Li15], enabling new classifications of the disease or the identification of meaningful groups in the disease previously considered homogenous [Cas19, Cho20, Hwa21].

Given these strengths of TDA, we hypothesized that TDA would provide new and deeper insights into the cardiac remodeling of chronic primary MR. The objective of this study was 3-fold. First, to visualize the cardiac remod-

eling pattern of chronic primary MR patients by creating a network model from complex clinical data. Second, to discover novel phenogroups not previously acknowledged in chronic primary MR. Third, to demonstrate the clinical implication of these new insights and/or phenogroups from the analysis.

1.5 Lower bound of Hausdorff dimension of weighted singular vectors

In 1937, Khintchine introduced the notion of singularity in the sense of Diophantine approximation. Recall that a vector $x = (x_1, \dots, x_d) \in \mathbb{R}^d$ is said to be *singular* if, for every $\epsilon > 0$, there exists $T_0 > 1$ such that for all $T > T_0$ the system of inequalities

$$\max_{1 \le i \le d} |qx_i - p_i|^d < \frac{\epsilon}{T} \quad \text{and} \quad 0 < q < T \tag{1.1}$$

admits an integer solution $(\mathbf{p}, q) = (p_1, \dots, p_d, q) \in \mathbb{Z}^d \times \mathbb{Z}$.

The name *singular* is derived from the fact that the set of singular vectors is a Lebesgue nullset. On the other hand, the computation of the Hausdorff dimension of the set of singular vectors, or more generally singular matrices, has been a challenge until the breakthrough [DFSU] using a variational principle in the parametric geometry of numbers. Historically, the first breakthrough was made in [Che11] to prove that the Hausdorff dimension of the set of 2-dimensional singular vectors is 4/3, which was extended in [CC16] to d-dimensional singular vectors. They proved that the set of d-dimensional singular vectors has Hausdorff dimension $d^2/(d+1)$. For general $m \times n$ singular matrices, it was proved in [KKLM17] that the Hausdorff dimension of $m \times n$ singular matrices is at most $mn(1 - \frac{1}{m+n})$, and finally, it was shown in [DFSU] that the upper bound is sharp.

In this part of the thesis, we consider the weighted version of the singularity as follows: Let $w = (w_1, \dots, w_d) \in \mathbb{R}^d_{>0}$ be an ordered d-tuple of positive real numbers such that $\sum_i w_i = 1$ and $w_1 \ge \cdots \ge w_d$. We say that a vector $x = (x_1, \dots, x_d) \in \mathbb{R}^d$ is *w-singular* if for every $\epsilon > 0$ there exists $T_0 > 1$ such that for all $T > T_0$ the system of inequalities

$$\max_{1 \le i \le d} |qx_i - p_i|^{\frac{1}{w_i}} < \frac{\epsilon}{T} \quad \text{and} \quad 0 < q < T \tag{1.2}$$

admits an integer solution $(\mathbf{p}, q) = (p_1, \dots, p_d, q) \in \mathbb{Z}^d \times \mathbb{Z}$. Denote by $\mathrm{Sing}(w)$ the set of w-singular vectors in $\mathbb{R}^d$. Here and hereafter we always assume that the weight vector w satisfies the above assumption.

Note that if all weights have the same value, that is, $w_i = 1/d$ for all $i = 1, \dots, d$, then the weighted system (1.2) gives the unweighted system (1.1).

In the weighted setting, it was shown in [LSST20] that the set of 2-dimensional w-singular vectors has Hausdorff dimension $2 - \frac{1}{1+w_1}$. The aim of Chapter 7 is to extend this 2-dimensional result to higher dimensions regarding the lower bound of the Hausdorff dimension.

Theorem 1.5.1. *For $d \geq 2$, the Hausdorff dimension of* $\mathrm{Sing}(w)$ *is at least* $d - \frac{1}{1+w_1}$.

One of the main ingredients of the proof of Theorem 1.5.1 is Dani's correspondence, which says that w-singular vectors correspond to certain divergent trajectories in the space $\mathcal{L}_{d+1}$ of unimodular lattices in $\mathbb{R}^{d+1}$. More precisely, let $a_t := \mathrm{diag}\left(e^{w_1 t}, \dots, e^{w_d t}, e^{-1}\right) \in \mathrm{SL}_{d+1}(\mathbb{R})$ and let

$$h(x) := \begin{pmatrix} I_d & x \\ 0 & 1 \end{pmatrix} \in \mathrm{SL}_{d+1}(\mathbb{R}) \quad \text{for } x \in \mathbb{R}^d,$$

where I_d is the $d \times d$ identity matrix. Then x is w-singular if and only if the diagonal orbit $\left(a_t h(x) \mathbb{Z}^{d+1}\right)_{t \geq 0}$ is divergent.

Our method for the proof of Theorem 1.5.1 is motivated by the method in [LSST20], hence we also have the following result as in [LSST20, Theorem 1.5].

Theorem 1.5.2. *For any $\Lambda \in \mathcal{L}_{d+1}$ and any nonempty open subset U in $\mathbb{R}^d$, the Hausdorff dimension of the set*

$$\{x \in U : (a_t h(x) \Lambda)_{t \geq 0} \text{ is divergent}\}$$

is at least $d - \frac{1}{1+w_1}$.

Theorem 1.5.2 implies the following corollary as in [LSST20, Corollary 1.6] (see also [GS20, AGMS21]).

Corollary 1.5.3. *The Hausdorff dimension of the set*

$$\{\Lambda \in \mathcal{L}_{d+1} : (a_t \Lambda)_{t \geq 0} \text{ is divergent}\}$$

is at least $\dim \mathrm{SL}_{d+1}(\mathbb{R}) - \frac{1}{1+w_1} = (d+1)^2 - 1 - \frac{1}{1+w_1}$.

Recently, Solan [Sol] established a variational principle in the parametric geometry of numbers for general flows. Following his notations, we consider the following two subgroups:

$$H = \{g \in \mathrm{SL}_{d+1}(\mathbb{R}) : a_{-t} g a_t \to I_{d+1} \text{ as } t \to \infty\},$$
$$H' = \{h(x) \in \mathrm{SL}_{d+1}(\mathbb{R}) : x \in \mathbb{R}^d\}.$$

Note that H is the unstable horospherical subgroup of a_1. In the unweighted setting ($w_1 = \cdots = w_d$), the two subgroups H and H' are the same, but in general, H is bigger than H'. One of the applications of the variational principle for general flows in [Sol] is to give an upper bound of the Hausdorff dimension of the set

$$\mathrm{Sing}(H, \Lambda; a_t) = \{h \in H : (a_t h \Lambda)_{t \geq 0} \text{ is divergent}\}.$$

More precisely, [Sol, Corollary 2.34] implies that the Hausdorff dimension of $\mathrm{Sing}(H, \Lambda; a_t)$ is at most $\dim H - \frac{1}{1+w_1}$. On the other hand, Theorem 1.5.2 implies that the Hausdorff dimension of $\mathrm{Sing}(H, \Lambda; a_t)$ is at least $\dim H - \frac{1}{1+w_1}$, hence we have the following corollary.

Corollary 1.5.4. *The Hausdorff dimension of* $\mathrm{Sing}(H, \Lambda; a_t)$ *is* $\dim H - \frac{1}{1+w_1}$.

Chapter 7 is organized as follows. In Section 7.1, we recall fractal structures and self-affine structures. We estimate the lower bound of Hausdorff dimension of the associated fractal set. In Section 7.2, we generalize the lattice point counting results in [LSST20, Section 3] to higher dimensional cases. In Section 7.3, we construct a fractal set contained in the set of weighted singular vectors and prove Theorem 1.5.1 by estimating Hausdorff dimension of the fractal set.

Chapter 2

Dynamics on Metric graphs

2.1 Geometry on metric graphs

In this section, we describe the geometry on metric graphs following [BPP16]. We first define a graph combinatorially and then regard it as a topological space. With the metric on the graph induced by edge lengths, the graph is considered as a metric space. Following the theory of metric spaces, we define the geometric boundary and the space of geodesics of the graph.

2.1.1 Metric graphs

Followed by [Ser02], we define a *graph* $\mathbb{X}$ to be a data

$$(VX, EX, \cdot^-, \cdot^+, \bar{\cdot}),$$

where VX and $EX(\subset VX \times VX)$ are sets and $\cdot^-, \cdot^+ : EX \to VX$ and $\bar{\cdot} : EX \to EX$ are maps satisfying $\bar{e}^+ = e^-$ for all $e \in EX$. We call a set VX the *set of vertices* and a set EX the *set of edges*. For each $e \in EX$, we call e^-, e^+ and $\bar{e}$ the *inital vertex*, the *terminal vertex* and the *oppisite edge* of e.

A *topological realization* of a graph $\mathbb{X}$ is the topological space $(I_e)_{e\in EX}/\sim$, where I_e is a closed unit interval for all $e \in EX$ and quotient are provided by the equivalence relation that identifies I_e and $I_{\bar{e}}$ by $t \mapsto 1 - t$ and identifies the origin of I_e and $I_{e'}$ if and only if $e^- = e'^-$.

A *metric graph* $(\mathbb{X}, L)$ is a pair consisting of a graph $\mathbb{X}$ and an *edge length map* $L : EX \to \mathbb{R}_{>0}$ such that $L(e) = L(\bar{e})$ for all $e \in EX$. We further assume L has a positive lower bound. We abuse the notation for simplicity that if

$e^- = x$ and $e^+ = y$, then $L(x, y) := L(e)$. We call a metric graph $(\mathbb{X}, L)$ a *simlicial graph* if $L \equiv 1$.

The *geometric realization* of a metric graph $(\mathbb{X}, L)$ is the topological realization of $\mathbb{X}$ endowed with a metric induced by L. That is, the metric is a path metric that for all edge $e \in EX$, the length of e in the topological realization is given by $L(e)$. We denote the geometric realization of a metric graph $(\mathbb{X}, L)$ by $X = |\mathbb{X}|_L$ and the metric on X by d_X.

We let $\mathbb{X}$ be a finite simplicial graph and $\widetilde{\mathbb{X}}$ be the universal covering tree of $\mathbb{X}$. Let $\Gamma \subset \mathrm{Isom}(\widetilde{X})$ be a discrete subgroup such that $X = \widetilde{X}/\Gamma$. The geometric realization of $\widetilde{\mathbb{X}}$, denoted by $\widetilde{X} = |\widetilde{\mathbb{X}}|_L$, is endowed with the lifted metric $\widetilde{d}_X$ of the metric d_X on X.

We define the *geometric boundary* $\partial_\infty \widetilde{X}$ of $\widetilde{X}$ by the quotient space of the set of geodesic rays $\rho : \mathbb{R}_{\geq 0} \to \widetilde{X}$ where two geodesic lines ρ and ρ' are equivalent if and only if there exists a real number $a \in \mathbb{R}$ such that $\lim_{t\to\infty} d_X(\rho(t), \rho'(t + a)) = 0$. Equivalently, $\partial_\infty \widetilde{X}$ is the set of geodesic rays starting from $x_0 \in \widetilde{X}$ for fixed x_0. We endow $\partial_\infty X$ with the quotient topology of the compact-open topology.

2.1.2 Spaces of geodesics

The *geodesic* in $\widetilde{X}$ is an isometry from $\mathbb{R}$ into $\widetilde{X}$. Let $\mathscr{G}\widetilde{X}$ be the *space of geodesics* in $\widetilde{X}$. We endow $\mathscr{G}\widetilde{X}$ with the metric $d_{\mathscr{G}\widetilde{X}}$ defined by

$$d_{\mathscr{G}\widetilde{X}}(\ell, \ell') = \int_{-\infty}^{\infty} d_{\widetilde{X}}(\ell(t), \ell'(t)) e^{-|t|} dt, \quad \forall \ell, \ell' \in \mathscr{G}\widetilde{X}. \tag{2.1}$$

The metric $d_{\mathscr{G}\widetilde{X}}$ induces the topology of uniform convergence on compact subsets on $\mathscr{G}\widetilde{X}$ and hence $\mathscr{G}\widetilde{X}$ is a proper metric space. We note that Γ naturally induces the isometric action on $\mathscr{G}\widetilde{X}$ by $(\gamma.\ell)(t) = \gamma.(\ell(t))$ for all $\gamma \in \Gamma$ and $\ell \in \mathscr{G}\widetilde{X}$. In this sense, we may consider the quotient space $\Gamma\backslash\mathscr{G}\widetilde{X}$ and denote it by $\mathscr{G}X$.

The *geodesic flow* $(\varphi_t)_{t\in\mathbb{R}}$ on $\mathscr{G}\widetilde{X}$ is the one-parameter group of homeomorphisms of $\mathscr{G}\widetilde{X}$ defined by

$$(\varphi_t.\ell)(s) = \ell(s + t), \quad \forall \ell \in \mathscr{G}\widetilde{X}, t \in \mathbb{R}.$$

The *footprint projection* in the $\mathrm{Isom}(\widetilde{X})$-equivariant $\frac{1}{2}$-Hőlder continuous map $\pi : \mathscr{G}\widetilde{X} \to \widetilde{X}$ defined by $\pi(\ell) = \ell(0)$ for all $\ell \in \mathscr{G}\widetilde{X}$. The *antipodal map* is the $\mathrm{Isom}(\widetilde{X})$-equivariant isometric map $\iota : \mathscr{G}\widetilde{X} \to \mathscr{G}\widetilde{X}$ defined by $(\iota\ell)(t) = \ell(-t)$

for all $\ell \in \mathscr{G}\widetilde{X}$. It is easily checked that $\iota \circ \varphi_t = \varphi_{-t} \circ \iota$ for all $t \in \mathbb{R}$ and $\pi \circ \iota = \pi$. We note that the maps φ_t, ι and π are Γ-equivariant so that they are well-defined on $\mathscr{G}X$.

The *strong stable leaf* of $\ell \in \mathscr{G}\widetilde{X}$ is

$$W^{ss}(\ell) = \{\ell' \in \mathscr{G}\widetilde{X} \ : \ \lim_{t\to+\infty} d_{\widetilde{X}}(\ell(t), \ell'(t)) = 0\},$$

and the *strong unstable leaf* of $\ell \in \mathscr{G}\widetilde{X}$ is

$$W^{su}(\ell) = \iota W^{ss}(\iota\ell) = \{\ell' \in \mathscr{G}\widetilde{X} \ : \ \lim_{t\to-\infty} d_{\widetilde{X}}(\ell(t), \ell'(t)) = 0\}.$$

For $\ell \in \mathscr{G}\widetilde{X}$, the *Hamenstädt's distance* $d_{W^{ss}}$ ($d_{W^{su}}$, respectively) on W^{ss} (W^{su}, respectively) is defined by

$$d_{W^{ss}}(\ell, \ell') = \lim_{t\to-\infty} e^{\frac{1}{2}d_{\widetilde{X}}(\ell(t),\ell'(t))-t}, \quad \forall \ell, \ell' \in W^{ss}, \tag{2.2}$$

$$d_{W^{su}}(\ell, \ell') = \lim_{t\to+\infty} e^{\frac{1}{2}d_{\widetilde{X}}(\ell(t),\ell'(t))-t}, \quad \forall \ell, \ell' \in W^{su}. \tag{2.3}$$

We suppose $\mathbb{X}$ is a simplicial graph, that is, a grpah without any edge length function. Then $\widetilde{\mathbb{X}}$ is the simplicial tree. The *space of discrete geodesics* of $\widetilde{\mathbb{X}}$ is the space $\mathscr{G}\widetilde{\mathbb{X}}$ of geodesics ℓ from $\mathbb{R}$ to the geometric realization $\widetilde{X}_1 = |\widetilde{\mathbb{X}}|_1$ such that $\ell(0) \in VX$. The action of Γ on $\widetilde{\mathbb{X}}$ induces the action of Γ on $\mathscr{G}\widetilde{\mathbb{X}}$ so that we may consider the quotient space $\Gamma\backslash\mathscr{G}\widetilde{\mathbb{X}}$. We denote $\Gamma\backslash\mathscr{G}\widetilde{\mathbb{X}}$ by $\mathscr{G}\mathbb{X}$. We remark that the geometric realization $\widetilde{X}_1$ is distinguished from $\widetilde{X}$ in that $\widetilde{X}_1$ is constructed without an edge legngth function ℓ. The *discrete-time geodesic flow* $(\varphi_t)_{t\in\mathbb{Z}}$ on $\mathscr{G}\widetilde{\mathbb{X}}$ is the one-parameter discrete group of homeomorphisms of $\mathscr{G}\widetilde{\mathbb{X}}$ consisting of the intergral time maps of the continuous-time geodesic flow of the geometric realization $\widetilde{X}$. Formally, we have $(\varphi_t.\ell)(s) = \ell(s+t)$ for all $\ell \in \mathscr{G}\widetilde{\mathbb{X}}, t \in \mathbb{Z}$.

We introduce notations that are used in the remaining parts of the thesis. For $x, y \in \widetilde{X}$, we denote by $\ell_{x,y}$ a geodesic starting from x to the direction of y. For $x \in \widetilde{X}$ and $\xi \in \partial_\infty\widetilde{X}$, we denote by $\ell_{x,\xi}$ a geodesic starting from x to the direction of ξ.

2.2 Potentials, Critical exponents, and Gibbs cocycles

In [BPP16], a potential $\widetilde{F}$ for Γ is defined by a continuous Γ-invariant function on the unit tangent bundle of $\widetilde{X}$. For $x, y \in \widetilde{X}$, the quantity

$$\int_x^y \widetilde{F} = \int_0^{d_{\widetilde{X}}(x,y)} \widetilde{F}(v_{\varphi_t \ell}) dt$$

is used for defining the critical exponent and Gibbs cocycles. In this section, we use only the quantity that we call an integrated potential for developing dynamical theory on metric graphs instead of the potential $\widetilde{F}$.

2.2.1 Potentials

Comparing the manifold case, well-known potential functions on the manifold are not defined on metric graphs when considering their meaning. For example, the geometric potential on the manifold means the expoenential rate of changing volume of the unit tangent bundle of strong stable leaf along the geodesic flow. In metric graphs, the exponential rate of changing volume is discontinuous along the geodesic flow so that it cannot be differentiable. Although we cannot define the geoemtric potential for metric graphs, we have the exponential rate of changing volume on a geodesic in $\widetilde{X}$. In this thesis, we define the integrated potential along the geodesic in metric graphs as follows.

Definition 2.2.1. For $\ell \in \mathscr{G}\widetilde{X}$ and $t \geq 0$, we call $\widetilde{\mathcal{I}}(\ell, t)$ a *integrated potential* for Γ along the geodesic ℓ until time t if it satisfies

1. It is Γ-invariant, i.e. $\widetilde{\mathcal{I}}(\ell, t) = \widetilde{\mathcal{I}}(\gamma\ell, t)$ for all $\gamma \in \Gamma$;
2. $\widetilde{\mathcal{I}}(\ell, t) = \widetilde{\mathcal{I}}(\ell', t)$ if $\ell|_{[0,t]} = \ell'|_{[0,t]}$ for all $t \geq 0$;
3. $\widetilde{\mathcal{I}}(\ell, t) + \widetilde{\mathcal{I}}(\varphi_t\ell, s) = \widetilde{\mathcal{I}}(\ell, t+s)$ for all $s \geq 0$.

For $r \in \mathbb{R}$, we denote $\widetilde{\mathcal{I}}_r(\ell, t) := \widetilde{\mathcal{I}}(\ell, t) - rt$. The quotient function $\mathcal{I} : \mathscr{G}X \times \mathbb{R}_{\geq 0} \to \mathbb{R}$ is called a *integrated potential* along ℓ until t.

Let $\widetilde{\mathcal{I}}, \widetilde{\mathcal{I}}^* : \mathscr{G}\widetilde{X} \times \mathbb{R}_{\geq 0} \to \mathbb{R}$ be integrated potentials for Γ. We say $\widetilde{\mathcal{I}}$ is *cohomologous* to $\widetilde{\mathcal{I}}^*$ if there exists Γ-invariant function $H : \widetilde{X} \to \mathbb{R}$ satisfying

$$\widetilde{\mathcal{I}}^*(\ell, t) - \widetilde{\mathcal{I}}(\ell, t) = H(\ell(t)) - H(\ell(0)) \tag{2.4}$$

for all $\ell \in \mathscr{G}\widetilde{X}$ and $t \geq 0$.

2.2.2 Critical exponents and Gibbs cocycles

We fix an integrated potential $\widetilde{\mathcal{I}}$ for Γ. We define $\widetilde{\mathcal{I}}^+ = \widetilde{\mathcal{I}}$ and $\widetilde{\mathcal{I}}^-(\ell, t) = \widetilde{\mathcal{I}}(\ell \circ \iota, t)$ for all $\ell \in \mathscr{G}\widetilde{X}$ and $t \geq 0$. The quotient functions $\mathcal{I}^\pm : \mathscr{G}X \times \mathbb{R}_{\geq 0} \to \mathbb{R}$ are induced from $\widetilde{\mathcal{I}}^\pm$.

Definition 2.2.2. Let $x, y \in \widetilde{X}$. The *critical exponent* of $(\Gamma, \mathcal{I})$ is the element $\delta = \delta_{\Gamma,\mathcal{I}} \in [-\infty, +\infty]$ defined by

$$\delta = \limsup_{n \to +\infty} \frac{1}{n} \log \sum_{\gamma \in \Gamma : n-1 < d_{\widetilde{X}}(x, \gamma y) \leq n} e^{\widetilde{\mathcal{I}}(\ell_{x,\gamma y}, d_{\widetilde{X}}(x, \gamma y))}.$$

The *Poincaré series* of $(\Gamma, \mathcal{I})$ is the map $Q = Q_{\Gamma,\mathcal{I},x,y} : \mathbb{R} \to [0, +\infty]$ defined by

$$Q(s) = \sum_{\gamma \in \Gamma} e^{\widetilde{\mathcal{I}}_s(\ell_{x,\gamma y}, d_{\widetilde{X}}(x, \gamma y))}.$$

It follows from [BPP16] that the critical exponent $\delta_{\Gamma,\mathcal{I}}$ is the radius of convergence of the Poincaré series $Q_{\Gamma,\mathcal{I},x,y}$.

Definition 2.2.3. The *Gibbs cocycle* of dimension δ associated with the group Γ and the integrated potential $\widetilde{\mathcal{I}}^\pm$ is the map $C^\pm = C^\pm_{\delta,\Gamma,\mathcal{I}^\pm} : \partial_\infty \widetilde{X} \times \widetilde{X} \times \widetilde{X} \to \mathbb{R}$ defined by

$$\begin{aligned} C^+(\xi, x, y) &= \lim_{t \to +\infty} \left[\widetilde{\mathcal{I}}^+_\delta(\ell_{y,\xi}, t) - \widetilde{\mathcal{I}}^+_\delta(\ell_{x,\xi}, t) \right], \\ C^-(\xi, x, y) &= \lim_{t \to +\infty} \left[\widetilde{\mathcal{I}}^-_\delta(\varphi_t \ell_{y,\xi}, t) - \widetilde{\mathcal{I}}^-_\delta(\varphi_t \ell_{x,\xi}, t) \right]. \end{aligned} \tag{2.5}$$

where $\ell_{x,\xi}$ is any geodesic starting from x to ξ

Indeed, the Gibbs cocycle $C^\pm$ can be represented as

$$\begin{aligned} C^+(\xi, x, y) &= \widetilde{\mathcal{I}}_\delta(\ell_{y,p}, d_{\widetilde{X}}(y, p)) - \widetilde{\mathcal{I}}_\delta(\ell_{x,p}, d_{\widetilde{X}}(x, p)), \\ C^-(\xi, x, y) &= \widetilde{\mathcal{I}}_\delta(\ell_{p,y}, d_{\widetilde{X}}(y, p)) - \widetilde{\mathcal{I}}_\delta(\ell_{p,x}, d_{\widetilde{X}}(x, p)) \end{aligned} \tag{2.6}$$

where $p \in \widetilde{X}$ is the point at which geodesic lines $\ell_{y,\xi}$ and $\ell_{x,\xi}$ meet first. Thus the Gibbs cocycle is well-defined.

2.2.3 Systems of conductances

We define the *system of conductances* $\widetilde{c} : E\widetilde{X} \to \mathbb{R}$ by

$$\widetilde{c}(e) = \widetilde{\mathcal{I}}(\ell_e, L(e)), \tag{2.7}$$

where ℓ_e be a geodesic starting from e^- to the direction of e. For $x, y \in V\widetilde{X}$, let ℓ_{xy} be a geodesic in $\mathscr{G}\widetilde{X}$ starting from x to direction of y and $e_1, \ldots, e_n \in E\widetilde{X}$ be edges such that $\ell_{x,y}|_{[0,d_{\widetilde{X}}(x,y)]} \cap E\widetilde{X} = \{e_1, \ldots, e_n\}$ considering the order. By the definition of $\mathcal{I}$, we have

$$\mathcal{I}(\ell_{xy}, d_{\mathscr{G}\widetilde{X}}(x, y)) = \sum_{i=1}^{n} \widetilde{c}(e_i).$$

Since $\widetilde{c}$ is invariant under the action of Γ, we derive the system of conductance $c : EX \to \mathbb{R}$.

Let $\widetilde{\mathcal{I}}, \widetilde{\mathcal{I}}^*$ be two integrated potentials for Γ and $\widetilde{c}, \widetilde{c}^*$ be the system of conductances associated with them, respectively. If $\widetilde{\mathcal{I}}$ and $\widetilde{\mathcal{I}}^*$ are cohomologous via a function $H : \widetilde{X} \to \mathbb{R}$ in (2.4), then we have

$$\widetilde{c}^*(e) - \widetilde{c}(e) = H(e^+) - H(e^-)$$

for all $e \in E\widetilde{X}$.

It follows from the proposition 3.22. in [BPP16] that there is correspondence between the cohomology classes of the system of conductance and the potential. In fact, the dynamical theory on metric graphs associated with potentials can be interpreted in terms of systems of conductances. Though we define new objects $\widetilde{\mathcal{I}}$ replacing potentials, the classical theory in [BPP16] is applicable.

2.3 Gibbs measures

In this section, we define Patterson densities and the Gibbs measure for an integrated potential. Although we use an integrated potential instead of a potential, these measures are essentially the same as the ones in [BPP16]. Moreover, we prove important facts that cohomologous relation between two integrated potentials gives the equivalence of the Patterson densities and the uniqueness of the Gibbs measures (Proposition 2.3.2 and Proposition 2.3.6).

These propositions are key ingredients for Chapter 3.

2.3.1 Patterson densities

Definition 2.3.1. For $s \geq 0$, a family $(m_x^{\pm})_{x\in\widetilde{X}}$ of finite positive Borel measures on $\partial_\infty \widetilde{X}$ is a *conformal density* of dimension s for $(\Gamma, \widetilde{\mathcal{I}}^{\pm})$ if

1. $(m_x^{\pm})_{x\in\widetilde{X}}$ is Γ-equivariant, i.e. $\gamma_* m_x^{\pm} = m_{\gamma x}^{\pm}$ for all $\gamma \in \Gamma$ and $x \in \widetilde{X}$;
2. For all $x, y \in \widetilde{X}$,
$$\frac{dm_x^{\pm}}{dm_y^{\pm}}(\xi) = e^{-C^{\pm}(\xi,x,y)},$$
where $C^{\pm}(\xi, x, y) = C^{\pm}_{s,\Gamma,\widetilde{\mathcal{I}}^{\pm}}(\xi, x, y)$ is the Gibbs cocycle (2.5).

If $m_x^{\pm}$ is nonzero for all $x \in \widetilde{X}$, then we call $(m_x^{\pm})_{x\in\widetilde{X}}$ the *Patterson density* for $(\Gamma, \widetilde{\mathcal{I}}^{\pm})$.

By the Hopf-Tsuji-Sullivan-Roblin theorem, the Patterson densities $(m_x^{\pm})_{x\in\widetilde{X}}$ are unique up to a scalar multiple (see [BPP16]). Using the uniqueness of the Patterson density, we get the cohomological invariance of the equivalent class of the Patterson density as follows.

Proposition 2.3.2. *Let $\widetilde{\mathcal{I}}$ and $\widetilde{\mathcal{I}}^*$ be two cohomologous integrated potentials for Γ. Then the Patterson densities associated with $\widetilde{\mathcal{I}}$ and $\widetilde{\mathcal{I}}^*$ are equivalent.*

Proof. Since $\widetilde{\mathcal{I}}$ and $\widetilde{\mathcal{I}}^*$ are cohomologous, there exists Γ-invariant function $H : \widetilde{X} \to \mathbb{R}$ such that $\widetilde{\mathcal{I}}^*(\ell, t) - \widetilde{\mathcal{I}}(\ell, t) = H(\ell(t)) - H(\ell(0))$ for all $\ell \in \mathscr{G}\widetilde{X}$ and $t \geq 0$. Let $C^{\pm}$ and $C^{*\pm}$ be the Gibbs cocycles associated $\widetilde{\mathcal{I}}$ and $\widetilde{\mathcal{I}}^*$, respectively. Then by (2.6), we have for $\xi \in \partial_\infty \widetilde{X}$ and $x, y \in \widetilde{X}$,

$$\begin{aligned} C^{*+}(\xi, x, y) - C^{+}(\xi, x, y) &= H(x) - H(y) \\ C^{*-}(\xi, x, y) - C^{-}(\xi, x, y) &= H(y) - H(x). \end{aligned} \tag{2.8}$$

Let $(m_x^{\pm})_{x\in\widetilde{X}}$ be the Patterson density for $(\Gamma, \widetilde{\mathcal{I}}^{\pm})$. We define a family of measures $(m_x^{*\pm})_{x\in\widetilde{X}}$ by for all $\xi \in \partial_\infty \widetilde{X}$ and $x, y \in \widetilde{X}$,

$$dm_x^{*\pm}(\xi) := e^{\mp H(x)} dm_x^{\pm}(\xi).$$

Then Γ-equivariance of $(m_x^{*\pm}$ follows from Γ-invariance of H and Γ-equivaraince of $(m_x^{\pm})_{x\in\widetilde{X}}$. By (2.8), it can be checked that $(m_x^{*\pm})_{x\in\widetilde{X}}$ is the Patterson den-

sity for $(\Gamma, \widetilde{\mathcal{I}}^{*\pm})$. Since the Patterson density is unique up to a scalar multiple, we prove the proposition. □

For $x, y \in \widetilde{X}$, we define a *shadow* $\mathcal{O}_x(y)$ of y seen from x by a subset of $\partial_\infty \widetilde{X}$ consisting of the equivalent classes of geodesic rays starting from x to direction of y. We note that the shadows $\mathcal{O}_x(y)$ for $x, y \in VX$ forms the basis of the topology on $\partial_\infty \widetilde{X}$. Thus any Borel measures on $\partial_\infty \widetilde{X}$ are determined by the measure values on the shodows.

For $e \in EX$, let $\widetilde{e}$ be a lift of e to $\widetilde{X}$. We denote

$$\mathbf{m}_e := m_{\widetilde{e}^-}\left(\mathcal{O}_{\widetilde{e}^-}(\widetilde{e}^+)\right),$$

for a conformal density $(m_x)_{x \in \widetilde{X}}$. It follows from the Γ-equivariance of the conformal density that $\mathbf{m}$ is independent of the choice of lifts $\widetilde{e}$.

For $e, e' \in EX$, we denote $e \to e'$ if $e^+ = e'^-$ and $\bar{e} \neq e'$. The following proposition is a generalization of proposition 3.13 in [KN07].

Proposition 2.3.3. *For all $e \in EX$, we have*

$$\mathbf{m}_e = e^{c(e) - sL(e)} \sum_{e' : e \to e'} \mathbf{m}_{e'}.$$

Proof. For $e \in EX$, let $\widetilde{e} \in E\widetilde{X}$ be a lift of e. Let $\widetilde{e}' \in E\widetilde{X}$ be such that $\widetilde{e} \to \widetilde{e}'$. Then

$$\mathcal{O}_{\widetilde{e}^-}\left(\widetilde{e}^+\right) = \bigsqcup_{\widetilde{e} \to \widetilde{e}'} \mathcal{O}_{\widetilde{e}^-}\left((\widetilde{e}')^+\right) = \bigsqcup_{\widetilde{e} \to \widetilde{e}'} \mathcal{O}_{(\widetilde{e}')^-}\left((\widetilde{e}')^+\right),$$

and hence we have

$$m_{\widetilde{e}^-}\left(\mathcal{O}_{\widetilde{e}^-}\left(\widetilde{e}^+\right)\right) = \sum_{\widetilde{e} \to \widetilde{e}'} m_{\widetilde{e}^-}\left(\mathcal{O}_{(\widetilde{e}')^-}\left((\widetilde{e}')^+\right)\right).$$

By (2.6) and (2.7), we have

$$m_{\widetilde{e}^-}\left(\mathcal{O}_{(\widetilde{e}')^-}\left((\widetilde{e}')^+\right)\right) = e^{c(e) - sL(e)} m_{(\widetilde{e}')^-}\left(\mathcal{O}_{(\widetilde{e}')^-}\left((\widetilde{e}')^+\right)\right).$$

Thus we prove the proposition. □

Proposition 2.3.4. *There is a unique number $s \geq 0$ such that the measures $m_x^\pm$ in the conformal density of dimension s are nonzero and have no atoms. In fact, the critical exponent δ is the unique such number.*

From Proposition 2.3.4, we prove alternatively that the Patterson density exists and is unique up to scalar multiplication. This observation is a key ingredient for computing the critical exponent numerically, which is used in Chapter 4 and Chapter 5.

Proof. Let $(m_x) = (m_x^+)$ be the nonzero conformal density of dimension s. We denote by $\mathbf{m} = (\mathbf{m}_e)_{e \in EX}$. Then by the assumption, $\mathbf{m}$ has positive entries.

Let $A(s)$ be a square matrix whose rows and columns are indexed by EX defined by for all $e, f \in EX$,

$$[A(s)]_{ef} = \begin{cases} e^{c(e) - sL(e)} & \text{if } e \to f \\ 0 & \text{otherwise.} \end{cases}$$

Then by Proposition 2.3.3, $\mathbf{m}$ is the eigenvector of $A(s)$ corresponding to the eigenvalue 1. We note that $A(s)$ is nonnegative irreducible matrix by the assumption of X (see [Lim08]). By the Perron-Frobenius theorem, the spectral radius $\rho(A(s))$ of $A(s)$ is equal to 1.

By the Galfand's formula, we write

$$\rho(A(s)) = \lim_{n \to \infty} \|A(s)^n\|^{\frac{1}{n}} = \lim_{n \to \infty} \left(\sum_{e_1 \cdots e_n \in \mathscr{P}_n} e^{\sum_{i=1}^m c(e_i) - s \sum_{i=1}^n L(e_i)} \right)^{\frac{1}{n}},$$

where $\mathscr{P}_n$ is the set of edge paths in X consisting of n edges. Let $L_{\min} = \min\{L(e) : e \in EX\}$. Then

$$\begin{aligned} &\frac{d}{ds} \left(\sum_{e_1 \cdots e_n \in \mathscr{P}_n} e^{\sum_{i=1}^m c(e_i) - s \sum_{i=1}^n L(e_i)} \right)^{\frac{1}{n}} \\ &= \frac{1}{n} \left(\sum_{e_1 \cdots e_n \in \mathscr{P}_n} \left(-\sum_{i=1}^n L(e_i) \right) e^{\sum_{i=1}^n c(e_i) - s \sum_{i=1}^n L(e_i)} \right) \\ &\quad \cdot \left(\sum_{e_1 \cdots e_n \in \mathscr{P}_n} e^{\sum_{i=1}^m c(e_i) - s \sum_{i=1}^n L(e_i)} \right)^{\frac{1}{n} - 1} \\ &\leq -L_{\min} \left(\sum_{e_1 \cdots e_n \in \mathscr{P}_n} e^{\sum_{i=1}^m c(e_i) - s \sum_{i=1}^n L(e_i)} \right)^{\frac{1}{n}}. \end{aligned}$$

Thus we have

$$\frac{d}{ds}\rho(A(s)) \leq -L_{\min}\rho(A(s)) < 0.$$

Since $s \mapsto \rho(A(s))$ is strictly decreasing, there is unique s such that $\rho(A(s)) = 1$. □

2.3.2 Gibbs measures

Let $\partial^2_\infty \widetilde{X}$ be the subset of $\partial_\infty \widetilde{X} \times \partial_\infty \widetilde{X}$ that consists of pairs of distinct points at infinity of $\widetilde{X}$. *Hopf's parametrization* of $\mathscr{G}\widetilde{X}$ is the homeomorphism that identifies $\mathscr{G}\widetilde{X}$ with $\partial^2_\infty \widetilde{X} \times \mathbb{R}$, by the map $\ell \mapsto (\ell_-, \ell_+, t)$, where $\ell_\pm = \lim_{t\to\pm\infty} \ell(t)$ and t is the signed distance from the closest point to the fixed basepoint x_0 on the geodesic line ℓ to $\ell(0)$. In Hopf's parametrization, we have $\varphi_s(\ell_-, \ell_+, t) = (\ell_-, \ell_+, t + s)$ for all $s \in \mathbb{R}$, and for all $\gamma \in \Gamma$, we have $\gamma(\ell_-, \ell_+, t) = (\gamma\ell_-, \gamma\ell_+, t + t_{\gamma,\ell_-,\ell_+})$, where $t_{\gamma,\ell_-,\ell_+} \in \mathbb{R}$ depends only on γ, ℓ_-, and ℓ_+. The restriction of the antipodal map to $\mathscr{G}\widetilde{X}$ is the map $(\ell_-, \ell_+, t) \mapsto (\ell_+, \ell_-, -t)$.

Definition 2.3.5. The *Gibbs measure* $\widetilde{m}_{\mathcal{I}}$ on $\mathscr{G}\widetilde{X}$ is the measure on $\mathscr{G}\widetilde{X}$ given by the density

$$d\widetilde{m}_{\mathcal{I}}(\ell) = e^{C^-(\ell_-,x_0,\ell(0))+C^+(\ell_+,x_0,\ell(0))} dm^-_{x_0}(\ell_-) dm^+_{x_0}(\ell_+) dt$$

in Hopf's parametrization with respect to the basepoint x_0.

We note that the Gibbs measure is independent of the choice of a base point x_0. The following proposition gives cohomological invariance of the Gibbs measure.

Proposition 2.3.6. *Let $\widetilde{\mathcal{I}}$ and $\widetilde{\mathcal{I}}^*$ be two cohomologous integrated potentials for Γ. Then the Gibbs measures $\widetilde{m}_{\widetilde{\mathcal{I}}}$ and $\widetilde{m}_{\widetilde{\mathcal{I}}^*}$ associated with $\widetilde{\mathcal{I}}$ and $\widetilde{\mathcal{I}}^*$, respectively, are the same up to a scalar multiple.*

Proof. By Proposition 2.3.2, we have

$$dm^{*\pm}_x(\xi) := e^{\mp H(x)} dm^\pm_x(\xi) \tag{2.9}$$

ignoring scalar multiple. Then by (2.8) and (2.9),

$$\begin{aligned} d\widetilde{m}_{\widetilde{\mathcal{I}}^*}(\ell) &= e^{C^{*-}(\ell_-,x_0,\ell(0))+C^{*+}(\ell_+,x_0,\ell(0))} dm_{x_0}^{*-}(\ell_-) dm_{x_0}^{*+}(\ell_+) dt \\ &= e^{C^{-}(\ell_-,x_0,\ell(0))+C^{+}(\ell_+,x_0,\ell(0))} dm_{x_0}^{*-}(\ell_-) dm_{x_0}^{*+}(\ell_+) dt \\ &= e^{C^{-}(\ell_-,x_0,\ell(0))+C^{+}(\ell_+,x_0,\ell(0))} dm_{x_0}^{-}(\ell_-) dm_{x_0}^{+}(\ell_+) dt \\ &= d\widetilde{m}_{\widetilde{\mathcal{I}}}(\ell). \end{aligned}$$

□

The Gibbs measure is invariant under the action of Γ and the geodesic flow φ_t. Thus, it derives a geodesic flow invariant measure $m_{\mathcal{I}}$ on $\Gamma\backslash\mathscr{G}\widetilde{X}$, we call it the *Gibbs measure* on $\Gamma\backslash\mathscr{G}\widetilde{X}$. In our case, $m_{\mathcal{I}}$ is finite and unique up to scalar multiplication.

For $\ell \in \mathscr{G}\widetilde{X}$ and $r > 0, T, T' \geq 0$, the *Bowen ball* around ℓ is

$$B(\ell; T, T', r) = \left\{ \ell' \in \mathscr{G}\widetilde{X} : \sup_{t\in[-T',T]} d_{\widetilde{X}}(\ell(t), \ell'(t)) < r \right\}.$$

The following proposition explains why the terminology of the Gibbs measure is appropriate. The proof is followed by proposition 4.5 in [BPP16].

Proposition 2.3.7. *The Gibbs measure $m_{\mathcal{I}}$ on $\Gamma\backslash\mathscr{G}\widetilde{X}$ satisfies the Gibbs property for the integrated potential $\mathcal{I}$, that is, for every compact subset K of $\Gamma\backslash\mathscr{G}\widetilde{X}$, ther exist $r > 0$ and $c = c_{K,r} \geq 1$ such that for all large enough $T, T' \geq 0$, for every $\ell \in \Gamma\backslash\mathscr{G}\widetilde{X}$ with $\varphi_{-T'}\ell, \varphi_T\ell \in K$, we have*

$$\frac{1}{c} \leq \frac{m_{\mathcal{I}}(B(\ell; T, T', r)}{e^{\mathcal{I}(\varphi_{-T'}\ell, T+T') - \delta(T+T')}} \leq c.$$

2.4 Variational principles

In this section, we define the topological pressure for an integrated potential analogous to [BPP16]. We also describe two well-known theorems: Kolmogorov-Sinai theorem (Theorem 2.4.1) and variational principle (Theorem 2.4.2). Kolmogorov-Sinai theorem is used in Section 3.1 for computing the topological pressure directly. By the variational principle, the topological pressure is equal to the critical exponent.

2.4.1 Entropy

Let (Z, T, m) be a measure-preserving dynamical system and $\mathcal{P} = \{P_1, P_2, \ldots, P_n\}$ be a finite measurable partition of Z. The *(static) entropy* of a partition $\mathcal{P}$ is defined by

$$H_m(\mathcal{P}) := -\sum_{i=1}^{n} m(P_i) \log m(P_i).$$

For partitions $\mathcal{P} = \{P_1, P_2, \ldots, P_n\}$ and $\mathcal{Q} = \{Q_1, Q_2, \ldots, Q_{n'}\}$, the *join* $\mathcal{P} \vee \mathcal{Q}$ of $\mathcal{P}$ and $\mathcal{Q}$ is a partition consiting of subsets $P_i \cap Q_j$ for all $1 \leq i \leq n$ and $1 \leq j \leq n'$. We note that the entropy $H_m(\mathcal{P} \vee T^{-1}\mathcal{P} \vee \cdots \vee T^{-k+1}\mathcal{P})$ is subadditive with respect to k. By Fekete lemma, the limit

$$h_m(\mathcal{P}, T) := \lim_{k\to\infty} \frac{1}{k} H_m(\mathcal{P} \vee T^{-1}\mathcal{P} \vee \cdots \vee T^{-k+1}\mathcal{P})$$

exists and we call $h_m(\mathcal{P}, T)$ the *entropy of the transformation T with respect to the partition $\mathcal{P}$*.

The *(measure theoretic or metric) entropy* of the transformation T is defined by

$$h_m(T) = \sup_{\mathcal{P}} h(\mathcal{P}, T),$$

where the supremum is taken over all finite meausrable partitions.

For a partition $\mathcal{P}$, if the smallest σ-algebra containing $\vee_{k=-\infty}^{\infty} T^{-k}\mathcal{P}$ is equal to the σ-algebra of Z up to measure zero sets, then we call $\mathcal{P}$ a *generator* with respect to T.

Theorem 2.4.1 (Kolmogorov-Sinai Theorem)**.** *If $\mathcal{P}$ is a generator with respect to T, then $h_m(T) = h_m(\mathcal{P}, T)$.*

Let $\mathscr{M}$ be the set of T-invariante Borel probability measures. The *topological entropy* h_{top} for T is defined by

$$h_{\text{top}} := \sup_{m\in\mathscr{M}} h_m(T).$$

For finite metric graphs, the topological entropy h_{top} for time-one map of geodesic flow is equal to the *volume entropy* h_{vol} [Gui94]. The volume entropy h_{vol} is defined by

$$h_{\text{vol}} = \lim_{r\to\infty} \frac{\log \text{vol}\widetilde{B}(x, r)}{r},$$

where $\widetilde{B}(x,r)$ is a ball in the universal covering tree of the graph with the center x and radius r. It is well-known that the volume entropy h_{vol} is independent of a choice of the center x of the ball.

2.4.2 Topological Pressure

Let $(Z,(\varphi_t)_{t\in\mathbb{R}})$ be a topological space endowed with a continuous one-parameter group of homeomorphisms and $\psi : Z \to \mathbb{R}$ be a locally constant bounded continuous map. Let $\mathscr{M}$ be the set of ϕ_t-invariant Borel probability measures. The *(metric) pressure* for ψ of a measure $m \in \mathscr{M}$ is defined by

$$P_\psi(m) := h_m(\varphi_1) + \int_Z \psi \, dm$$

and the *(topological) pressure* for ψ is defined by

$$P_\psi := \sup_{m\in\mathscr{M}} P_\psi(m).$$

We call a measure m an *equilibrium state* for ψ if $P_\psi = P_\psi(m)$.

In order to fit into our settings, we let $Z = \mathscr{G}X$ and $\mathcal{I}(\ell,t) = \int_0^t \psi(\varphi_s\ell)\, ds$ for all $\ell \in \mathscr{G}X$ and $t \geq 0$. Then we have

$$\int_{\mathscr{G}X} \psi \, dm = \sum_{e\in EX} \int_{[e]} \psi \, dm = \sum_{e\in EX} m([e])\mathcal{I}(\ell_e, L(e)) =: m(\mathcal{I}'),$$

where $[e]$ is the set of geodesics starting from e^- to dirction of e. With this observation, we define the metric pressure for $\mathcal{I}$ by

$$P_{\mathcal{I}}(m) := h_m(\varphi_1) + m(\mathcal{I}').$$

The topological pressure $P_{\mathcal{I}}$ for $\mathcal{I}$ and an equilibrium state for $\mathcal{I}$ is defined similarly. The following theorem is the main theorem of part 1 in [BPP16].

Theorem 2.4.2 (Variational Principle for finite metric graphs)**.** *Let X be a finite metric graph and $\mathcal{I}$ be an integrated potential. Then the topological pressure $P_{\mathcal{I}}$ is equal to the critical exponent $\delta_{\Gamma,\mathcal{I}}$ and the Gibbs measure $m_{\mathcal{I}}$ is the unique equilibrium state for $\mathcal{I}$.*

2.5 Coding

In this section, we describe a coding process of the discrete-time geodesic flow (Theorem 2.5.2). Then we identify the suspension flow with the continuous-time geodesic flow (Theorem 2.5.5). With this identification, we observe that a continuous-time geodesic flow invariant measure is represented by a product measure of a discrete-time geodesic flow invariant measure and the Lebesgue measure (Theorem 2.5.6). This observation is a crucial part of computational technique used in Chapter 3.

2.5.1 Two-sided subshifts of finite type

Definition 2.5.1. A two-sided topological *subshift of finite type* is a topological dynamical system (Σ, σ) constructed from a finite *alphabet* $\mathscr{A}$ and a *transition matrix* $A = (A_{ij})_{i,j\in\mathscr{A}} \in \{0,1\}^{\mathscr{A}\times\mathscr{A}}$, where Σ is the closed subset of the topological product space $\mathscr{A}^{\mathbb{Z}}$ defined by

$$\Sigma = \left\{ x = (x_n)_{n\in\mathbb{Z}} \in \mathscr{A}^{\mathbb{Z}} \ : \ \forall n \in \mathbb{Z},\ A_{x_n,x_{n+1}} = 1 \right\},$$

and $\sigma : \Sigma \to \Sigma$ is the two-sided *shift* defined by

$$(\sigma(x))_n = x_{n+1}$$

for all $x \in \Sigma$ and $n \in \mathbb{Z}$.

We note that Σ is comapct by Tychonoff's theorem.

For $p \le q$ in $\mathbb{Z}$, a finite word $(a_n)_{p\le n\le q} \in \mathscr{A}^{\{p,\dots,q\}}$ is called *admissible* if $A_{a_n,a_{n+1}} = 1$ for all $n \in \{p,\dots,q-1\}$. For an admissible word $(a_n)_{p\le n\le q}$, a *cylinder* is a subset of the form

$$[a_p,\dots,a_q] := \{(x_n)_{n\in\mathbb{Z}} \in \Sigma \ : \ \forall n \in \{p,\dots,q\},\ x_n = a_n\}.$$

A subshift of finite type is *transitive* if for all $x, y \in \mathscr{A}$, there exists an admissible word $(a_n)_{p\le n\le q}$ such that $a_p = x$ and $a_q = y$.

2.5.2 Coding discrete-time geodesic flows

We let $\mathscr{A} = EX$ and construct a subshift of finite type consisting of

$$\Sigma = \left\{ \mathbf{e} = (e_i)_{i\in\mathbb{Z}} \in \mathscr{A}^{\mathbb{Z}} \ : \ \forall i \in \mathbb{Z},\ e_i \to e_{i+1} \right\}$$

and the shift map $\sigma : \Sigma \to \Sigma$.

For $\ell \in \mathscr{G}\mathbb{X}$, let $\widetilde{\ell} \in \mathscr{G}\widetilde{\mathbb{X}}$ be a lift of ℓ with repsect to the quotient map by Γ. Let $\widetilde{e}_i(\widetilde{\ell})$ be the edge in $E\widetilde{X}$ whose topological realization is $\widetilde{\ell}([i, i+1])$, and let $e_i(\ell)$ be the quotient image of $\widetilde{e}_i(\widetilde{\ell})$ by Γ. That is,

$$e_i(\ell) = \text{ the } i\text{-th edge through } \ell \text{ in } \mathbb{X} \text{ starting from } \ell(0). \tag{2.10}$$

It is easily checked that $e_i(\ell)$ is independent of the choice of a lift $\widetilde{\ell}$ of ℓ.

Theorem 2.5.2. *The coding map $\Theta : \mathscr{G}\mathbb{X} \to \Sigma$ defined by*

$$\ell \mapsto \mathbf{e}(\ell) = (e_i(\ell))_{i\in\mathbb{Z}}$$

is a homeomorphism that conjugates the time-one discrete geodesic flow φ_1 and the shift σ; that is, the following diagram commutes

$$\begin{array}{ccc} \mathscr{G}\mathbb{X} & \xrightarrow{\varphi_1} & \mathscr{G}\mathbb{X} \\ {\scriptstyle\Theta}\downarrow & & \downarrow{\scriptstyle\Theta} \\ \Sigma & \xrightarrow{\sigma} & \Sigma. \end{array}$$

Furthermore, if we endow $\mathscr{G}\mathbb{X}$ with the quotient distance $d_{\mathscr{G}\mathbb{X}}$ of

$$d_{\mathscr{G}\widetilde{\mathbb{X}}}(\widetilde{\ell}, \widetilde{\ell}') = e^{-\sup\left\{n\in\mathbb{N} \,:\, \widetilde{\ell}|_{[-n,n]} = \widetilde{\ell}'|_{[-n,n]}\right\}}$$

on $\mathscr{G}\widetilde{\mathbb{X}}$ and Σ with the distance

$$d_\Sigma(\mathbf{e}, \mathbf{e}') = e^{-\sup\left\{n\in\mathbb{N} \,:\, \forall i\in\{-n,\dots,n\},\, \mathbf{e}_i = \mathbf{e}'_i\right\}},$$

then Θ is a bilipschitz homeomorphism.

Proof. Let $\widetilde{\ell}, \widetilde{\ell}' \in \mathscr{G}\widetilde{\mathbb{X}}$ with $\gamma\widetilde{\ell} = \widetilde{\ell}'$ for some $\gamma \in \Gamma$. Then we have $\gamma\widetilde{e}_i(\widetilde{\ell}) = \widetilde{e}_i(\gamma\widetilde{\ell}) = \widetilde{e}_i(\widetilde{\ell}')$ for all $i \in \mathbb{Z}$, hence the map Θ is well-defined.

For $\ell \in \mathscr{G}\mathbb{X}$, we have $\ell(i) = e_i(\ell)^-$ for all $i \in \mathbb{Z}$. Thus $\varphi_1\ell(i) = e_{i+1}(\ell)^- = (\sigma\mathbf{e}(\ell))_i^-$ for all $i \in \mathbb{Z}$ so that the map Θ is equivariant for φ_1 and σ.

Let $\widetilde{\ell}, \widetilde{\ell}' \in \mathscr{G}\widetilde{\mathbb{X}}$ with $\widetilde{\ell}|_{[-n,n]} = \widetilde{\ell}'|_{[-n,n]}$ for some $n \in \mathbb{N}$. Then we have $\widetilde{e}_i(\widetilde{\ell}) = \widetilde{e}_i(\widetilde{\ell}')$ for all $-n \le i \le n-1$. Thus

$$d_\Sigma(\Theta(\ell), \Theta(\ell')) \le e\, d_{\mathscr{G}\mathbb{X}}(\ell, \ell'),$$

that is, Θ is Lipschitz. In particular, Θ is continuous.

Now, we will construct an inverse $\Psi : \Sigma \to \mathscr{G}\mathbb{X}$ of Θ and show that it is Lipschitz. Let $\mathbf{e} = (e_i)_{i\in\mathbb{Z}} \in \Sigma$ and fix a lift $\widetilde{e}_0$ of e_0. By the construction of Σ, we may choose $\widetilde{e}_{-1}$ and $\widetilde{e}_1$ such that $\widetilde{e}_{-1} \to \widetilde{e}_0 \to \widetilde{e}_1$. Inductively, for given $\widetilde{e}_i, i \in \mathbb{Z}$, choose $\widetilde{e}_{i-1}$ or $\widetilde{e}_{i+1}$ satisfying $\widetilde{e}_{i-1} \to \widetilde{e}_i \to \widetilde{e}_{i+1}$. We define $\widetilde{\ell} : \mathbb{Z} \to V\widetilde{\mathbb{X}}$ by $\widetilde{\ell}(i) = \widetilde{e}_i^-$. Then $\widetilde{\ell} \in \mathscr{G}\widetilde{\mathbb{X}}$ and its image ℓ by the natural quotient map $\mathscr{G}\widetilde{\mathbb{X}} \to \mathscr{G}\mathbb{X}$ maps to $\mathbf{e}$ by Θ. We define $\Psi(\mathbf{e}) = \ell$. Note that ℓ is independent of the choice of lift $\widetilde{e}_0$ and hence Ψ is well-defined inverse of Θ. T For $\mathbf{e}, \mathbf{e}' \in \Sigma$ with $e_i = e'_i$ for all $-n \le i \le n$ for some $n \in \mathbb{N}$, let $\ell = \Psi(\mathbf{e})$ and $\ell' = \Psi(\mathbf{e}')$. Then $\ell|_{[-n,n+1]} = \ell'|_{[-n,n+1]}$ and hence

$$d_{\mathscr{G}\mathbb{X}}(\Psi(\mathbf{e}), \Psi(\mathbf{e}')) \le d_\Sigma(\mathbf{e}, be').$$

Thus Ψ is Lipschitz and continuous. □

For an integrated potential $\mathcal{I}$ for $\mathscr{G}\mathbb{X}$, we define a potential F_{symb} on Σ defined by for $\mathbf{e} = (e_i)_{i\in bZ} \in \Sigma$,

$$F_{\mathrm{symb}}(\mathbf{e}) = c(e_0),$$

where c is a system of conductances on $E\mathbb{X}$.

For the Gibbs measure $m_{\mathcal{I}}$ on $\mathscr{G}\mathbb{X}$, we derive the measure $m_{\mathrm{symb},\mathcal{I}}$ on Σ defined by

$$m_{\mathrm{symb},\mathcal{I}} = \Theta_* m_{\mathcal{I}}.$$

We call $m_{\mathrm{symb},\mathcal{I}}$ the Gibbs measure on Σ. The following proposition comes from p.112 in [BPP16].

Proposition 2.5.3. *The Gibbs measure $m_{\mathrm{symb},\mathcal{I}}$ on Σ satisfies the Gibbs property with the cosntant δ for the potential F_{symb}.*

2.5.3 Suspensions

Let (Σ, σ) be the subshift of finite type which is homeomorhpic to $(\mathscr{G}\mathbb{X}, \varphi_1)$ and $m_{\mathrm{symb},\mathcal{I}}$ be the Gibbs measure on Σ. Define a function $r : \Sigma \to \mathbb{R}_{>0}$ by for $\mathbf{e} = (e_i)_{i\in\mathbb{Z}}$,

$$r(\mathbf{e}) = L(e_0).$$

Definition 2.5.4. The *suspension* over (Σ, σ) with *roof function* r is the continuous-time dynamical system $(\Sigma_r, (\sigma_{r,t})_{t\in\mathbb{R}})$ constructed as follows.

(1) The space Σ_r is the quotient topological space $(\Sigma \times \mathbb{R})/\sim$, where $\sim$ is hte equivalence relation on $\Sigma \times \mathbb{R}$ generated by $(\mathbf{e}, , s + r(\mathbf{e})) \sim (\sigma(\mathbf{e}), s)$ for all $(\mathbf{e}, s) \in \Sigma \times \mathbb{R}$.

(1) For all $t \in \mathbb{R}$, the map $\sigma_{r,t} : \Sigma_r \to \Sigma_r$ is defined by

$$\sigma_{r,t}([\mathbf{e}, s]) = [\mathbf{e}, s + t],$$

where $[\mathbf{e}, s]$ is the equivalence class of $(\mathbf{e}, s) \in \Sigma \times \mathbb{R}$.

We endow Σ_r with the *Bowen-Walters distance* (see [BW72] and [BS00]). Note that the set

$$\mathscr{F} = \{(\mathbf{e}, s) \ : \ \mathbf{e} \in \Sigma, \ 0 \leq s < r(\mathbf{e})\}$$

is a measurable strict funcamental domain for the equivalence relation of Σ_r. Then $\sigma_{r,t}$ can be defined on $\mathscr{F}$ equivalently by for $(\mathbf{e}, s) \in \mathscr{F}$,

$$\sigma_{r,t}(\mathbf{e}, s) = (\sigma^n(\mathbf{e}), s'),$$

where $n \in \mathbb{N}$ and $s' \in \mathbb{R}$ are such that

$$t + s = \sum_{i=0}^{n=1} r(\sigma^i \mathbf{e}) + s' \quad \text{and} \quad 0 \leq s' < r(\sigma^n \mathbf{e}).$$

We define the Gibbs measure $m_{\mathrm{symb},\mathcal{I},r}$ on Σ_r using the identification with $\mathscr{F}$ by the pushforward of the restriction from $\Sigma \times \mathbb{R}$ to $\mathscr{F}$ of the product measure $dm_{\mathrm{symb},\mathcal{I}}ds$. Here, ds is the Lebesgue measure on $\mathbb{R}$.

2.5.4 Coding continuous-time geodesic flows

From now, in order to distinguish the discrete-time and continuous-time situation, we use the left exponent $\sharp$ to indicate a discrete-time object whenever needed. For instance, we set ${}^{\sharp}X = |\mathbb{X}|_1$ and we denote by $({}^{\sharp}\varphi_t)_{t\in\mathbb{Z}}$ the discrete-time geodesic flow on $\mathscr{G}\mathbb{X}$.

For $\ell \in \mathscr{G}X$, let

$$\tau^-(\ell) = \sup\{t < 0 \ : \ \ell(t) \in VX\}.$$

The following theorem is from [BS00].

Theorem 2.5.5. *The continuous-time dynamical system $(\mathscr{G}X, (\varphi_t)_{t\in\mathbb{R}})$ is isomorphic to the suspension $(\Sigma_r, (\sigma_{r,t})_{t\in\mathbb{R}})$ by a bilipschitz homeomorphism $\Theta_r : \mathscr{G}X \to \Sigma_r$ defined by*

$$\ell \mapsto [\Theta\left(\varphi_{\tau^-(\ell)}\ell\right), -\tau^-(\ell)].$$

For the Gibbs measure $m_{\mathcal{I}}$ on $\mathscr{G}X$, we endow the measure $m_{\mathrm{symb},\mathcal{I}}$ on Σ_r defined by

$$m_{\mathrm{symb},\mathcal{I}} = (\Theta_r)_* m_{\mathcal{I}}.$$

We call $m_{\mathrm{symb},\mathcal{I}}$ the Gibbs measure on Σ_r.

The following theorem is the key observation of φ_t-invariant measures on the space of geodesics for this thesis. The proofs for symbolic cases are in [LL09]. Using the coding map described above, the theorem follows.

Theorem 2.5.6. *1. $P_{\mathcal{I}}$ is given by the unique number t_0 such that the topological pressure of $\mathscr{G}\mathbb{X}$ for $c - t_0 L$ is equal to 0.*

2. *For ${}^\sharp\varphi_n$-invariant meausre ${}^\sharp m$ on $\mathscr{G}\mathbb{X}$, the measure m on $\mathscr{G}X$ of the form $dm = d^\sharp m ds$ is φ_t-invariant. Conversely, any φ_t-invariant measure m on $\mathscr{G}X$ is the product measure (after normalizing if necessary) of some ${}^\sharp\varphi_n$-invariant measure on $\mathscr{G}\mathbb{X}$ and the Lebesgue measure on $\mathbb{R}$.*

3. *For the Gibbs measure ${}^\sharp m_{c-t_0 L}$ on $\mathscr{G}\mathbb{X}$, the Gibbs meausre $m_{\mathcal{I}}$ on $\mathscr{G}X$ is represented by*

$$dm_{\mathcal{I}} = \frac{d^\sharp m_{c-t_0 L} ds}{\int_{\mathscr{G}\mathbb{X}} r \; d^\sharp m_{c-t_0 L}}.$$

Chapter 3

Equivalence of boundary measures

In [Lyo94], Lyons found the condition to the equivalence of three measures (visibility measure, Patterson-Sullivan measure, and harmonic measure) on the boundary of the universal covering tree of simplicial graphs. The simplicial graph in [Lyo94] is assumed that every vertex has degree at least 2 and some vertex has degree more than 2. If $e_1, \ldots, e_n$ is an edge path without backtracking whose intermediate vertices have degree 2, then we may regard the edge path as an edge with length n. Thus the simplicial graph is indeed the metric graph with integer edge lengths. Lyons constructed the three measures as Markov measures of which transition probabilities are obtained from some combinatorial matrix computations. Comparing these transition probabilities, Lyons proves that two of the three measures coincide if and only if there are certain edge lengths as follows.

Theorem 3.0.1 (Lyons)**.**

1. *The visibility measures and the Patterson-Sullivan meausres coincide if and only if for all $e \in EX$,*

$$L(e) = \frac{1}{h_{\mathrm{vol}}} \log(\deg(e^-) - 1)(\deg(e^+) - 1);$$

2. *The visibility measures and the harmonic measures coincide if and only*

if there exists $c > 0$ such that for all $e \in EX$,

$$L(e) = c\left(1 - \frac{1}{\deg(e^-)} - \frac{1}{\deg(e^+)}\right);$$

3. *The Patterson-Sullivan measures and the harmonic measures coincide if and only if for all $e \in EX$,*

$$\frac{L(e)e^{h_{\mathrm{vol}}L(e)}}{e^{2h_{\mathrm{vol}}L(e)} - 1} = K(e^-)K(e^+),$$

where for $x \in VX$,

$$K(x)^2 = \frac{1 + \sum_{e^-=x} \frac{1}{e^{2h_{\mathrm{vol}}L(e)}-1}}{\sum_{e^-=x} \frac{1}{L(e)}}.$$

However, the constructions are not naturally generalized to metric graphs with real edge lengths. In this chapter, we introduce new methods for constructing boundary measures dynamically. Moreover, we prove the generalized statements of Theorem 3.0.1 in Section 3.4. Our results are different from Theorem 3.0.1 in two respects: (1) we assume that edge lengths can be real numbers, (2) we consider the cases in that two boundary measures are equivalent not only coincide.

We first set notations used in this chapter. Denote the set of edge paths without backtracking in $\mathscr{G}\mathbb{X}$ of length n by $\mathscr{P}_n$.

For any $e_1 \cdots e_n \in \mathscr{P}_n$, define a *cylinder* of $\mathscr{G}\mathbb{X}$ by

$$^\sharp[e_1 \cdots e_m] := \{^\sharp\ell \in \mathscr{G}\mathbb{X} \ : \ ^\sharp\ell([i-1, i]) = e_i, \ \forall i = 1, \ldots, m\}$$

We note that the family $\{[e]\}_{e \in EX}$ forms a partition for $\mathscr{G}\mathbb{X}$ and it is a generator with resepct to $^\sharp\varphi_n$. For $1 \le k \le m$, define

$$[\underline{e_1 \cdots e_k} \cdots e_m] = \{\ell \in \mathscr{G}X \ : \ e_1 \cdots e_m \subset \operatorname{Im}\ell, \ \ell(0) \in e_1 \cdots e_k\}$$

If $z_i = e_i^-$ for $i = 1, \ldots, m$ and $z_{m+1} = e_m^+$, then we also denote $[\underline{e_1 \cdots e_k} \cdots e_m]$ by $[\underline{z_1 \cdots z_{k+1}} \cdots z_{m+1}]$.

3.1 Visibility measures

Let $\widetilde{M}$ be a complete simply connected Riemannian manifold, with dimension at least 2 and pinched sectional curvature at most -1 and Γ be a non-elementary discrete group of isometries of $\widetilde{M}$. The geometric potential $\widetilde{F}_G : T^1\widetilde{M} \to \mathbb{R}$ is defined by

$$\widetilde{F}_G(\mathbf{v}) = -\left.\frac{d}{dt}\right|_{t=0} \log \mathrm{Jac}\left(\varphi_t|_{W^{su}(\mathbf{v})}\right)(\mathbf{v}),$$

where $\mathrm{Jac}\left(\varphi_t|_{W^{su}(\mathbf{v})}\right)$ is the Jacobian (see [PPS12]). The geoemtric potential is the negative of the pointwise exponential growth rate of the Jacobian of the geodesic flow restricted to the strong unstable manifold. We note that

$$\int_0^t \widetilde{F}_G(\varphi_s\mathbf{v})ds = -\log \mathrm{Jac}\left(\varphi_t|_{W^{su}(\mathbf{v})}\right)(\mathbf{v}) \tag{3.1}$$

is the negative of the exponential growth rate of the volume on the strong unstable manifold $W^{su}(\mathbf{v})$ under the geodesic flow φ_t.

Let $\ell \in \mathscr{G}\widetilde{X}$ and $B^{su}(\ell, \epsilon)$ be the ball in $W^{su}(\ell)$ with the center ℓ and radius $\epsilon > 0$. Then by the definition of $d_{\mathscr{G}\widetilde{X}}$ (2.1), we have for sufficiently small ϵ,

$$B^{su}(\ell, \epsilon) = \{\ell' \in W^{su}(\ell) \ : \ \pi(\ell') = \pi(\ell)\}.$$

For $t > 0$, we observe that

$$\varphi_{-t}B^{su}(\varphi_t\ell, \epsilon) = \{\ell' \in W^{su}(\ell) \ : \ \ell|_{[0,t]} = \ell'|_{[0,t]}\}.$$

From the observation, we define (3.1) on the metric graph by the logarithm of the ratio of the measures of $\varphi_{-t}B^{su}(\varphi_t\ell, \epsilon)$ and $B^{su}(\varphi_t\ell, \epsilon)$.

Now, let $x \in V\widetilde{X}$ and $\ell \in \mathscr{G}\widetilde{X}$ with $\pi(\ell) = x$. Let $y \in V\widetilde{X}$ be the first vertex meeting along ℓ at time t. Then we may approximate (3.1) on the metric graph by

$$\log \frac{1}{\deg(y) - 1}.$$

We define the analogue of the geometric potential on metric graphs as follows.

For $x \in V\widetilde{X}$, we denote the degree of x by $d(x)$ which is the number of edges in $\widetilde{X}$ starting from x. For convenience, we define a notation $\delta(x) := d(x) - 1$.

Definition 3.1.1. The *integrated geometric potential* $\widetilde{\mathcal{I}}_G(\ell, t)$ along the geodesic

$\ell \in \mathscr{G}\widetilde{X}$ until time $t \geq 0$ is defined by

$$\widetilde{\mathcal{I}}_G(\ell, t) := \sum_{i=1}^{n} \log \frac{1}{\delta(x_i)},$$

where $x_1, \ldots, x_n \in V\widetilde{X}$ are vertices in $\ell|_{(0,t]}$ considering the order.

Let $\mathscr{M}$ be the set of all φ_t-invariante Borel probability measure on $\mathscr{G}X$. For simplicity, we denote the metric potential for $\mathcal{I}_G$ of $m \in \mathscr{M}$ by $P_G(m)$ and the topological potential for $\mathcal{I}_G$ by P_G.

Theorem 3.1.2. *For all $m \in \mathscr{M}$, we have $P_G(m) \leq 0$. Hence we have $P_G \leq 0$.*

Proof. Let $m \in \mathscr{M}$. Then by Theorem 2.5.6 2, there exists a ${}^\sharp\varphi_n$-invariant measure ${}^\sharp m$ on $\mathscr{G}\widetilde{\mathbb{X}}$ such that

$$dm = \frac{d^\sharp m ds}{\int_{\mathscr{G}\mathbb{X}} r \, d^\sharp m}.$$

It follows that $h_m(\varphi_1) = h_{\sharp_m}({}^\sharp\varphi_1) / \int_{\mathscr{G}\widetilde{\mathbb{X}}} r \, d^\sharp m$ (see [Abr59]). By Theorem 2.4.1, we have

$$h_{\sharp_m}({}^\sharp\varphi_1) = \lim_{n\to\infty} -\frac{1}{n} \sum_{e_1\cdots e_n \in \mathscr{P}_n} {}^\sharp m([e_1 \cdots e_n]) \log {}^\sharp m([e_1 \cdots e_n]).$$

Then

$$\begin{aligned}
&\sum_{e_1\cdots e_n \in \mathscr{P}_n} {}^\sharp m([e_1 \cdots e_n]) \log {}^\sharp m([e_1 \cdots e_n]) \\
&= \sum_{e_1\cdots e_n \in \mathscr{P}_n} \frac{{}^\sharp m([e_1 \cdots e_n])}{{}^\sharp m([e_1 \cdots e_{n-1}])} {}^\sharp m([e_1 \cdots e_{n-1}]) \\
&\qquad \cdot \left(\log \frac{{}^\sharp m([e_1 \cdots e_n])}{{}^\sharp m([e_1 \cdots e_{n-1}])} + \log {}^\sharp m([e_1 \cdots e_{n-1}]) \right) \\
&= \sum_{e_1\cdots e_{n-1} \in \mathscr{P}_{n-1}} {}^\sharp m([e_1 \cdots e_{n-1}]) \left(\sum_{e_n : e_{n-1} \to e_n} \frac{{}^\sharp m([e_1 \cdots e_n])}{{}^\sharp m([e_1 \cdots e_{n-1}])} \log \frac{{}^\sharp m([e_1 \cdots e_n])}{{}^\sharp m([e_1 \cdots e_{n-1}])} \right) \\
&\quad + \sum_{e_1\cdots e_{n-1} \in \mathscr{P}_{n-1}} \left(\sum_{e_n : e_{n-1} \to e_n} \frac{{}^\sharp m([e_1 \cdots e_n])}{{}^\sharp m([e_1 \cdots e_{n-1}])} \right) {}^\sharp m([e_1 \cdots e_{n-1}]) \log {}^\sharp m([e_1 \cdots e_{n-1}]).
\end{aligned}$$

Here, we note that

$$\sum_{e_n:e_{n-1}\to e_n} \frac{{}^\sharp m([e_1\cdots e_n])}{{}^\sharp m([e_1\cdots e_{n-1}])} = 1$$

and

$$\begin{aligned}
&\sum_{e_1\cdots e_{n-1}\in\mathscr{P}_{n-1}} {}^\sharp m([e_1\cdots e_{n-1}]) \left(\sum_{e_n:e_{n-1}\to e_n} \frac{{}^\sharp m([e_1\cdots e_n])}{{}^\sharp m([e_1\cdots e_{n-1}])} \log \frac{{}^\sharp m([e_1\cdots e_n])}{{}^\sharp m([e_1\cdots e_{n-1}])} \right) \\
&\qquad \geq \sum_{e_1\cdots e_{n-1}\in\mathscr{P}_{n-1}} {}^\sharp m([e_1\cdots e_{n-1}]) \left(\sum_{e_n:e_{n-1}\to e_n} \frac{1}{\delta(e_{n-1}^+)} \log \frac{1}{\delta(e_{n-1}^+)} \right) \\
&\qquad = \sum_{e_1\cdots e_{n-1}\in\mathscr{P}_{n-1}} {}^\sharp m([e_1\cdots e_{n-1}]) \log \frac{1}{\delta(e_{n-1}^+)} \\
&\qquad = \sum_{e\in EX} \sum_{\substack{e_1,\ldots,e_{n-2}\in EX \\ e_1\cdots e_{n-2}\in\mathscr{P}_{n-2} \\ e_1\cdots e_{n-2}\to e}} {}^\sharp m([e_1\cdots e_{n-2}e]) \log \frac{1}{\delta(e^+)} \\
&\qquad = \sum_{e\in EX} {}^\sharp m([e]) {}^\sharp\mathcal{I}_G(\ell_e, L(e)) \\
&\qquad = {}^\sharp m({}^\sharp\mathcal{I}'_G)
\end{aligned}$$

Thus we have

$$\begin{aligned}
&\sum_{e_1\cdots e_n\in\mathscr{P}_n} {}^\sharp m([e_1\cdots e_n]) \log {}^\sharp m([e_1\cdots e_n]) \\
&\qquad \geq \sum_{e_1\cdots e_{n-1}\in\mathscr{P}_{n-1}} {}^\sharp m([e_1\cdots e_{n-1}]) \log {}^\sharp m([e_1\cdots e_{n-1}]) + {}^\sharp m({}^\sharp\mathcal{I}'_G) \\
&\qquad \geq \cdots \geq \sum_{e\in EX} {}^\sharp m([e]) \log {}^\sharp m([e]) + (n-1) {}^\sharp m({}^\sharp\mathcal{I}'_G)
\end{aligned}$$

so that

$$h_{{}^\sharp m}({}^\sharp\varphi_1) \leq \lim_{n\to\infty} -\frac{1}{n} \left(\sum_{e\in EX} {}^\sharp m([e]) \log {}^\sharp m([e]) + (n-1) {}^\sharp m(\mathcal{I}'_G) \right) = -{}^\sharp m({}^\sharp\mathcal{I}'_G).$$

For all $m \in \mathscr{M}$,

$$P_G(m) = h_m(\varphi_1) + m(\mathcal{I}'_G) = \frac{h_{\sharp m}(^\sharp\varphi_1) + {}^\sharp m(^\sharp\mathcal{I}'_G)}{\int_{\mathscr{G}\mathbb{X}} r \, d^\sharp m} \leq 0.$$

□

We define a measure m_L on $\mathscr{G}X$ such that

$$m_L\left([\underline{z_1 \cdots z_k} \cdots z_m]\right) = \frac{d_X(z_1, z_k)}{\delta(z_1) \cdots \delta(z_m)}.$$

Then m_L is a finite positive Borel measure on $\mathscr{G}X$ which is φ_t invariant. We denote $\widehat{m}_L = \frac{m_L}{\|m_L\|}$.

Theorem 3.1.3. *We have $h_{\widehat{m}_L} + \widehat{m}_L(\mathcal{I}'_G) = 0$, i.e. $\widehat{m}_L$ is the equilibrium state for $\mathcal{I}_G$ and $P_G = 0$.*

Proof. Let ${}^\sharp m_L$ be a measure on $\mathscr{G}\mathbb{X}$ such that

$${}^\sharp m_L([e_1 \cdots e_m]) = \frac{1}{\delta(e_1^-) \cdots \delta(e_m^+)}$$

and denote ${}^\sharp\widehat{m}_L = \frac{{}^\sharp m_L}{\|{}^\sharp m_L\|}$. Then

$$d\widehat{m}_L = \frac{d^\sharp \widehat{m}_L ds}{\int_{\mathscr{G}\mathbb{X}} r \, d^\sharp m}.$$

We note that ${}^\sharp m_L$ is a Markov measure. Thus

$$\begin{aligned}
h_{\widehat{m}_L} \int_{\mathscr{G}\mathbb{X}} r \, d^\sharp m &= h_{{}^\sharp \widehat{m}_L} \\
&= -\sum_{e_1e_2 \in \mathscr{P}_2} {}^\sharp \widehat{m}_L([e_1e_2]) \log \frac{{}^\sharp \widehat{m}_L([e_1e_2])}{{}^\sharp \widehat{m}_L([e_1])} \\
&= -\sum_{e_1e_2 \in \mathscr{P}_2} {}^\sharp \widehat{m}_L([e_1e_2]) \log \frac{{}^\sharp m_L([e_1e_2])}{{}^\sharp m_L([e_1])} \\
&= -\sum_{e_1e_2 \in \mathscr{P}_2} {}^\sharp \widehat{m}_L([e_1e_2]) \log \frac{1}{\delta(e_2^-)} \\
&= -\sum_{e_1 \in EX} {}^\sharp \widehat{m}_L([e_1]) \log \frac{1}{\delta(e_1^+)} \\
&= -{}^\sharp \widehat{m}_L({}^\sharp \mathcal{I}'_G) \\
&= -\widehat{m}_L(\mathcal{I}'_G) \int_{\mathscr{G}\mathbb{X}} r \, d^\sharp m.
\end{aligned}$$

□

Definition 3.1.4. The *visibility measures* $(\lambda_x^\pm)_{x \in \widetilde{X}}$ are Patterson density for $\mathcal{I}_G^\pm$. We denote the Gibbs measure $m_{\mathcal{I}_G}$ by λ for simlicity.

Lemma 3.1.5. *There exists $C > 0$ such that the following holds: For $x, y \in V\widetilde{X}$, if $x, z_1, \ldots, z_m, y \in V\widetilde{X}$ are vertices containing in the geodesic segment between x and y (considering the order), then*

$$\lambda_x^\pm(\mathcal{O}_x(y)) = \frac{C}{\delta(z_1) \cdots \delta(z_m)}.$$

Proof. We prove only for the case of λ_x^+. The proof for the case of λ_x^- is not quite different. As we describe in Section 2.3.1, the visibility measures are determined by the values $\lambda_x^+(\mathcal{O}_x(y))$ for all $x \sim y \in V\widetilde{X}$. Therefore, by Proposition 2.3.3, it suffices to show that the constant vector

$$\left(\lambda_{xy}^+\right)_{x \sim y \in V\widetilde{X}} := (C)_{x \sim y \in V\widetilde{X}}$$

forms the eigenvector of $A_{\mathcal{I}_G}$ corresponding to the eigenvalue 1.

Let $x \sim y \in V\widetilde{X}$. Then

$$e^{\mathcal{I}_G(\ell_{xy}, L(x,y))} \sum_{z\,:\,y\sim z\neq x} \lambda^+_{yz} = \frac{1}{\delta(y)} \sum_{z\,:\,y\sim z\neq x} C = C = \lambda^+_{xy}.$$

Since the Patterson density is unique up to scalar multiplication, we may choose $C > 0$ for given scale of the visibility measure. □

Remark 3.1.6. *Lemma 3.1.5 is the natural extension for metric graphs of the visibility measures in [Lyo94]. In Lyons' setting, the visibility measure at x is the solid angle seen from x. In fract, the lemma implies that the Lyons' visibility measures are $d(x)\lambda^+_x$ in the terms of the our settings However, we observe that the visibility measures in our definition and Lyons' definition are equivalent and hence their Gibbs measures coincide.*

Theorem 3.1.7. *We have*

$$\frac{m_L}{\|m_L\|} = \frac{\lambda}{\|\lambda\|}.$$

Proof. The proof is immediate from the uniqueness of the equilibrium state. However, we prove the theorem by direct calculation.

Let $z_1, \ldots, z_m$ be vertices in X lying on a geodesic segment. Then

$$\begin{aligned}
&\lambda([\underline{z_1 \cdots z_k} \cdots z_m]) \\
&= \sum_{i=1}^{k-1} \lambda([z_1 \cdots \underline{z_i z_{i+1}} \cdots z_m]) \\
&= \sum_{i=1}^{k-1} \lambda^-_{z_1}(\mathcal{O}_{z_2}(z_1)) \frac{1}{\delta(z_1)\cdots\delta(z_i)} \lambda^+_{z_m}(\mathcal{O}_{z_{m-1}}(z_m)) \frac{1}{\delta(z_{i+1})\cdots\delta(z_m)} d_X(z_i, z_{i+1}) \\
&= C^2 \frac{d_X(z_1, z_k)}{\delta(z_1)\cdots\delta(z_m)} \\
&= C^2 m_L([\underline{z_1 \cdots z_k} \cdots z_m]).
\end{aligned}$$

□

3.2 Patterson-Sullivan measures

Patterson-Sullivan meausres were introduced in [Pat76], [Sul79] for a Kleinian group actin on the boundary of a hyperbolic space. It was extended in [Coo93]

to a group acting geometrically (see also [Bou95], [BM96], [HP97], [Pau97], and [CP99], [Fur02]). Patterson-Sullivan measures on the universal covering trees of finite simplicial graphs were studied in [Lyo94] and [CP97]. In [BPP16], Patterson-Sullivan measures are generalized with potential functions which is Patterson densities. In this historical observation, we define Patterson-Sullivan measures in our setting as follows.

We call the Patterson density for $\mathcal{I} \equiv 0$ the *Patterson-Sullivan measures* (PS measures), denoted by $(\mu_x^{\pm})_{x \in \widetilde{X}}$. In this case, the critical exponent δ of which PS measures are nonzero and have no atoms is equal to the volume entropy h_{vol}.

Recall that the boundary $\partial_\infty \widetilde{X}$ of the univeral covering tree of a metric grpah adopts the *visual distance* defined as follows.

$$d_{\partial_\infty \widetilde{X}}(\rho, \rho') = e^{-\sup\{t \geq 0 \,:\, \rho|_{[0,t]} = \rho'|_{[0,t]}\}}.$$

Lyons proves for simplicial graphs that the volume entropy (or critical exponent for $^\sharp\widetilde{\mathcal{I}} \equiv 0$) is equal to the Hausdorff dimension of $\partial_\infty \widetilde{\mathbb{X}}$ for the visual distance and the Patterson-Sullivan measures coincides with the Hausdorff measures for the Hausdorff dimension [Lyo94]. These observations are extended to metric grpahs in [BPP16]. From these results, the values of the Patterson-Sullivan measures are characterized by the eigenvalue of some matrix [Lyo94, KN07].

Moreover, We denote the Gibbs measure for $\mathcal{I} \equiv 0$ by μ which is called the *Bowen-Margulis measure* [Rob03]. The Bowen-Margulis measure has an important meaning in that it maximizes the measure-theoretic entropy.

3.3 Harmonic measures

Let M be a compact connected Riemannian manofold with pinched negative sectional curvatures and $\widetilde{M}$ be the universal cover of M. The harmonic measures on the boundary of $\widetilde{M}$ is defined by the hitting measure for Brownian motion. The harmonic measures are equivalent each other and their Radon-Nikodym derivatives are the Martin kernel K. The harmonic potential $\widetilde{F}_H : T^1\widetilde{M} \to \mathbb{R}$ is defined by

$$\widetilde{F}_H(\mathbf{v}) = -\left.\frac{d}{dt}\right|_{t=0} \log K(\ell_{\mathbf{v}}(0), \ell_{\mathbf{v}}(t), (\ell_{\mathbf{v}})_+),$$

where ℓ is the geodesic starting at $\pi(\mathbf{v})$ to direction of $\mathbf{v}$. In this section, we define the harmonic measures and harmonic potential for metric graphs analogous to the manifold cases.

Let $(\Omega, \mathbb{P})$ be a probability space and $B_t^x : \Omega \to \widetilde{X}$ be a Brownian motion starting from $x \in \widetilde{X}$. For $x, y \in \widetilde{X}$ and $t \in \mathbb{R}$, we denote the heat kernel by $p(t, x, y)$. The *green function* $G : \widetilde{X} \times \widetilde{X} \to \mathbb{R}$ is defined by

$$G(x, y) = \int_0^\infty p(t, x, y)\, dt.$$

Since we assume degree of each vertex in $\widetilde{X}$ is more than or equal to 3, the Brownian motion is transitive. Thus the green function G has finite values.

We first define the harmonic measures $(\nu_x^+)_{x \in \widetilde{X}}$ as follows.

Definition 3.3.1. The *harmonic measures* $(\nu_x^+)_{x \in \widetilde{X}}$ is defined on $\partial_\infty \widetilde{X}$ by

$$\nu_x^+ = (B_\infty^x)_* \mathbb{P}.$$

In order to define the harmonic meausres $(\nu_x^-)_{x \in \widetilde{X}}$, we define the integrated harmonic potential from $(\nu_x^+)_{x \in \widetilde{X}}$.

Definition 3.3.2. The *Martin kernel* $K : \widetilde{X} \times \widetilde{X} \times \partial_\infty \widetilde{X} \to \mathbb{R}$ is defined by a Radon-Nikodym derivative of harmonic measures as follows. For $x, y \in \widetilde{X}$ and $\xi \in \partial_\infty \widetilde{X}$,

$$K(x, y, \xi) = \frac{d\nu_y^+}{d\nu_x^+}(\xi).$$

The *integrated harmonic potential* $\widetilde{\mathcal{I}}_H(\ell, t)$ along the geodesic $\ell \in \mathscr{G}\widetilde{X}$ until time $t \geq 0$ is defined by

$$\widetilde{\mathcal{I}}_H(\ell, t) := -\log K(\ell(0), \ell(t), \ell_+).$$

The *Martin boundary* is the boundary of the image of the embedding defined by $y \mapsto K(x_0, \cdot, y)$ on $\widetilde{X}$. In fract, the harmonic measures are defined on the Martin boundary. However, we may regard they defined on $\partial_\infty \widetilde{X}$ since the Martin boundary and the Gromov boundary coincide [HL19].

Theorem 3.3.3. *For $x, y \in \widetilde{X}$,*

$$K(x, y, (\ell_{xy})_+) = \frac{G(y, y)}{G(x, y)}.$$

Thus we have for $x, y \in V\widetilde{X}$ and $e \in E\widetilde{X}$ with $e^- = x$ and $e^+ = y$,

$$\widetilde{c}(e) = \widetilde{\mathcal{I}}_H(\ell_e, L(e)) = \log \frac{G(x,y)}{G(y,y)}.$$

To prove the theorem we first introduce the lemma.

Lemma 3.3.4. *For $x, y \in \widetilde{X}$, we have*

$$\frac{G(x,y)}{G(y,y)} = \mathbb{P}_x[\tau_y < \infty],$$

where $\mathbb{P}_x$ is the probability measure on Ω supported on the Brownian motion starting from x.

Proof. Let

$$L_t^x := \int_0^T \mathbb{1}_{\{B_t = x\}}\, dt.$$

Then

$$\begin{aligned}\mathbb{E}_x[L_\infty^y] &= \mathbb{E}_x\left[\int_0^\infty \mathbb{1}_{\{B_t=y\}}\, dt\right] = \int_0^\infty \mathbb{P}_x[B_t = y] \\ &= \int_0^\infty p(t,x,y)\, dt = G(x,y).\end{aligned}$$

Let τ is a first return time map on Ω and $A_T := \{\omega \in \Omega : \tau_y(\omega) < T\}$. For a constant $K > 0$ and a function f, we denote by $K \wedge f := \min\{K, f\}$. For $s \geq 0$, we define a map $\theta_s : \Omega \to \Omega$ such that for $t, s \geq 0$ and $\omega \in \Omega$, $B_t(\theta_s(\omega)) = B_{t+s}(\omega)$. Then for $K > 0$, we have

$$\begin{aligned}\mathbb{E}_x[K \wedge L_\infty^y] &= \mathbb{E}_x\left[(K \wedge L_\infty^y) \circ \theta_{\tau_y}\ ;\ \tau_y < \infty\right] \\ &= \mathbb{E}_x\left[\lim_{T\to\infty} \mathbb{1}_{A_T}(K \wedge L_\infty^y) \circ \theta_{\tau_y}\right] \\ &= \lim_{T\to\infty} \mathbb{E}_x\left[\mathbb{1}_{A_T}(K \wedge L_\infty^y) \circ \theta_{\tau_y}\right] && \text{by LDCT} \\ &= \lim_{T\to\infty} \mathbb{E}_x\left[\mathbb{1}_{A_T}\mathbb{E}_{B_{\tau_y}}[K \wedge L_\infty^y]\right] && \text{by SMP of } B_t \\ &= \mathbb{E}_x\left[\lim_{T\to\infty} \mathbb{1}_{A_T}\mathbb{E}_{B_{\tau_y}}[K \wedge L_\infty^y]\right] && \text{by LDCT} \\ &= \mathbb{E}_x\left[\mathbb{1}_{A_T}\mathbb{E}_{B_{\tau_y}}[K \wedge L_\infty^y]\ ;\ \tau_y < \infty\right] \\ &= \mathbb{P}_x[\tau_y < \infty]\ \mathbb{E}_y[K \wedge L_\infty^y],\end{aligned}$$

where LDCT means Lebesgue dominant convergence themreom and SMP means strong Markov property. Letting $K \to \infty$, we have

$$G(x,y) = \mathbb{E}_x[L^y_\infty] = \mathbb{P}_x[\tau_y < \infty]\ \mathbb{E}_y[L^y_\infty] = \mathbb{P}_x[\tau_y < \infty]\ G(y,y).$$

□

Proof of Theorem 3.3.3. For $x, y \in \widetilde{X}$ and $\ell_{xy} \in \mathscr{G}\widetilde{X}$, let $z \in \mathrm{Im}(\ell_{xy})$ not lying between x and y. Inspired from the proof of the lemma 6.8 in [BPP16], we claim that

$$\frac{\nu^+_y(\mathcal{O}_x(z))}{\nu^+_x(\mathcal{O}_x(z))} = \frac{G(y,z)}{G(x,z)}.$$

Let $C_x(z)$ be the subset of $\widetilde{X}$ consisting of the points different from z on the geodesic rays from z to the points in $\mathcal{O}_x(z)$. Using the Markov property of the Brownian motion, we have

$$\nu^+_y(\mathcal{O}_x(z)) = \mathbb{P}[B^y_\infty \in \mathcal{O}_x(z)] = G(y,z)\ \mathbb{P}[\forall t > 0,\ B^x_t \in C_x(z)].$$

It holds for x instead of y so that we prove the claim.

By the claim, we have

$$K(x,y,(\ell_{xy})_+) = \lim_{\substack{z=\ell_{xy}(t)\\ t\to\infty}} \frac{\nu^+_y(\mathcal{O}_x(z))}{\nu^+_x(\mathcal{O}_x(z))} = \lim_{\substack{z=\ell_{xy}(t)\\ t\to\infty}} \frac{G(y,z)}{G(x,z)}.$$

By Lemma 3.3.4, we have

$$\frac{G(y,z)}{G(x,z)} = \frac{G(y,z)}{G(z,z)}\frac{G(z,z)}{G(x,z)} = \frac{\mathbb{P}_y[\tau_z < \infty]}{\mathbb{P}_x[\tau_z < \infty]} = \frac{1}{\mathbb{P}_x[\tau_y < \infty]} = \frac{G(y,y)}{G(x,y)},$$

where the third equality holds by the Markov property of the Brownian motion and the structure of the tree $\widetilde{X}$. □

We denote the metric potential for $\mathcal{I}_H$ of $m \in \mathscr{M}$ by $P_H(m)$ and the topological potential for $\mathcal{I}_H$ by P_H.

Theorem 3.3.5. *The harmonic measures $(\nu^+_x)_{x\in\widetilde{X}}$ are Patterson density for $\mathcal{I}_H$ and $P_H = 0$.*

Proof. By the construction of the harmonic measures, $(\nu_x)_{x\in\widetilde{X}}$ are finite Borel measures. It follows from the Γ-invariance of $\mathbb{P}$ that $(\nu_x)_{x\in\widetilde{X}}$ is Γ-equivariant.

For distinct $x, y \in \widetilde{X}$, by the Markov property of Brownian motion, we have

$$\begin{aligned}\nu_x^+(\mathcal{O}_x(y)) &= \mathbb{P}_x[B_\infty \in \mathcal{O}_x(y)] = \mathbb{P}_x[\tau_y < \infty]\, \mathbb{P}_y[B_\infty \in \mathcal{O}_x(y)] \\ &= e^{\widetilde{\mathcal{I}}_H((\ell_{x,y})_+, x, y)} \nu_y^+(\mathcal{O}_x(y)).\end{aligned}$$

Therefore, $(\nu_x^+)_{x\in\widetilde{X}}$ satisfy the second condition of the Patterson density for $\widetilde{\mathcal{I}}_H$ with $P_H = 0$. □

Based on Theorem 3.3.5, we define the harmonic measures $(\nu_x^\pm)_{x\in\widetilde{X}}$ by Patterson density for $\mathcal{I}_H^\pm$. We denote the Gibbs measure $m_{\mathcal{I}_H}$ by ν for simplicity.

We define the random walk $({}^\sharp B_n)_{n\in\mathbb{N}}$ on $V\widetilde{X}$ associated with the Brownian motion. For $x, y \in \widetilde{X}$, the transition probability ${}^\sharp p(x, y)$ from x to y is defined by

$${}^\sharp p(x, y) := \mathbb{P}\left[\tau_y < \tau_{N(x)\setminus\{y\}}\right] = \frac{1/L(x, y)}{\sum_{z\in N(x)} 1/L(x, z)},$$

where $N(x) = \{z \in V\widetilde{X} \ : \ z \text{ is adjacent to } x\}$ and $L(x, z)$ is the length of the edge between x and z. The second equality is from [LP17]. We denote the green function of the random walk $({}^\sharp B_n)_{n\in\mathbb{N}}$ by ${}^\sharp G$. We let $\pi(x) = \sum_{z\in N(x)} 1/L(x, z)$ for all $x \in V\widetilde{X}$. It follows that $(\pi(x))_{x\in V\widetilde{X}}$ is proportional to the *stationary distribution* on $V\widetilde{X}$ since

$$\pi(y) = \sum_{x:x\sim y} \pi(x)\, {}^\sharp p(x, y).$$

We denote by ${}^\sharp\mathbb{P}$ the probability measure induced by the stationary distribution and ${}^\sharp p$ on the discrete state space.

We associate the random walk $({}^\sharp B_n)_{n\in\mathbb{N}}$ with the Brownian motion $(B_t)_{t\in\mathbb{R}}$ in terms of the Green function as follows.

Lemma 3.3.6. *For $x, y \in V\widetilde{X}$, we have*

$$G(x, y) = {}^\sharp G(x, y).$$

Proof. In the proof of Lemma 3.3.4, $G(x, y) = \mathbb{E}_x[L_\infty^y]$ is the expectation of the number of which the Brownian motion B_t^x hits y. That is equal to the expectation of the number of which the random walk ${}^\sharp B_n$ starting from x hits y. From [Bar17], the expectation is equal to ${}^\sharp G(x, y)$. □

The following lemma gives the explicit formula for the harmonic measures $(\nu_x^+)_{x\in\widetilde{X}}$ in terms of the Green function for the random walk $({}^\sharp B_n)_{n\in\mathbb{N}}$.

Lemma 3.3.7. *For $x \sim y \in V\widetilde{X}$, we have*

$$\nu_x^+(\mathcal{O}_x(y)) = \frac{{}^\sharp G(x,x)}{\pi(x)L(x,y)}\left(1 - \frac{{}^\sharp G(y,x)}{{}^\sharp G(x,x)}\right).$$

Proof. For $x \sim y \in V\widetilde{X}$, let $\overline{C_x(y)}$ be the subset of $\widetilde{X}$ consisting of the points containing y on the geodesic rays from y to the points in $\mathcal{O}_x(y)$. Then we have

$$\begin{aligned}
\nu_x^+(\mathcal{O}_x(y)) &= \mathbb{P}_x\left[B_\infty^x \in \mathcal{O}_x(y)\right] \\
&= {}^\sharp\mathbb{P}_x\left[{}^\sharp B_\infty^x \in \mathcal{O}_x(y)\right] \\
&= {}^\sharp G(x,x)\,{}^\sharp p(x,y)\,{}^\sharp\mathbb{P}_y\left[\forall n \geq 0,\ {}^\sharp B_n \in \overline{C_x(y)}\right] \\
&= {}^\sharp G(x,x)\,{}^\sharp p(x,y)\,{}^\sharp\mathbb{P}_y\left[\tau_x = \infty\right] \\
&= \frac{{}^\sharp G(x,x)}{\pi(x)L(x,y)}\left(1 - \frac{{}^\sharp G(y,x)}{{}^\sharp G(x,x)}\right).
\end{aligned}$$

□

Remark 3.3.8. *Lemma 3.3.7 is the natural extension for metric graphs of the harmonic measures in [Lyo94]. In Lyons' setting, the harminc measure at x is the hitting measure for simple random walk starting from x which corresponds to unit current flow (see [Lyo90]). In fract, the lemma implies that the Lyons' harmonic measures are $\frac{G(x,x)}{\pi(x)}\nu_x^+$ in the terms of the our settings However, we observe that the harmonic measures in our definition and Lyons' definition are equivalent and hence their Gibbs measures coincide.*

3.4 Equivalence conditions

In this section, we prove the main theorems of this chapter. We first need the following lemma to prove the necessary condition of the theorems.

Lemma 3.4.1. *Let $\mathcal{I}, \mathcal{I}'$ be integrated potentials on $\mathscr{G}X \times \mathbb{R}_{\geq 0}$ and c, c' be associated system of conductances. If there exists a function $g : VX \to \mathbb{R}$ such that*

$$c(e) - P_{\mathcal{I}}L(e) = c'(e) - P_{\mathcal{I}'}L(e) + g(e^+) - g(e^-),$$

then the Patterson densities $(m_x^{\pm})_{x\in\widetilde{X}}$ *for* $\mathcal{I}^{\pm}$ *and* $((m')_x^{\pm})_{x\in\widetilde{X}}$ *for* $(\mathcal{I}')^{\pm}$ *are equivalent.*

Proof. Recall that the Patterson density $(m_x^{\pm})_{x\in\widetilde{X}}$ is uniquely determined by the values $\{m_x^{\pm}(\mathcal{O}_x(y))\}_{x\sim y\in V\widetilde{X}}$ and

$$\begin{aligned} m_x^{\pm}(\mathcal{O}_x(y))) &= e^{-\widetilde{\mathcal{I}}^{\pm}(\ell_{xy},d(x,y))+P_{\mathcal{I}}d(x,y)}m_y^{\pm}(\mathcal{O}_x(y)) \\ &= e^{-\widetilde{\mathcal{I}}^{\pm}(\ell_{xy},d(x,y))+P_{\mathcal{I}}d(x,y)}\sum_{x\neq z\in N(y)} m_y^{\pm}(\mathcal{O}_y(z)). \end{aligned} \tag{3.2}$$

Recall that for $e\in EX$ and its lift $\widetilde{e}\in E\widetilde{X}$, we denote

$$\mathbf{m}_e^+ := m_{\widetilde{e}^-}^+\left(\mathcal{O}_{\widetilde{e}^-}(\widetilde{e}^+)\right).$$

Then $(\mathbf{m}_e^+)_{e\in EX}$ is the right eigenvector of the matrix $A_{\mathcal{I}}\in \mathrm{Mat}(EX,\mathbb{R})$ corresponding to the eigenvalue 1, where $A_{\mathcal{I}}$ is defined by

$$[A_{\mathcal{I}}]_{ef} = \begin{cases} e^{c(e)-P_{\mathcal{I}}L(e)} & \text{if } e\to f \\ 0 & \text{otherwise} \end{cases}$$

for all $e,f\in EX$. We note that $A_{\mathcal{I}}$ is irreducible by the assumption of X (see [Lim08]). By the Perron-Frobenius theorem, the eigenvalue 1 is simple so that the eigenvector of A corresponding to the eigenvalue 1 is unique upto scalar multiplication.

By the observation, we have

$$\mathbf{m}_e^+ = e^{c(e)-P_{\mathcal{I}}L(e)}\sum_{f:e\to f}\mathbf{m}_f^+ = e^{c'(e)-P_{\mathcal{I}'}L(e)+g(e^+)-g(e^-)}\sum_{f:e\to f}\mathbf{m}_f^+$$

and hence

$$e^{g(e^-)}\mathbf{m}_e^+ = e^{c'(e)-P_{\mathcal{I}'}L(e)}\sum_{f:e\to f}e^{g(f^-)}\mathbf{m}_f^+.$$

That is, $\left(e^{g(e^-)}\mathbf{m}_e^+\right)_{e\in EX}$ is the eigenvector of $A_{\mathcal{I}'}$ corresponding to the eigenvalue 1. Since 1 is a simple eigenvalue, there exists $c_0>0$ such that $\mathbf{m}'^+_e = c_0e^{g(e^-)}\mathbf{m}_e^+$ for all $e\in EX$ so $(m_x^+)_{x\in\widetilde{X}}$ and $((m')_x^+)_{x\in\widetilde{X}}$ are equivalent.

It can be check that

$$\mathbf{m}_e^- := m_{\widetilde{e}^-}^-\left(\mathcal{O}_{\widetilde{e}^-}(\widetilde{e}^+)\right).$$

is the left eigenvector of the matrix $A_{\mathcal{I}}$. Thus we have that $(m_x^-)_{x\in\widetilde{X}}$ and $((m')_x^-)_{x\in\widetilde{X}}$ are equivalent by similar argument. □

Theorem 3.4.2. *The visibility measures $(\lambda_x^\pm)_{x\in\widetilde{X}}$ and the PS measures $(\mu_x^\pm)_{x\in\widetilde{X}}$ are equivalent if and only if for all $e \in EX$,*

$$L(e) = \frac{1}{h_{\mathrm{vol}}} \log \delta(e^-)\delta(e^+).$$

Proof. We first assume that the visibility measures $(\lambda_x^\pm)_{x\in\widetilde{X}}$ and the Patterson measures $(\mu_x^\pm)_{x\in\widetilde{X}}$ are equivalent. Let $e_1 \cdots e_k$ be a cycle in X and $e_1^- = x$ and $e_1^+ = y$. Take their lifts $\widetilde{e}_1, \ldots, \widetilde{e}_k, \widetilde{x}, \widetilde{y}$ such that $\widetilde{e}_1 \cdots \widetilde{e}_k$ is an edge path in $\widetilde{X}$ and $\widetilde{x} = \widetilde{e}_1^-$ and $\widetilde{y} = \widetilde{e}_1^+$. Let $\gamma \in \Gamma$ be such that $\gamma\widetilde{x} = \widetilde{e}_k^+$. Then we have

$$\begin{aligned}
\widetilde{\lambda}\left([\underline{\widetilde{e}_1} \cdots \widetilde{e}_k(\gamma\widetilde{e}_1)]\right) &= \lambda_{\widetilde{x}}^-\left(\mathcal{O}_{\widetilde{y}}(\widetilde{x})\right) \lambda_{\gamma\widetilde{y}}^+\left(\mathcal{O}_{\gamma\widetilde{x}}(\gamma\widetilde{y})\right) \frac{L(e_1)}{\delta(e_1^-)\cdots\delta(e_k^-)\delta(x)\delta(y)} \\
&= \lambda_{\widetilde{x}}^-\left(\mathcal{O}_{\widetilde{y}}(\widetilde{x})\right) \lambda_{\widetilde{y}}^+\left(\mathcal{O}_{\widetilde{x}}(\widetilde{y})\right) \frac{L(e_1)}{\delta(x)\delta(y)} \frac{1}{\delta(e_1^-)\cdots\delta(e_k^-)} \qquad (3.3) \\
&= \widetilde{\lambda}\left([\underline{\widetilde{e}_1}]\right) \frac{1}{\delta(e_1^-)\cdots\delta(e_k^-)}
\end{aligned}$$

and

$$\begin{aligned}
\widetilde{\mu}\left([\underline{\widetilde{e}_1} \cdots \widetilde{e}_k(\gamma\widetilde{e}_1)]\right) &= \mu_{\widetilde{x}}^-\left(\mathcal{O}_{\widetilde{y}}(\widetilde{x})\right) \mu_{\gamma\widetilde{y}}^+\left(\mathcal{O}_{\gamma\widetilde{x}}(\gamma\widetilde{y})\right) e^{-h_{\mathrm{vol}}\left(\sum_{i=1}^k L(e_i)+L(e_1)\right)} L(e_1) \\
&= \mu_{\widetilde{x}}^-\left(\mathcal{O}_{\widetilde{y}}(\widetilde{x})\right) \mu_{\widetilde{y}}^+\left(\mathcal{O}_{\widetilde{x}}(\widetilde{y})\right) e^{-h_{\mathrm{vol}} L(e_1)} L(e_1) e^{-h_{\mathrm{vol}} \sum_{i=1}^k L(e_i)} \qquad (3.4) \\
&= \widetilde{\mu}\left([\underline{\widetilde{e}_1}]\right) e^{-h_{\mathrm{vol}} \sum_{i=1}^k L(e_i)}.
\end{aligned}$$

Since we assume the visibility measures $(\lambda_x^\pm)_{x\in\widetilde{X}}$ and the Patterson measures $(\mu_x^\pm)_{x\in\widetilde{X}}$ are equivalent, we have $\widetilde{\lambda} = \widetilde{\mu}$. Combining with (3.3) and (3.4), we have

$$\begin{aligned}
\frac{1}{\delta(e_1^-)\cdots\delta(e_k^-)} &= \frac{\widetilde{\lambda}\left([\underline{\widetilde{e}_1} \cdots \widetilde{e}_k(\gamma\widetilde{e}_1)]\right)}{\widetilde{\lambda}\left([\underline{\widetilde{e}_1}]\right)} \\
&= \frac{\widetilde{\mu}\left([\underline{\widetilde{e}_1} \cdots \widetilde{e}_k(\gamma\widetilde{e}_1)]\right)}{\widetilde{\mu}\left([\underline{\widetilde{e}_1}]\right)} = e^{-h_{\mathrm{vol}} \sum_{i=1}^k L(e_i)}
\end{aligned}$$

so that

$$\prod_{i=1}^{k} \frac{1}{\delta(e_i^-)} e^{h_{\mathrm{vol}} L(e_i)} = 1 \tag{3.5}$$

for any cycle $e_1 \cdots e_k$ in X.

Now we define

$$\theta(e) := \frac{1}{\delta(e^-)} e^{h_{\mathrm{vol}} L(e)}, \quad e \in EX.$$

For $e \in EX$, let P_1 and P_2 be two distinct edge paths starting from e^+ to e^- that do not contain e. We note that the edge paths exsit by the assumption of X. Then by (3.5), we have three equalities

$$\begin{aligned} \theta(e) \left(\prod_{e' \in \mathsf{P}_1} \theta(e') \right) &= 1 \\ \left(\prod_{e' \in \mathsf{P}_1} \theta(e') \right) \left(\prod_{e'' \in \mathsf{P}_2} \theta(\bar{e}'') \right) &= 1 \\ \theta(\bar{e}) \left(\prod_{e'' \in \mathsf{P}_2} \theta(\bar{e}'') \right) &= 1 \end{aligned}$$

Using the three equalities, we observe that

$$\theta(e) = \left(\prod_{e' \in \mathsf{P}_1} \theta(e') \right)^{-1} = \prod_{e'' \in \mathsf{P}_2} \theta(\bar{e}'') = \theta(\bar{e})^{-1}.$$

Thus if follows that for all $e \in EX$,

$$1 = \theta(e)\theta(\bar{e}) = \frac{1}{\delta(e^-)\delta(e^+)} e^{2h_{\mathrm{vol}} L(e)}$$

that is

$$L(e) = \frac{1}{2h_{\mathrm{vol}}} \log \delta(e^-)\delta(e^+).$$

Conversely, we assume for all $e \in EX$,

$$L(e) = \frac{1}{h_{\mathrm{vol}}} \log \delta(e^-)\delta(e^+).$$

Then we have

$$-h_{\mathrm{vol}}L(e) = \frac{1}{2}\log\frac{1}{\delta(e^-)\delta(e^+)} = \log\frac{1}{\delta(e^+)} - \frac{1}{2}\log\frac{1}{\delta(e^+)} + \frac{1}{2}\log\frac{1}{\delta(e^-)}.$$

By the Lemma 3.4.1, we complete the proof.

□

Theorem 3.4.3. *The visibility measures $(\lambda_x^{\pm})_{x\in\widetilde{X}}$ and the harmonic measures $(\nu_x^{\pm})_{x\in\widetilde{X}}$ are equivalent if and only if there exists $c > 0$ such that for all $e \in EX$,*

$$L(e) = c\left(1 - \frac{1}{d(e^-)} - \frac{1}{d(e^+)}\right).$$

Proof. We first assume that the visibility measures $(\lambda_x^{\pm})_{x\in\widetilde{X}}$ and the harmonic measures $(\nu_x^{\pm})_{x\in\widetilde{X}}$ are equivalent. Let $x \sim y \sim z \in V\widetilde{X}$ such that $x \neq z$. Then we have

$$\frac{\widetilde{\nu}\left([\underline{xy}z]\right)}{\widetilde{\nu}\left([\underline{xy}]\right)} = \frac{\nu_x^-(\mathcal{O}_y(x))\ \nu_y^+(\mathcal{O}_y(z))\frac{G(y,y)}{G(x,y)}L(x,y)}{\nu_x^-(\mathcal{O}_y(x))\ \nu_y^+(\mathcal{O}_x(y))\frac{G(y,y)}{G(x,y)}L(x,y)} = \frac{\nu_y^+(\mathcal{O}_y(z))}{\nu_y^+(\mathcal{O}_x(y))}.$$

By Lemma 3.3.7,

$$\nu_y^+(\mathcal{O}_y(z)) = \frac{{}^\sharp G(y,y)}{\pi(y)L(y,z)}\left(1 - \frac{{}^\sharp G(z,y)}{{}^\sharp G(y,y)}\right)$$

and

$$\nu_y^+(\mathcal{O}_x(y)) = \nu_y^+\left(\bigsqcup_{z:y\sim z\neq x}\mathcal{O}_y(z)\right) = \sum_{z:y\sim z\neq x}\nu_y^+(\mathcal{O}(z)).$$

We note that

$$\begin{aligned}(3.6)\qquad {}^\sharp\mathbb{P}_y\left[\tau_x < \infty\right] &= \sum_{z:y\sim z\neq x} {}^\sharp p(y,z)\,{}^\sharp\mathbb{P}_z\left[\tau_x < \infty\right] + {}^\sharp p(y,x)\\ &= \sum_{z:y\sim z\neq x} {}^\sharp p(y,z)\,{}^\sharp\mathbb{P}_z\left[\tau_y < \infty\right]{}^\sharp\mathbb{P}_y\left[\tau_x < \infty\right] + {}^\sharp p(y,x).\end{aligned}$$

and hence

$$1 = \sum_{z:y\sim z\neq x} {}^\sharp p(y,z)\,{}^\sharp\mathbb{P}_z\left[\tau_y<\infty\right] + {}^\sharp p(y,x)\,{}^\sharp\mathbb{P}_y\left[\tau_x<\infty\right]^{-1} \tag{3.7}$$
$$= \sum_{z:y\sim z\neq x} \frac{1}{\pi(y)L(y,z)}\frac{{}^\sharp G(z,y)}{{}^\sharp G(y,y)} + \frac{1}{\pi(y)L(y,x)}\frac{{}^\sharp G(x,x)}{{}^\sharp G(y,x)}.$$

Combining with Lemma 3.3.7, (3.6) and (3.7), we have

$$\frac{1}{{}^\sharp G(y,y)}\nu_y^+(\mathcal{O}_x(y)) = \sum_{z:y\sim z\neq x}\frac{1}{\pi(y)L(y,z)}\left(1-\frac{{}^\sharp G(z,y)}{{}^\sharp G(y,y)}\right)$$
$$= \frac{1}{\pi(y)L(y,x)}\left(\frac{{}^\sharp G(x,x)}{{}^\sharp G(y,x)}-1\right).$$

Thus we have

$$\frac{\widetilde{\nu}\left([\underline{xy}z]\right)}{\widetilde{\nu}\left([\underline{xy}]\right)} = \frac{\nu_y^+(\mathcal{O}_y(z))}{\nu_y^+(\mathcal{O}_x(y))} = \frac{\frac{1}{L(y,z)}\left(1-\frac{{}^\sharp G(z,y)}{{}^\sharp G(y,y)}\right)}{\frac{1}{L(y,x)}\left(\frac{{}^\sharp G(x,x)}{{}^\sharp G(y,x)}-1\right)}.$$

Similar to the proof of Theorem 3.4.2,

$$\frac{\widetilde{\lambda}\left([\underline{xy}z]\right)}{\widetilde{\lambda}\left([\underline{xy}]\right)} = \frac{1}{\delta(y)}.$$

By the uniqueness of the Gibbs measure,

$$\frac{1}{L(y,z)}\left(1-\frac{{}^\sharp G(z,y)}{{}^\sharp G(y,y)}\right) = \frac{1}{\delta(y)L(x,y)}\left(\frac{{}^\sharp G(x,x)}{{}^\sharp G(y,x)}-1\right) =: \eta(y)$$

is indepdent of x, z and

$$\delta(y)\eta(y) = \frac{1}{L(x,y)}\left(1-\frac{{}^\sharp G(y,x)}{{}^\sharp G(x,x)}\right)\frac{{}^\sharp G(x,x)}{{}^\sharp G(y,x)} = \frac{\eta(x)}{1-L(x,y)\eta(x)}.$$

Then we have

$$\frac{1}{\eta(x)} - \frac{1}{\delta(y)\eta(y)} = L(x,y) = L(y,x) = \frac{1}{\eta(y)} - \frac{1}{\delta(x)\eta(x)}.$$

Let

$$c := \frac{1}{\eta(x)} + \frac{1}{\delta(x)\eta(x)} = \frac{1}{\eta(x)}\frac{d(x)}{\delta(x)}$$

which is independent of x. Then we have

$$L(x,y) = c\left(\frac{\delta(x)}{d(x)} - \frac{1}{d(y)}\right) = c\left(1 - \frac{1}{d(x)} - \frac{1}{d(y)}\right).$$

Conversely, we assume that

$$L(e) = c\left(1 - \frac{1}{d(e^-)} - \frac{1}{d(e^+)}\right).$$

Let $x, y, z_1, \ldots, z_n \in V\widetilde{X}$ be such that $z_1, \ldots, z_n$ are on the geodesic segment between x and y considering the order. We claim that

$$\frac{{}^\sharp G(x,y)}{{}^\sharp G(y,y)} = \frac{1}{\delta(z_1)\cdots\delta(z_n)\delta(y)}\frac{d(y)}{d(x)}.$$

Fix $y \in V\widetilde{X}$ and consider

$$\frac{{}^\sharp G(x,y)}{{}^\sharp G(y,y)} = {}^\sharp\mathbb{P}_x\left[\tau_y < \infty\right]$$

as a function of x. Then it is the unique solution of the following Dirichlet proble [LP17]

$$\begin{cases} \Delta f(x) = 0 \text{ on } V\widetilde{X} \setminus \{y\} \\ f(y) = 1 \end{cases}$$

where Δ is the *(right normalized) graph Laplacian operator* defined by

$$\Delta f(x) = \sum_{v : v \sim x} {}^\sharp p(x,v)(f(x) - f(v))$$

for a function $f : V\widetilde{X} \to \mathbb{R}$. We will show that the function

$$f(x) := \begin{cases} \frac{1}{\delta(z_1)\cdots\delta(z_n)\delta(y)}\frac{d(y)}{d(x)} & \text{if } x \neq y \\ 1 & \text{if } x = y \end{cases}$$

is also a solution of the Dirichlet problem. For $x \neq y$, we have

$$\begin{aligned}
\Delta f(x) &= f(x) - \sum_{v:x\sim v} {}^\sharp p(x,v) f(v) \\
&= f(x) - {}^\sharp p(x,z_1) f(z_1) - \sum_{v:x\sim v\neq z_1} {}^\sharp p(x,v) f(v) \\
&= \frac{1}{\delta(z_1)\cdots\delta(z_n)\delta(y)} \frac{d(y)}{d(x)} - \frac{1}{\pi(x)L(x,z_1)} \frac{1}{\delta(z_2)\cdots\delta(z_n)\delta(y)} \frac{d(y)}{d(z_1)} \\
&\qquad - \sum_{v:x\sim v\neq z_1} \frac{1}{\pi(x)L(x,v)} \frac{1}{\delta(x)\delta(z_1)\cdots\delta(z_n)\delta(y)} \frac{d(y)}{d(v)} \\
&= \frac{d(y)}{\pi(x)\delta(z_1)\cdots\delta(z_n)\delta(y)} \\
&\quad \cdot \left[\frac{\pi(x)}{d(x)} - \frac{1}{L(x,z_1)} \frac{\delta(z_1)}{d(z_1)} - \sum_{v:x\sim v\neq z_1} \frac{1}{L(x,v)} \frac{1}{\delta(x)d(v)} \right] \\
&= \frac{d(y)}{\pi(x)\delta(z_1)\cdots\delta(z_n)\delta(y)} \\
&\quad \cdot \left[\frac{1}{L(x,z_1)} \left(\frac{1}{d(x)} - \frac{\delta(z_1)}{d(z_1)} \right) + \sum_{v:x\sim v\neq z_1} \frac{1}{L(x,v)} \left(\frac{1}{d(x)} - \frac{1}{\delta(x)d(v)} \right) \right].
\end{aligned}$$

By the assumption,

$$\frac{1}{d(x)} - \frac{\delta(z_1)}{d(z_1)} = \frac{1}{d(x)} + \frac{1}{d(z_1)} - 1 = -\frac{1}{c} L(x,z_1)$$

and

$$\frac{1}{d(x)} - \frac{1}{\delta(x)d(v)} = \frac{1}{\delta(x)} \left(1 - \frac{1}{d(x)} - \frac{1}{d(v)} \right) = \frac{1}{\delta(x)} \frac{1}{c} L(x,v).$$

Thus $\Delta f(x) = 0$ so we prove the claim by the uniqueness of the solution of the Dirichlet problem. By the claim and Lemma 3.3.6, for all $e \in EX$,

$$\log \frac{G(e^-,e^+)}{G(e^+,e^+)} = \log \frac{{}^\sharp G(e^-,e^+)}{{}^\sharp G(e^+,e^+)} = \log \frac{1}{\delta(e^+)} + \log d(e^+) - \log d(e^-).$$

We complete the proof by Lemma 3.4.1. □

Theorem 3.4.4. *The PS measures* $(\mu_x^\pm)_{x\in\widetilde{X}}$ *and the harmonic meausres* $(\nu_x^\pm)_{x\in\widetilde{X}}$

are equivalent if and only if for all $e \in EX$,

$$\frac{L(e)e^{h_{\mathrm{vol}}L(e)}}{e^{2h_{\mathrm{vol}}L(e)}-1} = K(e^-)K(e^+),$$

where for $x \in VX$,

$$K(x)^2 = \frac{1+\sum_{e^-=x}\frac{1}{e^{2h_{\mathrm{vol}}L(e)}-1}}{\sum_{e^-=x}\frac{1}{L(e)}}.$$

Proof. We first assume that the Pattterson measures $(\mu_x^{\pm})_{x\in\widetilde{X}}$ and the harmonic measures $(\nu_x^{\pm})_{x\in\widetilde{X}}$ are equivalent. Let $x \sim y \sim z \in V\widetilde{X}$ such that $x \neq z$. We denote $\mu_{xy} = \mu_x^+(\mathcal{O}_x(y))$. Then we have

$$\begin{aligned}\frac{\widetilde{\mu}\left([\underline{xyz}]\right)}{\widetilde{\mu}\left([\underline{xy}]\right)} &= \frac{\mu_x^-(\mathcal{O}_y(x))\ \mu_y^+(\mathcal{O}_y(z))\ e^{-h_{\mathrm{vol}}L(x,y)}L(x,y)}{\mu_x^-(\mathcal{O}_y(x))\ \mu_y^+(\mathcal{O}_x(y))\ e^{-h_{\mathrm{vol}}L(x,y)}L(x,y)} = \frac{\mu_y^+(\mathcal{O}_y(z))}{\mu_y^+(\mathcal{O}_x(y))} \\ &= e^{-h_{\mathrm{vol}}L(x,y)}\frac{\mu_{yz}}{\mu_{xy}},\end{aligned}$$

where the last equality is from the property of the Patterson denstiy

$$\mu_y^+(\mathcal{O}_x(y)) = \sum_{z:y\sim z\neq x}\mu_{yz} = e^{h_{\mathrm{vol}}L(x,y)}\mu_{xy}.$$

By the uniqueness of the Gibbs measure, we have

$$e^{-h_{\mathrm{vol}}L(x,y)}\frac{\mu_{yz}}{\mu_{xy}} = \frac{\nu_y^+(\mathcal{O}_y(z))}{\nu_y^+(\mathcal{O}_x(y))}.$$

Then by the proof of Theorem 3.4.3,

$$\mu_{yz}L(x,z)\left(1-\frac{\sharp G(z,y)}{\sharp G(y,y)}\right)^{-1} = e^{h_{\mathrm{vol}}L(x,y)}\mu_{xy}L(y,x)\left(\frac{\sharp G(x,x)}{\sharp G(y,x)}-1\right)^{-1} =: \zeta(y)$$

is independet of x and z. Since

$$\begin{aligned}\zeta(y) &= e^{h_{\mathrm{vol}}L(x,y)}\mu_{xy}L(y,x)\left(\frac{{}^\sharp G(x,x)}{{}^\sharp G(y,x)}-1\right)^{-1}\\ &= e^{h_{\mathrm{vol}}L(x,y)}\frac{{}^\sharp G(y,x)}{{}^\sharp G(x,x)}\mu_{xy}L(y,x)\left(1-\frac{{}^\sharp G(y,x)}{{}^\sharp G(x,x)}\right)^{-1}\\ &= e^{h_{\mathrm{vol}}L(x,y)}\frac{{}^\sharp G(y,x)}{{}^\sharp G(x,x)}\zeta(x),\end{aligned}$$

we have

$$\frac{{}^\sharp G(y,x)}{{}^\sharp G(x,x)} = e^{-h_{\mathrm{vol}}L(x,y)}\frac{\zeta(y)}{\zeta(x)}.$$

Then

$$\begin{aligned}\mu_{xy} &= \zeta(y)e^{-h_{\mathrm{vol}}L(x,y)}\frac{{}^\sharp G(x,x)}{{}^\sharp G(y,x)}\frac{1}{L(y,x)}\left(1-\frac{{}^\sharp G(y,x)}{{}^\sharp G(x,x)}\right)\\ &= \zeta(y)\frac{\zeta(x)}{\zeta(y)}\frac{1}{L(y,x)}\left(1-e^{-h_{\mathrm{vol}}L(x,y)}\frac{\zeta(y)}{\zeta(x)}\right)\\ &= \frac{1}{L(y,x)}\left(\zeta(x)-e^{h_{\mathrm{vol}}L(x,y)}\zeta(y)\right).\end{aligned}$$

By the property of the Patterson density,

$$\begin{aligned}\frac{1}{L(x,y)}\left(\zeta(y)-e^{h_{\mathrm{vol}}L(x,y)}\zeta(x)\right) = \mu_{yx} &= \sum_{v:x\sim v\neq y} e^{-h_{\mathrm{vol}}L(x,y)}\mu_{xv}\\ &= \sum_{v:x\sim v\neq y} e^{-h_{\mathrm{vol}}L(x,y)}\frac{1}{L(x,v)}\left(\zeta(x)-e^{h_{\mathrm{vol}}L(x,v)}\zeta(v)\right).\end{aligned}$$

Then

$$\pi(x)e^{-h_{\mathrm{vol}}L(x,y)}\zeta(x) = \frac{\zeta(y)}{L(x,y)} + \sum_{v:x\sim v\neq y} e^{-h_{\mathrm{vol}}(L(x,v)+L(x,y))}\frac{\zeta(v)}{L(x,v)}.$$

Let

$$\beta(x) := \sum_{w:x\sim w} e^{-h_{\mathrm{vol}}L(x,w)}\frac{\zeta(w)}{L(x,w)}.$$

Then

$$\pi(x)\zeta(x) = \beta(x) + \frac{\zeta(y)}{L(x,y)}\left(e^{h_{\mathrm{vol}}L(x,y)}-e^{-h_{\mathrm{vol}}L(x,y)}\right)$$

and hence

$$\frac{e^{h_{\mathrm{vol}}L(x,y)} - e^{-h_{\mathrm{vol}}L(x,y)}}{L(x,y)} = \frac{\pi(x)\zeta(x) - \beta(x)}{\zeta(y)}.$$

We note that the left side is invariant under interchanging x and y. Thus there exists c_1 such that

$$\frac{c_1}{\zeta(x)\zeta(y)} = \frac{\pi(x)\zeta(x) - \beta(x)}{\zeta(y)} = \frac{e^{h_{\mathrm{vol}}L(x,y)} - e^{-h_{\mathrm{vol}}L(x,y)}}{L(x,y)} \tag{3.8}$$

or $c_1 = \zeta(x)\left(\pi(x)\zeta(x) - \beta(x)\right)$. Hence

$$\begin{aligned}
\pi(x)\zeta(x)^2 - c_1 &= \zeta(x)\beta(x) \\
&= \zeta(x) \sum_{v:x\sim v} e^{-h_{\mathrm{vol}}L(x,v)} \frac{\zeta(v)}{L(x,v)} \\
&= \sum_{v:x\sim v} e^{-h_{\mathrm{vol}}L(x,v)} \frac{c_1}{e^{h_{\mathrm{vol}}L(x,v)} - e^{-h_{\mathrm{vol}}L(x,v)}} \\
&= c_1 \sum_{v:x\sim v} \frac{1}{e^{2h_{\mathrm{vol}}L(x,v)} - 1}
\end{aligned}$$

so we have

$$\zeta(x)^2 = \frac{c_1}{\pi(x)} \left(1 + \sum_{v:x\sim v} \frac{1}{e^{2h_{\mathrm{vol}}L(x,v)} - 1}\right).$$

We let $K(x) := \zeta(x)/\sqrt{c_1}$ and combining with (3.8), we finally get

$$\frac{L(e)e^{h_{\mathrm{vol}}L(e)}}{e^{2h_{\mathrm{vol}}L(e)} - 1} = K(e^-)K(e^+).$$

Conversely, we assume that

$$\frac{L(e)e^{h_{\mathrm{vol}}L(e)}}{e^{2h_{\mathrm{vol}}L(e)} - 1} = K(e^-)K(e^+), \tag{3.9}$$

where

$$K(x)^2 = \frac{1 + \sum_{e^-=x} \frac{1}{e^{2h_{\mathrm{vol}}L(e)}-1}}{\sum_{e^-=x} \frac{1}{L(e)}}. \tag{3.10}$$

For $x, y \in V\widetilde{X}$, we claim that

$$\frac{\sharp G(x,y)}{\sharp G(y,y)} = e^{-h_{\mathrm{vol}} d(x,y)} \frac{K(x)}{K(y)},$$

where we denote $d_{\widetilde{X}} = d$ for simplicity. Similar to the proof of Theorem 3.4.3, we fix $y \in V\widetilde{X}$ and consider the right handside as a function of x, denote $f(x)$. We will prove that f is a solution of the Dirichlet problem. It is obvious that $f(y) = 1$. For $x \neq y$,

$$\begin{aligned}
\Delta f(x) &= f(x) - \sum_{v:x\sim v} {}^{\sharp}p(x,v) f(v) \\
&= e^{-h_{\mathrm{vol}} d(x,y)} \frac{K(x)}{K(y)} - \sum_{v:x\sim v} \frac{e^{-h_{\mathrm{vol}} d(v,y)}}{\pi(x) L(x,v)} \frac{K(v)}{K(y)}.
\end{aligned}$$

Let $z \in V\widetilde{X}$ be adjacent to x and contained in the geodesic segment between x and y. Then by (3.9) and (3.10), we have

$$\begin{aligned}
&\sum_{v:x\sim v\neq z} \frac{e^{-h_{\mathrm{vol}} d(v,y)}}{\pi(x) L(x,v)} \frac{K(v)}{K(y)} \\
&= \frac{1}{\pi(x)K(y)} \sum_{v:x\sim v\neq z} \frac{e^{-h_{\mathrm{vol}}(d(v,y)-L(x,v))}}{e^{2h_{\mathrm{vol}} L(x,v)} - 1} \frac{1}{K(x)} \\
&= \frac{e^{-h_{\mathrm{vol}} d(x,y)}}{\pi(x)K(y)K(x)} \sum_{v:x\sim v\neq z} \frac{1}{e^{2h_{\mathrm{vol}} L(x,v)} - 1} \\
&= \frac{e^{-h_{\mathrm{vol}} d(x,y)}}{\pi(x)K(y)K(x)} \left(\pi(x)K(x)^2 - 1 - \frac{1}{e^{2h_{\mathrm{vol}} L(x,z)} - 1} \right) \\
&= e^{-h_{\mathrm{vol}} d(x,y)} \frac{K(x)}{K(y)} - \frac{e^{-h_{\mathrm{vol}} d(x,y)}}{\pi(x)K(y)K(x)} \frac{e^{2h_{\mathrm{vol}} L(x,z)}}{e^{2h_{\mathrm{vol}} L(x,z)} - 1}.
\end{aligned} \tag{3.11}$$

Similarly, (3.9) implies

$$\begin{aligned}
\frac{e^{-h_{\mathrm{vol}} d(z,y)}}{\pi(x) L(x,z)} \frac{K(z)}{K(y)} &= \frac{1}{\pi(x)K(y)} \frac{e^{-h_{\mathrm{vol}}(d(z,y)-L(x,z))}}{e^{2h_{\mathrm{vol}} L(x,z)} - 1} \frac{1}{K(x)} \\
&= \frac{e^{-h_{\mathrm{vol}} d(x,y)}}{\pi(x)K(y)K(x)} \frac{e^{2h_{\mathrm{vol}} L(x,z)}}{e^{2h_{\mathrm{vol}} L(x,z)} - 1}.
\end{aligned} \tag{3.12}$$

Combining (3.11) and (3.12), we have $\Delta f(x) = 0$ for $x \neq y$. Thus we prove the claim.

By the claim and Lemma 3.3.6, for all $e \in EX$,

$$\log \frac{G(e^-, e^+)}{G(e^+, e^+)} = \log \frac{{}^\sharp G(e^-, e^+)}{{}^\sharp G(e^+, e^+)} = -h_{\mathrm{vol}} L(e) - \log K(e^+) + \log K(e^-).$$

We complete the proof by Lemma 3.4.1. □

Chapter 4

Brain network analysis 1: Tinnitus on hearing loss patients

4.1 Materials and Methods

4.1.1 Patients

All procedures in this study were approved by the institutional reviewboards of Seoul National University Bundang Hospital (IRB-B-2006-621-105) and the need for informed consent from the participants has been waived by the IRB. Table 4.1 summarizes the characteristics of the two groups. A total of 65 tinnitus patients with bilateralHL from the database of Seoul National University Bundang Hospitalwere included in the HL-T group. The average hearing threshold (average of the pure tone audiometry [PTA] thresholds at 500, 1,000,2,000, and 4,000 Hz) of the subjects in the HL-T group was more than 25 dB HL bilaterally. The mean age of the participants in the HL-Tgroup was 66.6 ± 10.1 years (range: 32–82 years), and 21 (32.3%)were male. Of 65 subjects, 39 (60%) reported pure-tone tinnitus whilethe remaining 26 (40%) reported narrow-band noise tinnitus. A total of 44 (67.78%) subjects had bilateral tinnitus while the remaining 21 had unilateral tinnitus.

For the HL-NT group, 104 hearing threshold-matched individualswith bilateral HL (> 25 dB) without tinnitus were selected from ourdatabase. The mean age of the HL-NT group was 67.5 ± 13.4 years (range: 19–86 years),

and 50 (47.6%) were male. The mean age andmean PTA thresholds at all frequencies (measured at 250, 500, 1,000, 2,000, 3,000, 4,000, and 8,000 Hz bilaterally) showed no statistically significant differences between the HL-T and HL-NT groups (Table 4.1). Individuals with otologic disorders such as otosclerosis and Meniere's disease, chronic headache, psychiatric or neurological disorders, current psychotropic/central nervous system-active medications, historyof drug/alcohol abuse, and/or a history of head injury (with loss of consciousness) or seizures were excluded from the study to ensure ahomogeneous sample. The data that support the findings of this study are available from the corresponding author upon reasonable request.

	HL-T group	HL-NT group	P value
Number of subjects	65	104	
Male:Female	21:44	50:54	
Mean age	66.6 ± 10.1	67.5 ± 13.4	0.631
Mean PTA threshold			
Right			
250 Hz	29.1 ± 9.1	29.2 ± 11.8	0.930
500 Hz	32.4 ± 9.1	35.5 ± 11.4	0.070
1,000 Hz	39.9 ± 8.4	41.9 ± 11.1	0.237
2,000 Hz	44.7 ± 8.4	46.8 ± 11.7	0.213
3,000 Hz	51.4 ± 9.1	53.1 ± 14.1	0.398
4,000 Hz	57.1 ± 8.5	58.7 ± 15.1	0.426
8,000 Hz	69.5 ± 11.3	71.6 ± 18.2	0.392
Left			
250 Hz	30.5 ± 10.0	30.2 ± 13.9	0.905
500 Hz	34.7 ± 9.3	36.4 ± 12.8	0.368
1,000 Hz	40.8 ± 8.4	43.0 ± 12.2	0.200
2,000 Hz	45.6 ± 8.6	47.8 ± 13.3	0.247
3,000 Hz	52.0 ± 7.3	54.1 ± 15.5	0.321
4,000 Hz	57.9 ± 8.2	60.0 ± 17.6	0.378
8,000 Hz	70.1 ± 10.5	71.7 ± 18.5	0.692

Table 4.1: *Demographic and audiological characteristics of the study subjects.* HL-T, hearing loss with tinnitus; HL-NT, hearing loss without tinnitus.

4.1.2 EEG recording

The EEG recordings were performed in accordance with a standard diagnostic and neuromodulation treatment protocol after obtaininginformed consent. Participants refrained from alcohol consumption for 24 hr before EEG recording, and from caffeinated beverages on the day of recording, to prevent alcohol-related changes in the EEG [VD12a] and a caffeine-induced decrease in alpha waves, respectively [BCJ11, Fox12].

Each participant sat upright on a comfortable chair in a well-lit room that was shielded against sound and stray electric fields. Then, EEG recordings were obtained for 5 min using a tin electrode cap (ElectroCap, Eaton, OH) and Mitsar EEG-201 amplifier (Mitsar,St. Petersburg, Russia). The vigilance of the participants was determined according to EEG parameters such as the appearance of spindles or slowing of the alpha rhythm, where enhanced theta power reflects drowsiness [MMWJ10]. The EEG was recorded with 19 electrodes using the International 10–20 system and referenced to linked ears; the impedance of all electrodes was kept below 5 kΩ during EEG recording. Data were collected under eyes-closed conditions (sampling rate,1,024 Hz; band-pass, 0.15–200 Hz), using WinEEG software (version 2.84.44; Mitsar). The data were resampled to 128 Hz, band-pass filtered (fast Fourier transform filter) to 2–44 Hz, and transposed into Eureka! Software [SC05]. Then, the data were plotted and carefully inspected for manual artifact rejection. All episodic artifacts, such as eye movements, eye blinks, body movement, teeth clenching, and electrocardiogram artifacts, were removed from the EEG signals. An independent component analysis (ICA) was also performed to confirm that all artifacts had been removed. The power spectra were compared (a) after visual artifact rejection only, and (b) after visual artifact and ICA component rejection. There was no statistically significant difference in the mean power of the delta (2–3.5 Hz), theta (4–7.5 Hz), alpha1 (8–10 Hz), alpha2 (10–12 Hz), beta1 (13–18 Hz), beta2 (18.5–21 Hz), beta3 (21.5–30 Hz), or gamma (30.5–44 Hz) frequency band [Han18, Kim16, Lee19, Lee20, Son17, VSD18] between the two approaches. Therefore, we reported the results of the two-step artifact correction data. Average Fourier cross-spectral matrices were computed for the aforementioned bands from delta to gamma.

4.1.3 Source localization analysis

Standardized low-resolution brain electromagnetic tomography (sLORETA) was used to estimate the intracerebral electrical sources that generated the scalp-recorded activity in each of the eight frequency bands [Pas02]. sLORETA computes neuronal activity in current density (A/m2) without assuming a predefined number of active sources. The solution space used in this study is implemented in the LORETA-Key software. The sLORETA-key template consists of 6,239 voxels (voxel size: $5 \times 5 \times 5$ mm) and is restricted to cortical gray matter and hippocampi, as defined by the digitized Montreal Neurological Institute (MNI) 152 template [Fuc02]. Scalp electrode coordinates on the MNI brain are referred from the international 5% system [Jur07]. The analysis procedures were conducted for both the T and NT groups on the average EEG data at sensor level (19 electrodes) and on average EEG data that was source-localized to a specific set of regions of interest (ROI) (84 BAs in Table 4.2).

4.1.4 Metric graph

The network in this study was modeled as a fully connected undirected graph with 84 nodes and 3,486 undirected edges. Each node of the network represents a BA. The lagged coherence between a pair of BAs provides a weight for the edge that connects them. Weighted and binary graph models are frequently used for modeling brain networks [Moh16]. This study focused primarily on the geometric properties of brain networks. In the metric graph, edge lengths are assigned based on the multiplicative inverse of the lagged linear coherence between the endpoints of the edges. This assignment method is in turn based on the relationship between conductance and resistance in the electric network. The edge lengths induce the path metric, which is defined by the infimum of the total lengths of the paths between two points.

4.1.5 Volume entropy

As a metric graph, the brain network is not cyclic and has no terminal vertices. The volume entropy, denoted by h_{vol}, is characterized using the following equation:

$$h_{\mathrm{vol}} = \lim_{r \to \infty} \frac{\log N_r}{r},$$

where N_r is the number of edge paths in the metric graph (without backtracking), the total length of which is less than r [Lim08]. In other words,

Brodmann areas	Abbreviation	Name of the Brodmann area
BA01	S1	Primary somatosensory cortex
BA02	S2	Secondary somatosensory cortex
BA03	S3	Tertiary somatosensory cortex
BA04	M1	Primary motor cortex
BA05	SPS	Superior parietal sulcus
BA06	SMA	Supplementary motor area
BA07	SPG	Superior parietal gyrus
BA08	Pre-SMA	Pre-supplementary motor area
BA09	DLPFC	Dorsolateral prefrontal cortex
BA10	FPC	Fronto-polar cortex
BA11	OFC	Orbital frontal cortex
BA13	Insula	Insula
BA17	V1	Primary visual cortex
BA18	V2	Secondary visual cortex
BA19	Cuneus	Cuneus
BA20	ITG	Inferior temporal gyrus
BA21	MTG	Medial temporal gyrus
BA22	STG	Superior temporal gyrus
BA23	PCC1	Posterior cingulate cortex1
BA24	dACC	Dorsal anterior cingulate cortex
BA25	sgACC	Subgenual anterior cingulate cortex
BA27	PHC1	Parahippocampal gyrus1
BA28	HIP1	Hippocampal area1
BA29	RSC1	Retrosplenial cortex1
BA30	RSC2	Retrosplenial cortex2
BA31	PCC2	Posterior cingulate cortex2
BA32	prACC	Pregenual anterior cingulate cortex
BA33	rACC	Rostral anterior cingulate cortex
BA34	HIP	Hippocampus
BA35	HIP2	Hippocampal area2
BA36	PHC2	Parahippocampal gyrus2
BA37	OTC	Occipital-temporal cortex
BA38	TP	Temporal pole
BA39	AG	Angular gyrus
BA40	IPS	Intra-parietal sulcus
BA41	A1	Primary auditory cortex
BA42	A2	Secondary auditory cortex
BA43	PCG	Postcentral gyrus
BA44	OPCG	Opercular part of inferior frontal gyrus
BA45	IFG	Inferior frontal gyrus
BA46	MPFC	Medial prefrontal cortex
BA47	VLPFC	Ventro-lateral prefrontal cortex

Table 4.2: *All the Brodmann areas included in the study.*

the volume entropy is equal to the asymptotic exponential growth rate of the number of edge paths, and N_r becomes closer to $e^{h_{\text{vol}}r}$ as r approaches ∞.

Although volume entropy is defined abstractly in mathematical terms, we can compute it algorithmically. We first defined a matrix $L(h)$ with rows and columns indexed by directed edges in the metric graph, as follows:

$$[L(h)] = \begin{cases} e^{-hL(f)} & \text{if } e^+ = f^-,\ e^- \neq f^+ \\ 0 & \text{otherwise.} \end{cases}$$

Regarding the spectral properties of $L(h)$, the largest eigenvalue of $L(0)$ is a positive real number >1. As h increases, the largest absolute eigenvalue of $L(h)$ decreases. Therefore, there is a unique positive constant h, such that the largest absolute eigenvalue of $L(h)$ is 1. The constant h is equal to the volume entropy h_{vol} of the metric graph.

4.1.6 Afferent node capacity

The eigenvector $x = (x_e)_{e \in EX}$ of $L(h_{\text{vol}})$ associated with an eigenvalue of 1, which is determined uniquely, assigns a positive value to each directed edge. We call these positive values the *edge capacities*, which are associated with volume entropy h_{vol}. The edge capacity indicates the extent to which the edge affects the spread of information in the brain network.

It follows from the definition of $L(h_{\text{vol}})$ that two directed edges with the same terminal node have similar edge capacities if the graph has rich connections. Because we modeled the brain network as a fully connected network, this property can be observed therein. We converted the edge capacities of directed edges with the same terminal node to the node capacity of their terminal node by summing the edge capacities. The resulting node capacity becomes a new local measure of nodes, and thus also of BAs; we call this local measure the *afferent node capacity*. The efferent node capacity can be determined by summing the edge capacities of edges with identical initial nodes. However, the efferent node capacity cannot be used as a local measure of BAs, because its value does not vary according to the edge capacity. One way to interpret edge paths in a brain network is to regard them as information flows. Volume entropy can then be used to investigate information flow along the edges after a sufficient amount of time has passed. Related to the volume entropy, the afferent node capacity of a given node becomes larger when information frequently flows through the node. The volume entropy and afferent node capacity are highly related to each other and serve as global and local network measures, respectively. An alternative method to convert functional data on the edges

to node data is discussed in a previous study [LeeH19].

Remark 4.1.1. *The afferent node capacity is proportional to the total mass of the Patterson-Sullivan measure. In fact, the afferent node capacity at $v \in VX$ is equal to $\delta(v)\|\mu_{\widetilde{v}}\|$. We note that $\|\mu_{\widetilde{v}}\|$ is independent of a choice of a lift $\widetilde{v}$ of v since Patterson-Sullivan measures are Γ-equivariant. To prove this, we have that for the eigenvector $(x_e)_{e\in EX}$ of $L(h_{\mathrm{vol}})$,*

$$x_e = e^{-h_{\mathrm{vol}}L(e)}\mu_{\widetilde{e}^-}(\mathcal{O}_{\widetilde{e}^-}(\widetilde{e}^+)) = \mu_{\widetilde{e}^+}(\mathcal{O}_{\widetilde{e}^-}(\widetilde{e}^+)) = \|\mu_{\widetilde{e}^+}\| - \mu_{\widetilde{e}^+}(\mathcal{O}_{\widetilde{e}^+}(\widetilde{e}^-)).$$

The first equality follows from Proposition 2.3.3 and the secon equality follows from the definition of the Patterson density (Definition 2.3.1). Then the afferent node capacity at $v \in VX$ is

$$\sum_{e\,:\,e^+=v} x_e = \sum_{e\,:\,e^+=v} (\|\mu_{\widetilde{e}^+}\| - \mu_{\widetilde{e}^+}(\mathcal{O}_{\widetilde{e}^+}(\widetilde{e}^-))) = \delta(v)\|\mu_{\widetilde{v}}\|.$$

Since we model the brain network as a complete graph with 84 vertices, $\delta(v) \equiv 83$ for all $v \in VX$.

4.1.7 Statistical analysis

For each BA and frequency band, we used a permutation test [Was13] to determine the difference in distribution of afferent node capacities between the T and NT groups. The permutation test is the most powerful and intuitive nonparametric statistical approach and is particularly useful for small samples. Because the relatively small size of our dataset made it difficult to analyze the data distribution, the permutation test was considered appropriate. We compared the average afferent node capacity between the two groups under the assumption that the samples were identically distributed. We used 10,000 permutations and a significance level of $p < 0.05$ when comparing volume entropy and afferent node capacity between the two groups. The statistical analysis was performed using Python software (version 3.7.0; Python Software Foundation, Beaverton, OR, USA).

4.2 Results

4.2.1 Comparison of volume entropy between the HL-T and HL-NT groups

The statistical analysis gives no significant difference between theHL-T and HL-NT groups in terms of volume entropy for any frequency bands. The distributions of volume entropy in the HL-T andHL-NT groups are in Figure 4.1.

From the result of the statistical analysis, we may assume that the networks in the HL-T and HL-NT groups are well-normalized, that is, the distributions of the global measure (volume entropy) between two groups are not statistically different. Based on the assumption, comparing the afferent node capacities, which are highly related to the volume entropy, is more meaningful than not normalized case.

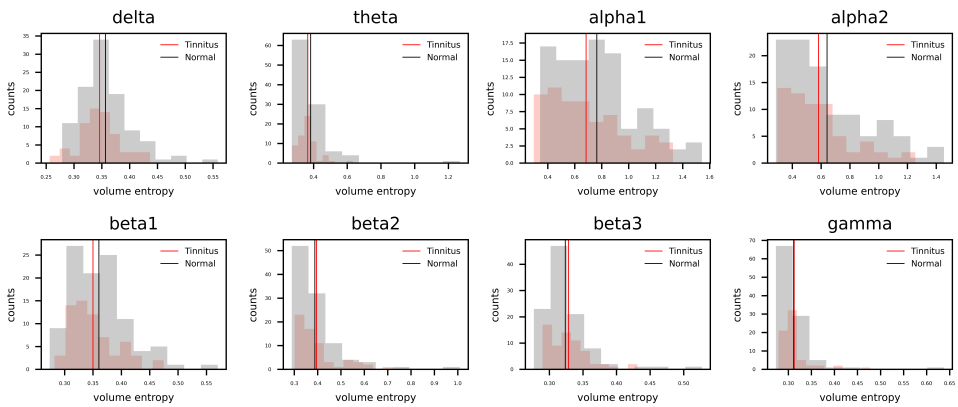

Figure 4.1: *Histogram of volume entropy.* The histograms show the distribution of volume entropy on various frequency bands in the HL-T (red) and HL-NT (black) groups. The red vertical line means the average of volume entropy in the HL-T group and the black vertical line means the average of volume entropy in the HL-NT group.

4.2.2 Comparison of afferent node capacity between the HL-T and HL-NT groups

Figure 4.2 depicts the afferent node capacity distribution of the 84 BAs for all eight frequency bands. Figure 4.3 illustrates the relative afferent node capacity of the HL-T and HL-NT groups. As summarized in Table 4.3, the HL-T and

HL-NT groups showed statistically significant differences in afferent node capacity for a total of 14 ROIs for the theta, alpha2, and beta3 frequency bands. Fo rthese 14 ROIs, the afferent node capacity is summarized in Figure 4.3.

frequency band	Abbreviation	BA	P-value	Tinnitus	Non-tinnitus
theta	OFC	11L	0.00003	0.77201489	0.38964517
	sgACC	25L	0.00741	0.8021413	0.54459024
	VLPFC	47L	0.00388	0.72965909	0.46009869
	MTG	21R	0.00671	0.57059879	0.83148991
alpha2	RSC1	29L	0.00941	1.17301991	1.39255565
	OPCG	44L	0.00214	0.57080755	0.31750684
	IFG	45L	0.00833	0.4669897	0.26588954
	PCC1	23R	0.00125	1.03064385	1.3262293
	RSC1	29R	0.00535	1.15502661	1.41378237
beta3	Insula	13R	0.00853	0.93953276	0.66183085
	HIP1	28R	0.00117	1.04740913	0.72378116
	HIP	34R	0.00648	1.0233051	0.73847828
	HIP2	35R	0.00317	1.01532414	0.72952998
	PHC2	36R	0.00697	0.95658985	0.70022195

Table 4.3: *Result of statistical inference with significant level 0.01.* Tinnitus, an average of afferent node capacity on the ROI in the tinnitus group; Non-tinnitus, an average of afferent node capacity on the ROI in the non-tinnitus group.

As illustrated in Figure 4.4 and summarized in Table 4.3, the HL-T group showed a significantly higher afferent node capacity in the left orbitofrontal cortex (OFC; $p < .01$), left subgenual anterior cingulate cortex (sgACC; $p < .01$), and left ventrolateral prefrontal cortex (VLPFC; $p < .01$) compared with the HL-NT group for the theta frequency band. By contrast, the mean afferent node capacity at theright medial temporal gyrus (medTG) for the theta frequency band was significantly higher in the HL-NT group compared with the HL-Tgroup ($p < .01$) (Figure 4.5, upper panel).

For the alpha2 frequency band, the afferent node capacity in the left opercular part of the inferior frontal gyrus (OPCG; $p < .01$) and left inferior frontal gyrus (IFG) ($p < .01$) was significantly higher in the HL-T group compared with the HL-NT group. By contrast, the afferent node capacity in left retrosplenial cortex 1 (RSC1; $p < .01$), right posterior cingulate cortex 1 (PCC1;

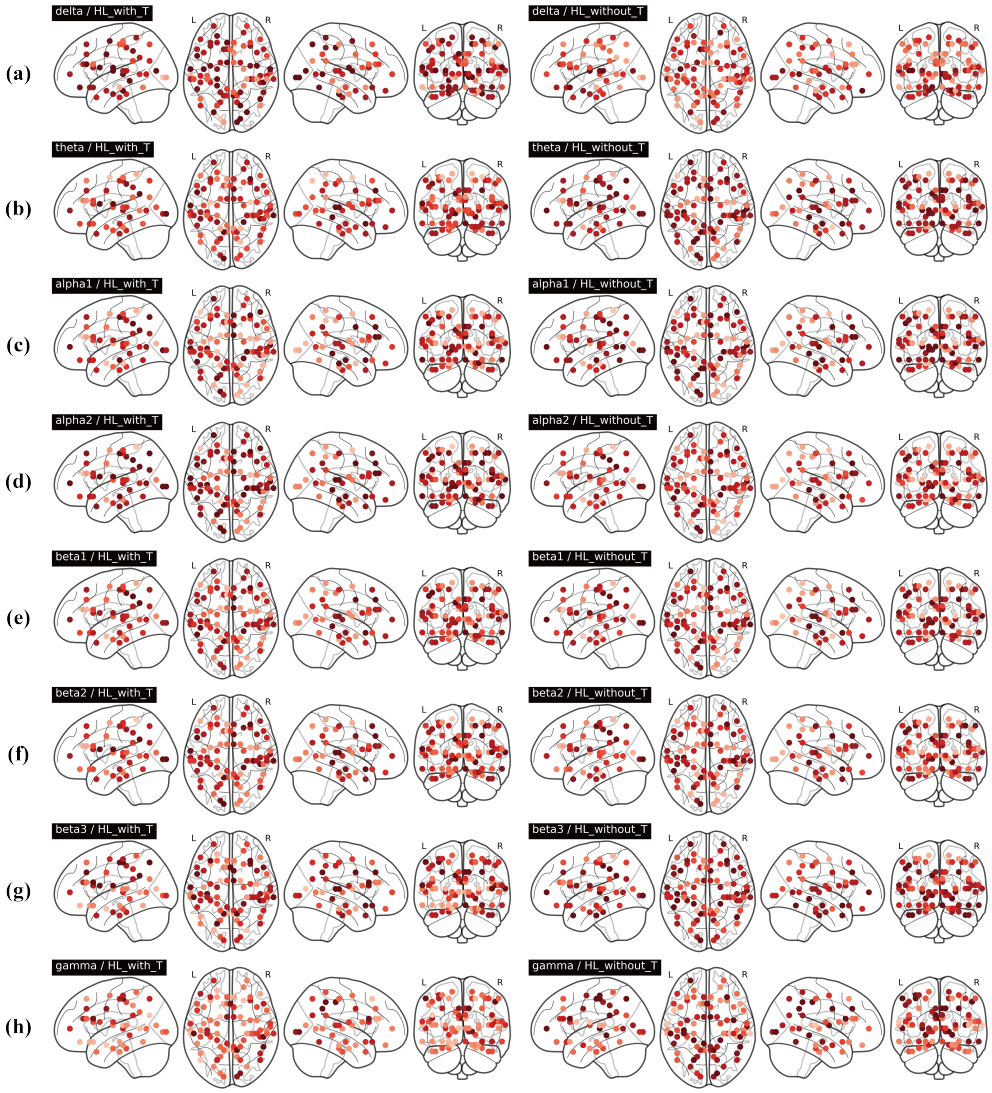

Figure 4.2: *Distribution of afferent node capacities on the Brodmann areas.* **(a)-(h)** represent the distribution of afferent node capacities on the 84 Brodmann areas in left: HL-T and right: HL-NT groups in **(a)** delta, **(b)** theta, **(c)** alpha1, **(d)** alpha2, **(e)** beta1, **(f)** beta2, **(g)** beta3 and **(h)** gamma frequency band. The figures have been drawn using Python nilearn package (Version 0.2.5).

$p < .01$), and right RSC1 ($p < .01$) was significantly higher in the HL-NT group compared with the HL-T group (Figure 4.5, middle panel).

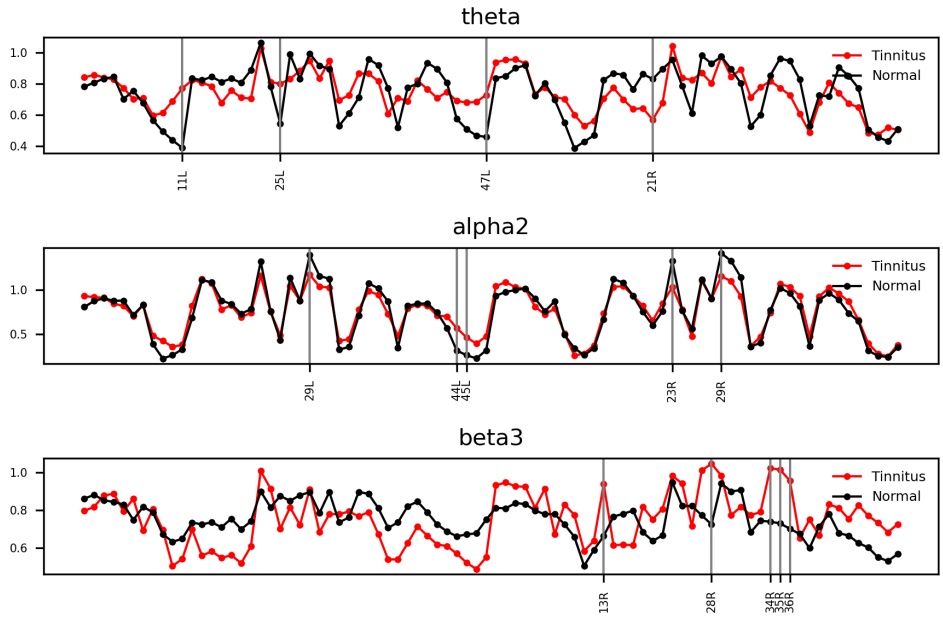

Figure 4.3: *Afferent node capacity for two groups.* Average of afferent node capacities on each Brodmann area are calculated in the HL-T (red) and HL-NT (black) groups in *upper*: theta, *middle*: alpha2 and *bottom*: beta3 frequency band. The gray vertical lines on the significantly different Brodmann areas. Any other frequency bands have no significantly different Brodmann areas.

For the beta3 frequency band, the afferent node capacity in the right insula ($p < .01$), right hippocampus ($p < .01$), right hippocampal area (HIP) 1 ($p < .01$), right HIP2 ($p < .01$), and right parahippocampal gyrus (PHC) 2 ($p < .01$) was significantly higher in the HL-T group compared with the HL-NT group (Figure 4.5, lower panel).

For the delta, alpha1, beta1, beta2, and gamma frequency bands, no significant difference was observed between the HL-T and HL-NT groups in terms of afferent node capacity for any of the 84 ROIs.

4.3 Discussion

In the present study, we compared HL-T and HL-NT groups, in terms of the afferent node capacity of 84 ROIs in the brain, via lagged linear connectivity analysis of eight rs-qEEG frequency bands. The HL-T group showed

significantly higher afferent node capacity in the left OFC, left sgACC, and left VLPFC compared with the HL-NT group for the theta frequency band, while the HL-NT group had a significantly higher afferent node capacity in the right medTG compared with theHL-T group. For the alpha2 frequency band, the HL-T group had a significantly higher afferent node capacity in the left IFG ($p < .01$) compared with the HL-NT group, while the HL-NT group showed significantly higher values in the bilateral RSC1 and right PCC1 compared with the HL-T group. For the beta3 frequency band, the HL-T group showed a significantly higher afferent node capacity in the right insula, right hippocampus, and parahippocampus compared with the HL-NT group. Thus, the HL-T and HL-NT groups showed marked differences in the spread of neural information among many cortical areas for different frequency bands.

As summarized above, the HL-T group had a significantly higher afferent node capacity in the right hippocampus and parahippocampus compared with the HL-NT group for the beta3 frequency band. The HL-NT group also showed higher afferent node capacity in the bilateral RSC1 for the alpha2 frequency band. Considering that an increase in qEEG alpha waves reflects top-down, inhibitory control processes [AR89], the relatively increased afferent node capacity in the bilateral RSC1 for the alpha2 frequency band in the HL-NT group may reflect relatively decreased inhibitory control processes in the bilateral RSC1.

It has been suggested that tinnitus is the result of Bayesian inference, and may be generated to reduce perceptual uncertainty [DJV14, DVF14]. The Bayesian brain can be conceptualized as a probability machine that constantly makes predictions based on its model of the world, and then updates these predictions by active exploration of the environment via the senses [Fri10], to reduce the uncertainty that is inherent to a changing environment [DVF14]. Against this background, sensory perception can be viewed as the result of memory-based predictions that are verified and updated with additional sensory input. If sensory input is not available, for example, due to HL, then the missing auditory information can be retrieved from memory [DJV14, DVF14]. The model of the world maintained by the brain can be described as a cognitive map stored in the hippocampal-parahippocampal area and OFC [WS16]. A cognitive map can be defined as an abstract map of causal relationships, that is, a set of mental representations that binds external sensory features (hippocampus/parahippocampus) with internal motivational or emotional factors (OFC) to form an integrated relational database [Tol48, WS16]. These same

areas are involved in predictions of sensory stimuli to reduce perceptual uncertainty [Wei18]. The updating of sensory predictions involves a cascade from early unisensory encoding in primary sensory cortices to reliability-weighted fusion in parietal–temporal cortices, and then to causal inference (primarily in the OFC) of behaviorally relevant (insula) signals [Cao19]. The VLPFC suppresses behaviorally irrelevant sensory stimuli in a cross-modal context to minimize perceptual bias [Cao19].

The findings of this study can be interpreted in the context of the Bayesian brain to derive a model for tinnitus [DJV14, DVF14, HSV19, Lee17, VD16]. Some individuals with HL develop tinnitus, which is characterized by increased information transmission efficiency in a network that comprises the lateral OFC, VLPFC, sgACC, and parahippocampal and hippocampal areas, as well as the insula.

The parahippocampus is involved in auditory memory and thus may also play a role in the generation of tinnitus in cases of HL [DeR06, DERL11]. Indeed, parahippocampal activity was more common in tinnitus subjects compared with non-tinnitus controls in a recent connectomics study [Moh16]. Transient suppression of hippocampal activity by amytal injections into the anterior choroid alartery could also suppress tinnitus [DeR06]. Furthermore, in a recent study describing partial peripheral reafferentation via the use of a hearing aid in tinnitus subjects, pre-hearing aid parahippocampal activity was shown to be a negative prognostic factor for tinnitus improvement [Han20].

The parahippocampus has been suggested to act as a gatekeeper to the hippocampus, filtering out irrelevant or redundant auditory input [Bou08, TM97]. In a recent proof-of-concept study, tinnitus patients with marked HL exhibited increased parahippocampal activity compared with healthy controls; moreover, the range of HL correlated with changes in cortical activity in the parahippocampus [VD16]. In another recent study, subjects with HL-T showed increased functional connectivity between the parahippocampus and auditory cortex compared with subjects with HL-NT [VAD19]. Based on this literature and a recent Bayesian brain model explaining the generation of tinnitus in terms of Bayesian updating of missing auditory information (and thus the generation of phantom auditoryperception) [DVF14], we surmise that, when opened, a “parahippocampal sensory gate” generates phantom sounds from auditory memories stored in the hippocampus, to compensate for missing auditory information due to HL. The posterior hippocampus/parahippocampus contains a cognitive map of the causal relationships between sensory inputs in

space and time [WS16]. This is also consistent with studies on the neural correlates of "multisensory inference" [Wei18]. The significantly higher afferent node capacity of the (para)hippocampal area in our HL-T group suggests a crucial role of the parahippocampus in the generation of tinnitus, by promoting the spread of stored auditory information to other cortical areas. However, this compensatory generation of phantom auditory perception by the parahippocampus does not occur in all subjects with HL: unnecessary retrieval of parahippocampal auditory memory may be contingent upon interactions with other cortical areas. The OFC also contains a cognitive map of the world; however, it is based on behavioral relevance rather than contextual multisensory input [WS16]. This suggests that for individuals who develop tinnitus, the missing auditory information is deemed salient by the parahippocampus, which drives it to distribute the missing auditory input across the brain. Previous studies have suggested that the insula, especially the anterior insula, engages in mathematical tasks, that is, the tracking of risk and risk prediction errors [BBWR09, Bos10]. In addition, activation of the insula due to a perceived threat or risk prediction error has been found to be closely related to activation of the ACC or IFG [CTBDS09]. This is not surprising, as the insula is part of the salience network (SN) incharge of salience processing and executive control [See07]. Therefore, we speculate that, in our HL-T group, decreased peripheral auditory input may have been regarded as a behaviorally salient stimulus by the insula, which may promote the generation of tinnitus by pulling auditory memories from the (para)hippocampus and aforementioned prefrontal areas. Also, as the IFG is a part of the central executive network (CEN) that is related to activity inhibition, emotion, and working memory [Lan21], the modulatory role of the SN with regard to the function of the CEN may have resulted in better perception of the parahippocampal memory-based tinnitus. Salience is also related to the subjective value that the brain (sgACC) ascribes to missing information, irrespective of the stimulus type, as demonstrated by a meta-analysis [CR14]. Furthermore, the sgACC and parahippocampal area are part of a general network processing aversive/unpleasant stimuli [Mou11], which is also present in tinnitus [JVD12, VD15]. The VLPFC forms part of a Bayesian inference model of the suppression of irrelevant sensory information [Cao19]. In a broader sense, the VLPFC suppresses the "silent" model of the world and generates a new model that encompasses tinnitus [DCK14].

In summary, in the presence of HL, a highly activated network (measured by afferent node capacity) consisting of the OFC, sgACC,and VLPFC, in which

Bayesian inferences related to decreased peripheral auditory input generate tinnitus by retrieving stored auditory memories from the (para)hippocampus, generates a model of the world incorporating tinnitus because the brain considers the missing auditory input behaviorally relevant. By contrast, the HL-NT group showed significantly higher afferent node capacity in the right PCC1 and right medTG for the alpha2 and theta frequency bands, respectively, compared with the HL-T group. The PCC is a core component of the DMN, which shows a high rate of metabolism in healthy subjects not focused on the outside world, and decreases in activity across a range of cognitive loads [Rai01, Shu97]. The PCC has long been regarded as a posterior hub ofthe DMN [Fox17, XYL16] and has recently been suggested to regulate the DMN [WCCL19]. Whether a new model of the world is required depends on the current needs, behavioral flexibility, and prior knowledge about the environment of a given individual [Pea11]. Based on Bayesian inference, the PCC is involved in detecting sensory changes and drives subsequent shifts inself-referential processing and thus behavior [Pea11]. The PCC is also the main cortical hub of the parasympathetic and digestive systems [BMBN13]. The PCC does not consider a decrease in auditory input salient. The MedTG has been suggested as a component of the DMN [Mur18], and microstate analysis suggested that it is an important component of a "tinnitus generating network" [VTD19]. The MedTG is involved in updating auditory predictions made by the Bayesian brain [Cao19]; because the brain does not consider HL as salient, it does not update missing auditory information via the retrieval of parahippocampal memories.

The difference in tinnitus generation between the HL-T and HL-NT groups may be explained as follows: (a) when the brain detects decreased auditory input and the prefrontal "Bayesian inferential system" is active enough to fill in for the decreased peripheral sensory input to reduce uncertainty, and regards it as a sufficiently salient event, to generate phantom auditory perception by retrieving auditory memories stored in the parahippocampus, the brain ultimately generates tinnitus (the HL-T group); whereas (b) when the DMN of the brain surpasses the Bayesian inferential system and thus auditory memory retrieval is interrupted, the subject does not perceive tinnitus(the HL-NT group).

Using a volume entropy model of the brain, the present study uncovered different patterns of cortical information flow that may regulate tinnitus perception in individuals with HL. The increased information flow seen in the prefrontal Bayesian inferential network in the HL-T group suggests that HL

was treated as an event of sufficient salience to generate phantom auditory perception, by retrieving auditory memories from the parahippocampus; thus, tinnitus is perceived. In contrast, in the HL-NT subjects, activation of the DMN prevented Bayesian inference and thus the generation of phantom auditory perception. In other words, the present study suggests that the balance of activity between the Bayesian inferential network and DMN determines whether tinnitus is generated in a brain with decreased peripheral auditory input. Follow-up neuromodulatory studies of the cortical areas responsible for tinnitus generation, and investigation of changes in volume entropy in the brain, could validate the current findings.

The current study has several limitations that should be addressed in future follow-up studies. First, 44 out of 65 subjects had lateral tinnitus while the other 21 had unilateral tinnitus. Because the laterality of tinnitus may have affected the results [Van11], follow-up studies in tinnitus subjects with homogenous laterality should be performed. Second, the male to female ratio of the two study groups showed statistically significant difference. This may have biased the results of the current study since male- and female tinnitus patients show different cortical, prefrontal, in particular, activity patterns [VJD12]. Future studies controlled for the sex ratio should be performed to check the reproducibility of the current study. Third, future studies subdividing the HL-T group into low-and high-distressed tinnitus or acute- or chronic tinnitus may give us further information on other culprit brain areas of tinnitus generation such as the posterior cingulate cortex (PCC), based on previous qEEG studies showing connectivity changes in the PCC according to the chronicity of tinnitus [Lan21] or the level of tinnitus-related distress [VD15].

4.4 Conclusion

Taken together, the current study suggests that the balance of activity between the Bayesian inferential network (updating missing auditory information by retrieving auditory memories from the hippocampus/parahippocampus) and DMN (maintaining the“silent status quo”)determines whether phantom auditory perception occurs in a brain with decreased peripheral auditory input using the volume entropy model of the brain. Also, this study could be applied for treating tinnitus by offering potential target areas for neuromodulatory approaches.

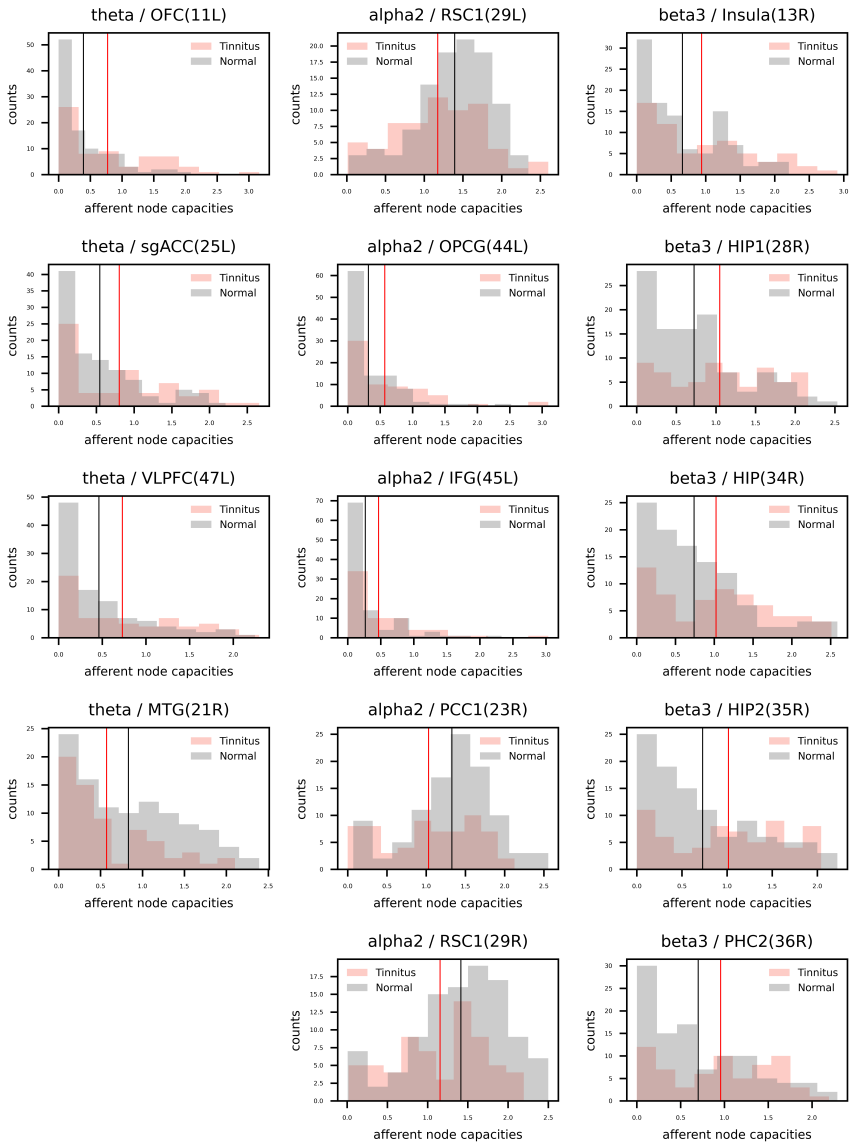

Figure 4.4: *Histogram of afferent node capacity.* The histograms show the distribution of afferent node capacity on significantly different (frequency band)/(Brodmann area) pairs in the HL-T (red) and HL-NT (black) groups. The red vertical line means the average of afferent node capacities in the HL-T group and the black vertical line means the average of afferent node capacities in the HL-NT group.

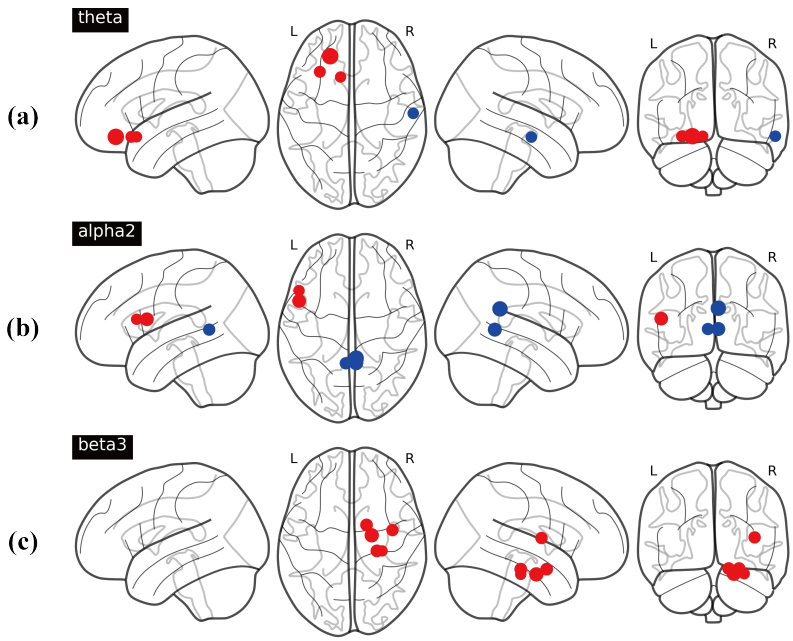

Figure 4.5: *Significantly different Brodmann areas.* The pointed regions are significantly different Brodmann areas in **(a)** theta, **(b)** alpha2 and **(c)** beta3 frequency band networks. The size of dot means difference in afferent node capacities on corresponding Brodmann area between two groups. On the red point, an average afferent node capacity in the HL-T is greater than that in the HL-NT group and the opposite is true on the blue point. **(a)** contains left OFC, left sgACC, left VLPFC and right MTG. **(b)** contains left RSC1, left OPCG, left IFG, right PCC1 and right RSC1. **(c)** contains right Insula, right HIP1, right HIP, right HIP2 and right PHC2. The figures have been illustrated using Python nilearn package (Version 0.2.5).

Chapter 5

Brain network analysis 2: Tinnitus on sudden sensorineural hearing loss patients

5.1 Materials and Methods

Metric graph modeling and dynamical invariants (volume entropy and afferent node capacity) used for analysis are the same as in Chapter 4

5.1.1 Participants

We retrospectively reviewed the medical records of patients with unilateral SSNHL who visited the outpatient clinic of Seoul National University Bundang Hospital (SNUBH) between September 2014 and June 2021. In total, 15 patients (6 males and 9 females) who met the diagnostic criteria for unilateral SSNHL but did not complain of tinnitus were recruited to the NT group. The average hearing threshold [average of the pure tone audiometry (PTA) thresholds at 500, 1,000, 2,000, and 4,000 Hz] of the NT group for the contralesional normal ear was 21.4 ± 10.6 dB HL. The mean age of the patients in the NT group was 60.1 ± 17.1 years (range: 29-78 years), and six of them (40.0%) complained of right-sided hearing loss. The mean duration of deafness was 29.2 ± 30.8 months.

The comparison (T) group initially comprised 65 patients presenting with both unilateral SSNHL and tinnitus, as identified in the SNUBH database. These patients were matched with those in the NT group based on sex and the average hearing threshold on the contralesional (symptom-free) side. In total, 35 patients were excluded due to bilateral hearing loss >40 dB HL or underlying otologic diseases; the 30 remaining patients (12 males and 18 females) had an average contralesional hearing threshold of 19.8 ± 9.9 dB HL and mean age of 55.2 ± 10.8 years (range: 38–77 years). The mean PTA threshold of all frequencies (measured at 250, 500, 1,000, 2,000, 4,000, and 8,000 Hz bilaterally) on both the lesional and contralesional sides was not significantly different between the T and NT groups. All but one patient (96.7%) in the T group showed left-sided symptoms. The mean duration of deafness in the T group was 13.0 ± 19.8 months, which was significantly different compared to that in the NT group (p-value = 0.022, Mann–Whitney test). Detailed demographic and audiological characteristics of the study subjects are listed in Table 5.1. Subjects with chronic otitis media, otosclerosis, Meniere's disease, vestibular schwannoma, psychiatric/neurological diseases, a history of drug or alcohol abuse, and/or a history of head trauma were excluded from the study, which was approved by the Institutional Review Board (IRB) of SNUBH (IRB No. B-2112-725-103). The requirement for informed consent was waived.

5.1.2 Electroencephalography recording

The EEG data acquisition and preprocessing procedures were conducted according to our previously reported protocols [Kim16, Son17, Han18, Lee19]. Prior to EEG recording, the participants were instructed not to drink alcohol for 24 h, and to avoid caffeinated beverages on the day of recording to preclude alcohol-induced changes in the EEG signal and caffeine-induced reductions in alpha and beta power, respectively [SK02, Kor16].

Electroencephalograms were recorded over 5 min using a tin electrode cap (Electro-Cap International Inc., Eaton, OH, USA), EEG-201 amplifier (Mitsar, St. Petersburg, Russia), and WinEEG software (version 2.84.44; Mitsar), in a fully lit room shielded from sound and stray electric fields. During recording, each patient sat upright with the eyes closed. Nineteen electrodes were placed according to the 10–20 system of electrode placement and referenced to linked ears. The impedance of all electrodes was kept below 5 kΩ during EEG recording. The vigilance of the participants was meticulously monitored by

	SSNHL-T group	SSNHL-NT group	p-value
Number of subjects	30	15	
Male : Female	12 : 18	6 : 9	
Mean age	55.2 ± 10.8	60.1 ± 17.1	
Mean PTA thresholds (dB HL)			
Lesional side			
250 Hz	57.5 ± 25.4	64.7 ± 28.3	0.256
500 Hz	66.0 ± 21.9	73.0 ± 24.1	0.128
1,000 Hz	70.7 ± 20.7	82.3 ± 15.0	0.056
2,000 Hz	74.2 ± 21.7	84.3 ± 13.4	0.057
4,000 Hz	81.2 ± 18.9	86.0 ± 16.2	0.291
8,000 Hz	90.0 ± 13.4	90.3 ± 14.2	0.855
Contralesional side			
250 Hz	11.5 ± 7.4	12.3 ± 8.1	0.891
500 Hz	13.5 ± 8.6	13.3 ± 6.7	0.805
1,000 Hz	18.0 ± 9.7	16.7 ± 10.3	0.687
2,000 Hz	19.7 ± 11.5	24.0 ± 15.2	0.338
4,000 Hz	30.0 ± 15.5	33.7 ± 18.7	0.570
8,000 Hz	39.7 ± 21.4	52.0 ± 26.5	0.122

Table 5.1: *Demographic and audiological characteristics of the study participants.*

checking for abnormal EEG patterns, including slowing of the alpha rhythm or the emergence of sleep spindles [MMWJ10]. Data were obtained at a sampling rate of 1,024 Hz, and filtered using a high-pass filter with a cutoff of 0.15 Hz and low-pass filter with a cutoff of 200 Hz. The raw data were resampled to 128 Hz, band-pass filtered using a fast Fourier transform filter with a Hanning window at 2–44 Hz, and transposed into Eureka! Software [SC05]. All episodic artifacts, such as eye movements and blinks, body movements, teeth clenching, and electrocardiogram artifacts, were carefully inspected and removed. An independent component analysis (ICA) was performed to verify that all artifacts had been fully removed. The power spectra were compared after removing visual artifacts, and then after removing visual artifacts and performing ICA; there were no significant differences in the mean power of the delta (2–3.5 Hz), theta (4–7.5 Hz), alpha 1 (8–10 Hz), alpha 2 (10–12 Hz), beta 1 (13–18 Hz), beta 2 (18.5–21 Hz), beta 3 (21.5–30 Hz), or gamma (30.5–44 Hz)

frequency bands between the two approaches [Kim16, Son17, Han18, Lee20]. All of the results reported herein were obtained after applying the two-step artifact correction process, and average Fourier cross-spectral matrices were computed for the aforementioned bands (from delta to gamma). No patients exhibited abnormal EEG patterns during the measurements.

5.2 Results

5.2.1 Comparison of the volume entropy between the sudden sensorineural hearing loss-with tinnitus and sudden sensorineural hearing loss-without tinnitus groups

The distributions of volume entropy in the T and NT groups are illustrated in Figure 5.1. The statistical analysis revealed that volume entropy was significantly higher in the T than NT group for the beta 2 frequency band. For the other seven frequency bands, no statistically significant differences were observed between the two groups. From these results, it can be inferred that there was an increase in the overall information flow for the beta 2 frequency band in the T group.

5.2.2 Comparison of afferent node capacity between the sudden sensorineural hearing loss-with tinnitus and sudden sensorineural hearing loss-without tinnitus groups

The comparisons of afferent node capacity between the T and NT groups for all eight frequency bands are summarized in Figure 5.2. For 14 ROIs for all frequency bands except alpha 2 and beta 3, significantly higher afferent node capacities were seen in the T group, while for 9 ROIs for the delta, alpha 2, beta 2, and gamma frequency bands, afferent node capacities were higher in the NT group. The afferent node capacities for all ROIs, and for ROIs in which afferent node capacity differed significantly between the two groups, are illustrated in Figure 5.3, respectively.

In the T group, the afferent node capacity was significantly higher in the left superior parietal sulcus (SPS, BA05), left PHC (BA36), and left angular gyrus (AG, BA39) for the delta band; right temporal pole (TP, BA39) for the theta band; and right SPS (BA05), right secondary visual cortex (V2, BA18), right dorsal anterior cingulate cortex (dACC, BA24), right posterior cingulate cortex (PCC, BA31), right pregenual anterior cingulate cortex (prACC,

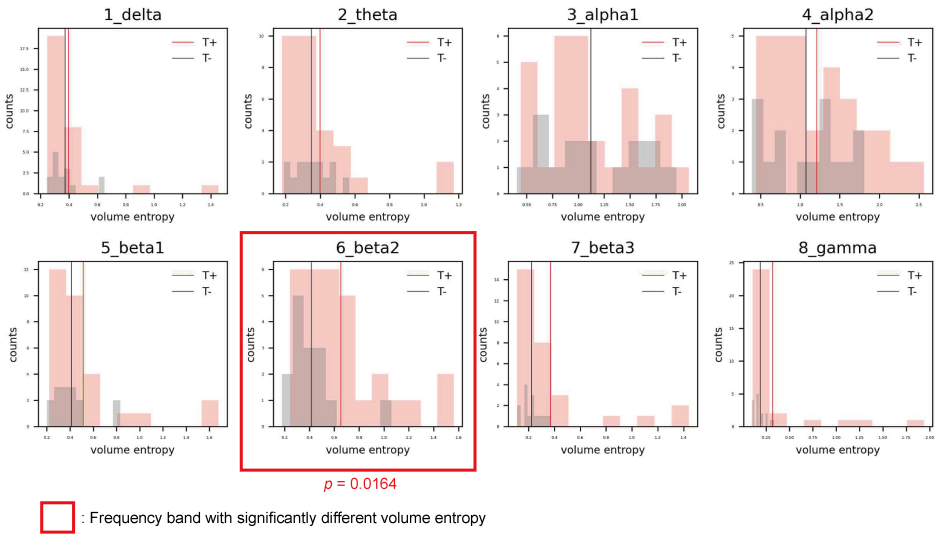

Figure 5.1: Histograms showing the distribution of volume entropy for each frequency band in the sensorineural hearing loss with tinnitus (T; red) and sensorineural hearing loss without tinnitus (NT; black) groups. The red and black vertical lines indicate the average volume entropy in the T and NT groups, respectively.

BA32), and right intraparietal sulcus (IPS, BA40) for the alpha 1 band. The right dACC (BA24) and left medial temporal gyrus (MTG, BA21) showed significantly higher afferent node capacities for the beta 1 and beta 2 bands, respectively. For the gamma frequency band, the afferent node capacity of the T group was significantly higher than that of the NT group in the left occipitotemporal cortex (OTC, BA37), left TP (BA38), and right AG (BA39). By contrast, for the ROIs in the NT group other than those mentioned above, afferent node capacity was significantly higher compared to the T group. In detail, higher afferent node capacity was observed in the right insula (BA13), right MTG (BA21), right superior temporal gyrus (STG, BA22), and right subgenual anterior cingulate cortex (sgACC, BA25) for the delta band; right STG (BA22), right sgACC (BA25) and right retrosplenial cortex (RSC1, BA29) for the alpha 2 band; left hippocampal area (HIP1, BA28) for the beta 2 band; and left insula (BA13), left sgACC (BA25), right insula (BA13), and right primary visual cortex (V1, BA17) for the gamma band.

5.3 Discussion

Many psychological disorders, such as depression, anxiety, and schizophrenia, are caused by aberrant neural activity or functional connectivity within the triple network [Men11, Sha19]. The triple brain network has recently been implicated in tinnitus [DeR22], but proof of its involvement is lacking. Tinnitus is commonly accompanied by underlying comorbidities such as presbycusis [Gib13] and SSNHL; the rate of comorbid tinnitus in the latter condition is 66–93% [Din18].

Herein, we compared the volume entropy and afferent node capacity of 84 ROIs between T and NT groups via linear connectivity analysis of eight resting-state qEEG frequency bands. The T group had significantly higher volume entropy in the beta 2 frequency band than the NT group. The T group had significantly higher afferent node capacities in the left SPS, left PHC2, and left AG than the NT group for the delta frequency band, while the NT group had significantly higher afferent node capacities in the right insula, right MTG, right STG, and right sgACC. For the theta frequency band, the T group had significantly higher afferent node capacity in the right TP. For the alpha 1 frequency band, the T group had significantly higher afferent node capacities in the right SPS, right dACC, right PCC2, right prACC, and right IPS, while the NT group had significantly higher afferent node capacities in the right STG and right sgACC for the alpha 2 band. For the beta 1 band, the T group showed significantly higher afferent node capacity in the right dACC. For the gamma frequency band, the T group showed significantly higher afferent node capacities in the left TP and right AG, while the NT group demonstrated higher afferent node capacities in the left and right insula, and left sgACC. Overall, the T and NT groups showed different patterns of neural information flow in various frequency bands.

5.3.1 New insight into the generation of tinnitus in patients with sudden sensorineural hearing loss provided by a triple network model

As described above, the T group had significantly higher afferent node capacities in the left and right AG for the delta and gamma frequency bands, respectively, as well as in the right PCC for the alpha 1 frequency band, and left and right TP for the theta and gamma frequency bands, respectively. The AG, PCC, and TP are responsible for the activation of, or are func-

tionally connected with, the DMN [FM08, Seg13, Hu17]. The PCC is a core element of the DMN; it shows elevated metabolic activity when an individual is not focused on the outside world, and decreased activity during attention-demanding tasks [Shu97, Rai01]. The TP may be crucial for socioemotional processes and disorders; it is a component of the dorsomedial prefrontal cortex, which is composed of various DMN networks [Ols07, And10]. [Lai09] demonstrated that the bilateral AGs in the DMN network are engaged in dynamic self-referencing processes in the resting state, and [Bin99] similarly observed activation of the AG during task-free semantic and conceptual processing at rest [Bin99, Lai09]. These findings can be interpreted in the context of the volume entropy model: DMN regions may have been activated to a greater degree in the T than NT group.

The posterior parietal cortex (PPC), which is located between the visual and somatosensory cortices, is a major domain in the human brain cortex, along with the temporal and prefrontal cortices. It consists of the SPS (BA05), superior parietal gyrus (SPG; BA07), AG (BA39), and IPS (BA40) [Whi17]. Key nodes of the CEN that participate in goal-directed judgments and decision-making include the dorsolateral prefrontal cortex (DPC) and PPC [Mul06, KS07, Whi10]. In our study, significantly higher afferent node capacities in the T than NT group were observed in the bilateral SPS nd right IPS, which are both part of the CEN. Similarly, significantly higher afferent node capacities were seen in the T group in the right prACC and right dACC, which are key components of the SN [See07, Stu21]. The SN functions as a large-scale brain network involved in the detection of salient external stimuli, such as tinnitus.

Tinnitus seems to be the consequence of increased activity in the triple network, which has also been implicated in Bayesian processing. Predictions are generated in the DMN during the resting state [Pez21], while prediction errors are computed in the left insula (SN) [Fic21] and left DPC and ventrolateral prefrontal cortex (CEN) [Fic21]. Prediction errors generated by the left SN rompt the goal-oriented CEN to reduce uncertainty. The CEN subsequently generates new predictions based on intentions, and new prediction errors are detected by the left SN via active sampling of the environment.

The DMN and frontoparietal network are essential for the conscious perception of stimuli. Studies of patients with loss of consciousness have demonstrated that auditory stimuli can reach the auditory cortex, but for conscious awareness thereof the auditory cortex must be functionally connected

to consciousness-enabling networks [Bol04, Bol05, Lau04, Dem12] such as the DMN and frontoparietal network [Dem12, Ake14]. Furthermore, auditory stimuli only enter into conscious awareness when certain networks are coactivated [Bol08, Sad09]. All components of the triple network are important for the conscious awareness of internally generated phantom sounds.

5.3.2 Activation of auditory processing and noise-canceling pathways in sudden sensorineural hearing loss patients without tinnitus

Regardless of whether tinnitus is generated by peripheral or central neural networks along auditory pathways, specific functional cortical regions are involved [Jas90]. A recent meta-analysis of studies that have investigated tinnitus-related abnormalities in brain structures and functions demonstrated that temporal gyrus regions, such as the STG and MTG, are crucial for simple peripheral auditory processing and semantic memory [Che20]. Moreover, the connections of the temporal gyrus with the primary auditory cortex and frontal lobe constitute hierarchical structures necessary for the execution of auditory processing [Ish19]. In particular, the temporal lobes are highly activated in patients whose tinnitus is suppressed by narrowband noise or lidocaine injections [Mir00]. Similar to the temporal gyrus, the insula plays a role in auditory temporal processing, as does the central auditory nervous system (which is also involved in speech perception). Aspects of temporal processing involving the insula include organization of acoustic stimuli into meaningful sound units, frequency discrimination, and sound localization [BML03]. Increased information flow in auditory pathways indicates intentional modification of neural projections to promote auditory processing and reduce the influence of the tinnitus-generating network. Our results accord with those findings in that we found significantly higher afferent node capacities of the right STG, right MTG, and right insula for the delta frequency band; right STG for the alpha 2 frequency band; and both insulae for the gamma frequency band in the NT group. Activation of auditory pathways strongly implies that the temporal gyrus and insula serve as central processing units, compensate for auditory deafferentation in patients with SSNHL, and prevent the generation of tinnitus.

The sgACC extends into the nucleus accumbens-ventral tegmental area and is involved in the processing of aversive sounds (particularly tinnitus)

and social distress [Muh06, VD12b]. Neuroimaging studies have demonstrated involvement of the limbic system in tinnitus, and a "dysfunctional noise-canceling mechanism" has been proposed [Rau10]. According to this concept, patients perceive tinnitus only if the noise canceling system malfunctions, and thus fails to suppress the tinnitus signal produced by auditory cortical changes. Together, the ACCs (particularly the pregenual and rostral ACCs and sgACC) and anterior insula may comprise the noise-canceling system [Rau10, DeR12, Son15]. In our study, higher afferent node capacities were observed in the right sgACC for the delta and alpha 2 frequency bands, and left sgACC for the gamma frequency band, in the NT group; this suggests that both sides of the sgACC were activated in the NT group, thereby triggering the noise-canceling system and disrupting the tinnitus-generating pathway. In other words, the sgACC may be the core region of what has been described as the "descending noise-canceling pathway," such that upregulation thereof may suppress tinnitus. These results are in accordance with a transcranial neuromodulation study demonstrating an inhibitory effect on tinnitus of pgACC and rostral ACC activity modulation [VD11].

5.3.3 Study strengths and limitations

Using a volume entropy model, this study demonstrated differences in information flow and afferent node capacity between SSNHL patients with and without tinnitus. The application of our volume entropy model in conjunction with the triple network model could reveal the factors responsible for the selective generation of tinnitus in patients with SSNHL. When information flow is increased in regions of the DMN and CEN after sudden-onset hearing loss, the anticorrelation between the DMN and CEN is disrupted, and the SN perceives tinnitus as normal (and thus generates symptoms, as seen in our T group). However, tinnitus will not be perceived when the information flow auditory network is activated to a greater extent than the tinnitus-generating triple network, and tinnitus generation will be effectively blocked after the activation of noise-canceling pathways (as seen in the NT group). Noninvasive neuromodulation techniques, such as transcranial magnetic stimulation and direct current stimulation, have shown promising results in studies of tinnitus when applied to temporoparietal and prefrontal cortical regions [DeR05, Joo14, Cim20]. By applying these techniques to triple network regions in studies based on our volume entropy model, new treatment protocols may emerge involving the deacti-

vation of tinnitus-generating regions simultaneous with activation of tinnitus-suppressing regions. In this manner, the outcomes of refractory tinnitus could be improved. Our findings could lead to personalized therapies for patients with tinnitus, particularly those who have experienced sudden hearing loss.

This study also had several limitations. First, due to the relative scarcity of SSNHL patients without tinnitus, the NT group was not large enough for a detailed analysis of the distribution of information flow, which may have reduced the statistical significance of the comparison of afferent node capacity among regions. Follow-up studies including more subjects are warranted to validate our findings. Second, the laterality of the SSNHL could not be fully matched between the T group and NT group due to the limited number of subjects with SSNHL without tinnitus. Because the laterality of the deafness can affect the cortical plastic changes and the oscillatory patterns are different between left- and right sided tinnitus according to our own previous report [Van11], future studies controlling for the laterality of hearing loss should be performed to check the replicability of the current study. Also, as summarized in Table 1, the duration of deafness showed significant differences between the two groups due to the paucity of subjects with SSNHL without tinnitus. Therefore, future follow-up studies utilizing larger subject groups matched for the duration of deafness are warranted. Third, the activities of certain cortical regions not associated with tinnitus were highly correlated in our study. For instance, higher afferent node capacity was observed in the right V2 (BA18) for the alpha 1 frequency band in the T group, whereas significantly higher afferent node capacity in the right V1 (17R) was seen for the gamma frequency band in the NT group. The visual cortex is not involved in generation of tinnitus but could play a role in the multisensory processing of auditory stimuli [KY11, Roh19]. Therefore, future studies should evaluate the potential role of the visual cortices in the generation or suppression of tinnitus. Fourth, the frequency spectrum was limited to the traditional frequency bands; extending it to include the infraslow (0.01–0.1 Hz) and slow (0.1–1 Hz) bands may yield additional relevant information, but studies with larger study populations are required to test this due to the problem of multiple comparisons. Fifth, we did not check for anticorrelations within and between components of the triple network, which may have provided a more complete picture of the interactions of auditory areas with the triple network and noise-canceling system. However, this would require analysis of the infraslow band; most research of this nature is based on functional magnetic resonance imaging, where the BOLD

signal correlates with the infraslow EEG band [Pan13, Tho14, Gro17]. Sixth, state-of-the-art functional cortical atlas such as the gradient-weighted Markov Random Field (gwMRF) model combining the local gradient and global similarity approaches for the functional classification of human cerebral cortex [Sch18] may be advantageous over BA-based ROI mapping. Future studies based on the recently developed functional atlas to check the replicability of the current study are warranted.

5.4 Conclusion

Using a volume entropy model of the brain, we showed that activity within the triple network (comprising the DMN, CEN, and SN) has a major role in the selective generation of tinnitus after sudden hearing loss. By contrast, tinnitus suppressing networks (i.e., networks activating both temporal auditory processing and noise-canceling pathways) exhibited activity surpassing that of the triple network in our NT group, thereby effectively blocking tinnitus generation. This study could inform neuromodulatory treatments for tinnitus targeting the triple network.

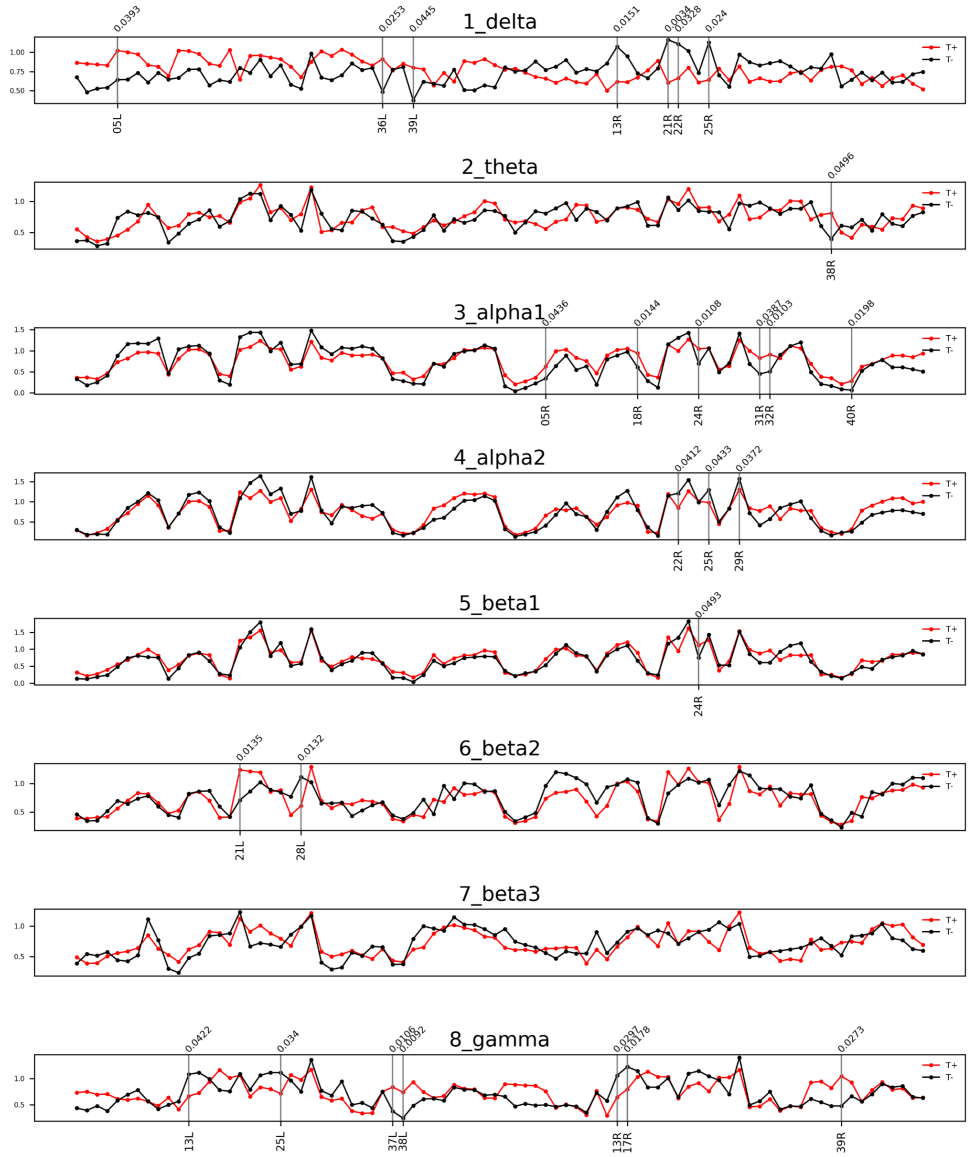

Figure 5.2: Frequency bands in Brodmann areas (BAs) showing differences in afferent node capacity between the sudden sensorineural hearing loss patients with tinnitus (T) and sudden sensorineural hearing loss patients without tinnitus (NT) ($p < 0.05$). The red and black lines represent the T and NT groups, respectively. The black vertical lines denote BAs in which the frequency bands showed significant group differences. The figures were generated using the Nilearn (version 0.2.5) Python package.

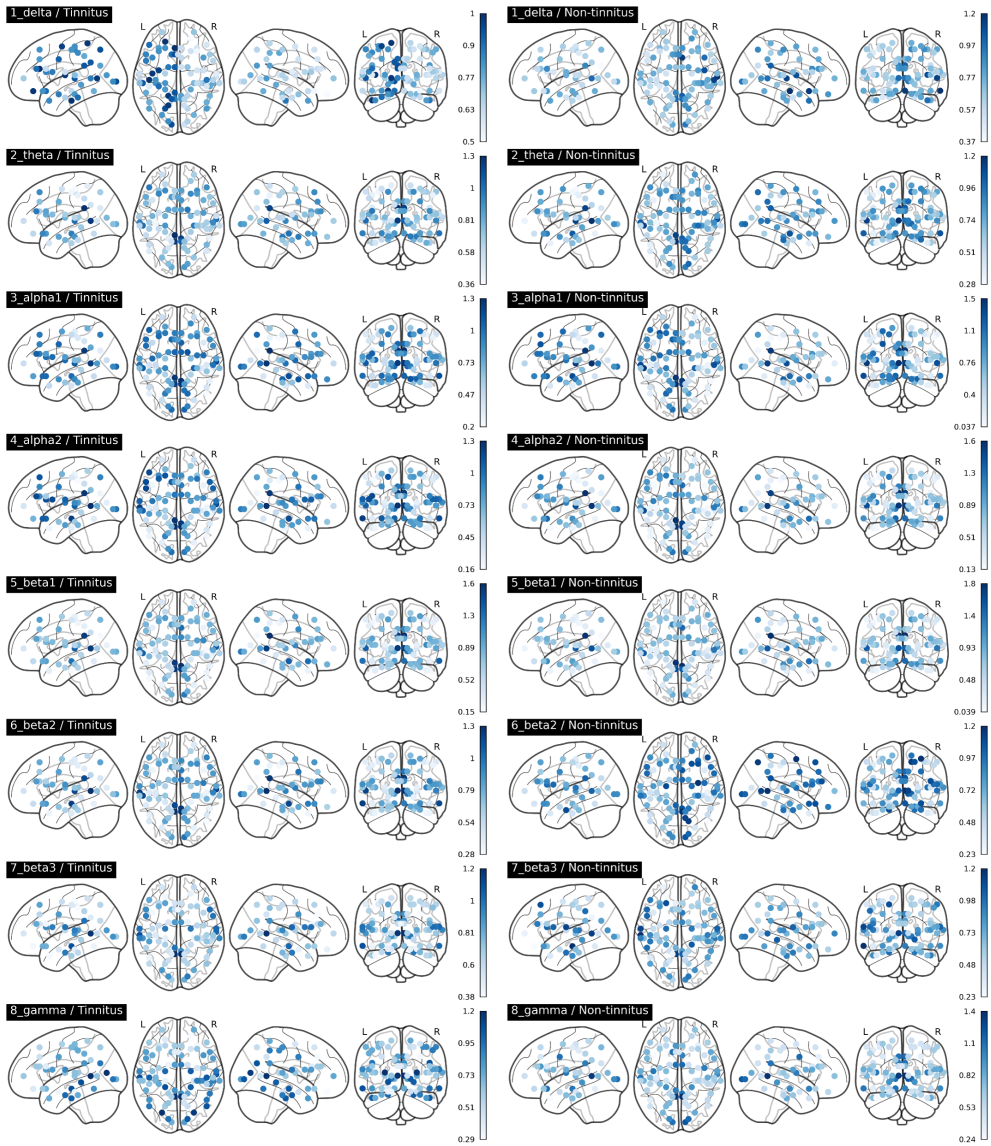

Figure 5.3: Afferent node capacity in all regions of interest in Brodmann areas, for all frequency bands ($p < 0.05$). The figures were generated using the Nilearn (version 0.2.5) Python package. The color scales of blue dots represent the average afferent node capacities at each Brodmann area of the sudden sensorineural hearing loss patients with- and without tinnitus groups; darker dots represent higher afferent node capacity.

Chapter 6

Topological data analysis: Mitral regurgitation

6.1 Methods

6.1.1 Study participants

A total of 1,276 patients with chronic moderate or severe MR were consecutively enrolled in this multicenter prospective valvular heart disease registry from 11 Asian tertiary hospitals (Korea, Japan, Hong Kong, and Singapore) between April 2013 and February 2016 [Ama20]. Among these, we extracted 1,147 patients with isolated primary MR without other significant coexistent valvular heart disease. After excluding those with missing values in any of the 14 variables required for TDA, 850 patients were included for the final analysis in the derivation cohort, including 318 moderate MR and 532 severe MR (Figure 6.1). The comparison of baseline characteristics between the derivation cohort and the entire population including the patients with missing values in any of the features used for TDA is presented in Table 6.1. Meanwhile, the validation cohort consisted of 257 consecutive patients with chronic primary MR diagnosed at the Seoul National University Hospital from February 2016 to June 2019.

The study conforms to the principles of the Helsinki declaration, and the study protocol was approved by the ethics committees of all participating centers. Informed written consent was obtained from all participating patients.

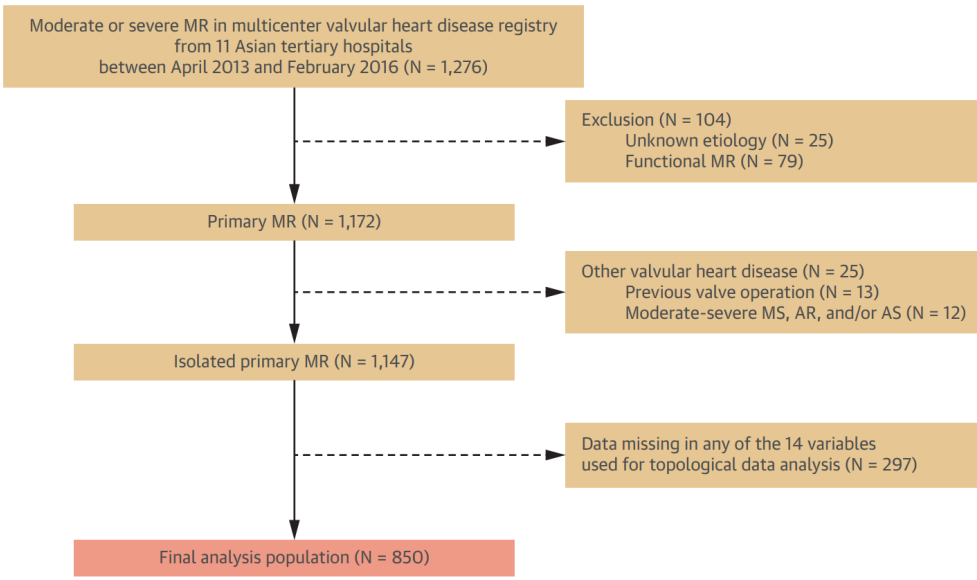

Figure 6.1: *Flowchart of patient selection for the derivation cohort.* Of 1,276 patients with chronic moderate or severe mitral regurgitation (MR), 850 patients were retained in the final analysis after excluding those with either significant co-existent valvular heart disease other than MR or those who underwent valve surgery and those with missing values in any of the 14 variables required for topological data analysis. AR, aortic regurgitation; AS, aortic stenosis; MS, mitral stenosis.

6.1.2 Echocardiographic evaluation

All patients underwent a comprehensive 2-dimensional and Doppler transthoracic echocardiography using commercially available ultrasound machines according to the contemporary international guidelines (Section 6.5) [Lan15, Nag16, Rud10]. The severity of MR was comprehensively assessed considering the effective regurgitant orifice area and/or regurgitant volume by the proximal isovelocity surface area method or the Doppler volumetric method according to the contemporary guidelines [Ama20, Zog17]. Generally, in primary MR, an effective regurgitant orifice area $\geq$0.4 cm^2 and regurgitant volume $\geq$60 mL are consistent with severe MR, and 0.20–0.39 cm^2 and $\geq$50 mL with moderate MR. In the case of late systolic regurgitation such as MR caused by prolapse, we additionally considered other parameters, such as the left ventricular (LV) size, to assess the severity of MR.

Variables	Derivation cohort	Entire population	P
	N=850	N=1,147	
Age, years	56.9±14.2	57.0±14.3	0.866
Male sex, n (%)	492 (57.9)	668 (58.2)	0.937
Body mass index, kg/m2	23.7±4.1	23.6±4.5	0.746
Systolic blood pressure, mmHg	126.5±18.0	126.4±18.3	0.878
Diastolic blood pressure, mmHg	73.3±11.2	73.3±11.3	0.936
Heart rate, bpm	71.1±11.7	71.4±12.8	0.605
NYHA functional class II-IV	312 (38.4)	382 (33.3)	0.818
Severe MR, n (%)	532 (62.5)	671 (58.5)	0.065
Etiology, n (%)			0.255
Prolapse/flail	718 (83.5)	960 (83.3)	
Rheumatic change	67 (7.9)	86 (7.5)	
Others	65 (7.6)	101 (8.8)	
Comorbidities, n (%)			
Hypertension	303 (35.6)	429 (67.4)	0.710
Diabetes mellitus	69 (8.1)	104 (9.1)	0.716
Dyslipidemia	130 (15.3)	171 (14.9)	0.950
Atrial fibrillation	109 (12.8)	151 (13.2)	0.975
End-stage renal disease	10 (1.2)	14 (1.2)	0.945
Echocardiographic parameters			
LV end-diastolic volume, ml	145.6±48.5	143.9±48.7	0.979
LV end-systolic volume, ml	52.7±23.6	52.7±25.1	0.453
LV ejection fraction, %	64.0±7.1	63.8±7.3	0.534
Interventricular septal thickness, mm	9.3±1.5	9.3±1.5	0.752
Posterior LV wall thickness, mm	9.2±1.4	9.2±1.4	0.693
E velocity, m/s	1.1±0.4	1.1±0.8	0.741
e' velocity, cm/s	7.7±2.4	7.8±2.5	0.268
E/e' ratio	16.2±8.3	15.8±8.1	0.266
Maximal TR velocity, m/s	2.6±0.5	2.6±0.5	0.878
Left atrial volume index, ml/m2	73.1±44.5	73.2±71.4	0.875

Table 6.1: *Baseline characteristics of the cohort before and after excluding patients with missing values.* E velocity, early diastolic transmitral inflow velocity; e' velocity, early diastolic mitral annular tissue velocity; LV, left ventricular; MR, mitral regurgitation; NYHA, New York Heart Association; TR, tricuspid regurgitation.

6.1.3 Topological data analysis

The entire 14 variables were used for analysis—age, body mass index, systolic and diastolic blood pressure, heart rate, LV end-diastolic and end-systolic volumes, left ventricular ejection fraction (LVEF), interventricular septal and posterior LV wall thickness, left atrial volume, early diastolic transmitral inflow velocity, early diastolic mitral annular velocity (e' velocity), and the maximal tricuspid regurgitation velocity (TRVmax). TDA was used in the current analysis because of its versatility in dealing with the high-dimensional data sets, bringing new insights that may be different from those obtained with traditional data mining methods. We performed TDA with a cloud-based analytic platform (version 8.8, Ayasdi Inc). Using TDA, we generated a network representation called the Mapper network of high-dimensional geometric data space [SMC07, Car09], using the 14 variables mentioned in the previous text to calculate the metric and the lens essential for TDA.

The Mapper network is an "analog of Reeb graph." Each node of the network represents a cluster of patients with similar features. The similarity between the 2 subjects was measured using a specific dimensionality reduction method, which we call a lens. An edge connects 2 nodes if the 2 corresponding clusters share the same subjects. Nodes were color-coded according to the average value of the feature of interest (eg, echocardiographic variables) for each node. In common, red to orange represents a higher value, yellow to green an intermediate value, and turquoise to blue a lower value of the feature.

A normalized correlation metric was used to measure the dissimilarity between 2 patients on a standard normalized data set. All features were normalized to have a zero mean and 1 SD. This was combined with Isomap with 2 components (resolution: 30, gain: 3.0, equalized) as lenses (Figure 6.2 A-C). A detailed introduction to the Mapper algorithm and the geometrical/topological concept is described in Section 6.5.2.

6.1.4 Phenogrouping based on patient-patient similarity network model

After a network model of patients with chronic primary MR was generated, we extracted distinct subgroups from the network, ie, the group of patients who share the common characteristics. The adequacy of grouping was supported with the agglomerative hierarchical clustering and the Louvain method (Section 6.5.3).

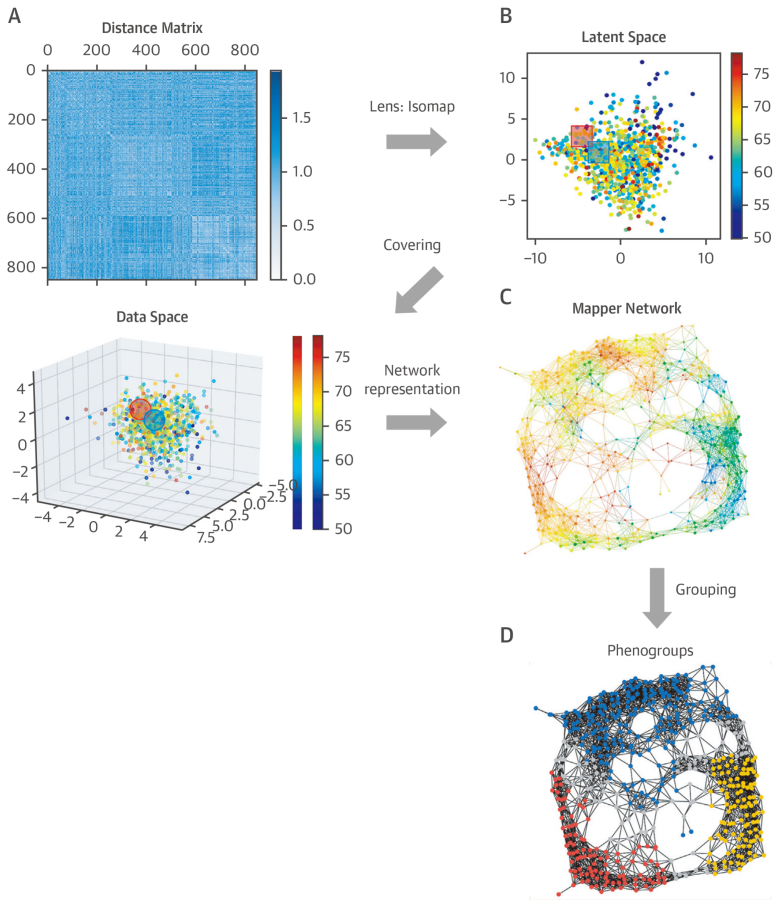

Figure 6.2: *Schematic diagram of the network model development from the topological data analysis.* **(A)** (*Upper*) Distance matrix of mitral regurgitation patients using normalized correlation. (*Lower*) The original space of the dataset is visualized by principal component analysis with 3 components. The red and blue clusters that come from the rectangles in the latent space form the nodes in the Mapper network. **(B)** Latent space is the image of the Isomap, which is a method to reduce the dimension, a 2-dimensional space in this case. The subjects with similar characteristics are covered in a rectangle. A cover is the set of these rectangles, which ultimately covers the whole space. **(C)** The Mapper network is generated from the patients' data for visualization and exploration of the data. **(D)** Phenogroups in the Mapper network are identified by applying the agglomerative hierarchical clustering and the Louvain algorithm.

First, we performed agglomerative hierarchical clustering to the Mapper network so that the node-set was partitioned into some clusters (Section 6.5.3). The densities of nodes were visualized by coloring with "rows per node," ie, the number of patients in each node. In the topological map colored by the number of subjects per node (ie, "rows per node"), we found 3 notable groups in the network model (Figure 6.2 D) with a relatively large number of patients clustered (ie, the areas represented by red to orange nodes in the center) (Figure 6.3 A). To group the subjects with high-density into clusters, the distance was set so that nodes with similar densities were close—the Louvain method slightly adjusted the clusters to obtain the most statistically stable partition. Finally, we reduced each subset of the partition so that any 2 subsets do not share a patient in common. The patients in each reduced subset of nodes formed a group of patients (Figure 6.2 D). Consequently, we discovered 3 groups based on the Mapper network (Figure 6.3 B). Details are described in Section 6.5.3.

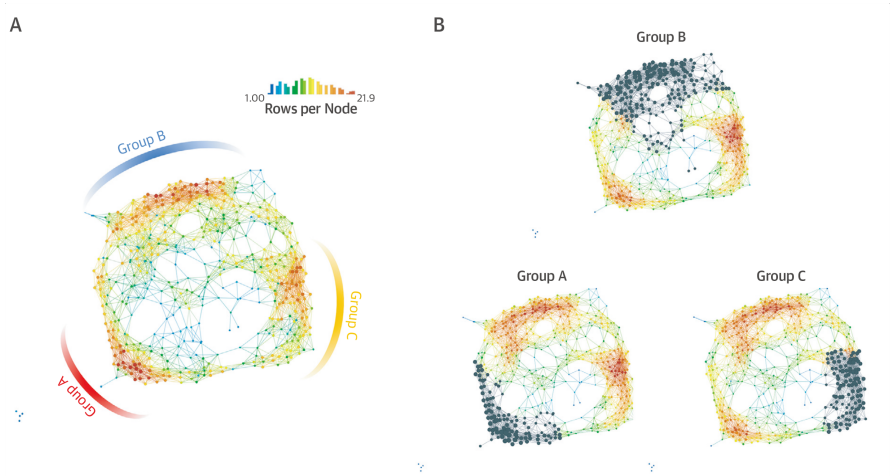

Figure 6.3: *Phenotypic groups of chronic primary mitral regurgitation patients based on the network model.* **(A)** The patient-patient similarity network model is colored to represent the number of subjects per node (i.e., Rows per node). In the upper right corner of the network, a histogram shows the range of the number of patients for each color. Red nodes—meaning a large number of subjects per node—are clustered into three distinct regions. **(B)** Three groups were recognized in the lower left region (group A), upper region (group B), and lower right region (group C).

6.1.5 Clinical outcomes

The clinical outcome was defined as a composite of surgery for symptomatic MR and cardiovascular death. Patients with symptomatic MR were defined as those with New York Heart Association functional class II, III, or IV, ie, any symptoms associated with heart failure. Patients were followed until September 2018 or for 5 years after the initial echocardiographic examination. We considered the patients censored when there was open heart surgery for reasons other than symptomatic MR and non-cardiovascular death.

6.1.6 Statistical analysis

Continuous variables were tested for normality and expressed as mean ± SD. Categorical variables are shown in number (percentage). For comparisons between 3 groups, the 1-way analysis of variance and Kruskal-Wallis tests or the chi-square test and Fisher exact test were used. Pairwise post hoc analysis was conducted using the Tukey HSD test. Event-free survival was estimated by the Kaplan-Meier method and compared using the log-rank test. HRs were calculated using Cox regression and presented with a 95% CI and P value.

To evaluate the additive prognostic value of patient phenogrouping by TDA, we first calculated the Mitral Regurgitation International Database (MIDA) mortality risk score (3 points are given for age ≥65 years and symptoms; 2 points for pulmonary arterial systolic pressure >50 mm Hg; and 1 point for atrial fibrillation, left atrial dimension ≥55 mm, LV enddiastolic dimension ≥40 mm, LVEF ≤60%) for each patient [Gri18], and then calculated the Harrell's C-index, the net reclassification improvement, and integrated discrimination improvement when the group information obtained from the network model was added on the MIDA risk score.

A 2-sided $P < 0.05$ was considered statistically significant. We used R version 3.5.3 (R Core Team, 2020, R Foundation for Statistical Computing) and SPSS version 25 (IBM Corp., Release 2017) for statistical analysis.

6.2 Results

6.2.1 Study population of the derivation cohort

A total of 850 patients (mean age 56.9 ± 14.2 years; 492 men [57.9%]) with chronic primary MR were included in the final analysis. The most common

etiology of MR was mitral valve prolapse/flail leaflet (83.5%). A total of 312 subjects (38.4%) presented symptoms related to MR at the time of echocardiographic evaluation. Details of the baseline characteristics are listed in Table 6.2.

6.2.2 Patient-patient similarity network model and distinct phenogroups of primary MR patients

Based on the similarity of patients with chronic primary MR, the geometric network model was presented in a 2-dimensional space. The patient-patient similarity network revealed 3 groups that were mainly located in the left lower region (group A), the top (group B), and the right lower region (group C) (Figure 6.3). Meanwhile, these 3 distinct patient phenogroups obtained using TDA could not be recognized with other analytical methods, such as the principal component analysis or hierarchical clustering (Figure 6.4).

When nodes were colored with orange to red for high values and turquoise to blue for low values for each echocardiographic variable, each feature showed different smooth gradients across the network (Figure 6.5, Figure 6.6). When the LV end-systolic volume (blue $\leq$26.5 mL and red $\geq$77.2 mL) and LVEF (blue $\leq$58.5% and red $\geq$70.7%) were shown by color across the geometric network, subjects with a dilated LV chamber and decreased LV systolic function were mostly gathered in the right lower corner of the network corresponding to group C region (Figure 6.5 A,B). Those with preserved LV systolic function and relatively normal LV end-systolic volume were located on the left upper side of the network corresponding to the region of group B, but only partially in group A. These distributions were discordant with those colored by the e' velocity (blue $\leq$4.1 cm/s and red $\geq$10.6 cm/s) and TRVmax (blue $\leq$1.9 m/s and red $\geq$3.2 m/s) (Figure 6.5 C,D). Specifically, most nodes with substantially decreased e' velocity were on the right and upper part of the network corresponding to the regions of groups B and C. Similarly, patients with an elevated TRVmax were located from the right side of group B region to the right lower part of the network, mainly within group C region. The network models of the remaining 10 variables are in Figure 6.6.

6.2.3 Characteristics of primary MR phenogroups

For group comparison, 69 subjects allocated in 2 phenogroups or more were excluded from the analysis, and therefore a total of 781 patients were analyzed.

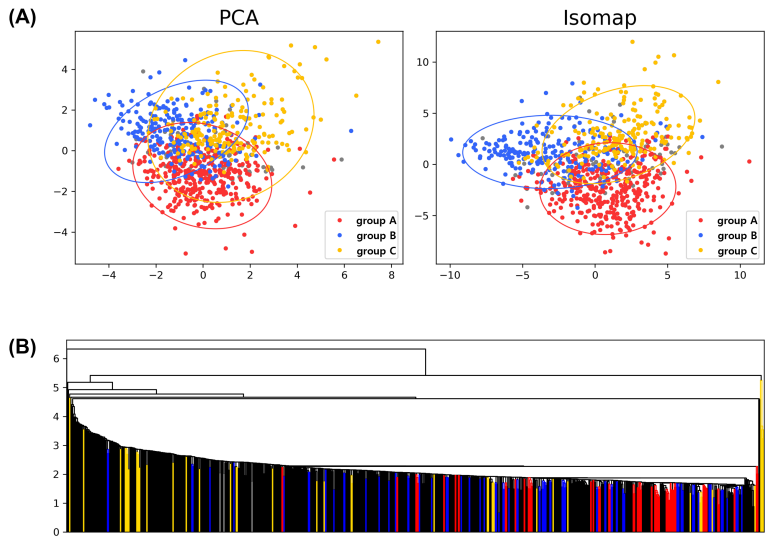

Figure 6.4: *Failure to reproduce the phenogroups from the topological data analysis with other dimensionality reduction methods and hierarchical clustering.* **(A)** Latent space obtained from commonly used two-dimensionality reduction methods, principal component analysis (PCA), and Isomap. Each point corresponds to a patient and is colored according to the groups identified from topological data analysis. **(B)** Hierarchical clustering to the patient space. The horizontal axis means patients, and the vertical axis means thresholds at which clusters are merged. Each segment is colored according to groups identified from topological data analysis. Note that the groups identified by TDA cannot be reproduced by any of these methods nor can the characteristics of each feature "visualized" by the network.

Demographic, clinical characteristics, and echocardiographic data were significantly different between the 3 groups (Table 6.3). The comparison of groups, including the patients overlapping in each group, is presented separately in Table 6.4.

Group A was the youngest (average age 41.8 $\pm$ 10.2 years; $P < 0.05$ vs others), with a lower prevalence of comorbidities, such as hypertension, dyslipidemia, and atrial fibrillation. Group B was the oldest (average age 65.4 $\pm$ 10.4 years; $P < 0.05$ vs others) with the highest systolic blood pressure (135.1 $\pm$ 17.2 mm Hg; $P < 0.05$ vs others) and the highest prevalence of hypertension (50.0%; $P < 0.05$ vs others). The average age and prevalence of comorbidities in group C were intermediate between groups A and B, but

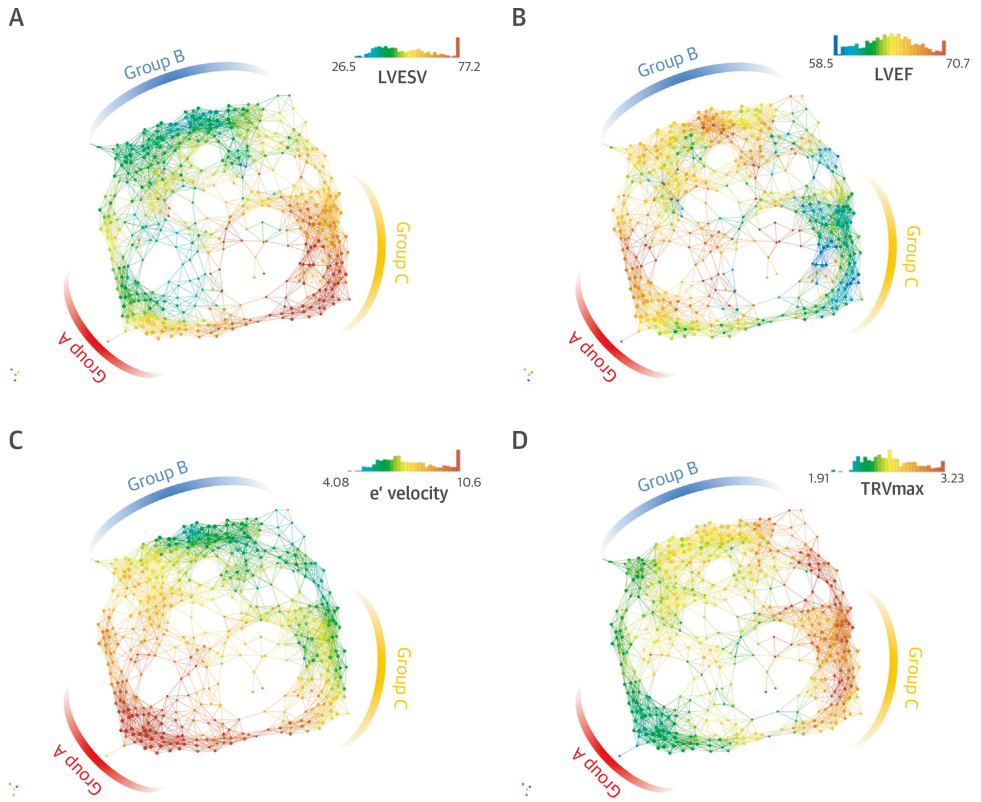

Figure 6.5: *Patient-patient similarity network model of chronic primary mitral regurgitation patients in the derivation cohort colored by left ventricular (LV) remodeling parameters.* A network model was generated by topological data analysis using 14 demographic and echocardiographic variables. The network model is color-coded to reflect the indicated variable in the upper right corner of each network; red orange indicating a higher level of the variable, yellow green intermediate level, and turquiose blue indicating lower/normal level. In the upper right corner of each network, a histogram shows the range and distribution of each color value. **(A)** LV end-systolic volume (LVESV) (ml), **(B)** LV ejection fraction (LVEF) (%), **(C)** early diastolic mitral annular tissue velocity (e' velocity) (cm/s), and **(D)** maximal tricuspid regurgitation velocity (TRVmax) (m/s).

atrial fibrillation was most frequent in group C (26.5%; $P < 0.05$ vs others). Besides, group C had the highest proportion of subjects with symptomatic MR and severe MR among the 3 groups. The proportion of subjects with dyspnea

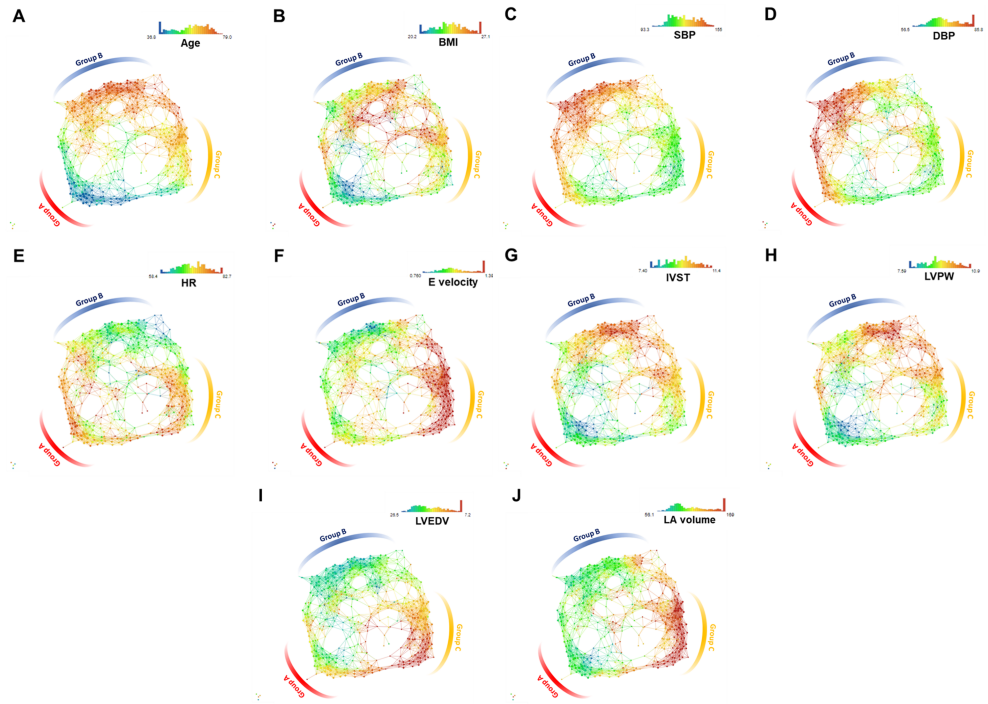

Figure 6.6: *Patient-patient similarity network model of chronic primary mitral regurgitation patients in the derivation cohort.* A network model was generated by topological data analysis using 14 demographic and echocardiographic variables from the derivation cohort. The network model is color-coded to reflect the indicated variable in the upper right corner of each network; red orange indicating a higher level of variables, yellow green intermediate level, and turquoise blue indicating lower/normal level. In the upper right corner of each network, a histogram shows the range and distribution of each color value. **(A)** Age (years), **(B)** body mass index (BMI) (kg/m^2), **(C)** systolic blood pressure (SBP) (mmHg), **(D)** diastolic blood pressure (DBP) (mmHg), **(E)** heart rate (HR) (bpm), **(F)** early diastolic transmitral inflow velocity (E velocity) (m/s), **(G)** interventricular septal thickness (IVST) (mm), **(H)** left ventricular posterior wall thickness (LVPW) (mm), **(I)** left ventricular end-diastolic volume (LVEDV) (ml), and **(J)** left atrial (LA) volume (ml).

(New York Heart Association functional classification II-IV) increased in the order of groups A, B, and C (24.2%, 38.1%, and 53.2%; $P < 0.001$).

Regarding the echocardiographic parameters, LVEF was similar between groups A and B. The e' velocity and TRVmax, variables commonly used to

assess the diastolic function, were significantly lower and higher, respectively, in group B than in group A, whereas LV volumes were larger in group A than group B. Group C had the largest LV volume, the highest TRVmax, and the lowest LVEF and e' velocity among the 3 phenogroups. Based on these characteristics, we could summarize group A as the "compensatory LV dilation" group, group B as the "LV diastolic dysfunction" group, and group C as having both characteristics.

6.2.4 Association of the distinct phenotypic groups with clinical outcome and its additive value

During a median follow-up of 3.5 years [IQR 0.89-5.00 years], 60 patients received surgery for symptomatic MR ($n = 58$) or died from cardiovascular causes ($n = 2$). Group C had the worst event-free survival for the composite outcome ($P < 0.001$ by log-rank test) (Figure 6.7). Notably, group B had an event-free survival rate comparable to group A ($P = 0.142$ by log-rank test). These trends were similar for subgroups stratified by the severity of MR (Figure 6.8) and symptom status (Figure 6.9).

After adjusting for the MIDA risk score with multivariate Cox regression analysis, the grouping information obtained from the network model was an independent predictor for the composite outcome (adjusted HR: 1.918; 95% CI 1.257-2.927; $P = 0.003$). The addition of the phenogrouping by the network model to the MIDA risk score increased the C-index (0.685 to 0.705; $P = 0.028$) and resulted in a significantly improved prediction of the composite outcome (net reclassification improvement 0.373; 95% CI: 0.113-0.634; $P = 0.005$; integrated discrimination improvement 0.056; 95% CI: 0.013-0.098; $P = 0.010$).

6.2.5 Validation of network model of primary MR

The validation cohort consisted of 257 chronic primary MR patients (mean age 61.9 ± 16.3 years; 128 men [49.8%]) with a higher proportion of moderate MR ($n = 188$, 73.2%) than the derivation cohort (Table 6.5). The 2-dimensional network model and its colored distribution of the same parameters demonstrated a pattern similar to that of the derivation cohort, albeit with fewer nodes and edges because of the smaller number of subjects (Figure 6.10). By the same analytic approach, we discovered 3 phenogroups with distinct characteristics as in the derivation cohort (Table 6.6), after excluding 36 subjects

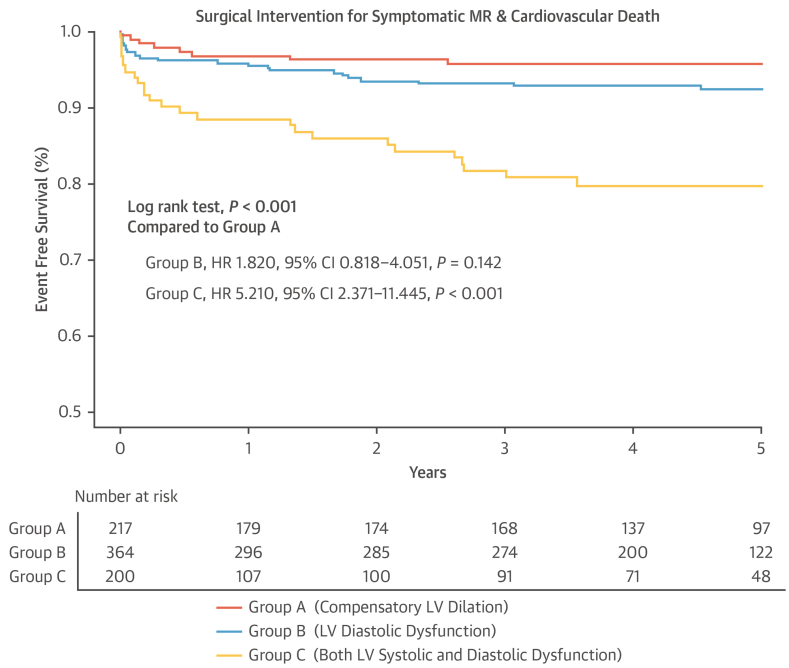

Figure 6.7: *Kaplan-Meier curve for cumulative event-free survival in the phenogroups of mitral regurgitation (MR) patients discovered in the network model.* The composite endpoint was surgery for symptomatic MR and cardiovascular death. Three phenogroups of chronic primary MR were discovered in the network model. CI, confidence interval; HR, hazard ratio; LV, left ventricular.

allocated in 2 or more phenogroups. The relationship between the phenogroups and clinical outcome was similar to that in the derivation cohort (Figure 6.10 F).

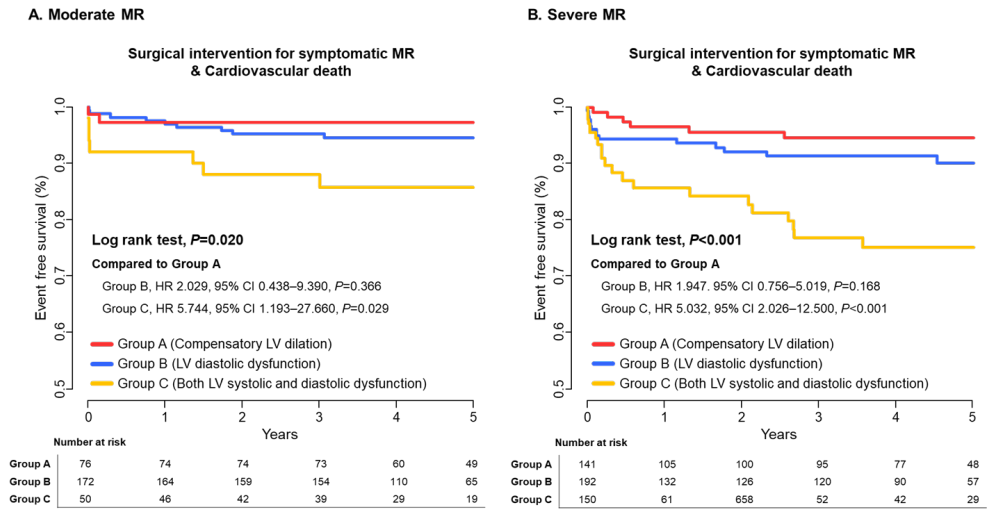

Figure 6.8: *Kaplan-Meier curves for cumulative event-free survival in moderate and severe mitral regurgitation (MR).* Patients with chronic primary MR in the derivation cohort were stratified according to the severity; **(A)** moderate MR and **(B)** severe MR. The composite endpoint of surgery for symptomatic MR and cardiovascular death were compared between the three groups discovered in the network model of chronic primary MR. Kaplan-Meier curves for cumulative event-free survival were drawn for each stratum. CI, confidence interval; HR, hazard ratio; LV, left ventricular.

Variables	Total
	N=850
Age, years	56.9±14.2
Male sex, n (%)	492 (57.9)
Body mass index, kg/m^2	23.7±4.1
Systolic blood pressure, mmHg	126.5±18.0
Diastolic blood pressure, mmHg	73.3±11.2
Heart rate, bpm	71.1±11.7
NYHA functional class II-IV, n (%) (N=812)	312 (38.4)
Severe MR, n (%)	532 (62.5)
Etiology, n (%)	
Prolapse/flail	718 (83.5)
Rheumatic change	67 (7.9)
Others	65 (7.6)
Comorbidities, n (%)	
Hypertension	303 (35.6)
Diabetes mellitus	69 (8.1)
Dyslipidemia	130 (15.3)
Atrial fibrillation	109 (12.8)
End-stage renal disease	10 (1.2)
Echocardiographic parameters	
LV end-diastolic volume, ml	145.6±48.5
LV end-systolic volume, ml	52.7±23.6
LV ejection fraction, %	64.0±7.1
LV ejection fraction ≥60%, n (%)	664 (78.1)
LV ejection fraction 50–59.9%, n (%)	163 (19.2)
LV ejection fraction <50%, n (%)	23 (2.7)
Interventricular septal thickness, mm	9.3±1.5
Posterior LV wall thickness, mm	9.2±1.4
E velocity, m/s	1.1±0.4
e' velocity, cm/s	7.7±2.4
E/e' ratio	16.2±8.3
Maximal TR velocity, m/s	2.6±0.5
Left atrial volume index, ml/m^2	73.1±44.5

Table 6.2: *Baseline characteristics of the derivation cohort.* E velocity, early diastolic transmitral inflow velocity; e' velocity, early diastolic mitral annular tissue velocity; LV, left ventricular; MR, mitral regurgitation; NYHA, New York Heart Association; TR, tricuspid regurgitation.

Variables	Group A	Group B	Group C	P
	N=217	N=364	N=200	
Age, years	41.8±10.2†	65.4±10.4*	57.2±10.9*,†	<0.001
Male, n (%)	132 (60.8)	199 (54.7)	118 (59.0)	0.503
Body mass index, kg/m2	22.2±3.3†	24.4±4.5*	23.8±3.7*	0.008
Systolic blood pressure, mmHg	124.5±15.2†	135.1±17.2*	113.7±14.0*,†	<0.001
Diastolic blood pressure, mmHg	74.0±10.1	75.4±11.3	67.9±10.4*,†	<0.001
Hart rate, bpm	73.9±11.3†	67.8±11.2*	73.3±12.0†	0.484
NYHA functional class II-IV, n (%) (N=747)	50/207 (24.2)†	135/354 (38.1)*	99/186 (53.2)*,†	<0.001
Severe MR, n (%)	141 (65.0)†	192 (52.7)*	150 (75.0)*,†	<0.001
Etiology, n (%)				
Prolapse/flail	196 (90.3)	322 (88.5)	140 (70.0)	
Rheumatic change	10 (4.6)	10 (2.7)	43 (21.5)	<0.001
Others	11 (5.1)	32 (8.8)	17 (8.5)	
Comorbidities, n (%)				
Hypertension	31 (14.3)†	182 (50.0)*	58 (29.0)*,†	<0.001
Diabetes mellitus	12 (5.5)	36 (9.9)	17 (8.5)	0.204
Dyslipidemia	13 (6.0)†	88 (24.2)*	21 (10.5)	<0.001
Atrial fibrillation	11 (5.1)	31 (8.5)	53 (26.5)*,†	<0.001
End-stage renal disease	1 (0.5)	4 (1.1)	4 (2.0)	0.312
Echocardiographic parameters				
LV end-diastolic volume, ml	148.2±39.4†	124.2±37.6*	180.1±55.3*,†	<0.001
LV end-systolic volume, ml	50.7±15.3†	43.7±15.5*	71.2±32.8*,†	<0.001
LV ejection fraction, %	65.6±5.3	64.9±6.2	60.8±9.5*,†	<0.001
LV ejection fraction ≥60%, n (%)	191 (88.0)	287 (78.8)	130 (65.0)	<0.001
LV ejection fraction 50–59.9%, n (%)	26 (12.0)	71 (19.5)	53 (26.5)	
LV ejection fraction <50%, n (%)	0 (0.0)	6 (1.6)	17 (8.5)	
Interventricular septal thickness, mm	8.6±1.4†	9.8±1.5*	9.4±1.3*,†	<0.001
Posterior LV wall thickness, mm	8.6±1.3†	9.6±1.4*	9.3±1.2*,†	<0.001
E velocity, m/s	1.0±0.3	1.0±0.3	1.4±0.4*,†	<0.001
e' velocity, cm/s	10.1±2.2†	6.7±1.7*	7.1±1.9*,†	<0.001
E/e' ratio	10.7±3.5†	16.5±7.3*	21.4±10.1*,†	<0.001
Maximal TR velocity, m/s	2.3±0.3†	2.6±0.4*	2.9±0.6*,†	<0.001
Left atrial volume index, ml/m2	54.9±22.3	62.5±27.4	110.5±64.6*,†	<0.001

Table 6.3: *Baseline characteristics according to phenogroups in the network model.* *P <0.05 compared with group A and †P <0.05 compared with group B. E velocity, early diastolic transmitral inflow velocity; e' velocity, early diastolic mitral annular tissue velocity; LV, left ventricular; MR, mitral regurgitation; NYHA, New York Heart Association; TR, tricuspid regurgitation.

Variables	Group A	Group B	Group C	P
	N=250	N=416	N=229	
Age, years	43.6±11.2†	65.1±10.5*	57.8±11.3*,†	<0.001
Male, n (%)	152 (60.8)	232 (55.8)	138 (60.3)	0.539
Body mass index, kg/m2	22.2±3.3†	24.4±4.5*	24.1±3.8*	<0.001
Systolic blood pressure, mmHg	124.8±15.3	134.0±17.5	113.0±14.7*,†	<0.001
Diastolic blood pressure, mmHg	74.1±10.1	75.5±11.2	68.9±10.8*,†	<0.001
Hart rate, bpm	75.1±12.1†	70.1±11.8*	76.6±41.1†	0.557
NYHA functional class II-IV, n (%)	57 (23.9)†	159 (39.5)*	117 (54.9)*,†	<0.001
Severe MR, n (%)	165 (66.0)†	228 (54.8)*	171 (74.7)*,†	<0.001
Etiology, n (%)				
Prolapse/Flail	185 (74.0)	271 (65.1)	100 (43.7)	
Rheumatic change	12 (4.8)	13 (3.1)	45 (19.7)	<0.001
Others	12 (4.8)	34 (8.2)	17 (7.4)	
Comorbidities, n (%)				
Hypertension	43 (17.2)†	213 (51.2)*	73 (31.9)*,†	<0.001
Diabetes mellitus	13 (5.2)	40 (9.6)	19 (8.3)	0.155
Dyslipidemia	17 (6.8)†	94 (22.6)*	22 (9.6)*,†	<0.001
Atrial fibrillation	15 (6.0)	43 (10.3)	62 (27.1)*,†	<0.001
End-stage renal disease	1 (0.4)	5 (1.2)	5 (2.2)	0.223
Echocardiographic parameters				
LV end-diastolic volume, ml	147.7±10.2†	126.8±40.0*	178.1±54.7*,†	<0.001
LV end-systolic volume, ml	50.8±15.6†	44.6±15.9*	69.7±31.7*,†	<0.001
LV ejection fraction, %	65.5±5.2	64.8±6.2	61.2±9.2*,†	<0.001
LV ejection fraction ≥60%, n (%)	221 (88.4)	327 (78.6)	151 (65.9)	<0.001
LV ejection fraction 50–59.9%, n (%)	29 (11.6)	83 (20.0)	61 (26.6)	
LV ejection fraction <50%, n (%)	0 (0.0)	6 (1.4)	17 (7.4)	
Interventricular septal thickness, mm	5.6±1.4†	9.7±1.5*	9.5±1.3*	<0.001
Posterior LV wall thickness, mm	8.6±1.3†	9.5±1.4*	9.3±1.2*	<0.001
E velocity, m/s	1.1±0.3	1.1± 0.3	1.4±0.4*,†	<0.001
e' velocity, cm/s	9.9±2.2†	6.7±1.8*	7.0±1.9*	<0.001
E/e' ratio	11.0±3.5†	16.8±7.4*	21.3±9.9*,†	<0.001
Maximal TR velocity, m/s	2.3±0.3†	2.6±0.5*	2.9±0.6*,†	<0.001
Left atrial volume index, ml/m2	56.6±23.3†	64.6±28.6*	107.7±62.2*,†	<0.001

Table 6.4: *Baseline characteristics according to phenogroups in the network model (Sensitivity analysis).* *P <0.05 compared with group A and †P <0.05 compared with group B. E velocity, early diastolic transmitral inflow velocity; e' velocity, early diastolic mitral annular tissue velocity; LV, left ventricular; MR, mitral regurgitation; NYHA, New York Heart Association; TR, tricuspid regurgitation.

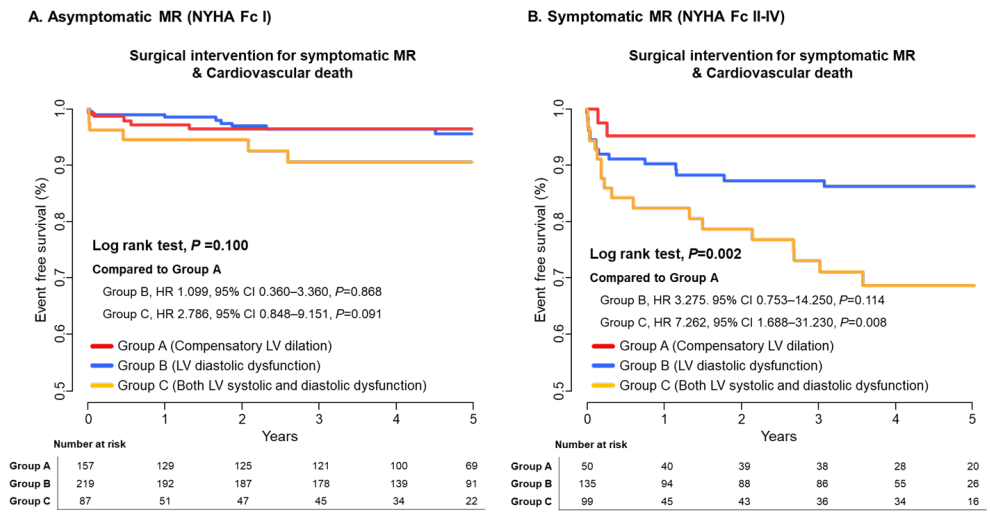

Figure 6.9: *Kaplan-Meier curves for cumulative event-free survival in mitral regurgitation (MR) patients with or without symptoms.* Patients in the derivation cohort were stratified according to the symptoms of MR; New York Heart Association functional class (NYHA Fc) II-IV defined as symptomatic MR. The composite endpoint of surgery for symptomatic MR and cardiovascular death were compared between the three groups discovered in the network model of chronic primary MR. Kaplan-Meier curves for cumulative event-free survival were drawn for each stratum. CI, confidence interval; HR, hazard ratio; LV, left ventricular.

variables	Total
	N=257
Age, years	61.9±16.3
Male sex, n (%)	128 (49.8)
Body mass index, kg/m2	22.9±3.36
Systolic blood pressure, mmHg	123.2±18.2
Diastolic blood pressure, mmHg	72.2±11.8
Heart rate, bpm	74.7±16.5
NYHA functional class II-IV, n (%)	78 (30.3)
Severe MR, n (%)	69 (26.8)
Etiology	
Prolapse/flail	203 (79.0)
Rheumatic change	34 (13.2)
Others	20 (7.8)
Echocardiographic parameters	
LV end-diastolic volume, ml	50.9±22.2
LV end-systolic volume, ml	130.2±43.2
LV ejection fraction, %	60.8±6.7
LV ejection fraction ≥60%, n (%)	140 (63.3)
LV ejection fraction 50–59.9%, n (%)	70 (31.7)
LV ejection fraction <50%, n (%)	11 (4.9)
Interventricular septal thickness, mm	9.3±1.4
Posterior LV wall thickness, mm	9.2±1.4
E velocity, m/s	1.1±0.4
e' velocity, cm/s	7.4±2.4
E/e' ratio	17.0±9.6
Maximal TR velocity, m/s	2.6±0.5
Left atrial volume index, ml/m2	80.3±65.7

Table 6.5: *Baseline characteristics of the validation cohort.* E velocity, early diastolic transmitral inflow velocity; e' velocity, early diastolic mitral annular tissue velocity; LV, left ventricular; MR, mitral regurgitation; NYHA, New York Heart Association; TR, tricuspid regurgitation.

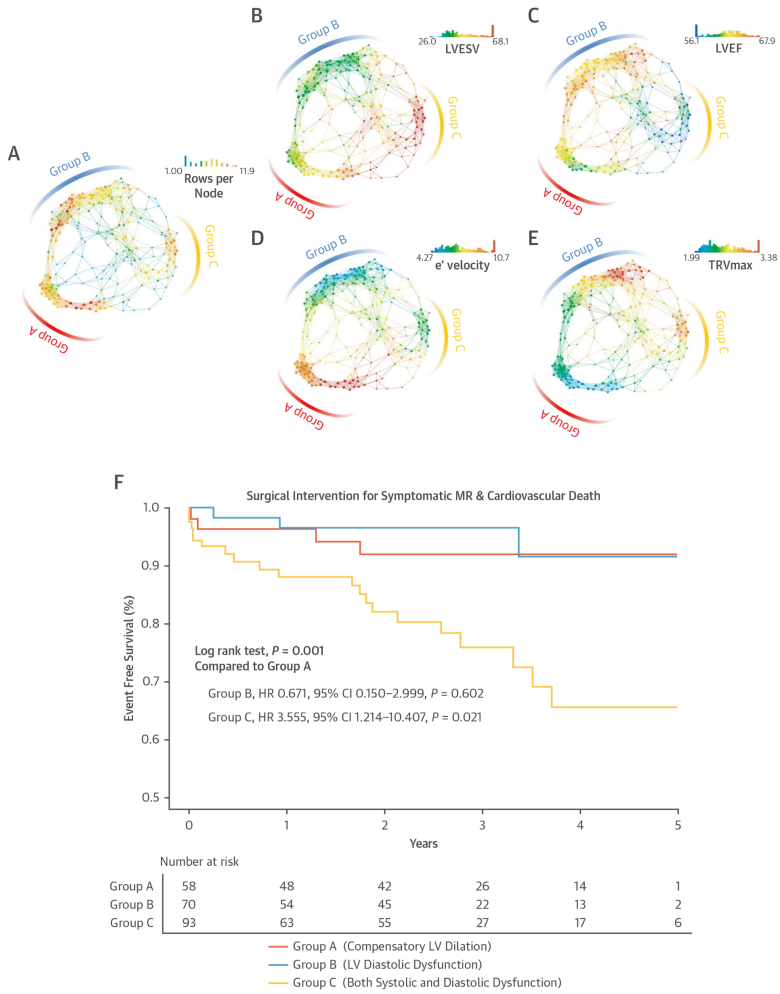

Figure 6.10: *Patient-patient similarity network model of chronic primary mitral regurgitation (MR) patients in the validation cohort.* A network model was generated by topological data analysis using 14 demographic and echocardiographic variables from the validation cohort. **(A)** A large number of subjects per node are clustered into three distinct regions; lower left region (group A), upper region (group B), and lower right region (group C). **(B E)** The network model is color-coded to reflect the given parameter in the upper right corner of each figure; red orange indicating a higher level of the variable, yellow green intermediate level, and turquiose blue indicating lower/normal level. In the upper right corner of each network, a histogram shows the range and distribution of the variable for each color; **(B)** left ventricular (LV) end-systolic volume (LVESV) (ml), **(C)** LV ejection fraction (LVEF) (%), **(D)** early diastole mitral annular tissue velocity (e' velocity) (cm/s), and **(E)** maximal tricuspid regurgitation velocity (TRVmax) (m/s). **(F)** The composite endpoint of surgery for symptomatic MR and cardiovascular death is shown for the validation cohort. CI, confidence interval; HR, hazard ratio.

Variables	Group A	Group B	Group C	P
	N=58	N=70	N=93	
Age, years	45.5 [33.0–50.0]†	74.5 [66.3–79.8]*	65.0 [57.0–74.0]*,†	<0.001
Male, n (%)	25 (43.1)	32 (45.7)	52 (55.9)	0.237
Body mass index, kg/m2	21.8 [20.0–23.5]†	23.4 [21.4–25.6]*	23.1 [21.2–25.0]	0.007
Systolic blood pressure, mmHg	119.7±12.4†	137.3±16.2*	115.6±18.2†	0.022
Diastolic blood pressure, mmHg	73.8±11.3	74.5±9.1	69.6±12.8†	0.015
Hart rate, bpm	71.0 [64.0–80.8]	69.5 [64.0–78.0]	75.0 [65.0–85.0]*,†	0.052
NYHA functional class II-IV, n (%)	8 (13.8)†	25 (35.7)*	30 (32.3)*	0.017
Severe MR, n (%)	10 (17.2)	10 (14.3)	32 (34.4)†	0.005
Etiology, n (%)				
Prolapse/flail	54 (93.1)	59 (84.3)	59 (63.4)	
Rheumatic change	2 (3.4)	5 (7.1)	24 (25.8)	<0.001
Others	2 (3.4)	6 (8.6)	10 (10.8)	
Echocardiographic parameters				
LV end-diastolic volume, ml	121.5 [112.2–135.2]†	104.5 [89.0–120.0]*	144.0 [115.0–179.0]*,†	<0.001
LV end-systolic volume, ml	47.0 [42.0–52.8]†	38.0 [31.3–43.0]*	57.0 [47.0–75.0]*,†	<0.001
LV ejection fraction, %	61.0 [59.0–64.0]	64.0 [61.0–66.0]	58.0 [54.0–62.0]*,†	<0001
LV ejection fraction ≥60%, n (%)	37 (63.8)	60 (85.7)	43 (46.2)	
LV ejection fraction 50–59.9%, n (%)	21 (36.2)	10 (14.3)	39 (14.9)	<0.001
LV ejection fraction <50%, n (%)	0 (0.0)	0 (0.0)	11 (11.8)	
Interventricular septal thickness, mm	8.0 [8.0–9.8]†	10.0[9.0–10.0]*	9.0 [8.0–10.0]*	<0.001
Posterior LV wall thickness, mm	8.5 [7.0–9.0]†	10.0 [9.0–10.0]*	9.0 [8.0–10.0]*	<0.001
E velocity, m/s	0.9 [0.7–1.0]	0.9 [0.7–1.2]	1.3 [1.1–1.5]*,†	<0.001
e' velocity, cm/s	9.7 [8.6–11.0]†	6.0 [4.9–7.0]*	6.8 [5.2–8.2]*,†	<0.001
E/e' ratio	9.0 [7.6–10.6]†	14.1 [11.2–21.6]*	20.0 [13.4–25.0]*,†	<0.001
Maximal TR velocity, m/s	2.2 [2.0–2.3]†	2.6 [2.4–3.0]*	2.7 [2.4–3.0]*	<0.001
Left atrial volume index, ml/m2	46.5 [35.2–58.2]	54.6 [45.5–76.5]	88.2 [66.4–128.2]*,†	<0.001

Table 6.6: *Baseline characteristics of validation cohort according to phenogroups in the network model.* *P <0.05 compared with group A and †P <0.05 compared with group B. E velocity, early diastolic mitral inflow velocity; e' velocity, early diastolic mitral annular tissue velocity; LV, left ventricular; MR, mitral regurgitation; NYHA, New York Heart Association; TR, tricuspid regurgitation.

6.3 Discussion

This study applied a topology-based approach for chronic primary MR patients to develop a patientpatient similarity network (fig. 6.11). Our findings can be summarized as follows. First, the network of chronic primary MR patients by TDA intuitively visualized the pattern of LV structural and functional remodeling. Second, 3 distinct phenogroups of chronic primary MR patients were set apart based on the patient-patient similarity network, each with distinctive characteristics. Third, a specific phenogroup of patients (ie, group B) with both significant MR and predominant LV diastolic dysfunction showed a clinical outcome comparable to that of those with only compensatory LV dilation but preserved systolic function.

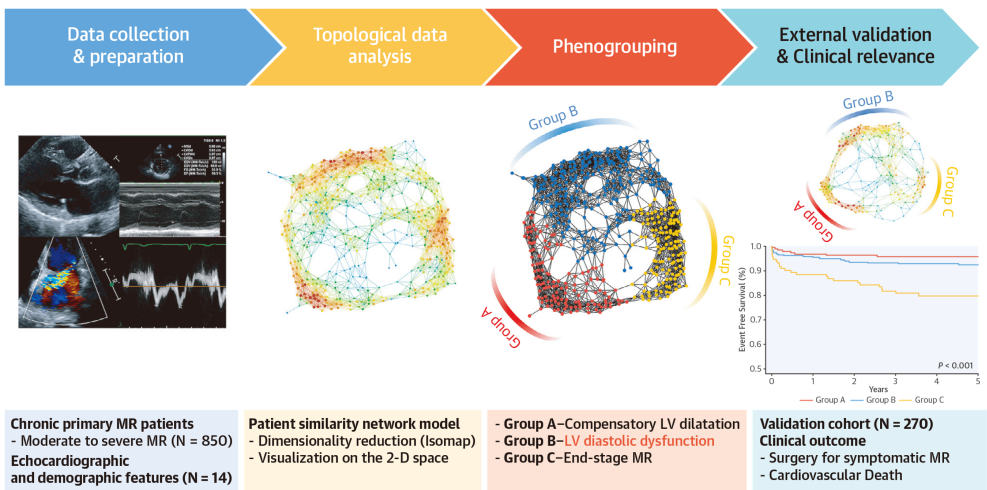

Figure 6.11: *A step-by-step process to understand the cardiac remodeling pattern by chronic primary mitral regurgitation (MR) using topological data analysis and to demonstrate the clinical relevance of the new phenogroups.* A large demographic and echocardiographic data of chronic primary MR patients were collected from the international multicenter registry. The distance matrix for topological data analysis was created by calculating the normalized correlation and processed with Isomap. The high-dimensional data undergoes dimensionality reduction into a 2-dimensional topological map. The network was represented by nodes (dots) and edges (lines), which we call a patient-patient similarity network model. Based on the network model, new phenogroups with distinct characteristics were discovered using the agglomerative hierarchical clustering and the Louvain method. Lastly, we evaluated the clinical relevance of these novel phenogroups and their clinical implications. LV, left ventricular.

There are certain unique points in the methods used. First, TDA can "picturize" or "visualize" the distribution of the multiple complex data holistically, and provides a more intuitive understanding of the entire data set and its complex connections. Second, it would have been possible to discover that a certain echocardiographic parameter is predictive of the outcome had the conventional hypothesis-driven analysis been used for the same data set. However, it would have been nearly impossible to identify a certain "group" of patients sharing similar characteristics. Rather than discovering the importance of a certain parameter, it would be clinically more useful to determine which type of patient is at high risk. Third, TDA reduces the possibility of missing critical insights by clustering the data in the original high dimensional space, whereas other dimensionality reduction methods first reduce the data into a few attributes. Thus, other dimensionality reduction and/or clustering methods may fall short of reproducing our phenogroups (Figure 6.4), verifying the uniqueness of TDA.

Group A in our analysis verifies a well-known compensatory mechanism following LV volume overload by chronic MR, in which the LV chamber expands to accommodate higher volumes and maintain a relatively normal end-diastolic pressure [GM18]. After the early stage with preserved LV systolic function, pump failure and deterioration of myocardial diastolic properties progress with an increase in ventricular stiffness [Cor91]. This advanced structural and functional LV remodeling in chronic MR is manifested in group C.

On the other hand, the network revealed a distinctive phenotype of chronic primary MR (ie, group B) not described in the current published data. Group B is characterized by impaired LV relaxation and LV hypertrophy, differing from the commonly established compensatory LV dilation phenotype. Notably, LV diastolic dysfunction with LV hypertrophy is often seen in elderly patients with hypertension and is commonly associated with LV stiffness [Con95, Zan07, Wes08]. Besides, patients in group B had a higher proportion of symptomatic patients. The cardiac remodeling observed in group B could contribute to patients' breathlessness, thus complicating the symptomatology of the MR patients. Therefore, it remains to be verified whether the diastolic dysfunction is a result of comorbidities, chronic MR, or a mixture of both.

Although compensatory dilation of LV and systolic dysfunction have gained attention, diastolic dysfunction has not been sufficiently considered when assessing MR patients and determining the optimal timing for surgical intervention [Bau17, Wri21]. This might be because it is challenging to determine the

diastolic function in MR with the enhanced early transmitral inflow and reduced systolic pulmonary vein flow by the regurgitant flow [Ros01]. Although our analysis does not prove the causal relationship between the phenogroups and clinical outcome, it should be highlighted that the presence of diastolic dysfunction is as important as the compensatory mechanism of LV dilation in MR patient evaluation. Furthermore, future studies are warranted to confirm our findings on whether there is a causality between chronic primary MR and diastolic dysfunction.

6.3.1 Study limitation

First, the features used for TDA were acquired by noninvasive imaging and not by invasive hemodynamic studies such as right heart catheterization. In addition, variables indicating the LV functional reserve (eg, stress echocardiography) and the right ventricular structure and/or function were also not collected and, therefore, not included for analysis. Although advanced echocardiography, such as speckle tracking echocardiography, was not done, we tried to analyze the echocardiography data that is most likely to be standardized across any institutions. As such, our findings can be generalized to any center involved in managing or treating these patients, which is a strength of this study. Second, the validation data set was limited in numbers. However, we reproduced the network model and phenotypic groups using the validation cohort and could demonstrate their relationship with clinical outcomes. Last, the MIDA risk score has been initially proposed as a system to predict mortality, and its use as a predictor of the composite clinical outcome can be criticized as an excessive extrapolation of the score. However, there is no specific scoring system to predict the composite clinical outcome in primary MR patients to now, and our analysis shows that the MIDA risk score is also a significant predictor for the composite outcome of surgery for symptomatic MR and cardiovascular death (HR: 1.323; 95% CI: 1.204- 1.453; $P < 0.001$).

6.4 Conclusion

The patient-patient similarity network model generated by TDA intuitively visualized the patterns of cardiac structural and functional remodeling in chronic primary MR. The geometric network revealed an important distinct phenogroup of chronic primary MR patients with predominant diastolic dys-

function, which has been overlooked in the current published data. These findings suggest that diastolic dysfunction deserves equal attention as ventricular dilatation or pump failure when trying to understand the progression or clinical presentation of chronic primary MR.

6.5 Supplemental Methods

6.5.1 Echocardiographic evaluation

All patients underwent a comprehensive 2-dimensional and Doppler transthoracic echocardiography using commercially available ultrasound machines. The left ventricular end-diastolic and end-systolic volumes were determined from 2-dimensional images according to the contemporary international guidelines [Nag16], and the LV ejection fraction was calculated using the modified biplane method. The LV wall thickness was assessed in the parasternal views at or immediately below the level of the mitral valve leaflet tips at end-diastole [Nag16]. Pulse-wave Doppler was used to measure early diastolic transmitral inflow velocity. Pulse-wave tissue Doppler was applied to measure early diastolic mitral annular velocity at the septal mitral annulus [Rud10]. Continuous-wave Doppler was applied to obtain the maximal tricuspid regurgitation velocity [Zog17].

6.5.2 Mapper

The Mapper [SMC07, Car09], which is an efficient visualization and dimensionality reduction method that preserves the topological properties of the data point cloud, is an application of the Reeb graph to data analysis. The Mapper is based on the clustering and lens function.

For a topological space X and a real-valued continuous map f defined on X, the Reeb graph is obtained by identifying the poinmts which are in the same connected component of the level set $f^{-1}(a) = \{x \in X : f(x) = a\}$ for $a \in \mathbb{R}$ (Figure 6.12). Note that, however, the Reeb graph of a discrete space is itself. Thus, to apply the concept of the Reeb graph to data analysis, we adjust the concept of the Reeb graph to the data point cloud. We use an interval instead of a value $f(a)$ of a function f, so level set $f^{-1}(a)$ are replaced by pullback covering. On each element of the pullback covering, an alternative concept of the connected component is identified with clustering. Moreover, in this study, we use an $\mathbb{R}^2$-valued function, which we call lens function, instead

of a real-valued function f in order to preserve more topological information. Details of the process and the setting in this paper for each step are described below.

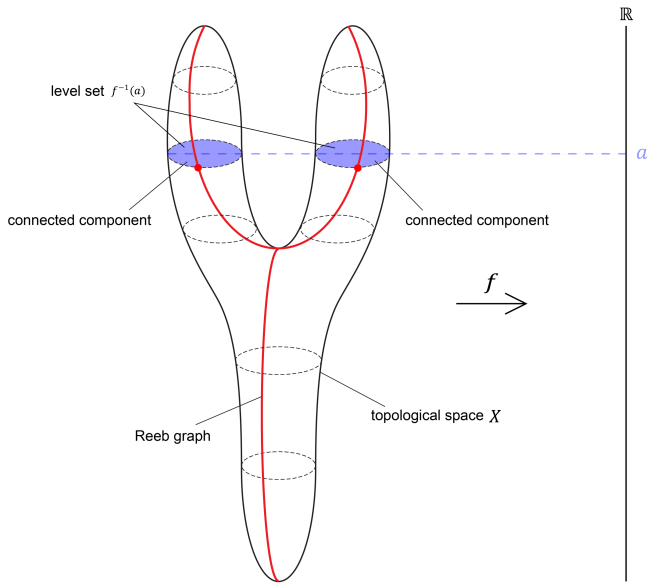

Figure 6.12: *Reeb graph of a topological space X with respect to a function f.* Two blue circles are level set $f^{-1}(a)$ of a real number a. Each circle is a connected component that is to be identified as a red point. The red line is the Reeb graph.

Distance

We choose a distance between the data points (or vector) as the *normalized correlation* (or the correlation distance), which is formulated as follows: For tow points x and y in $\mathbb{R}^M$,

$$d_{nc}(x, y) := 1 - \frac{(x - \bar{x}) \cdot (y - \bar{y})}{\|x - \bar{x}\| \|y - \bar{y}\|} = 1 - \text{corr}(x, y),$$

where $\bar{x}$ is the mean of elements of x, $\cdot$ is the dot product in $\mathbb{R}^M$, $\|\cdot\|$ is the Euclidean norm and $\text{corr}(\cdot, \cdot)$ is the degree of correlation. However, it should be noted that the normalized correlation is not a distance (not satisfying the triangular inequality), but the square root of the normalized correlation is a distance on the space of normalized vectors. More precisely, if we denote the

normalized vector by $\hat{x}$, i.e. $\hat{x} = (x - \bar{x})/\|x - \bar{x}\|$, then

$$\sqrt{d_{nc}(x,y)} = \sqrt{1 - \frac{(x-\bar{x})\cdot(y-\bar{y})}{\|x-\bar{x}\|\|y-\bar{y}\|}} = \frac{1}{\sqrt{2}}\sqrt{(\hat{x}-\hat{y})\cdot(\hat{x}-\hat{y})} = \frac{1}{\sqrt{2}}\|\hat{x}-\hat{y}\|.$$

The normalization amounts to x being projected to a point in the sphere $S^{M-2} = \{x \in H : \|x\| = 1\}$ of the hyperplane $H = \{x = (x_1, \ldots, x_M) : x_1 + \cdots + x_M = 0\}$. Thus the nomalized correlation is interpreted as a variant of Euclidean distance on S^{M-2}.

Lens function

The *lens functions*. corresponding to the continuous map f for the Reeb graph, are $\mathbb{R}^2$-valued function defined on data points. In this study, we use a function $\varphi : X \to \mathbb{R}^2$ which we call Isomap. Isomap is a nonlinear dimensionality reduction method that minimizes the difference between the geodesic distance in the k-nearest neighborhood metric graph ($k$nn graph) of the original space and the corresponding Euclidean distance in the latent space.

For the Isomap algorithm, we first need to construct the k-nearest neighborhood metric graph from the data. The nodes of the graph consist of the data points, and for each data point x_i, the k-nearest data points $x_{i_1}, \ldots, x_{i_k}$ and x_i are connected by edges of length $d_{nc}(x_i, x_{i_1}), \ldots, d_{nc}(x_i, x_{i_k})$, respectively. The geodesic distance between a pair of nodes (x_i, x_j), denoted by $d_g(x_i, x_j)$, is defined by the shortest path length between x_i and x_j.

The value of φ at N data points $x_1, \ldots, x_N$ are obtained by minimizing the stress function defiend as follows:

$$\text{stress}(x_1, \ldots, x_N) := \left(\sum_{i \neq j} [d_g(x_i, x_j) - \|\varphi(x_i) - \varphi(x_j)\|]^2 \right)^{\frac{1}{2}}.$$

We get a new 2-dimensional space $\varphi(X) \subset \mathbb{R}^2$, which we call the latent space of Isomap (Figure 6.13).

Covering

To handle and simplify the complex configuration of the data, the entire space should be adequately 'covered' over the entire dataset and then expressed in a simpler configuration, which is the basic idea of TDA. Covering is the process

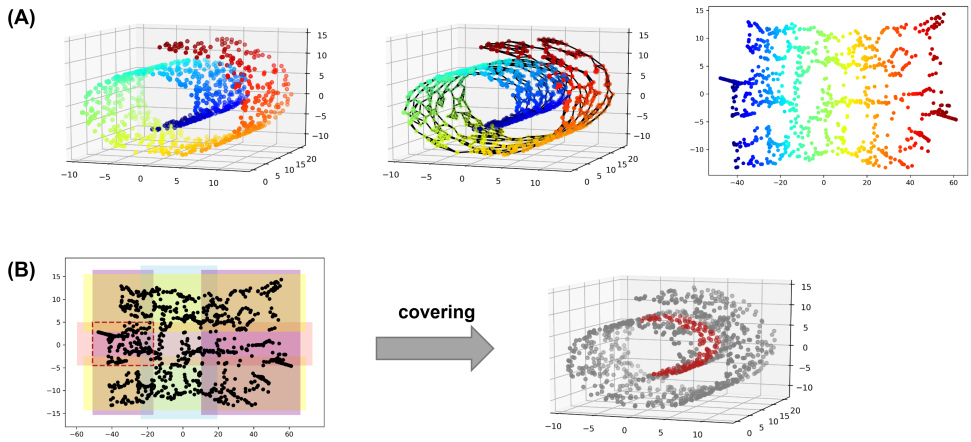

Figure 6.13: *Process of Isomap and covering.* **(A)** (*left*) Data point cloud in the original space; (*middle*) k-nearest neighborhood graph of data point cloud with $k = 5$; (*right*) Latent space obtained from the Isomap function φ. **(B)** (*left*) The coverings $\mathcal{C} = \{I_a : a \in A\}$ and $\mathcal{D} = \{J_b : b \in B\}$ of the axes corresponding to φ, gives the covering $\mathcal{C} \times \mathcal{D}$. For example, the purple rectangle in the middle is an element of $\mathcal{C} \times \mathcal{D}$. In this figure, the resolution is 3, and the gain is 1.2 for both axes of the range of φ. We set equalize option, i.e., each rectangle corresponding to $I_a \times J_b$ to contain the same number of data points; (*right*) red points correspond to the points in the red dotted rectangle in the laten space of the left-side figure.

of setting the function to 'cover' the entire space of the dataset. For the lens function, we make coverings $\mathcal{C} = \{I_a : a \in A\}$ and $\mathcal{D} = \{J_b : b \in B\}$, where A and B are finite sets, consisting of intervals I_a and J_b on the axis of the range of the lens function. The covering $\mathcal{C} \times \mathcal{D} = \{I_a \times J_b : a \in A, b \in B\}$ consists of rectangles $I_a \times J_b$ that cover the range of φ (Figure 6.13). There are two parameters when determining the covering. One is the *resolution*, which is the number of intervals, i.e. $|A|$ and $|B|$. The other is the *gain*, which is related to the overlapping ratio p between each interval by $p = 1 - 1/(\text{gain})$. In this article, the resolution is 30, and the gain is 3.0 for the two axes of the range of φ with *equalize* option in which the number of data points in each rectangle is constant. These resolution, gain, and option settings are also the default settings of the Ayasdi mapper.

Clustering

We will replace the connected components of the Reeb graph by clusters based on the assumption that the nearby points in the data point cloud belong to the same connected component. Clustering used in Mapper has two characteristics: 1. take input as a distance matrix; 2. do not predetermine the number of clusters. The *single linkage clustering*, which is based on the *single linkage distance* $D(A, B) = \min_{x \in A, y \in B} d_{nc}(x, y)$ between subset A and B of the dataset space, satisfies the two conditions above. With the initial state that each point is a cluster, the clusters are sequentially combined into larger clusters according to close single linkage distance $D(\cdot, \cdot)$. We stopped in the proper step and obtained the resulting clusters.

After clustering, we make each cluster a node and connect the nodes with edges if two clusters contain the same data point. To examine the distribution of variables on the Mapper network, we color the nodes according to the average value of the variable of the points in each node.

6.5.3 Grouping

In order to find groups in the resulting Mapper network, we use agglomerative hierarchical clustering and the Louvain (AHCL) algorithm. The AHCL algorithm consists of two-step of algorithms: 1. Agglomerative hierarchical clustering; 2. Louvain method (Figure 6.14). The result of the AHCL algorithm is a partition; that is, there are disjoint subsets of node-set, and each node is contained in some subset. However, if two nodes are connected by an edge and contained in different subsets, two nodes contain a patient in common. Then the patient is included in both subsets. In order to avoid statistical issues, we reduce each subset by taking the interior of the subset, that is, no two subsets share a node in common. More precise descriptions are given below.

Agglomerative hierarchical clustering

We first find an initial partition for Louvain method using agglomerative hierarchical clustering. In order to apply agglomerative hierarchical clustering to the network, the distance between any two nodes should be defined. As our aim of clustering is to group nodes with similar color values, we set an edge length as the difference between the color values of two nodes. In this article, 'Rows per Node' is used for color value as we want to group dense point sets.

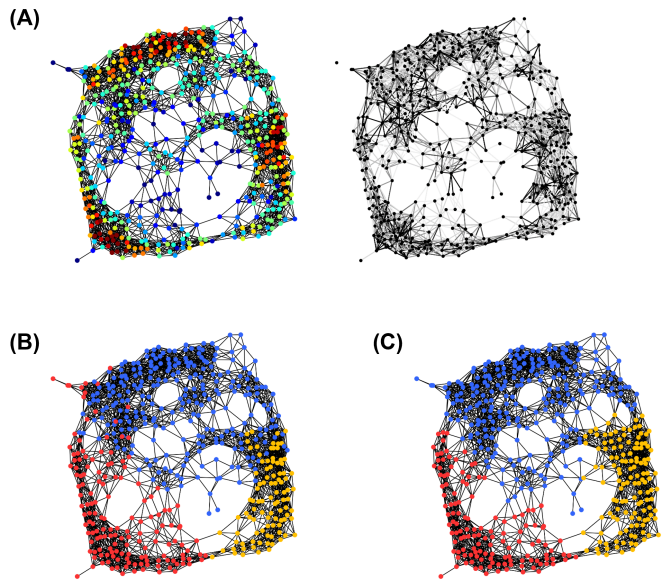

Figure 6.14: *Process of agglomerative hierarchical clustering and the Louvain method.* **(A)** (*left*) Mapper network colored by rows per node; (*right*) Edge lengths computed from rows per node. **(B)** Result of applying Ward linkage method for geodesic distance. **(C)** Result of applying Louvain method after (B).

The distance between non-adjacent nodes is given by the shortest length of the paths between them. In this distance setting, we use the Ward linkage method [War63] in order to obtain subsets of similar size, the desired property for statistical analysis.

Louvain method

The Louvain method is a method to extract groups from networks [BGLL08]. The method proceeds in the direction of maximizing modularity by slightly changing the given partition. The partition from agglomerative hierarchical clustering may not be well grouped. That is, the modularity is not maximized, but through the Louvain method, we obtain modularity maximized partition (Figure 6.14). The improvement of the Louvain method [LDB08] has one more parameter called resolution. Higher resolution tends to reduce the number of subsets of the partition. We applied the Louvain method for various resolutions, and we took the most stable result among the partitions divided into

three (Figure 6.15).

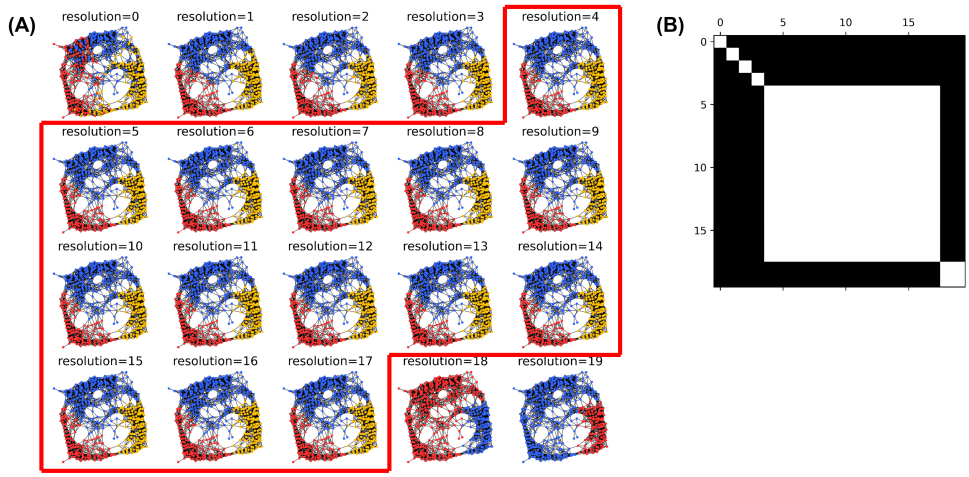

Figure 6.15: *Stable partition under varying resolution.* **(A)** Partition results by the Louvain method for resolution from 0 to 19. **(B)** Row and column indices are resolutions in (A). The color of the component is white if the corresponding partitions are exactly the same and black, if else. Resolutions 4 through 17 give the same partition with three subsets.

Chapter 7

Lower bound of Hausdorff dimension of weighted singular vectors

7.1 Fractal structure and Hausdorff dimension

7.1.1 Fractal structure

A *tree* $\mathcal{T}$ is a connected graph without cycles. If we take a vertex τ_0 and fix it (we call it a *root*), then $\mathcal{T}$ is a *rooted tree*. In this paper, we identify $\mathcal{T}$ with the set of vertices of $\mathcal{T}$. It can be checked directly from the definition of $\mathcal{T}$ that any $\tau \in \mathcal{T}$ can be joined to τ_0 by a unique geodesic edge path. We define the *height* of τ as the length of the geodesic edge path joining τ, τ_0 and denote the set of vertices of height n by $\mathcal{T}_n$. For any $\tau \in \mathcal{T}_n$, there exists a unique $\tau_{n-1} \in \mathcal{T}_{n-1}$ such that τ and τ_{n-1} are adjacent. Then we say τ is a *son* of τ_{n-1} and denote the set of all sons of τ_{n-1} by $\mathcal{T}(\tau_{n-1})$. The *boundary* of $\mathcal{T}$, denoted by $\partial\mathcal{T}$, is the set of all sequences $\{\tau_n\} = \{\tau_n\}_{n\in\mathbb{N}\cup\{0\}}$ where τ_n is a son of τ_{n-1} for all $n \in \mathbb{N}$.

A *fractal structure* on $\mathbb{R}^d$ is a pair $(\mathcal{T}, \beta)$ where $\mathcal{T}$ is a rooted tree and β is a map from $\mathcal{T}$ to the set of nonempty compact subsets of $\mathbb{R}^d$. A *fractal* associated to $(\mathcal{T}, \beta)$ is a set

$$\mathcal{F}(\mathcal{T}, \beta) = \bigcup_{\{\tau_n\}\in\partial\mathcal{T}} \bigcap_{n=0}^{\infty} \beta(\tau_n).$$

A fractal structure $(\mathcal{T}, \beta)$ is said to be *regular* if it satisfies the followings:

- each vertex of $\mathcal{T}$ has at least one son;
- if τ is a son of τ', then $\beta(\tau) \subset \beta(\tau')$;
- for any $\{\tau_n\} \in \partial\mathcal{T}$, $\mathrm{diam}\beta(\tau_n) \to 0$ as $n \to \infty$.

7.1.2 Self-affine structure and lower bound

A *self-affine structure* on $\mathbb{R}^d$ is a fractal structure $(\mathcal{T}, \beta)$ on $\mathbb{R}^d$ such that for $\tau \in \mathcal{T}$ the compact subset $\beta(\tau)$ of $\mathbb{R}^d$ is given by a d-dimensional rectangle with size $L^{(1)}(\tau) \times \cdots \times L^{(d)}(\tau)$. A self-affine structure is *regular* if it is a regular fractal structure.

The following theorem is a generalization of [LSST20, Theorem 2.1] for d-dimensional self-affine structures.

Theorem 7.1.1. *Let $(\mathcal{T}, \beta)$ be a regular self-affine structure on $\mathbb{R}^d$ that associates to sequences $\{\rho_n\}, \{C_n\}, \{L_n^{(j)}\}$ for $j = 1, \dots, d$ of positive real numbers indexed by $\mathbb{N} \cup \{0\}$ with the following properties:*

1. *The sequence $\{L_n^{(j)}\}$ is decreasing in $n \in \mathbb{N} \cup \{0\}$ for each $j = 1, \dots, d$.*
2. *There exists $1 \le \ell < d$ such that*

$$L_n^{(1)} = \cdots = L_n^{(\ell)} < L_n^{(\ell+1)} \le \cdots \le L_n^{(d)} \quad \text{and} \quad L^{(j)}(\tau) = L_n^{(j)}$$

   for all $n \in \mathbb{N} \cup \{0\}$, $j = 1, \dots, d$, and $\tau \in \mathcal{T}_n$;

3. *$C_0 = 1$ and $\#\mathcal{T}(\tau) \ge C_n$ for all $n \in \mathbb{N}$ and $\tau \in \mathcal{T}_{n-1}$;*
4. *$\rho_n \le 1$ for all $n \in \mathbb{N}$ and*

$$\mathrm{dist}(\beta(\tau), \beta(\kappa)) \ge \rho_{n+1} L_n^{(1)}$$

   for all $\tau_n \in \mathcal{T}_n$ and distinct $\tau, \kappa \in \mathcal{T}(\tau_n)$.

We denote by

$$\begin{aligned} P_n &= \prod_{i=0}^{n} C_i, \\ D_n &= \max\{i \geq n : L_i^{(d)} \geq L_n^{(1)}\}, \\ s &= \sup\left\{ t > 0 : \lim_{n\to\infty} \frac{\log(P_n (L_n^{(1)})^t \rho_{n+1}^t \cdot \prod_{i=n+1}^{D_n} \rho_i^{\ell} C_i)}{\max\{D_n - n, 1\}} = \infty \right\}. \end{aligned}$$

If $s > d - \ell$, then $\dim_H \mathcal{F}(\mathcal{T}, \beta) \geq s$.

Using Theorem 7.1.1, we obtain the following corollary which is a generalization of [LSST20, Corollary 2.3 and Corollary 2.4] for d-dimensional self-affine structures.

Corollary 7.1.2. *With the notations in Theorem 7.1.1, suppose that there exists $k, n_0 \in \mathbb{N}$ such that for all $n \geq n_0$ the followings hold:*

(i) $\frac{L_{kn}^{(d)}}{L_{kn-1}^{(d)}} \leq \frac{L_n^{(1)}}{L_{n-1}^{(1)}}$ *and* $L_{kn_0-1}^{(d)} < L_{n_0-1}^{(1)}$,

(ii) $e^{n/k} \leq C_n \leq e^{kn}$,

(iii) $e^{-kn} \leq \rho_n \leq e^{-n/k}$,

(iv) $\rho_n^{\ell} C_n \prod_{j=\ell+1}^{d} L_n^{(j)} / L_{n-1}^{(j)} \geq n^{-k}$.

If the limit

$$\lim_{n\to\infty} \frac{\log\left(C_n \prod_{j=\ell+1}^{d} L_n^{(j)} / L_{n-1}^{(j)}\right)}{-\log\left(L_n^{(1)} / L_{n-1}^{(1)}\right)}$$

exists and is equal to $r > 0$, then $\dim_H \mathcal{F}(\mathcal{T}, \beta) \geq d - \ell + r$.

Proof of Corollary 7.1.2. By the assumptions (iii) and (iv), since the sequence $\{L_n^{(j)}\}$ is decreasing in $n \in \mathbb{N} \cup \{0\}$ for each $j = 1, \ldots, d$, we have

$$\log\left(C_n \prod_{j=\ell+1}^{d} L_n^{(j)} / L_{n-1}^{(j)}\right) = O(n),$$

which implies that $-\log\left(L_n^{(1)}/L_{n-1}^{(1)}\right) \to \infty$ as $n \to \infty$. Hence, using

$$\frac{\log\left(P_n \prod_{j=\ell+1}^{d} L_n^{(j)}\right)}{-\log L_n^{(1)}} = \frac{\log\left(C_0 \prod_{j=\ell+1}^{d} L_0^{(j)}\right) + \sum_{i=1}^{n} \log\left(C_i \prod_{j=\ell+1}^{d} L_i^{(j)}/L_{i-1}^{(j)}\right)}{-\log L_0^{(1)} - \sum_{i=1}^{n} \log\left(L_i^{(1)}/L_{i-1}^{(1)}\right)},$$

it follows that

$$\lim_{n\to\infty} \frac{\log\left(C_n \prod_{j=\ell+1}^{d} L_n^{(j)}/L_{n-1}^{(j)}\right)}{-\log\left(L_n^{(1)}/L_{n-1}^{(1)}\right)} = \lim_{n\to\infty} \frac{\log\left(P_n \prod_{j=\ell+1}^{d} L_n^{(j)}\right)}{-\log L_n^{(1)}}.$$

Let us denote by

$$s = d - \ell + r = d - \ell + \lim_{n\to\infty} \frac{\log\left(P_n \prod_{j=\ell+1}^{d} L_n^{(j)}\right)}{-\log L_n^{(1)}}.$$

By the regularity of the given self-affine structure $(\mathcal{T}, \beta)$, we have that $L_n^{(1)} \to 0$ as $n \to \infty$, which implies

$$s = \sup\left\{ t > 0 : \lim_{n\to\infty} P_n (L_n^{(1)})^t \prod_{j=\ell+1}^{d} \frac{L_n^{(j)}}{L_n^{(1)}} = \infty \right\}. \tag{7.1}$$

We will show that $\dim_H \mathcal{F}(\mathcal{T}, \beta) \geq s$ using the equality (7.1).

Recall that $D_n = \max\left\{ i \geq n : L_i^{(d)} \geq L_n^{(1)} \right\}$. Since the sequence $\{L_n^{(j)}\}$ is decreasing in $n \in \mathbb{N} \cup \{0\}$ for each $j = 1, \ldots, d$, we have

$$\begin{aligned}
L_{kn}^{(d)} &= L_{kn_0-1}^{(d)} \prod_{i=kn_0}^{kn} \frac{L_i^{(d)}}{L_{i-1}^{(d)}} \leq L_{kn_0-1}^{(d)} \prod_{i=n_0}^{n} \frac{L_{ki}^{(d)}}{L_{ki-1}^{(d)}} \\
&\leq L_{kn_0-1}^{(d)} \prod_{i=n_0}^{n} \frac{L_i^{(1)}}{L_{i-1}^{(1)}} && \text{by assumption } (i) \\
&= L_{kn_0-1}^{(d)} \frac{L_n^{(1)}}{L_{n_0-1}^{(1)}} \\
&\leq L_n^{(1)} && \text{by assumption } (i).
\end{aligned}$$

Hence we have $D_n \leq kn$.

Given $t > 0$, $\epsilon > 0$, it follows from the assumptions (ii), (iii), and $D_n \le kn$ that $\rho_{D_n+1}^{\ell} C_{D_n+1} \le e^{k(D_n+1)} \le e^{k(kn+1)}$. Since $P_n^{\epsilon} = (\prod_{i=0}^{n} C_i)^{\epsilon} \ge e^{\frac{n(n+1)\epsilon}{2k}}$, we have

$$\rho_{D_n+1}^{\ell} C_{D_n+1} \le P_n^{\epsilon} \tag{7.2}$$

for all large enough $n \ge 1$. Similarly, it follows from the assumptions (iii), (iv), and $D_n \le kn$ that

$$\begin{aligned}\rho_{n+1}^{t} \prod_{i=n+1}^{D_n+1} \left(\rho_i^{\ell} C_i \prod_{j=\ell+1}^{d} \frac{L_i^{(j)}}{L_{i-1}^{(j)}} \right) &\ge e^{-tk(n+1)} \prod_{i=n+1}^{D_n+1} i^{-k} \ge e^{-tk(n+1)} (kn+1)^{-k(kn-n)} \\ &\ge e^{-tk(n+1)-k(kn-n)\log(kn+1)}.\end{aligned}$$

The inequality $P_n^{-\epsilon} \le e^{-\frac{n(n+1)\epsilon}{2k}}$ implies that

$$\rho_{n+1}^{t} \prod_{i=n+1}^{D_n+1} \left(\rho_i^{\ell} C_i \prod_{j=\ell+1}^{d} \frac{L_i^{(j)}}{L_{i-1}^{(j)}} \right) \ge P_n^{-\epsilon} \tag{7.3}$$

for all large enough $n \ge 1$.

Fix a real number t with $d - \ell < t < s$ and take sufficiently small ϵ such that $d - \ell < t/(1-3\epsilon) < s$. By the equality (7.1), we have

$$\lim_{n\to\infty} P_n (L_n^{(1)})^{t/(1-3\epsilon)} \prod_{j=\ell+1}^{d} \frac{L_n^{(j)}}{L_n^{(1)}} \ge 1 \tag{7.4}$$

for all large enough $n \ge 1$.

For all large enough $n \ge 1$ so that the above inequalities (7.2), (7.3), and

(7.4) hold, we have

$$\begin{aligned}
P_n(L_n^{(1)})^t\rho_{n+1}^t\prod_{i=n+1}^{D_n}\rho_i^\ell C_i &\geq P_n^{1-\epsilon}(L_n^{(1)})^t\rho_{n+1}^t\prod_{i=n+1}^{D_n+1}\rho_i^\ell C_i && \text{by (7.2)}\\
&= P_n^{1-\epsilon}(L_n^{(1)})^t\rho_{n+1}^t\left(\prod_{j=\ell+1}^{d}\frac{L_n^{(j)}}{L_{D_n+1}^{(j)}}\right)\cdot\prod_{i=n+1}^{D_n+1}\left(\rho_i^\ell C_i\prod_{j=\ell+1}^{d}\frac{L_i^{(j)}}{L_{i-1}^{(j)}}\right)\\
&\geq P_n^{1-\epsilon}(L_n^{(1)})^t\rho_{n+1}^t\left(\prod_{j=\ell+1}^{d}\frac{L_n^{(j)}}{L_n^{(1)}}\right)\cdot\prod_{i=n+1}^{D_n+1}\left(\rho_i^\ell C_i\prod_{j=\ell+1}^{d}\frac{L_i^{(j)}}{L_{i-1}^{(j)}}\right)\\
&\geq P_n^{1-\epsilon}(L_n^{(1)})^t\left(\prod_{j=\ell+1}^{d}\frac{L_n^{(j)}}{L_n^{(1)}}\right)P_n^{-\epsilon} && \text{by (7.3)}\\
&\geq P_n^{1-\epsilon}(L_n^{(1)})^t\left(\prod_{j=\ell+1}^{d}\frac{L_n^{(j)}}{L_n^{(1)}}\right)^{1-3\epsilon}P_n^{-2\epsilon}P_n^{\epsilon}\\
&= \left(P_n(L_n^{(1)})^{t/(1-3\epsilon)}\prod_{j=\ell+1}^{d}\frac{L_n^{(j)}}{L_n^{(1)}}\right)^{1-3\epsilon}P_n^{\epsilon}\\
&\geq P_n^{\epsilon} && \text{by (7.4).}
\end{aligned}$$

It follows that for all large enough $n \geq 1$,

$$\log\left(P_n(L_n^{(1)})^t\rho_{n+1}^t\prod_{i=n+1}^{D_n}\rho_i^\ell C_i\right) \geq \epsilon\log P_n \gg \epsilon n^2 \geq \epsilon\frac{n}{k-1}(D_n-n),$$

where the implied constant is independent of n. Hence $\dim_H \mathcal{F}(\mathcal{T},\beta) \geq t$ by Theorem 7.1.1. Since we choose arbitrary t with $d-\ell < t < s$, it concludes Corollary 7.1.2. □

By *elementary squares* of $\beta(\tau)$ for $\tau \in \mathcal{T}$, we mean closed squares contained in $\beta(\tau)$ whose side length is equal to $L^{(1)}(\tau)$.

Lemma 7.1.3. *For $n \in \mathbb{N}\cup\{0\}$ with $D_n > n$, let $\kappa \in \mathcal{T}_n$ and $\tau \in \mathcal{T}_{i-1}$ where $n+1 \leq i \leq D_n$. Then for any elementary square S of $\beta(\kappa)$,*

$$\#\{\tau' \in \mathcal{T}(\tau) : \beta(\tau')\cap S \neq \varnothing\} \leq (16d)^d\rho_i^{-\ell}.$$

Proof. Through this proof, we denote the size of a rectange R in $\mathbb{R}^d$ by $l_1(R)\times$

$\cdots \times l_d(R)$.

For a fixed elementary square S of $\beta(\kappa)$, let $R_0 = \beta(\tau) \cap S$ and

$$\mathcal{S} = \{\beta(\tau') \cap S : \tau' \in \mathcal{T}(\tau), \beta(\tau') \cap S \neq \varnothing\}.$$

If $R_0 = \varnothing$, then there is nothing to prove since $\#\{\tau' \in \mathcal{T}(\tau) : \beta(\tau') \cap S \neq \varnothing\} = 0$.

Let $j_i \in \{1, \ldots, d-1\}$ be an integer such that $L_i^{(d)} \geq \cdots \geq L_i^{(j_i+1)} \geq L_n^{(1)} > L_i^{(j_i)} \geq \cdots \geq L_i^{(1)}$. Note that $j_i \geq \ell$. Let R_0' be the rectangle with the same center as R_0 such that

$$l_j(R_0') = \begin{cases} 4L_{i-1}^{(j)} & \text{for } j = 1, \ldots, j_i \\ 4L_n^{(1)} & \text{for } j = j_i + 1, \ldots, d. \end{cases}$$

Similarly, for $R \in \mathcal{S}$ let R' be the rectange with the same center such that

$$l_j(R') = \begin{cases} L_i^{(j)} + \frac{\rho_i}{4\sqrt{d}} L_{i-1}^{(1)} & \text{for } j = 1, \ldots, j_i \\ L_n^{(1)} & \text{for } j = j_i + 1, \ldots, d. \end{cases}$$

We denote by r_0 (resp. r) the center of R_0' (resp. R'). Here, we note that r_0 and r are contained in both $\beta(\tau)$ and S. For $x \in R'$ and $j = 1, \ldots, d$,

$$|x_j - (r_0)_j| \leq |x_j - r_j| + |r_j - (r_0)_j| \leq \frac{1}{2} l_j(R') + \min(L_{i-1}^{(j)}, L_n^{(1)}) \leq \frac{1}{2} l_j(R_0').$$

Thus for all $R \in \mathcal{S}$, $R' \subset R_0'$.

For any distinct $R_1, R_2 \in \mathcal{S}$, let $\tau_1', \tau_2' \in \mathcal{T}(\tau)$ be such that $R_1 = \beta(\tau_1') \cap S$ and $R_2 = \beta(\tau_2') \cap S$, and let r_1, r_2 be the centers of R_1', R_2', respectively. Suppose $\|r_1 - r_2\|_\infty = |(r_1)_j - (r_2)_j| > 0$ for some $j = 1, \ldots, j_i$. Then for any $x \in R_1'$ and $y \in R_2'$, we have

$$\begin{aligned} |x_j - y_j| &\geq |(r_1)_j - (r_2)_j| - |x_j - (r_1)_j| - |y_j - (r_2)_j| \\ &\geq \frac{1}{\sqrt{d}} \operatorname{dist}(\beta(\tau_1'), \beta(\tau_2')) + L_i^{(j)} - \frac{1}{2} l_j(R_1') - \frac{1}{2} l_j(R_2') \\ &\geq \left(\frac{\rho_i}{\sqrt{d}} L_{i-1}^{(1)} + L_i^{(j)} \right) - \frac{1}{2} l_j(R_1') - \frac{1}{2} l_j(R_2') \\ &= \frac{3\rho_i}{4\sqrt{d}} L_{i-1}^{(1)} > 0. \end{aligned}$$

Thus $R_1' \cap R_2' = \varnothing$.

Now we suppose $\|r_1 - r_2\|_\infty = |(r_1)_j - (r_2)_j| > 0$ for some $j = j_i + 1, \dots, d$. Observe that

$$L_n^{(1)} \geq l_j(R_1) + l_j(R_2) + \frac{1}{\sqrt{d}}\mathrm{dist}(\beta(\tau_1'), \beta(\tau_2')) > l_j(R_1) + l_j(R_2),$$

which implies that

$$|(r_1)_j - (r_2)_j| = L_n^{(1)} - \frac{1}{2}l_j(R_1) - \frac{1}{2}l_j(R_2) > \frac{1}{2}L_n^{(1)}.$$

Thus, for any fixed $R_1 \in \mathcal{S}$ and $j = j_i + 1, \dots, d$,

$$\#\{R_2 \in \mathcal{S} \setminus \{R_1\} : \|r_1 - r_2\|_\infty = |(r_1)_j - (r_2)_j| \text{ and } R_1' \cap R_2' \neq \varnothing\} \leq 1.$$

Combining above two arguments, we conclude that every points of R_0' is covered by at most $d - j_i + 1$ rectangles of $\{R' : R \in \mathcal{S}\}$. It follows that

$$\begin{aligned}\left(\frac{\rho_i}{4\sqrt{d}}L_{i-1}^{(1)}\right)^{j_i}\left(L_n^{(1)}\right)^{d-j_i}\#\mathcal{S} &\leq \left(L_i^{(j)} + \frac{\rho_i}{4\sqrt{d}}L_{i-1}^{(1)}\right)^{j_i}\left(L_n^{(1)}\right)^{d-j_i}\#\mathcal{S} \\ &= \mathrm{vol}(R')\#\mathcal{S} \\ &\leq (d - j_i + 1)\mathrm{vol}(R_0') \\ &\leq d4^d\left(L_{i-1}^{(1)}\right)^{j_i}\left(L_n^{(1)}\right)^{d-j_i},\end{aligned}$$

hence, using $j_i \geq \ell$,

$$\#\mathcal{S} \leq d^{1+j_i/2}4^{d+j_i}\rho_i^{-j_i} \leq (16d)^d\rho_i^{-\ell}.$$

This inequality completes the proof. □

Let μ be the unique probability measure on $\mathcal{F}(\mathcal{T}, \beta)$ satisfying the following property: For all $y \in \mathcal{F}(\mathcal{T}, \beta)$ and $n \in \mathbb{N}$,

$$\frac{\mu(\{x \in \mathcal{F}(\mathcal{T}, \beta) : \tau_n(x) = \tau_n(y)\})}{\mu(\{x \in \mathcal{F}(\mathcal{T}, \beta) : \tau_{n-1}(x) = \tau_{n-1}(y)\})} = \frac{1}{\#\mathcal{T}(\tau_{n-1}(y))}, \tag{7.5}$$

where $x = \bigcap_{n\geq 0}\beta(\tau_n(x))$. We remark that for any $n \in \mathbb{N}$ and $\kappa \in \mathcal{T}_n$, it follows

from (7.5) that

$$\mu(\beta(\kappa)) \le \frac{\mu(\mathcal{F}(\mathcal{T},\beta))}{C_0 \dots C_n} = \frac{1}{P_n} \tag{7.6}$$

Lemma 7.1.4. *Let $n \in \mathbb{N}$ and $\kappa \in \mathcal{T}_n$. Then for any elementary square S of $\beta(\kappa)$, one has*

$$\mu(S) \le (16d)^{d(D_n-n)} P_n^{-1} \prod_{i=n+1}^{D_n} \rho_i^{-\ell} C_i^{-1}.$$

Proof. If $D_n = n$, then it follows from (7.6). Assume $D_n > n$. Applying Lemma 7.1.3 for $i = n+1, \dots, D_n$, we have

$$\#\{\tau \in \mathcal{T}_{D_n} : \beta(\tau) \cap S \neq \varnothing\} \le (16d)^{d(D_n-n)} \prod_{i=n+1}^{D_n} \rho_i^{-\ell}. \tag{7.7}$$

Since $S \cap \mathcal{F}(\mathcal{T},\beta)$ can be covered by rectangles $\{\beta(\tau) : \tau \in \mathcal{T}_{D_n}, \beta(\tau) \cap S \neq \varnothing\}$, we have

$$\begin{aligned}
\mu(S) &\le \sum_{\substack{\tau \in \mathcal{T}_{D_n} \\ \beta(\tau)\cap S \neq \varnothing}} \mu(\beta(\tau)) \\
&\le \mu(\beta(\kappa)) \prod_{i=n+1}^{D_n} C_i^{-1} \cdot \#\{\tau \in \mathcal{T}_{D_n} : \beta(\tau) \cap S \neq \varnothing\} \\
&\le (16d)^{d(D_n-n)} P_n^{-1} \prod_{i=n+1}^{D_n} \rho_i^{-\ell} C_i^{-1}.
\end{aligned}$$

In the last inequality, we use (7.6) and (7.7). □

Let U be an open subset of $\mathbb{R}^d$ with $U \cap \mathcal{F}(\mathcal{T},\beta) \neq \varnothing$. If $U \cap \mathcal{F}(\mathcal{T},\beta)$ is a single point set, then we denote by $n(U)$ the smallest $n \in \mathbb{N}$ such that $\operatorname{diam}(U) \ge \rho_{n+1} L_n^{(1)}$. In that case, there is a unique $\kappa = \kappa(U) \in \mathcal{T}_{n(U)}$ such that $U \cap \mathcal{F}(\mathcal{T},\beta) \subset \beta(\kappa)$. If $U \cap \mathcal{F}(\mathcal{T},\beta)$ contains more than two points, then we denote by $n(U)$ the largest $n \in \mathbb{N}$ such that $U \cap \mathcal{F}(\mathcal{T},\beta) \subset \beta(\kappa)$ for some $\kappa = \kappa(U) \in \mathcal{T}_n$. We note that $\operatorname{diam}(U) \ge \rho_{n(U)+1} L_{n(U)}^{(1)}$ by the assumption (4) of Theorem 7.1.1.

Lemma 7.1.5. *Let U be an open subset of $\mathbb{R}^d$ with $U \cap \mathcal{F}(\mathcal{T},\beta) \neq \varnothing$. Let $n = n(U)$ and $\kappa = \kappa(U)$. Then there is a family $\mathcal{S}$ of elementary squares of*

$\beta(\kappa)$ *such that*

1. $\bigcup_{S\in\mathcal{S}} S \supset U \cap \mathcal{F}(\mathcal{T},\beta)$;
2. $\left(L_n^{(1)}\right)^t \cdot \#\mathcal{S} \le 2^{d-\ell}\rho_{n+1}^{-t}\mathrm{diam}(U)^t$ *for all* $t \ge d-\ell$.

Proof. If $\mathrm{diam}(U) \le L_n^{(1)}$, then there exists an elementary square S of $\beta(\kappa)$ such that $S \supset U \cap \mathcal{F}(\mathcal{T},\beta)$. We set $\mathcal{S} = \{S\}$ so that $\mathcal{S}$ satisfies two conditions.

Now we assume $\mathrm{diam}(U) > L_n^{(1)}$. Then $U \cap \mathcal{F}(\mathcal{T},\beta)$ can be covered by $\left\lceil \frac{\mathrm{diam}(U)}{L_n^{(1)}} \right\rceil^{d-\ell}$ elementary sqaures. Let $\mathcal{S}$ be the family of these elementary squares. Then

$$\begin{aligned}\left(L_n^{(1)}\right)^t \cdot \#\mathcal{S} &= \left(L_n^{(1)}\right)^t \left\lceil \frac{\mathrm{diam}(U)}{L_n^{(1)}} \right\rceil^{d-\ell} \le 2^{d-\ell}\left(\frac{\mathrm{diam}(U)}{L_n^{(1)}}\right)^{d-\ell}\left(L_n^{(1)}\right)^t \\ &\le 2^{d-\ell}\left(\frac{\mathrm{diam}(U)}{L_n^{(1)}}\right)^{t}\left(L_n^{(1)}\right)^t \le 2^{d-\ell}\rho_{n+1}^{-t}\mathrm{diam}(U)^t.\end{aligned}$$

□

Proof of theorem 7.1.1. For a real number t such that $d-\ell \le t < s$, there exists $n_0 = n_0(t)$ such that for all $n \ge n_0$,

$$P_n\left(L_n^{(1)}\right)^t \rho_{n+1}^t \prod_{i=n+1}^{D_n} \rho_i^\ell C_i \ge (16d)^{d\max\{D_n-n,1\}} \ge (16d)^{d(D_n-n)}. \tag{7.8}$$

Let $\mathcal{U}$ be an open cover of $\mathcal{F}(\mathcal{T},\beta)$. Assume that for all $U \in \mathcal{U}$, $\mathrm{diam}(U)$ is small enough so that $n(U) \ge n_0$. Since $\mathcal{F}(\mathcal{T},\beta)$ is compact, there exists a finite subcover $\mathcal{U}_0$ such that for all $U \in \mathcal{U}_0$, $U \cap \mathcal{F}(\mathcal{T},\beta) \ne \varnothing$.

For $U \in \mathcal{U}_0$, let $\mathcal{S}_U$ be a family of elementary squares given by Lemma 7.1.5. Let $\mathcal{Q} = \bigcup_{U\in\mathcal{U}_0}\mathcal{S}_U$ and $n(S) = n(U)$ for $S \in \mathcal{S}_U$. We note that S may belong to different $\mathcal{S}_U$. However, $n(S)$ is well-difined since a side length of S

is $L^{(1)}_{n(U)}$. Then $\mathcal{Q}$ covers $\mathcal{F}(\mathcal{T},\beta)$ and hence

$$\begin{aligned}
\sum_{U\in\mathcal{U}_0}\operatorname{diam}(U)^t &\geq \frac{1}{2^{d-\ell}}\sum_{S\in\mathcal{Q}}\rho_{n(S)+1}^t\left(L^{(1)}_{n(S)}\right)^t && \text{by Lemma 7.1.5}\\
&\geq \frac{1}{2^{d-\ell}}\sum_{S\in\mathcal{Q}}(16d)^{d(D_n-n)}P_{n(S)}^{-1}\prod_{i=n+1}^{D_n}\rho_i^{-\ell}C_i^{-1} && \text{by (7.8)}\\
&\geq \frac{1}{2^{d-\ell}}\sum_{S\in\mathcal{Q}}\mu(S) && \text{by Lemma 7.1.4}\\
&\geq \frac{1}{2^{d-\ell}}.
\end{aligned}$$

Thus we have $\dim_H\mathcal{F}(\mathcal{T},\beta)\geq t$. Since we choose arbitrary t with $d-\ell\leq t<s$, the proof is completed. □

7.2 Counting lattice points in convex sets

In this section, we will generalize the results in [LSST20, §3.2] for $\mathbb{R}^3$ to the general $\mathbb{R}^{d+1}$. In §7.2.1, we first recall the notations and lemmas in [LSST20, §3.1].

7.2.1 Preliminaries for lattice point counting

For a positive integer $D\geq 1$, we write the D-dimensional Euclidean space by $\mathcal{E}_D=\mathbb{R}^D$. For a convex body $K\subset\mathbb{R}^D$ and a lattice $\Lambda\subset\mathbb{R}^D$, let $\lambda_i(K,\Lambda)$ $(i=1,\dots,D)$ be the i-th successive minimum of Λ with respect to K, that is, the infimum of those numbers λ such that $\lambda K\cap\Lambda$ contains i linearly independent vectors. Let $\operatorname{vol}(\cdot)$ be the Lebesgue measure on $\mathbb{R}^D$ and let $\operatorname{cov}(\Lambda)$ be the covolume of a lattice Λ, which is the Lebesgue measure of a fundamental domain of Λ. Denote by

$$\theta(K,\Lambda):=\frac{\operatorname{vol}(K)}{\operatorname{cov}(\Lambda)}.$$

For an affine subspace H of $\mathbb{R}^D$, let $\operatorname{vol}_H(\cdot)$ be the Lebesgue measure on H with respect to the subspace Riemannian structure. We write $\operatorname{vol}_H(S)=\operatorname{vol}_H(S\cap H)$ for a Borel measurable subset S of $\mathbb{R}^D$ by abuse of notation. We say that a subspace H of $\mathbb{R}^D$ is Λ-rational if $H\cap\Lambda$ is a lattice in H, and denote by $\operatorname{cov}_H(\Lambda)$ the covolume of the lattice $H\cap\Lambda$ in H. We also use the same notations for the dual vector space $\mathcal{E}_D^*$ with respect to the standard

Euclidean structure.

We use $\|\cdot\|$ for the Euclidean norms on $\mathbb{R}^D$ and $\mathcal{E}_D^*$. For a normed vector space V, denote by $B_r(V)$ (or B_r if $V=\mathbb{R}^D$) the ball of radius r centered at $0\in V$. We use K-norms on $\mathbb{R}^D$ and $\mathcal{E}_D^*$ defined by

$$\begin{cases}\|\mathbf{v}\|_K=\inf\{r>0:\mathbf{v}\in rK\}, & \mathbf{v}\in\mathbb{R}^D,\\ \|\varphi\|_K=\sup_{\mathbf{v}\in K}|\varphi(\mathbf{v})|, & \varphi\in\mathcal{E}_D^*.\end{cases}$$

Recall that $\mathcal{L}_D$ is the space of unimodular lattices in $\mathbb{R}^D$, which can be identified with the homogeneous space $\mathrm{SL}_D(\mathbb{R})/\mathrm{SL}_D(\mathbb{Z})$. For $g\in\mathrm{SL}_D(\mathbb{R})$ let g^* be the adjoint action on $\mathcal{E}_D^*$ defined by $\varphi\mapsto\varphi\circ g$. Then g^* can be represented by the transpose of g with respect to the standard basis $\mathbf{e}_1,\dots,\mathbf{e}_D$ of $\mathbb{R}^D$ and the dual basis $\mathbf{e}_1^*,\dots,\mathbf{e}_D^*$ of $\mathcal{E}_D^*$.

The *dual lattice* of Λ in $\mathbb{R}^D$ is the lattice in $\mathcal{E}_D^*$ defined by

$$\Lambda^*=\{\varphi\in\mathcal{E}_D^*:\varphi(\mathbf{v})\in\mathbb{Z},\ \forall\mathbf{v}\in\Lambda\}.$$

Let us define the following two sets:

$$\mathcal{K}_\epsilon=\mathcal{K}_\epsilon(D)=\{\Lambda\in\mathcal{L}_D:\|\mathbf{v}\|\geq\epsilon,\ \forall\mathbf{v}\in\Lambda\smallsetminus\{0\}\}=\{\Lambda\in\mathcal{L}_D:\lambda_1(B_1,\Lambda)\geq\epsilon\};$$
$$\mathcal{K}_\epsilon^*=\mathcal{K}_\epsilon^*(D)=\{\Lambda\in\mathcal{L}_D:\|\varphi\|\geq\epsilon,\ \forall\varphi\in\Lambda^*\smallsetminus\{0\}\}.$$

Since $\mathcal{E}_D^*$ can be naturally identified with $\bigwedge_{\mathbb{R}}^{D-1}\mathbb{R}^D$ with the standard Euclidean structure, we have $\Lambda^*=\bigwedge_{\mathbb{Z}}^{D-1}\Lambda$.

A nonzero vector $\mathbf{v}\in\Lambda$ is said to be *primitive* if $(1/n)\mathbf{v}\notin\Lambda$ for all $n\in\mathbb{N}$. The set of primitive vectors in Λ is denoted by $\widehat{\Lambda}$.

We summarize the lemmas in [LSST20, §3.1].

Lemma 7.2.1. *Let $D\geq 2$. For every lattice Λ in $\mathbb{R}^D$ and every bounded centrally symmetric convex subset K of $\mathbb{R}^D$ with $\lambda_d(K,\Lambda)\leq 1$ we have*

$$\#(K\cap\widehat{\Lambda})=\big(\zeta(D)^{-1}+\eta(K,\Lambda)\big)\cdot\theta(K,\Lambda)$$

where ζ is the Riemann ζ-function and

$$|\eta(K,\Lambda)|\ll_D\lambda_D(K,\Lambda)-\lambda_D(K,\Lambda)\log\lambda_1(K,\Lambda).$$

Lemma 7.2.2. *Let $D\geq 2$. For every lattice Λ in $\mathbb{R}^D$ and every bounded*

centrally symmetric convex subset K of $\mathbb{R}^D$ with $\lambda_D(K,\Lambda) \le 1$ we have

$$\#(K \cap (\Lambda \smallsetminus \{0\})) = (1 + \alpha(K,\Lambda)) \cdot \theta(K,\Lambda)$$

where $|\alpha(K,\Lambda)| \ll_D \lambda_D(K,\Lambda)$

Lemma 7.2.3. *Let K and Λ be as in Lemma 7.2.2. Then*

$$\#(K \cap \Lambda) \asymp_D \theta(K,\Lambda).$$

Lemma 7.2.4. *Let $D \ge 1$. Let Λ be a lattice in $\mathbb{R}^D$ and K be a bounded centrally symmetric convex subset of $\mathbb{R}^D$ with nonempty interior. Then*

$$\#(K^\circ \cap \Lambda) \asymp_D \#(K \cap \Lambda) \asymp_D \#(\overline{K} \cap \Lambda).$$

Lemma 7.2.5. *Let K and Λ be as in Lemma 7.2.2. If $\lambda_i(K,\Lambda) \le s \le s' \le \lambda_{j+1}(K,\Lambda)$ where $1 \le i \le j \le D$, then*

$$\left(\frac{s'}{s}\right)^i \ll_D \frac{\#(s'K \cap \Lambda)}{\#(sK \cap \Lambda)} \ll_D \left(\frac{s'}{s}\right)^j.$$

Lemma 7.2.6. *Let $D \ge 2$. Let K be a bounded centrally symmetric convex subset of $\mathbb{R}^D$ with nonempty interior and let $\varphi \in \mathcal{E}_D^* \smallsetminus \{0\}$. Then*

$$\mathrm{vol}_{H_\varphi}(K) \asymp_D \|\varphi\| \mathrm{vol}(K)/\|\varphi\|_K.$$

We need the following auxiliary lemma.

Lemma 7.2.7. *Given $D \ge 2$ and $r > 0$, let $\Lambda \in \mathcal{K}_r^*(D)$, and let $\mathbf{v}, \mathbf{w} \in \Lambda$ be any nonzero linearly independent vectors. Then there exists a positive constant $c' = c'(D) > 0$ such that $\|\mathbf{v} \wedge \mathbf{w}\| \ge c' r^{D-2}$.*

Proof. Let Λ' be the 2-dimensional sublattice of Λ generated by $\mathbf{v}, \mathbf{w}$. By Minkowski's second theorem, we have

$$\|\mathbf{v} \wedge \mathbf{w}\| \ge \mathrm{cov}(\Lambda') \gg_2 \lambda_1(B_1,\Lambda')\lambda_2(B_1,\Lambda') \ge \lambda_1(B_1,\Lambda)\lambda_2(B_1,\Lambda). \tag{7.9}$$

Agian by Minkowski's second theorem, we have

$$\begin{aligned} 1 \ll_D \lambda_1(B_1,\Lambda)\cdots\lambda_D(B_1,\Lambda) &\le \lambda_1(B_1,\Lambda)\lambda_2(B_1,\Lambda)\lambda_D(B_1,\Lambda)^{D-2} \\ &\le \lambda_1(B_1,\Lambda)\lambda_2(B_1,\Lambda)\frac{1}{r^{D-2}}. \end{aligned} \tag{7.10}$$

The last inequality comes from $\Lambda \in \mathcal{K}_r^*(D)$. The result is following by combining (7.9) and (7.10). □

7.2.2 Lattice point counting in $\mathbb{R}^{d+1}$

For $d \geq 2$ and a $(d+1)$-tuple $\mathbf{r} = (r_1, \ldots, r_{d+1})$ of positive real numbers, we estimate the number of lattice points in the set

$$M_{\mathbf{r}} = \{(x_1, \ldots, x_{d+1}) \in \mathbb{R}^{d+1} : |x_i| \leq r_i,\ \forall i = 1, \ldots, d+1\}.$$

Let

$$M_{\mathbf{r}}^* = \{\varphi \in \mathcal{E}_{d+1}^* : |x_i^\varphi| \leq r_i,\ \forall i = 1, \ldots, d+1\},$$

where the element $\varphi \in \mathcal{E}_{d+1}^*$ is represented by $\varphi = \sum_{i=1}^{d+1} x_i^\varphi \mathbf{e}_i^*$.

Lemma 7.2.8. *Let $d \geq 2$. For any real number $c_0 > 1$, there exists positive real number $\tilde{c} < 1$ such that for every lattice Λ in $\mathbb{R}^{d+1}$ and every $(d+1)$-tuple $\mathbf{r}$ of positive real numbers with*

$$\lambda_{d+1}(M_{\mathbf{r}}, \Lambda) \leq \tilde{c} \quad \textit{and} \quad -\lambda_{d+1}(M_{\mathbf{r}}, \Lambda) \log \lambda_1(M_{\mathbf{r}}, \Lambda) \leq \tilde{c}$$

one has

$$\frac{1}{c_0 \zeta(d+1)} \theta(M_{\mathbf{r}}, \Lambda) \leq \#(M_{\mathbf{r}} \cap \widehat{\Lambda}) \leq \frac{c_0}{\zeta(d+1)} \theta(M_{\mathbf{r}}, \Lambda).$$

Proof. The proof follows directly from Lemma 7.2.1. □

Now we fix real numbers $s, r_1, \ldots, r_{d+1}$ such that $0 < s < 1/2$, $r_i \geq 1$ for each $i = 1, \ldots, d$, and $r_{d+1} = 1$. Denote by $\mathbf{r} = (r_1, \ldots, r_{d+1})$, $r_M = \max_{1 \leq i \leq d} r_i$, and $r_m = \min_{1 \leq i \leq d} r_i$. Define a norm

$$\|\varphi\|_{\mathbf{r}} = \max\{r_i |x_i^\varphi| : i = 1, \ldots, d+1\}.$$

It follows from the definition that

$$\|\varphi\|_{\mathbf{r}} \leq \|\varphi\|_{M_{\mathbf{r}}} \leq (d+1)\|\varphi\|_{\mathbf{r}}. \tag{7.11}$$

For $q > 0$ let

$$N_q(\mathbf{r}, s) = \left\{\varphi \in \mathcal{E}_{d+1}^* : |x_i^\varphi| \leq s,\ \forall i = 1, \ldots, d, \text{ and } \|\varphi\|_{\mathbf{r}} \leq q\right\}.$$

Note that $N_q(\mathbf{r}, s) = M^*_{\mathbf{r}'}$ where $\mathbf{r}' = (r'_1, \dots, r'_d, q)$ with $r'_i = \min\{q/r_i, s\}$. For a lattice Λ in $\mathbb{R}^{d+1}$ and $i = 1, \dots, d+1$, let $q_i(\Lambda, \mathbf{r}, s)$ be the infimum of those positive real number q such that $N_q(\mathbf{r}, s) \cap \Lambda$ contains i linearly independent vectors. We will give an upper bound of the number of

$$\mathcal{S}(\Lambda, \mathbf{r}, s) := \left\{ \mathbf{v} \in M_{\mathbf{r}} \cap \widehat{\Lambda} : \varphi(\mathbf{v}) = 0 \text{ for some } \varphi \in N_{(d+1)sr_M}(\mathbf{r}, s) \cap \widehat{\Lambda}^* \right\},$$

where $\widehat{\Lambda}^*$ is the set of primitive vectors in Λ^*.

Lemma 7.2.9. *For $d \geq 2$, let Λ be a unimodular lattice in $\mathbb{R}^{d+1}$ with $q_1(\Lambda, \mathbf{r}, s) \geq s^{-2}$. Then*

1. *if $r_m = r_M$ and $q_{d+1}(\Lambda, \mathbf{r}, s) \leq ds^{-1/2} r_M$, then*

$$\#\mathcal{S}(\Lambda, \mathbf{r}, s) \ll s^{1/2} \cdot \mathrm{vol}(M_{\mathbf{r}});$$

2. *if $r_m < r_M$ and $q_{d+1}(\Lambda, \mathbf{r}, s) \log q_{d+1}(\Lambda, \mathbf{r}, s) \leq sr_M$, then*

$$\#\mathcal{S}(\Lambda, \mathbf{r}, s) \ll s^2 \cdot \mathrm{vol}(M_{\mathbf{r}}).$$

Proof. For simplicity, we denote by $N_q = N_q(\mathbf{r}, s)$, $q_i = q_i(\Lambda, \mathbf{r}, s)$ and $\mathcal{S} = \mathcal{S}(\Lambda, \mathbf{r}, s)$. If $N_{(d+1)sr_M} \cap \widehat{\Lambda}^*$ is empty then there is nothing to prove. We assume that $N_{(d+1)sr_M} \cap \widehat{\Lambda}^*$ is nonempty. It follows from the definition that

$$\#\mathcal{S} \leq \sum_{\varphi \in N_{(d+1)sr_M} \cap \widehat{\Lambda}^*} \#(H_\varphi \cap M_{\mathbf{r}} \cap \widehat{\Lambda}) \tag{7.12}$$

with the notation $H_\varphi = \ker\varphi$.

We first claim that for every $\varphi \in N_{(d+1)sr_M} \cap \widehat{\Lambda}^*$,

$$\#(H_\varphi \cap M_{\mathbf{r}} \cap \widehat{\Lambda}) \ll \frac{\mathrm{vol}(M_{\mathbf{r}})}{\|\varphi\|_{M_{\mathbf{r}}}} \leq \frac{\mathrm{vol}(M_{\mathbf{r}})}{\|\varphi\|_{\mathbf{r}}}. \tag{7.13}$$

where the second inequality follows from (7.11). If $\#(H_\varphi \cap M_{\mathbf{r}} \cap \widehat{\Lambda}) < d+1$, then it follows from (7.11) that

$$\frac{\mathrm{vol}(M_{\mathbf{r}})}{\|\varphi\|_{M_{\mathbf{r}}}} \geq \frac{2^{(d+1)} r_1 \dots r_{d+1}}{(d+1)\|\varphi\|_{\mathbf{r}}} \geq \frac{2^{(d+1)} r_1 \dots r_{d+1}}{(d+1)^2 sr_M} \gg \#(H_\varphi \cap M_{\mathbf{r}} \cap \widehat{\Lambda}).$$

Otherwise, $H_\varphi \cap M_{\mathbf{r}} \cap \Lambda$ has d linearly independent vectors, hence it follows

from Lemma 7.2.3 and Lemma 7.2.6 that

$$\#(H_\varphi \cap M_{\mathbf{r}} \cap \widehat{\Lambda}) \ll \frac{\mathrm{vol}_{H_\varphi}(M_{\mathbf{r}})}{\mathrm{cov}_{H_\varphi}(\Lambda)} \ll \frac{\|\varphi\|\mathrm{vol}(M_{\mathbf{r}})}{\mathrm{cov}_{H_\varphi}(\Lambda)\|\varphi\|_{M_{\mathbf{r}}}} \ll \frac{\mathrm{vol}(M_{\mathbf{r}})}{\|\varphi\|_{M_{\mathbf{r}}}},$$

which concludes the claim.

By (7.12) and (7.13), it suffices to estimate

$$\begin{aligned}\eta :=& \sum_{\varphi \in N_{(d+1)sr_M} \cap \widehat{\Lambda}^*} \|\varphi\|_{\mathbf{r}}^{-1} \\ =& \frac{1}{(d+1)sr_M} \#(N_{(d+1)sr_M} \cap \widehat{\Lambda}^*) + \sum_{\varphi \in N_{(d+1)sr_M} \cap \widehat{\Lambda}^*} \int_{\|\varphi\|_{\mathbf{r}}}^{(d+1)sr_M} \frac{1}{q^2} \mathrm{d}q.\end{aligned} \tag{7.14}$$

We denote the first and second terms in the last line by η_1, η_2, respectively.

Observe that

$$\begin{aligned}\eta_2 =& \sum_{\varphi \in N_{(d+1)sr_M} \cap \widehat{\Lambda}^*} \int_{q_1}^{(d+1)sr_M} \frac{\mathbb{1}_q(\|\varphi\|_{\mathbf{r}})}{q^2} \mathrm{d}q \\ =& \int_{q_1}^{(d+1)sr_M} \sum_{\varphi \in N_{(d+1)sr_M} \cap \widehat{\Lambda}^*} \frac{\mathbb{1}_q(\|\varphi\|_{\mathbf{r}})}{q^2} \mathrm{d}q \\ \leq& \int_{q_1}^{(d+1)sr_M} \frac{\#(N_q \cap \widehat{\Lambda}^*)}{q^2} \mathrm{d}q.\end{aligned} \tag{7.15}$$

where $\mathbb{1}_q$ denotes the indicator function of the set $\{x \in \mathbb{R} : x \leq q\}$.

For $i = 2, \ldots, d$, if $q_{i-1} \leq q < q_i$ then $\#(N_q \cap \widehat{\Lambda}^*) = i \leq d$. Thus

$$\int_{q_1}^{q_d} \frac{\#(N_q \cap \widehat{\Lambda}^*)}{q^2} \mathrm{d}q \leq \int_{q_1}^{q_d} \frac{d}{q^2} \mathrm{d}q \leq \frac{d}{q_1} \ll s^2 \leq s^{1/2}, \tag{7.16}$$

where the third inequality follows from the assumption $q_1 \geq s^{-2}$.

Proof of the assertion (1). We claim that $\eta \ll s^{-1/2}$ under the assumption of (1), which concludes the assertion (1). Assume that $r_m = r_M$ and $q_{d+1} \leq ds^{-1/2} r_M$. Observe that by definition

$$N_{(d+1)s^{-1/2}r_M} = M^*_{(s,\ldots,s,(d+1)s^{-1/2}r_M)}. \tag{7.17}$$

We have an upper bound of η_1 as

$$\eta_1 \le \frac{\#(N_{(d+1)s^{-1/2}r_M} \cap \Lambda^*)}{(d+1)sr_M} \ll \frac{\mathrm{vol}(N_{(d+1)s^{-1/2}r_M})}{(d+1)sr_M} \ll s^{d-3/2} \le s^{1/2}. \tag{7.18}$$

The first inequality follows from $s < 1/2$, the second inequality follows from Lemma 7.2.3, and the third inequality follows from (7.17).

For an upper bound of η_2, we first compute

$$\begin{aligned} \int_{sr_M}^{(d+1)sr_M} \frac{\#(N_q \cap \widehat{\Lambda}^*)}{q^2}\mathrm{d}q &\le \int_{sr_M}^{(d+1)sr_M} \frac{\#(N_{(d+1)sr_M} \cap \Lambda^*)}{q^2}\mathrm{d}q \\ &\le \frac{\#(N_{(d+1)sr_M} \cap \Lambda^*)}{sr_M} \\ &\ll s^{1/2}, \end{aligned} \tag{7.19}$$

where the last inequality can be shown by the same as (7.18).

If $sr_M \le q_d$, then it follows from (7.16) and (7.19) that $\eta_2 \ll s^{1/2}$. Now we suppose that $sr_M > q_d$. For all $q_d < q \le sr_M = sr_m$, observe that

$$N_q = M^*_{(q/r_1,\dots,q/r_{d+1})} = \frac{q}{sr_M} N_{sr_M}.$$

Since $\lambda_d(N_q, \Lambda) = \lambda_d(\frac{q}{sr_M} N_{sr_M}, \Lambda) \le 1 \le sr_M/q$, it follows from Lemma 7.2.5 that

$$\#(N_q \cap \widehat{\Lambda}^*) \le \#\left(\frac{q}{sr_M} N_{sr_M} \cap \Lambda^*\right) \ll \left(\frac{q}{sr_M}\right)^d \#(N_{sr_M} \cap \Lambda^*).$$

By $sr_M \le ds^{-1/2}r_M$ and Lemma 7.2.3, we have

$$\begin{aligned} \#(N_q \cap \widehat{\Lambda}^*) &\ll \left(\frac{q}{sr_M}\right)^d \#(N_{ds^{-1/2}r_M} \cap \Lambda^*) \\ &\ll \left(\frac{q}{sr_M}\right)^d \mathrm{vol}(N_{ds^{-1/2}r_M}) \\ &\ll \left(\frac{q}{sr_M}\right)^2 s^{d-1/2} r_M \ll \frac{q^2 s^{-1/2}}{r_M}. \end{aligned}$$

The last line follows from $\frac{q}{sr_M} \leq 1$ and $s \leq 1$. Thus we have

$$\int_{q_d}^{sr_M} \frac{\#(N_q \cap \widehat{\Lambda}^*)}{q^2} \mathrm{d}q \ll \int_{q_d}^{sr_M} \frac{s^{-1/2}}{r_M} \mathrm{d}q \ll s^{1/2}.$$

It follows that $\eta_2 \ll s^{1/2}$ under the assumption of (1), which concludes the assertion (1). □

Proof of the assertion (2). We will prove that $\eta \ll s^2$ under the assumption of (2). By the assumption, we have $q_{d+1} \geq q_1 \geq s^{-2} \geq 4$ so that $q_{d+1} < sr_M < (d+1)sr_M$ since $q_{d+1} \log q_{d+1} \leq sr_M$. Thus $N_{(d+1)sr_M} \cap \Lambda^*$ contains $d+1$ linearly independent vectors. By Lemma 7.2.3, we have

$$\eta_1 \leq \frac{\#(N_{(d+1)sr_M} \cap \Lambda^*)}{(d+1)sr_M} \ll \frac{\mathrm{vol}(N_{(d+1)sr_M})}{(d+1)sr_M} \ll s^d \leq s^2. \tag{7.20}$$

By (7.15), it suffices to show that

$$\int_{q_1}^{(d+1)sr_M} \frac{\#(N_q \cap \widehat{\Lambda}^*)}{q^2} \mathrm{d}q \ll s^2.$$

We split the domain of integration as $(q_1, q_d) \cup (q_d, q_{d+1}) \cup (q_{d+1}, sr_M) \cup (sr_M, (d+1)sr_M)$ and estimate upper bounds of the integrals.

For each $q \in (sr_M, (d+1)sr_M)$, it follows from Lemma 7.2.3 that $\#(N_q \cap \widehat{\Lambda}^*) \ll \mathrm{vol}(N_q) \ll s^d q$. Thus we have

$$\int_{sr_M}^{(d+1)sr_M} \frac{\#(N_q \cap \widehat{\Lambda}^*)}{q^2} \mathrm{d}q \ll \int_{sr_M}^{(d+1)sr_M} \frac{s^d}{q} \mathrm{d}q = s^d \log(d+1) \ll s^2. \tag{7.21}$$

For each $q \in (q_{d+1}, sr_M)$, it follows from Lemma 7.2.3 that $\#(N_q \cap \widehat{\Lambda}^*) \ll \mathrm{vol}(N_q) \ll s^{d-1}q^2/r_M$. Thus we have

$$\int_{q_{d+1}}^{sr_M} \frac{\#(N_q \cap \widehat{\Lambda}^*)}{q^2} \mathrm{d}q \ll \int_{q_{d+1}}^{sr_M} \frac{s^{d-1}}{r_M} \mathrm{d}q \leq s^d \leq s^2. \tag{7.22}$$

By (7.16), the integral over (q_1, q_d) is bounded above by s^2.

Now it remains to show that the integral over (q_d, q_{d+1}) is bounded above

by s^2. Let $H = \mathrm{Span}_{\mathbb{R}}(N_{q_d} \cap \Lambda^*)$. We claim that for every $q \in (q_d, q_{d+1})$,

$$\mathrm{vol}_H(N_q) \le \frac{q}{q_{d+1}} \mathrm{vol}_H(N_{q_{d+1}}). \tag{7.23}$$

If H contains $\mathbf{e}^*_{d+1}$, then the claim is easily checked from the definition of N_q. Otherwise, we let $\mathbf{pr}^*$ be the orthogonal projection onto $\mathrm{Span}_{\mathbb{R}}\{\mathbf{e}^*_1, \dots, \mathbf{e}^*_d\}$. Then the volume of $\mathbf{pr}^*(N_q)$ is at most q/q_{d+1} times the volume of $\mathbf{pr}^*(N_{q_{d+1}})$ since $q/r_M < q_{d+1}/r_M < s$. Thus we prove the claim.

For each $q \in (q_d, q_{d+1})$, we have

$$\begin{aligned}
\#(N_q \cap \widehat{\Lambda}^*) &\ll \frac{\mathrm{vol}_H(N_q)}{\mathrm{cov}_H(\Lambda^*)} && \text{by Lemma 7.2.3} \\
&\le \frac{q}{q_{d+1}} \frac{\mathrm{vol}_H(N_{q_{d+1}})}{\mathrm{cov}_H(\Lambda^*)} && \text{by (7.23)} \\
&\ll \frac{q}{q_{d+1}} \#(N_{q_{d+1}} \cap H \cap \Lambda^*) && \text{by Lemma 7.2.3} \\
&\ll \frac{q}{q_{d+1}} \#(N^\circ_{q_{d+1}} \cap H \cap \Lambda^*) && \text{by Lemma 7.2.4} \\
&= \frac{q}{q_{d+1}} \#(N^\circ_{q_{d+1}} \cap \Lambda^*) \le \frac{q}{q_{d+1}} \#(N_{q_{d+1}} \cap \Lambda^*) \\
&\ll \frac{q}{q_{d+1}} \mathrm{vol}(N_{q_{d+1}}) && \text{by Lemma 7.2.3} \\
&\ll s^{d-1} \frac{q_{d+1} q}{r_M}.
\end{aligned}$$

Therefore, we have

$$\int_{q_d}^{q_{d+1}} \frac{\#(N_1 \cap \widehat{\Lambda}^*)}{q^2} \mathrm{d}q \ll \int_{q_d}^{q_{d+1}} s^2 \frac{q_{d+1}}{s r_M} \frac{1}{q} \mathrm{d}q \le s^2 \frac{q_{d+1} \log q_{d+1}}{s r_M} \le s^2. \tag{7.24}$$

By combining (7.16), (7.21), (7.22), and (7.24), the proof of (2) is completed. □

This proves Lemma 7.2.9. □

For a weight vector $w = (w_1, \dots, w_d)$ as in the introduction, let $1 \le \ell \le d-1$ be the unique integer such that $w_1 = \cdots = w_\ell > w_{\ell+1} \ge \cdots \ge w_d$, and denote by $\xi = \max(1, \frac{d-\ell}{\ell})$. For a fixed lattice $\Lambda \subset \mathbb{R}^{d+1}$ and fixed $\mathbf{r}, s$, we denote $q_i(\Lambda, \mathbf{r}, s)$ by $q_i(\Lambda)$ and $N_q(\mathbf{r}, s)$ by N_q for simplicity. Let us fix a constant $C \ge 1$ which is an implied constant for the conclusion of Lemma

7.2.9 (1) and (2).

Lemma 7.2.10. *Let $d \geq 2$, $s = \epsilon^2$, $\mathbf{r} = (r_1, \dots, r_{d+1}) = (\epsilon e^t, \dots, \epsilon e^t, 1)$, $\Lambda \in \mathcal{K}^*_{\epsilon^2} \cap \mathcal{L}'_{d+1}$, and $a_t = \mathrm{diag}(e^{w_1 t}, \dots, e^{w_d t}, e^{-t})$. Then there exists a positive real number $\tilde{\epsilon} \leq 1$ and $c = c(d) > (d+1)^{1/14}$ such that for all $\epsilon, t > 0$ with $ce^{-w_d t/(2d^3)} < \epsilon < \tilde{\epsilon}$, one has*

$$\#\mathcal{S}(a_t\Lambda, \mathbf{r}, s) \leq \epsilon^{1/2} \cdot \mathrm{vol}(M_{\mathbf{r}}).$$

Proof. We will prove the lemma for $\tilde{\epsilon} < 1/C^2$ and the constant c will be determined later. By Lemma 7.2.9 (1), it suffices to show that

$$q_1(a_t\Lambda) \geq s^{-2} \quad \text{and} \quad q_{d+1}(a_t\Lambda) \leq ds^{-1/2} r_d. \tag{7.25}$$

First, note that

$$N_q \cap (a_t\Lambda)^* = N_q \cap a^*_{-t}\Lambda^* = a^*_{-t}(a_t^* N_q \cap \Lambda^*),$$

where a_t^* denotes the transpose of a_t. Hence it is enough to show that $a_t^* N_{s^{-2}}$ has no nonzero lattice point of Λ^* for the first inequality of (7.25). Since $d \geq 2$ and $w_d \leq 1/d$, we have

$$e^{-\frac{t}{7}} < e^{-\frac{w_d t}{2d^3}} < ce^{-\frac{w_d t}{2d^3}} < \epsilon,$$

that is, $s^{-2} < r_1 s$. Thus we have

$$N_{s^{-2}} = M^*_{(s^{-2}/r_1, \dots, s^{-2}/r_1, s^{-2})} = M^*_{(\epsilon^{-5}e^{-t}, \dots, \epsilon^{-5}e^{-t}, \epsilon^{-4})},$$

which implies that

$$a_t^* N_{s^{-2}} = M^*_{(\epsilon^{-5}e^{(w_1-1)t}, \dots, \epsilon^{-5}e^{(w_d-1)t}, \epsilon^{-4}e^{-t})}.$$

Since for all $i = 1, \dots, d$

$$\frac{\epsilon}{(d+1)^{1/14}} > \frac{c}{(d+1)^{1/14}} e^{-\frac{w_d t}{2d^3}} > e^{-\frac{(d-1)w_d t}{7}} \geq e^{\frac{(w_i-1)t}{7}},$$

we have $\epsilon^{-5}e^{(w_i-1)t} < \frac{\epsilon^2}{\sqrt{d+1}}$ for all $i = 1, \dots, d$. It is clear that $\epsilon^{-4}e^{-t} < \epsilon^{-5}e^{(w_d-1)t} < \frac{\epsilon^2}{\sqrt{d+1}}$. Thus $a_t^* N_{s^{-2}}$ is contained in the interior of $B_{\epsilon^2}(\mathcal{E}^*_{d+1})$. Since $\Lambda \in \mathcal{K}^*_{\epsilon^2}$, there is no lattice point of Λ in $a_t^* N_{s^{-2}}$.

To show the second inequality of (7.25), we will construct a basis for Λ^* of which vectors are contained in $N_{ds^{-1/2}r_d} = N_{de^t}$. Since $de^t > r_d > r_d s$, we have

$$a_t^* N_{de^t} = a_t^* M^*_{(s,\dots,s,de^t)} = M^*_{(se^{w_1 t},\dots se^{w_d t},d)}.$$

Let $1/2 < r \leq 1$ be such that $r\mathbf{e}_{d+1} \in \widehat{\Lambda}$ from the assumption $\Lambda \in \mathcal{L}'_{d+1}$. Let $\mathbf{pr} : \mathbb{R}^{d+1} \to \mathbb{R}^d$ be the orthogonal projection onto $\mathrm{Span}(\mathbf{e}_1, \dots, \mathbf{e}_d)$. Note that $\mathbf{pr}(\Lambda)$ is a lattice with covolume $1/r$ in $\mathbb{R}^d$. If $\mathbf{v} \in \Lambda$ satisfies $\|\mathbf{pr}(\mathbf{v})\| = \lambda_1(B_1, \mathbf{pr}(\Lambda))$, then since $\Lambda \in \mathcal{K}^*_{\epsilon^2}$, it follows from Lemma 7.2.7 with $D = d+1$ that

$$\lambda_1(B_1, \mathbf{pr}(\Lambda)) \geq r\lambda_1(B_1, \mathbf{pr}(\Lambda)) = \|\mathbf{v} \wedge r\mathbf{e}_{d+1}\| \geq \bar{c}_1(\epsilon^2)^{d-1} \tag{7.26}$$

for some $\bar{c}_1 = \bar{c}_1(d) < 1$. Since $\mathrm{cov}(\mathbf{pr}(\Lambda)) = 1/r$, it follows from the Minkowski's second theorem and (7.26) that for any $0 < c_1 < \bar{c}_1$

$$c_1^{d-1}(\epsilon^2)^{(d-1)^2}\lambda_d(B_1, \mathbf{pr}(\Lambda)) \leq \lambda_1(B_1, \mathbf{pr}(\Lambda)) \cdots \lambda_d(B_1, \mathbf{pr}(\Lambda)) \ll 1,$$

hence there exists $c_2 = c_2(d) > 1$ such that

$$\lambda_d(B_1, \mathbf{pr}(\Lambda)) \leq c_2(\epsilon^{-2})^{(d-1)^2}. \tag{7.27}$$

Let $\{v^{(i)} : i = 1, \dots, d\}$ be a Minkowski reduced basis for $\mathbf{pr}(\Lambda)$ such that $\|v^{(i)}\| \leq 2^d \lambda_i(B_1, \mathbf{pr}(\Lambda))$. For each $i = 1, \dots, d$, let $\mathbf{v}_i \in \Lambda$ be such that $\mathbf{pr}(\mathbf{v}_i) = v^{(i)}$ and $|\mathbf{e}^*_{d+1}(\mathbf{v}_i)| < 1$. Then the vectors $\mathbf{v}_1, \dots, \mathbf{v}_d, \mathbf{v}_{d+1} = r\mathbf{e}_{d+1}$ form a basis for Λ. Recall that $\mathcal{E}^*_{d+1}$ can be naturally identified with $\bigwedge^d_{\mathbb{R}} \mathbb{R}^{d+1}$ with the standard Euclidean structure. Under this identification, we have $\Lambda^* = \bigwedge^d_{\mathbb{Z}} \Lambda$, hence the vectors $\bigwedge_{j \neq i} \mathbf{v}_j$ for $i = 1, \dots, d+1$ forms a basis for $\bigwedge^d_{\mathbb{Z}} \Lambda$. We now claim that the vectors $\bigwedge_{j \neq i} \mathbf{v}_j$ for $i = 1, \dots, d+1$ are contained in $a_t^* N_{de^t}$ via the above identification, which proves that $q_{d+1}(a_t\Lambda) \leq ds^{-1/2}r_d$.

For each $i = 1, \dots, d+1$, write

$$\bigwedge_{j \neq i} \mathbf{v}_j = \sum_{h=1}^{d+1} \left(x_h^{(i)} \bigwedge_{k \neq h} \mathbf{e}_k \right).$$

Note that $|x^{(d+1)}_{d+1}| = 1/r \leq 2 \leq d$ and $x^{(i)}_{d+1} = 0$ for each $i = 1, \dots, d$ since $\mathbf{v}_{d+1} = r\mathbf{e}_{d+1}$. By the definition of $\mathbf{v}_i$ and (7.27), since $\epsilon < 1$, we can choose

large enough $c_3 = c_3(d) > (d+1)^{d^2/7}$ for each $i = 1, \dots, d$,

$$\|\mathbf{v}_i\| \le \sqrt{1 + \|v^{(i)}\|^2} \le 2^d \sqrt{2} c_2 (\epsilon^{-2})^{(d-1)^2} \le c_3 (\epsilon^{-2})^{(d-1)^2}.$$

Thus for each $i = 1, \dots, d+1$ and $h = 1, \dots, d$,

$$|x_h^{(i)}| \le \left\| \bigwedge_{j \ne i} \mathbf{v}_j \right\| \le \prod_{j \ne i} \|\mathbf{v}_j\| \le c_3^d (\epsilon^{-2})^{d(d-1)^2}.$$

From the assumption $ce^{-w_d t/(2d^3)} < \epsilon$, it follows that

$$c^{2d^3} e^{-w_d t} < (\epsilon^2)^{d^3} < (\epsilon^2)^{d(d-1)^2+1}.$$

Choosing $c = c_3^{1/2d^2} > (d+1)^{1/14}$, we have

$$|x_h^{(i)}| \le c_3^d (\epsilon^{-2})^{d(d-1)^2} < \epsilon^2 e^{w_d t} = s e^{w_d t} \le s e^{w_i t},$$

which concludes the claim. □

Lemma 7.2.11. *Let $d \ge 2$, $\mathbf{r} = (r_1, \dots, r_{d+1})$, $\overline{b}_t = \operatorname{diag}\left(\overline{b}_{t,1}, \dots, \overline{b}_{t,d+1}\right)$, and $\Lambda \in \mathcal{K}^*_{\epsilon^2}$, where*

$$r_i = \begin{cases} \epsilon e^{\left(\xi - \frac{1}{\ell}(w_{\ell+1} + \cdots + w_d)\right)t} & \text{if} \quad 1 \le i \le \ell, \\ \epsilon e^{(\xi + w_i)t} & \text{if} \quad \ell + 1 \le i \le d, \\ 1 & \text{if} \quad i = d+1, \end{cases}$$

and

$$\overline{b}_{t,i} = \begin{cases} e^{\left(\xi w_i - \frac{1}{\ell}(w_{\ell+1} + \cdots + w_d)\right)t} & \text{if} \quad 1 \le i \le \ell, \\ e^{(1+\xi)w_i t} & \text{if} \quad \ell + 1 \le i \le d, \\ e^{-\xi t} & \text{if} \quad i = d+1. \end{cases}$$

Then there exists a positive real number $\tilde{s} \le 1$ such that for all $s, t > 0$ with $e^{-\delta t} < \epsilon < s < \tilde{s}$ where $\delta = \frac{1}{18d^2} \min\left(\xi w_d, \xi w_1 - \frac{1}{\ell}(w_{\ell+1} + \cdots + w_d)\right)$, one has

$$\#\mathcal{S}(\overline{b}_t \Lambda, \mathbf{r}, s) \le s \operatorname{vol}(M_{\mathbf{r}}). \tag{7.28}$$

Proof. Note that $r_m = r_1 < r_M = r_{\ell+1}$. Take $t_0 = t_0(w_1, \dots, w_d) > 0$ such

that for any $t > t_0$ we have

$$e^{\frac{w_d}{20}t} \geq (\xi + \frac{w_d}{2})t. \tag{7.29}$$

Denoting by $c_4 = e^{-\delta t_0}$, then $c_4 \in (0,1)$ depends only on the weights $w_1, \ldots, w_d$, and the inequality (7.29) holds whenever $e^{-\delta t} < c_4$. Let

$$\tilde{s} = \min\left(\frac{1}{C}, c_4, \frac{1}{\sqrt{d+1}}, \left(\frac{\mathrm{vol}(B_1)}{4^{d+1}}\right)^{1/d}\right) \leq 1.$$

By Lemma 7.2.9 (2), it suffices to show that for $e^{-\delta t} < \epsilon < s < \tilde{s}$,

$$q_1(\bar{b}_t\Lambda) \geq s^{-2} \quad \text{and} \quad q_{d+1}(\bar{b}_t\Lambda)\log q_{d+1}(\bar{b}_t\Lambda) \leq s\epsilon e^{(\xi+w_{\ell+1})t}.$$

Since $e^{-\delta t} < \epsilon < s$, it follows from $s^{-3}\epsilon^{-1} < \epsilon^{-4} < e^{4\delta t}$ that $s^{-2}/r_i < s$ for all $i = 1, \ldots, d$, hence

$$\begin{aligned}\bar{b}_t^* N_{s^{-2}} &= \bar{b}_t^* M^*_{(\frac{s^{-2}}{r_1},\ldots,\frac{s^{-2}}{r_d},s^{-2})} \\ &= M^*_{\left(e^{\xi(w_1-1)t}\epsilon^{-1}s^{-2},\ldots,e^{\xi(w_d-1)t}\epsilon^{-1}s^{-2},e^{-\xi t}s^{-2}\right)}.\end{aligned}$$

Since $\tilde{s} \leq \frac{1}{\sqrt{d+1}}$, we have for all $i = 1, \ldots, d$,

$$\frac{s^2\epsilon^3}{\sqrt{d+1}} > \epsilon^6 > e^{-6\delta t} > e^{-(\xi w_1 - \frac{1}{\ell}(w_{\ell+1}+\cdots+w_d))t} \geq e^{\xi(w_i-1)t},$$

and

$$\frac{s^2\epsilon^2}{\sqrt{d+1}} > \epsilon^5 > e^{-5\delta t} > e^{-\xi w_d t} > e^{-\xi t},$$

hence it follows that $\bar{b}_t^* N_{s^{-2}}$ is contained in the interior of $B_{\epsilon^2}(\mathcal{E}^*_{d+1})$. Since $\Lambda \in \mathcal{K}^*_{\epsilon^2}$, there is no lattice point of Λ in $\bar{b}_t^* N_{s^{-2}}$, which concludes $q_1(\bar{b}_t\Lambda) \geq s^{-2}$ as in the proof of the first inequality of (7.25).

Since $\xi = \max(1, \frac{d-\ell}{\ell}) < d$, we have

$$s\epsilon > \epsilon^2 > e^{-\frac{1}{9d^2}\xi w_d t} > e^{-\frac{1}{9d}w_d t}, \tag{7.30}$$

which implies that

$$e^{\frac{w_d}{2}t} = e^{-\frac{w_d}{2}t}e^{w_d t} < e^{-\frac{1}{9d}w_d t}e^{w_d t} < s\epsilon e^{w_d t},$$

hence $e^{(\xi+\frac{w_d}{2})t} < r_d s$. On the other hand, it is clear that $r_\ell s < e^{(\xi+\frac{w_d}{2})t}$, hence $\overline{b}_t^* N_{e^{(\xi+w_d/2)t}}$ is the set of $\varphi = x_1^\varphi \mathbf{e}_1^* + \cdots + x_{d+1}^\varphi \mathbf{e}_{d+1}^* \in \mathcal{E}_{d+1}^*$ such that

$$\begin{cases} |x_i^\varphi| \le s e^{\left(\xi w_i - \frac{1}{\ell}(w_{\ell+1}+\cdots+w_d)\right)t} & \text{for } 1 \le i \le \ell, \\ |x_i^\varphi| \le \epsilon^{-1} e^{(\xi w_i + \frac{w_d}{2})t} & \text{for } \ell+1 \le i \le d, \\ |x_i^\varphi| \le e^{\frac{1}{2}w_d t} & \text{for } i = d+1. \end{cases}$$

It follows from $\Lambda \in \mathcal{K}_{\epsilon^2}^*$ that $\lambda_1(B_1, \Lambda^*) \ge \epsilon^2$. By Minkowski's second theorem, we have

$$\epsilon^{2d} \lambda_{d+1}(B_1, \Lambda^*) \le \lambda_1(B_1, \Lambda^*) \cdots \lambda_{d+1}(B_1, \Lambda^*) \le \frac{2^{d+1}}{\mathrm{vol}(B_1)},$$

hence $\lambda_{d+1}(B_1, \Lambda^*) \le \frac{2^{d+1}}{\mathrm{vol}(B_1)} \epsilon^{-2d}$. Thus there exists a Minkowski reduced basis $\varphi_1, \ldots, \varphi_{d+1}$ of Λ^* such that $\|\varphi_i\| \le \frac{4^{d+1}}{\mathrm{vol}(B_1)} \epsilon^{-2d} \le \epsilon^{-3d}$ for all $i = 1, \ldots d+1$ since $\epsilon^d < \tilde{s}^d \le \frac{\mathrm{vol}(B_1)}{4^{d+1}}$. Recall that $w_1 = \cdots = w_\ell$, hence it can be easily checked that φ_i's are contained in $\overline{b}_t^* N_{e^{(\xi+w_d/2)t}}$. Thus $q_{d+1}(\overline{b}_t \Lambda) \le e^{(\xi+w_d/2)t}$ so that

$$\begin{aligned} q_{d+1}(\overline{b}_t\Lambda) \log q_{d+1}(\overline{b}_t\Lambda) &\le e^{(\xi+\frac{w_d}{2})t}(\xi + \frac{w_d}{2})t \\ &\le e^{(\xi+\frac{w_d}{2})t} e^{\frac{w_d t}{20}} && \text{by (7.29)} \\ &\le s\epsilon e^{(\xi+w_d)t} && \text{by (7.30)} \\ &\le s\epsilon e^{(\xi+w_{\ell+1})t}. \end{aligned}$$

□

7.3 Lower bound

7.3.1 Construction of the fractal set

For a given weight vector $w = (w_1, \ldots, w_d)$, recall that $1 \le \ell \le d-1$ is the unique integer such that $w_1 = \cdots = w_\ell > w_{\ell+1} \ge \cdots \ge w_d$, and $\xi = \max(1, \frac{d-\ell}{\ell})$ (see §7.2.2). We choose a real number $c_0 > 1$ such that

$$\frac{1}{10} < \left(\frac{2}{c_0} - c_0\right) \frac{1}{\zeta(d+1)} \quad \text{and} \quad \frac{c_0}{\zeta(d+1)} < 1, \tag{7.31}$$

using $1 < \zeta(d+1) < 2$. Let $\tilde{c} \le 1$ be a positive real number as in Lemma 7.2.8 with respect to the above c_0, and let $\tilde{\epsilon}, \tilde{s} \le 1$ be positive real numbers as in Lemmas 7.2.10 and 7.2.11, respectively. We fix the constants $\epsilon, t, r > 0$ with the following properties:

1. $0 < \epsilon < r < \frac{1}{10^4 4^d} \min\{\tilde{\epsilon}, \tilde{s}\}$;
2. $t \ge 1$ will be chosen large enough so that (7.34), (7.39), (7.41), (7.42), (7.44), (7.45), (7.46), (7.47) hold.

Let $\{\epsilon_n\}$ and $\{t_n\}$ be the sequence defined as follows: for $n \in \mathbb{N}$,

1. $\epsilon_n = \epsilon/n$;
2. $t_n - t_{n-1} = \xi n t$ and $t_0 = 1$.

We will construct the tree $\mathcal{T}$ whose vertices are in the set $\mathbb{Q}^d$ of rational vectors and the map β from $V\mathcal{T}$ to the set of compact subsets in $\mathbb{R}^{d+1}$, inductively. We first set the root of $\mathcal{T}$ to be zero, that is, $\tau_0 = \mathbf{0}$ and define

$$\beta(\tau_0) = \{x \in \mathbb{R}^d : |(\tau_0)_i - x_i| < e^{-w_i t_1}, \forall i = 1, \dots, d\}.$$

For each $\tau \in \mathcal{T}_n$ with $n \ge 1$, let

$$\tilde{\beta}(\tau) = \{x \in \mathbb{R}^d : |\tau_i - x_i| < \epsilon_{n+1} e^{-w_i t_{n+1} - t_n}, \forall i = 1, \dots, d\}.$$

Recall that $a_t = \operatorname{diag}\left(e^{w_1 t}, \dots, e^{w_d t}, e^{-t}\right)$ and $h(x) = \begin{pmatrix} I_d & x \\ 0 & 1 \end{pmatrix}$ for $x \in \mathbb{R}^d$. Denote by

$$b_n = \operatorname{diag}(e^{-\frac{1}{\ell}(w_{\ell+1}+\cdots+w_d)nt}, \dots, e^{-\frac{1}{\ell}(w_{\ell+1}+\cdots+w_d)nt}, e^{w_{\ell+1}nt}, \dots, e^{w_d nt}, 1).$$

Note that the first ℓ terms of b_n are the same.

For each $\kappa \in \mathcal{T}_{n-1}$, we define $\mathcal{T}(\kappa)$ as the set of all $\tau \in \tilde{\beta}(\kappa)$ with the following properties:

$$\begin{aligned} &a_{t_n} h(\tau)\mathbb{Z}^{d+1} \in \mathcal{L}'_{d+1}, \\ &a_{t_n} h(\tau)\mathbb{Z}^{d+1} \in \mathcal{K}^*_{\epsilon_n^2}, \\ &b_n a_{t_n} h(\tau)\mathbb{Z}^{d+1} \in \mathcal{K}^*_r. \end{aligned} \tag{7.32}$$

It follows from the definitions of $\mathcal{T}(\kappa)$ and $\mathcal{L}'_{d+1}$ that $\tau \in \mathbb{Q}^d$ and for any $\tau \in \mathcal{T}(\kappa)$ there exists the unique vector

$$\mathbf{v}(\tau) \in \{r\mathbf{e}_{d+1} : 1/2 < r \leq 1\} \cap a_{t_n} h(\tau)\mathbb{Z}^{d+1}. \tag{7.33}$$

Note that $(d+1)$-th coordinate of $\mathbf{v}(\tau)$ is qe^{-t_n} for some $q \in \mathbb{Z}$ such that $1/2 < qe^{-t_n} \leq 1$. Since $t_n \geq t_{n-1} + 1$, $\mathcal{T}_n$ has empty intersection with $\bigcup_{0\leq i\leq n-1} \mathcal{T}_i$, which implies that $\mathcal{T}$ is a rooted tree.

For each $\tau \in \mathcal{T}(\kappa)$ with $\kappa \in \mathcal{T}_{n-1}$, define

$$\beta(\tau) = \{x \in \mathbb{R}^d : |\tau_i - x_i| < \epsilon_n e^{-w_i t_{n+1} - t_n}, \forall i = 1, \ldots, d\}.$$

Note that for each $\tau \in \mathcal{T}(\kappa)$, it follows from the definitions of $\tilde{\beta}$ and β that $\beta(\tau) \subset \beta(\kappa)$. If follows from Lemma 7.3.1 below that each vertex of $\mathcal{T}$ has sons by choosing $t \geq 1$ large enough so that for any $n \in \mathbb{N}$

$$\frac{1}{100}\epsilon_n^d e^{\xi dnt} \geq 1. \tag{7.34}$$

Hence the pair $(\mathcal{T}, \beta)$ is a regular self-affine structure.

Lemma 7.3.1. *For every $n \in \mathbb{N}$ and $y \in \mathcal{T}_{n-1}$ one has*

$$\frac{1}{100}\epsilon_n^d e^{\xi dnt} \leq \#\mathcal{T}(y) \leq 2^{d+1}\epsilon_n^d e^{\xi dnt}.$$

For fixed $n \in \mathbb{N}$ and $y \in \mathcal{T}_{n-1}$, we let

$$\begin{aligned}
\Lambda &= a_{t_{n-1}} h(y)\mathbb{Z}^{d+1} \in \mathcal{L}'_{d+1} \cap \mathcal{K}^*_{\epsilon_{n-1}^2}, \\
\Lambda_1 &= a_{t_n} h(y)\mathbb{Z}^{d+1} = a_{\xi nt}\Lambda, \\
\Lambda_2 &= b_n a_{t_n} h(y)\mathbb{Z}^{d+1} = b_n a_{\xi nt}\Lambda,
\end{aligned}$$

and for $x \in \tilde{\beta}(y)$,

$$\begin{aligned}
\Lambda_1(x) &= a_{t_n} h(x)\mathbb{Z}^{d+1} = a_{t_n} h(x-y) a_{t_n}^{-1}\Lambda_1, \\
\Lambda_2(x) &= b_n a_{t_n} h(x)\mathbb{Z}^{d+1} = b_n a_{t_n} h(x-y) a_{t_n}^{-1} b_n^{-1}\Lambda_2.
\end{aligned}$$

The lattices $\Lambda_1(x)$ and $\Lambda_2(x)$ satisfy $\Lambda_1(x) \in \mathcal{L}'_{d+1} \cap \mathcal{K}^*_{\epsilon_n^2}$ and $\Lambda_2(x) \in \mathcal{K}^*_r$ if and only if $x \in \mathcal{T}(y)$. Hence Lemma 7.3.1 follows from the following lemma.

Lemma 7.3.2. *Let $n \in \mathbb{N}$ and $y \in \mathcal{T}_{n-1}$. Then*

$$\frac{1}{10}\epsilon_n^d e^{\xi dnt} \le \#\{x \in \tilde{\beta}(y) : \Lambda_1(x) \in \mathcal{L}'_{d+1}\} \le 2^{d+1}\epsilon_n^d e^{\xi dnt}, \tag{7.35}$$

$$\#\{x \in \tilde{\beta}(y) : \Lambda_1(x) \in \mathcal{L}'_{d+1} \smallsetminus \mathcal{K}^*_{\epsilon_n^2}\} \le \frac{8}{100}\epsilon_n^d e^{\xi dnt}, \tag{7.36}$$

$$\#\{x \in \tilde{\beta}(y) : \Lambda_2(x) \in \mathcal{L}'_{d+1} \smallsetminus \mathcal{K}^*_{r}\} \le \frac{1}{100}\epsilon_n^d e^{\xi dnt}. \tag{7.37}$$

Proof. Let $x \in \tilde{\beta}(y)$ with $\Lambda_1(x) \in \mathcal{L}'_{d+1}$. Then there exists s_x such that $1/2 < s_x \le 1$ and $\Lambda_1(x) \cap \mathbb{R}\mathbf{e}_{d+1} = \{s_x \mathbf{e}_{d+1}\}$. We denote $s_x \mathbf{e}_{d+1}$ by $\mathbf{v}(x)$.

First, we prove (7.35). It can be checked by a direct calculation that the map $x \mapsto a_{t_n} h(y-x) a_{t_n}^{-1}\mathbf{v}(x)$ is a bijection from $\{x \in \tilde{\beta}(y) : \Lambda_1(x) \in \mathcal{L}'_{d+1}\}$ to $M \cap \widehat{\Lambda}_1$ where

$$M = \{(z_1, \dots, z_{d+1}) : \max_{1\le i\le d} |z_i| \le \epsilon_n e^{\xi nt}|z_{d+1}|,\ 1/2 < |z_{d+1}| \le 1\}.$$

Thus it suffices to estimate $\#(M \cap \widehat{\Lambda}_1)$. Let

$$M^{(1)} = \{(z_1, \dots, z_{d+1}) : \max_{1\le i\le d} |z_i| \le \frac{1}{2}\epsilon_n e^{\xi nt},\ |z_{d+1}| \le 1\}$$
$$M^{(2)} = \{(z_1, \dots, z_{d+1}) : \max_{1\le i\le d} |z_i| \le \frac{1}{2}\epsilon_n e^{\xi nt},\ |z_{d+1}| \le \frac{1}{2}\}.$$

Since $M^{(1)} \smallsetminus M^{(2)} \subset M \subset 2M^{(2)}$, we have

$$\#(M^{(1)} \cap \widehat{\Lambda}_1) - \#(M^{(2)} \cap \widehat{\Lambda}_1) \le \#(M \cap \widehat{\Lambda}_1) \le \#(2M^{(2)} \cap \widehat{\Lambda}_1). \tag{7.38}$$

We will use Lemma 7.2.8 to estimate $\#(M^{(i)} \cap \widehat{\Lambda}_1)$ for $i = 1, 2$. Since $\Lambda \in \mathcal{K}^*_{\epsilon_{n-1}^2} \subset \mathcal{K}^*_{\epsilon_n^2}$, it follows from the natural identification $\mathcal{E}_d^{**} = \mathbb{R}^d$ and Minkowski second theorem that there exist contants $C_1, C_2 > 0$ depending only on d such that

$$\lambda_1(B_1, \Lambda) \ge C_1\epsilon_n^{2d} \text{ and } \lambda_{d+1}(B_1, \Lambda) \le C_2\epsilon_n^{-2}.$$

Since $\Lambda = a_{\xi nt}^{-1}\Lambda_1$, for $i = 1, 2$, we have

$$\begin{aligned}\lambda_1(M^{(i)}, \Lambda_1) &= \lambda_1(a_{\xi nt}^{-1}M^{(i)}, \Lambda) \ge \lambda_1(a_{\xi nt}^{-1}M^{(1)}, \Lambda) \\ &\ge \lambda_1(B_{(d+1)e^{\xi nt}}, \Lambda) \ge \frac{C_1}{d+1}e^{-\xi nt}\epsilon_n^{2d}\end{aligned}$$

and

$$\begin{aligned}\lambda_{d+1}(M^{(i)},\Lambda_1) &= \lambda_{d+1}(a_{\xi nt}^{-1}M^{(i)},\Lambda) \le \lambda_{d+1}(a_{\xi nt}^{-1}M^{(2)},\Lambda)\\ &\le \lambda_{d+1}(B_{\frac{1}{2}\epsilon_n e^{(1-w_1)\xi nt}},\Lambda) \le 2C_2 e^{(w_1-1)\xi nt}\epsilon_n^{-3}.\end{aligned}$$

Thus we can choose $t \ge 1$ large enough so that for all $n \in \mathbb{N}$

$$\lambda_{d+1}(M^{(i)},\Lambda_1) < \widetilde{c} \quad \text{and} \quad -\lambda_{d+1}(M^{(i)},\Lambda_1)\log\lambda_1(M^{(i)},\Lambda_1) < \widetilde{c}. \tag{7.39}$$

Using Lemma 7.2.8 and (7.38), we have

$$\left(\frac{2}{c_0} - c_0\right)\frac{1}{\zeta(d+1)}\epsilon_n^d e^{\xi dnt} \le \#(M \cap \widehat{\Lambda}_1) \le \frac{c_0}{\zeta(d+1)}2^{d+1}\epsilon_n^d e^{\xi dnt}.$$

By (7.31), we complete the proof of (7.35).

Next, we prove (7.36) and (7.37). Let $s_1 = \epsilon_n^2$, $s_2 = r$, $a^{(1)} = a_{\xi nt}$, $a^{(2)} = b_n a_{\xi nt}$, and

$$\mathcal{S}_j = \{x \in \tilde{\beta}(y) : \Lambda_i(x) \in \mathcal{L}'_{d+1} \smallsetminus \mathcal{K}^*_{s_j}\} \text{ for } j = 1, 2.$$

Recall that

$$\mathcal{S}(\Lambda,\mathbf{r},s) = \left\{\mathbf{v} \in M_{\mathbf{r}} \cap \widehat{\Lambda} : \varphi(\mathbf{v}) = 0 \text{ for some } \varphi \in N_{(d+1)sr_M}(\mathbf{r},s) \cap \widehat{\Lambda}^*\right\}.$$

We will show that

$$\#\mathcal{S}_j \le \#\mathcal{S}(\Lambda_j,\mathbf{r}_j,s_j) \quad (j=1,2) \tag{7.40}$$

for some $\mathbf{r}_j$ and apply Lemma 7.2.10 and 7.2.11.

Let $z^{(1)}$ and $z^{(2)}$ be vectors in $\mathbb{R}^d$ such that

$$\begin{aligned} z_i^{(1)} &= (y_i - x_i)e^{(w_i+1)t_n} \quad \text{for } 1 \le i \le d;\\ z_i^{(2)} &= \begin{cases}(y_i - x_i)e^{-\frac{1}{\ell}(w_{\ell+1}+\cdots+w_d)nt+(w_i+1)t_n} & \text{if } 1 \le i \le \ell,\\ (y_i - x_i)e^{w_i nt+(w_i+1)t_n} & \text{if } \ell+1 \le i \le d.\end{cases}\end{aligned}$$

Then $h(z^{(j)}) = a^{(j)}a_{t_{n-1}}h(y-x)(a^{(j)}a_{t_{n-1}})^{-1}$ for $j = 1, 2$ and

$$|z_i^{(1)}| \le \epsilon_n e^{\xi nt} =: r_i^{(1)} \quad \text{for } 1 \le i \le d;$$
$$|z_i^{(2)}| \le \begin{cases} \epsilon_n e^{\left(\xi - \frac{1}{\ell}(w_{\ell+1}+\cdots+w_d)\right)nt} =: r_i^{(2)} & \text{if } 1 \le i \le \ell, \\ \epsilon_n e^{(\xi+w_i)nt} =: r_i^{(2)} & \text{if } \ell+1 \le i \le d. \end{cases}$$

Since $\mathbf{v}(x) \in \Lambda_1(x) \cap \Lambda_2(x)$, for $j = 1, 2$,

$$\mathbf{w}_j(x) := h(z^{(j)})\mathbf{v}(x) \in \Lambda_j.$$

For $\mathbf{r}_j = (r_1^{(j)}, \dots, r_d^{(j)}, 1)$, the map $\mathcal{S}_j \to M_{\mathbf{r}_j} \cap \widehat{\Lambda}_j$ given by $x \mapsto \mathbf{w}_j(x)$ is injective. Hence, in order to show (7.40), we should find $\varphi_j \in N_{(d+1)s_j r_M^{(j)}}(\mathbf{r}_j, s_j) \cap \widehat{\Lambda}_i^*$ such that $\varphi_j(\mathbf{w}_j(x)) = 0$. It follows from the definition of $\mathcal{S}_j$ that for $x \in \mathcal{S}_j$, $a^{(j)}a_{t_{n-1}}h(x)\mathbb{Z}^{d+1} \notin \mathcal{K}_{s_j}^*$. Then there exists $\varphi_j \in \widehat{\Lambda}_j^*$ such that $\|h(z^{(j)})^*\varphi_j\| < s_j$, where $h(z^{(j)})^*$ is the adjoint action defined by $g^*\varphi(\mathbf{v}) = \varphi(g\mathbf{v})$ for all $g \in \mathrm{SL}_{d+1}(\mathbb{R})$, $\varphi \in \mathcal{E}_{d+1}^*$, and $\mathbf{v} \in \mathbb{R}^{d+1}$. It follows from direct calculation that

$$h(z^{(j)})^*\varphi_j = \left(\varphi_j(\mathbf{e}_1), \dots, \varphi_j(\mathbf{e}_d), \sum_{i=1}^{d} z_i^{(j)}\varphi_j(\mathbf{e}_i) + \varphi_j(\mathbf{e}_{d+1})\right).$$

By choosing $t \ge 1$ large enough so that for all $n \in \mathbb{N}$

$$\epsilon e^{\xi nt} \ge 1, \tag{7.41}$$

it follows from $\|h(z^{(j)})^*\varphi_j\| < s_j$ that

$$|\varphi_j(\mathbf{e}_i)| < s_j \quad \text{for } 1 \le i \le d;$$
$$|\varphi_j(\mathbf{e}_{d+1})| < s_j + ds_j r_M^{(j)} < (d+1)s_j r_M^{(j)}.$$

Hence we have $\varphi_j \in N_{(d+1)s_j r_M^{(j)}}$. It follows that

$$\begin{aligned} |\varphi_j(\mathbf{w}_j(x))| &= |h(z^{(j)})^*\varphi_j(h(-z^{(j)})\mathbf{w}_j(x))| = |h(z^{(j)})^*\varphi_j(\mathbf{v}(x))| \\ &\le |h(z^{(j)})^*\varphi_j(\mathbf{e}_{d+1})| \le \|h(z^{(j)})^*\varphi_j\| < s_j < 1. \end{aligned}$$

Since $\varphi_j(\mathbf{w}_j(x)) \in \mathbb{Z}$, it follows that $\varphi_j(\mathbf{w}_j(x)) = 0$. This proves (7.40).

We choose $t \geq 1$ large enough so that for all $n \in \mathbb{N}$

$$ce^{-w_d \xi nt/(2d^3)} < \epsilon_n \quad \text{and} \quad e^{-\delta nt} < \epsilon_n. \tag{7.42}$$

Since $\Lambda \in \mathcal{K}^*_{\epsilon^2_{n-1}} \subset \mathcal{K}^*_{\epsilon^2_n}$ and (7.42), it follows from Lemma 7.2.10 and 7.2.11 that

$$\begin{aligned}
\mathcal{S}_1 &\leq \#\mathcal{S}(\Lambda_1, \mathbf{r}_1, s_1) \leq \sqrt{\epsilon_n}\mathrm{vol}(M_{\mathbf{r}_1}) = 2^{d+1}\sqrt{\epsilon_n}\epsilon_n^d e^{\xi dnt}, \\
\mathcal{S}_2 &\leq \#\mathcal{S}(\Lambda_2, \mathbf{r}_2, s_2) \leq r\mathrm{vol}(M_{\mathbf{r}_2}) = 2^{d+1} r\epsilon_n^d e^{\xi dnt}.
\end{aligned}$$

By the assumption (1) for ϵ and r, this complete the proof. □

The following lemma is d-dimensional version of [LSST20, Lemma 4.1].

Lemma 7.3.3. $\mathcal{F}(\mathcal{T}, \beta) \subset \mathrm{Sing}(w)$.

Proof. This lemma directly follows from the same argument in the proof of [LSST20, Lemma 4.1]. □

7.3.2 The lower bound calculation

In this subsection we complete the proof of main results.

Proposition 7.3.4. *Let $w = (w_1, \dots, w_d) \in \mathbb{R}^d_{>0}$ where $w_1 = \cdots = w_\ell > w_{\ell+1} \geq \cdots \geq w_d > 0$ and $\sum_{i=1}^d w_i = 1$ and let $(\mathcal{T}, \beta)$ be the self-affine strunction on $\mathbb{R}^d$ in the previous section. Then*

$$\dim_H \mathcal{F}(\mathcal{T}, \beta) \geq d - \frac{1}{1 + w_1}.$$

We will prove Proposition 7.3.4 using Corollary 7.1.2. Let $C_n, L_n^{(1)}, \dots, L_n^{(d)}$ be the positive constants defined as follows:

$$C_n = \epsilon_n^d e^{\xi dnt}, \quad L_n^{(i)} = 2\epsilon_n e^{-w_i t_{n+1} - t_n}, \forall i = 1, \dots, d.$$

It can be easily checked that a regular self-affine structure $(\mathcal{T}, \beta)$ satisfies assumptions (1), (2), and (3) of Theorem 7.1.1. For the assumption (4) of Theorem 7.1.1, we need the following lemma.

Lemma 7.3.5. *Let $n \in \mathbb{N}$ be large and $\tau \in \mathcal{T}_{n-1}$. Then*

$$\mathrm{dist}(\beta(x), \beta(y)) \geq L_{n-1}^{(1)} \frac{c' r^{d-1}}{4\sqrt{d}\epsilon_{n-1}} e^{\frac{1}{\ell}(w_{\ell+1} + \cdots + w_d - \xi\ell)nt},$$

where $x, y \in \mathcal{T}(\tau)$ are distinct and c' is the positive constant in Lemma 7.2.7.

Proof. By the construction of $\mathcal{T}$ and the definition of b_n, there are $1/2 \le s_x, s_y \le 1$ such that

$$s_x \mathbf{e}_{d+1} \in b_n a_{t_n} h(x) \mathbb{Z}^{d+1}, \quad s_y \mathbf{e}_{d+1} \in b_n a_{t_n} h(y) \mathbb{Z}^{d+1}.$$

Let us denote by

$$\mathbf{v} = b_n a_{t_n} h(y-x)(b_n a_{t_n})^{-1} s_x \mathbf{e}_{d+1} \in b_n a_{t_n} h(y) \mathbb{Z}^{d+1},$$
$$\mathbf{v} \wedge s_y \mathbf{e}_{d+1} = s_x s_y \sum_{i=1}^{d} u_i \mathbf{e}_i \wedge \mathbf{e}_{d+1}.$$

Observe that

$$u_i = \begin{cases} (y_i - x_i) e^{(w_i+1)t_n - \frac{1}{\ell}(w_{\ell+1}+\cdots+w_d)nt} & \text{for } 1 \le i \le \ell, \\ (y_i - x_i) e^{(w_i+1)t_n + w_i nt} & \text{for } \ell+1 \le i \le d. \end{cases}$$

Since x and y are distinct, the vectors $\mathbf{v}$ and $e_y \mathbf{e}_{d+1}$ are linearly independent, hence it follows from Lemma 7.2.7 that

$$\sqrt{d}\|\mathbf{u}\|_\infty \ge s_x s_y \|\mathbf{u}\| = \|\mathbf{v} \wedge s_y \mathbf{e}_{d+1}\| \ge c' r^{d-1}, \tag{7.43}$$

where $\mathbf{u} = (u_1, \dots, u_d) \in \mathbb{R}^d$ and $\|\cdot\|_\infty$ denotes the max norm.

Let $x' \in \beta(x)$ and $y' \in \beta(y)$. Suppose that $\|\mathbf{u}\|_\infty = |u_i|$ for some $1 \le i \le \ell$. Then it follows from (7.43) that

$$\begin{aligned} \|y' - x'\| &\ge |y'_i - x'_i| \ge |y_i - x_i| - |x_i - x'_i| - |y_i - y'_i| \\ &\ge e^{-(w_i+1)t_n + \frac{1}{\ell}(w_{\ell+1}+\cdots+w_d)nt} \left(\frac{c' r^{d-1}}{\sqrt{d}} - 2\epsilon_n e^{-\xi w_i (n+1)t - \frac{1}{\ell}(w_{\ell+1}+\cdots+w_d)nt} \right) \\ &\ge e^{-(w_i+1)t_n + \frac{1}{\ell}(w_{\ell+1}+\cdots+w_d)nt} \frac{c' r^{d-1}}{2\sqrt{d}} \\ &\ge L^{(i)}_{n-1} \frac{c' r^{d-1}}{4\sqrt{d}\epsilon_{n-1}} e^{\frac{1}{\ell}(w_{\ell+1}+\cdots+w_d - \xi\ell)nt} \\ &\ge L^{(1)}_{n-1} \frac{c' r^{d-1}}{4\sqrt{d}\epsilon_{n-1}} e^{\frac{1}{\ell}(w_{\ell+1}+\cdots+w_d - \xi\ell)nt}. \end{aligned} \tag{7.44}$$

We choose $t \ge 1$ large enough so that the third line (7.44) holds for all $n \in \mathbb{N}$.

On the other hand, if $\|\mathbf{u}\|_\infty = |u_i|$ for some $\ell+1 \le i \le d$, then we have

$$\begin{aligned}
\|y'-x'\| &\ge |y_i'-x_i'| \ge |y_i-x_i| - |x_i-x_i'| - |y_i-y_i'| \\
&\ge e^{-(w_i+1)t_n - w_i nt}\left(\frac{c' r^{d-1}}{\sqrt{d}} - 2\epsilon_n e^{w_i nt - \xi w_i(n+1)t}\right) \\
&\ge e^{-(w_i+1)t_n - w_i nt}\frac{c' r^{d-1}}{2\sqrt{d}} \qquad (7.45) \\
&\ge L_{n-1}^{(1)}\frac{c' r^{d-1}}{4\sqrt{d}\epsilon_{n-1}} e^{(w_1-w_i)t_n - (\xi+w_i)nt} \\
&\ge L_{n-1}^{(1)}\frac{c' r^{d-1}}{4\sqrt{d}\epsilon_{n-1}} e^{(w_1-w_{\ell+1})t_n - (\xi+w_i)nt} \\
&\ge L_{n-1}^{(1)}\frac{c' r^{d-1}}{4\sqrt{d}\epsilon_{n-1}} e^{\frac{1}{\ell}(w_{\ell+1}+\cdots+w_d-\xi\ell)nt}. \qquad (7.46)
\end{aligned}$$

We choose $t \ge 1$ large enough so that the third line (7.45) and last line (7.46) hold for all $n \in \mathbb{N}$.

This concludes the proof of the lemma. □

We choose $t \ge 1$ large enough so that for all $n \in \mathbb{N}$

$$\rho_n := \frac{c' r^{d-1}}{4\sqrt{d}\epsilon_{n-1}} e^{\frac{1}{\ell}(w_{\ell+1}+\cdots+w_d-\xi\ell)nt} \le 1 \qquad (7.47)$$

since $w_{\ell+1}+\cdots+w_d < \xi\ell$. The assumption (4) of Theorem 7.1.1 follows from Lemma 7.3.5.

Proof of Proposition 7.3.4. We prove the proposition applying Corollary 7.1.2. It can be easily checked that for $k > 4\xi dt$, the assumptions of Corollary 7.1.2 hold. Then we have

$$\begin{aligned}
&\frac{\log(C_n L_n^{(\ell+1)}\cdots L_n^{(d)}/L_{n-1}^{(\ell+1)}\cdots L_{n-1}^{(d)})}{-\log(L_n^{(1)}/L_{n-1}^{(1)})} \\
&= \frac{\xi dnt - \xi(w_{\ell+1}+\cdots+w_d)(n+1)t - \xi(d-\ell)nt + o(n)}{\xi w_1(n+1)t + \xi nt + o(n)} \\
&\to \frac{\ell - (w_{\ell+1}+\cdots+w_d)}{1+w_1} = \ell - \frac{1}{1+w_1} \quad \text{as } n \to \infty
\end{aligned}$$

Hence Corollary 7.1.2 implies

$$\dim_H \mathcal{F}(\mathcal{T}, \beta) \geq (d - \ell) + \ell - \frac{1}{1 + w_1} = d - \frac{1}{1 + w_1}.$$

□

Proof of Theorem 1.5.1. If $w_1 = \cdots = w_d$, then the result follows from [CC16, Theorem 1.1]. If there exists $1 \leq \ell \leq d - 1$ such that $w_1 = \cdots = w_\ell > w_{\ell+1} \geq \cdots \geq w_d$, then the result follows from Lemma 7.3.3 and Proposition 7.3.4. □

Proof of Theorem 1.5.2. This theorem directly follows from the same argument in the proof of [LSST20, Theorem 1.5]. □

Bibliography

[Abr59] L. M. Abramov, *On the entropy of a flow*, Dokl. Akad. Nauk SSSR, **128** (1959), no. 5, 873-875.

[Bar17] M. T. Barlow, *Random walks and heat kernels on graphs*, Cambridge University Press, **438** (2017).

[BS00] L. Barreira and B, Saussol, *Multifractal analysis of hyperbolic flows*, Communications in Mathematical Physics, **214** (2000), no. 2, 339-371.

[Bou95] M. Bourdon, *Structure conforme au bord et flot geodesic d'un CAT (-1)-espace*, L'Enseignement Math, **41** (1995), 63-102.

[BM96] M. Burger and S. Mozes, *CAT (-1)-spaces, divergence groups and their commensurators*, Journal of the American Mathematical Society, **9** (1966), no. 1, 57-93.

[BPP16] A. Broise-Alamichel, J. Parkkonen and F. Paulin, *Equidistribution and counting under equilibrium states in negatively curved spaces and graphs of groups. Applications to non-Archimedean Diophantine approximation* (2016).

[BW72] R. Bowen and P. Walters, *Expansive one-parameter flows*, Journal of differential Equations, **12** (1972), no. 1, 180-193.

[Coo93] M. Coornaert, *Mesures de Patterson-Sullivan sur le bord d'un espace hyperbolique au sens de Gromov*, Pacific Journal of Mathematics, **159** (1993), no. 2, 241-270,

[CP97] M. Coornaert and A. Papadopoulos, *Upper and lower bounds for the mass of the geodesic flow on graphs*, Mathematical Proceedings of the Cambridge Philosophical Society, **121** (1997), no. 3, 479-493.

[CP99] M. Coornaert and A. Papadopooulos, *Spherical functions and conformal densities on spherically symmetric CAT (-1)-spaces*, Transactions of the American Mathematical Society, **351** (1999), no. 7, 2745-2762.

[Fur02] A. Furman, *Coarse-geometric perspective on negatively curved manifolds and groups*, Rigidity in dynamics and geometry (2002), 149-166.

[Gui94] L. Guillopé, *Entropies et spectres*, Osaka Journal of Mathematics, **31** (1994), no. 2, 247-289.

[Ham] U. Hamenstadt, *Harmonic measure and Bowen-Margulis measure are almost always singular*, preprint.

[HP97] S. Hersonsky and F. Paulin, *On the rigidity of discrete isometry groups of negatively curved spaces*, Commentarii Mathematici Helvetici, **72** (1997), no. 3, 349-388.

[HL19] S. Hong and S. Lim, *Martin boundary of Brownian motion on Gromov hyperbolic metric graphs*, arXiv preprint arXiv:1905.09504 (2019).

[Kai90] V. A. Kaimanovich, *Invariant measures of the geodesic flow and measures at infinity on negatively curved manifolds*, Annales de l'IHP Physique théorique, **53** (1990), no. 4, 361-393.

[KN07] I. Kapovich and T. Nagnibeda, *The Patterson–Sullivan embedding and minimal volume entropy for outer space*, Geometric and Functional Analysis, **17** (2007), no. 4, 1201-1236.

[Kat82] A. Katok, *Entropy and closed geodesies*, Ergodic theory and dynamical Systems, **2** (1982), no. 3-4, 339-365.

[Kat88] A. Katok, *Four applications of conformal equivalence to geometry and dynamics*, Ergodic Theory Dynam. Systems, **8** (1988), Charles Conley Memorial Issue, 139-152.

[Led87] F. Ledrappier, *Propriété de Poisson et courbure négative*, CR Acad. Sci. Paris Sér. I Math, **305** (1987), no. 5, 191-194.

[Led88] F. Ledrappier, *Ergodic properties of Brownian motion on covers of compact negatively-curve manifolds*, Boletim da Sociedade Brasileira de Matemática-Bulletin/Brazilian Mathematical Society, **19** (1988), no.1, 115-140.

[Led90] F. Ledrappier, *Harmonic measures and Bowen-Margulis measures*, Israel Journal of Mathematics, **71** (1990), no. 3, 275-287.

[LL09] F. Ledrappier and S. Lim, *Volume entropy of hyperbolic buildings*, arXiv preprint arXiv:0902.1168 (2009).

[LS20] F. Ledrappier and L. Shu, *Entropies for negatively curved manifolds*, Frontiers in Analysis and Probability (2020), 243-274.

[Lim08] S. Lim, *Minimal volume entropy for graphs*, Transactions of the American Mathematical Society, **360** (2008), no. 10, 5089-5100.

[Lyo90] R. Lyons, *Random walks and percolation on trees*, The annals of Probability, **18** (1990), no. 3, 931-968.

[Lyo94] R. Lyons, *Equivalence of boundary measures on covering trees of finite graphs*, Ergodic Theory and Dynamical Systems, **14** (1994), no. 3, 575-597.

[LP17] R. Lyons and Y. Peres, *Probability on trees and networks*, Cambridge University Press, **42** (2017).

[Pat76] S. Patterson, *The limit set of a Fuchsian group*, Acta mathematica, **136** (1976), 241-273.

[Pat87] S. Patterson, *Lectures on measures on limit sets of Kleinian groups, in Analytical and geometric aspects of hyperbolic space*, LMS Lecture Note Series, **111** (1987), 281-323.

[Pau97] F. Paulin, *On the critical exponent of a discrete group of hyperbolic isometries*, Differential Geometry and its Applications, **7** (1997), no. 3, 231-236.

[PPS12] F. Paulin, M. Pollicott and B. Schapira, *Equilibrium states in negative curvature*, arXiv preprint arXiv:1211.6242 (2012).

[Rob03] T. Roblin, *Ergodicité et équidistribution en courbure négative*, Société mathématique de France (2003).

[Ser02] J-P. Serre, *Trees*, Springer Science & Business Media (2002).

[Sul76] D. Sullivan, *Cycles for the dynamical study of foliated manifolds and complex manifolds*, Inventiones mathematicae, **36**, no. 1, 225-255.

[Sul79] D. Sullivan, *The density at infinity of a discrete group of hyperbolic motions*, Publications Mathématiques de l'IHÉS, **50** (1979), 171-202.

[Lee22] S. J. Lee, et al., *Triple network activation causes tinnitus in patients with sudden sensorineural hearing loss: A model-based volume-entropy analysis*, Frontiers in Neuroscience, 2000 (2022).

[Cho22] Y-J. Choi, et al., *Network analysis of cardiac remodeling by primary mitral regurgitation emphasizes the role of diastolic function*, JACC: Cardiovascular Imaging (2022).

[AR89] A. Axelsson and A. Ringdahl, *Tinnitus—a study of its prevalence and characteristics*, British journal of audiology, **23** (1989), 53-62.

[BMH13] D. Baguley, D. Mcferran and D. Hall, *Tinnitus*, The Lancet, **382** (2013), no. 9904, 1600-1607.

[BCJ11] R. J. Barry, A. R. Clarke, and S. J. Johnstone, *Caffeine and opening the eyes have additive effects on resting arousal measures*, Clinical Neurophysiology, **122** (2011), 2010–2015.

[BMBN13] F. Beissner, K. Meissner, K. J. Bar, and V. Napadow, *The autonomic brain: An activation likelihood estimation meta-analysis for central processing of autonomic function*, The Journal of Neuroscience, **33** (2013), 10503–10511.

[BBWR09] E. D. Boorman, T. E. Behrens, M. W. Woolrich, and M. F. Rushworth, *How green is the grass on the other side? Frontopolar cortex and the evidence in favor of alternative courses of action*, Neuron, **62** (2009), 733–743.

[Bos10] P. Bossaerts, *Risk and risk prediction error signals in anterior insula*, Brain Structure & Function, **214** (2010), 645–653.

[Bou08] N. N. Boutros, R. Mears, M. E. Pflieger, K. A. Moxon, E. Ludowig, and T. Rosburg, *Sensory gating in the human hippocampal and rhinal regions: Regional differences*, Hippocampus, **18** (2008), 310–316.

[Cao19] Y. Cao, C. Summerfield, H. Park, B. L. Giordano, and C. Kayser, *Causal inference in the multisensory brain*, Neuron, **102** (2019), 1076, e1078–1087.

[CTBDS09] G. I. Christopoulos, P. N. Tobler, P. Bossaerts, R. J. Dolan, and W, Schultz, *Neural correlates of value, risk, and risk aversion contributing to decision making under risk*, The Journal of Neuroscience, **29** (2009), 12574–12583.

[CR14] J. A. Clithero and A. Rangel, *Informatic parcellation of the network involved in the computation of subjective value*, Social Cognitive and Affective Neuroscience, **9** (2014), 1289–1302.

[DERL11] D. De Ridder, A. B. Elgoyhen, R. Romo, and B. Langguth, *Phantom percepts: Tinnitus and pain as persisting aversive memory networks*, Proceedings of the National Academy of Sciences of the United States of America, **108** (2011), 8075–8080.

[DeR06] D. De Ridder, H. Fransen, O. Francois, S. Sunaert, S. Kovacs, and P. Van De Heyning, *Amygdalohippocampal involvement in tinnitus and auditory memory*, Acta Oto-Laryngologica, Supplementum, **126** (2006), 50–53.

[DJV14] D. De Ridder, K. Joos and S. Vanneste, *The enigma of the tinnitus-free dream state in a Bayesian world*, Neural Plasticity (2014).

[DVF14] D. De Ridder, S. Vanneste and W. Freeman, *The Bayesian brain: phantom percepts resolve sensory uncertainty*, Neuroscience & Biobehavioral Reviews, **44** (2014), 4-15.

[DCK14] M. Donoso, A. G. Collins, and E. Koechlin, *Human cognition. Foundations of human reasoning in the prefrontal cortex*, Science, **344** (2014), 1481–1486.

[EK16] J. J. Eggermont and A. Kral, *Somatic memory and gain increase as preconditions for tinnitus: insights from congenital deafness*, Hearing research, **333** (2016), 37-48.

[ER12] J. J. Eggermont and L. E. Roberts, *The neuroscience of tinnitus: understanding abnormal and normal auditory perception*, Frontiers in systems neuroscience, **6** (2012), 53.

[Fox17] J. M. Fox, S. V. Abram, J. L. Reilly, S. Eack, M. B. Goldman, J. G. Csernansky, ... M. J. Smith, *Default mode functional connectivity is*

associated with social functioning in schizophrenia, Journal of Abnormal Psychology, **126** (2017), 392–405.

[Fox12] J. J. Foxe, K. P. Morie, P. J. Laud, M. J. Rowson, E. A. de Bruin, and S. P. Kelly, *Assessing the effects of caffeine and theanine on the maintenance of vigilance during a sustained attention task*, Neuropharmacology, **62** (2012), 2320–2327.

[Fri10] K. Friston, *The free-energy principle: A unified brain theory? Nature Reviews*, Neuroscience, **11** (2010), 127–138.

[Gal15] S. Gallus, et al., *Prevalence and determinants of tinnitus in the Italian adult population*, Neuroepidemiology, **45** (2015), no. 1, 12-19.

[Han18] J. J. Han, J. H. Jang, D. De Ridder, S. Vanneste, J. W. Koo, and J. J. Song, *Increased parietal circuit-breaker activity in delta frequency band and abnormal delta/theta band connectivity in salience network in hyperacusis subjects*, PLoS One, **13** (2018), e0191858

[Han20] J. J. Han, D. De Ridder, S. Vanneste, Y. C. Chen, J. W. Koo, and J. J. Song, *Pre-treatment ongoing cortical oscillatory activity predicts improvement of tinnitus after partial peripheral Reafferentation with hearing aids*, Frontiers in Neuroscience, **14** (2020), 410.

[HSV19] J. Hullfish, W. Sedley, and S. Vanneste, *Prediction and perception: Insights for (and from) tinnitus*, Neuroscience and Biobehavioral Reviews, **102** (2019), 1–12.

[JVD12] K. Joos, S. Vanneste, and D. De Ridder, D, *Disentangling depression and distress networks in the tinnitus brain*, PLoS One, **7** (2012), e40544

[Kim15] H-J. Kim, et al., *Analysis of the prevalence and associated risk factors of tinnitus in adults*, PloS one, **10** (2015), no. 5, e0127578.

[Kim16] S. H. Kim, J. H. Jang, S. Y. Lee, J. J. Han, J. W. Koo, S. Vanneste, ... J. J. Song, *Neural substrates predicting short-term improvement of tinnitus loudness and distress after modified tinnitus retraining therapy*, Scientific Reports, **6** (2016), 29140.

[Lan21] L. Lan, J. Li, Y. Chen, W. Chen, W. Li, F. Zhao, ... others, *Alterations of brain activity and functional connectivity in transition from acute to chronic tinnitus*, Human Brain Mapping, **42** (2021), 485–494

[LeeH19] H. Lee, et al., *Volume entropy for modeling information flow in a brain graph*, Scientific reports, **9** (2019), no.1, 1-13.

[Lee20] S. Y. Lee, B. Y. Choi, J. W. Koo, D. De Ridder, and J. J. Song, *Cortical oscillatory signatures reveal the prerequisites for tinnitus perception: A comparison of subjects with sudden Sensorineural hearing loss with and without tinnitus*, Frontiers in Neuroscience, **14** (2020), 596647.

[Lee17] S-Y. Lee, et al., *No auditory experience, no tinnitus: lessons from subjects with congenital-and acquired single-sided deafness*, Hearing research, **354** (2017), 9-15.

[Lee19] S. Y. Lee, J. Rhee, Y. J. Shim, Y. Kim, J. W. Koo, D. De Ridder, ... J. J. Song, *Changes in the resting-state cortical oscillatory activity 6 months after modified tinnitus retraining therapy*, Frontiers in Neuroscience, **13**, 1123.

[MMWJ10] M. Moazami-Goudarzi, L. Michels, N. Weisz, and D. Jeanmonod, *Temporo-insular enhancement of EEG low and high frequencies in patients with chronic tinnitus. QEEG study of chronic tinnitus patients*, BMC Neuroscience, **11** (2010), 40.

[Moh16] A. Mohan, D. De Ridder, and S. Vanneste, *Emerging hubs in phantom perception connectomics*, Neuroimage Clinic, **11** (2016), 181–194.

[Mou11] E. A. Moulton, I. Elman, G. Pendse, J. Schmahmann, L. Becerra, and D. Borsook, *Aversion-related circuitry in the cerebellum: Responses to noxious heat and unpleasant images*, The Journal of Neuroscience, **31** (2011), 3795–3804.

[Mur18] C, Murphy, E. Jefferies, S. A. Rueschemeyer, M. Sormaz, H. T. Wang, D. S. Margulies, and J. Smallwood, *Distant from input: Evidence of regions within the default mode network supporting perceptually decoupled and conceptually-guided cognition*, NeuroImage, **171**, 393–401.

[New01] M. E. J. Newman, S. H. Strogatz, and D. J. Watts, *Random graphs with arbitrary degree distributions and their applications*, Physical Review E, **64**(2) (2001), https://doi.org/10.1103/PhysRevE.64.026118.

[Nor02] A. Norena, et al., *Psychoacoustic characterization of the tinnitus spectrum: implications for the underlying mechanisms of tinnitus*, Audiology and Neurotology, **7** (2002), no. 6, 358-369.

[NE05] A. Noreña and J. J. Eggermont, *Enriched acoustic environment after noise trauma reduces hearing loss and prevents cortical map reorganization*, Journal of Neuroscience, **25** (2005), no. 3, 699-705.

[Oit15] J. Oiticica and R. S. M. Bittar, *Tinnitus prevalence in the city of São Paulo*, Brazilian journal of otorhinolaryngology, **81** (2015), 167-176.

[Pea11] J. M. Pearson, S. R. Heilbronner, D. L. Barack, B. Y. Hayden, and M. L. Platt, *Posterior cingulate cortex: Adapting behavior to a changing world*, Trends in Cognitive Sciences, **15** (2011), 143–151.

[Rai01] M. E. Raichle, et al., *A default mode of brain function*, Proceedings of the National Academy of Sciences, **98** (2001), no. 2, 676-682.

[RS07] M. E. Raichle and A. Z. Snyder, *A default mode of brain function: a brief history of an evolving idea*, Neuroimage, **37** (2007), no. 4, 1083-1090.

[STM] R. Schaette, C. Turtle and K. J. Munro, *Reversible induction of phantom auditory sensations through simulated unilateral hearing loss*, PloS one, **7** (2012), no. 6, e35238.

[Sch12] M. Schecklmann, et al., *Relationship between audiometric slope and tinnitus pitch in tinnitus patients: insights into the mechanisms of tinnitus generation*, PloS one, **7** (2012), no. 4, e34878.

[See07] W. W. Seeley, et al., *Dissociable intrinsic connectivity networks for salience processing and executive control*, Journal of Neuroscience, **27** (2007), no. 9, 2349-2356.

[SCF10] J. Shargorodsky, G. C. Curhan and W. R. Farwell, *Prevalence and characteristics of tinnitus among US adults*, The American journal of medicine, **123** (2010), no. 8, 711-718.

[SC05] L. Sherlin and M. Congedo, *Obsessive-compulsive dimension localized using low-resolution brain electromagnetic tomography (LORETA)*, Neuroscience Letters, **387** (2005), 72–74.

[Shu97] G. L. Shulman, J. A. Fiez, M. Corbetta, R. L. Buckner, F. M. Miezin, M. E. Raichle, and S. E. Petersen, *Common blood flow changes across visual tasks: II. Decreases in cerebral cortex*, Journal of Cognitive Neuroscience, **9** (1997), 648–663.

[Son17] J. J. Song, K. Kim, W. Sunwoo, G. Mertens, P. Van de Heyning, D. De Ridder, et al., *A quantitative electroencephalography study on Cochlear implant-induced cortical changes in single-sided deafness with tinnitus*, Frontiers in Human Neuroscience, **11** (2017), 210.

[Tol48] E. C. Tolman, *Cognitive maps in rats and men*, Psychological Review, **55** (1948), 189–208.

[TM97] E. Tulving, H. J. Markowitsch, *Memory beyond the hippocampus*, Current Opinion in Neurobiology, **7** (1997), 209–216.

[VAD19] S. Vanneste, O. Alsalman, and D. De Ridder, *Top-down and bottom-up regulated auditory phantom perception*, The Journal of Neuroscience, **39** (2019), 364–378.

[VD12a] S. Vanneste, D. De Ridder, *The use of alcohol as a moderator for tinnitus-related distress*, Brain Topography, **25** (2012), 97–105.

[VD15] S. Vanneste, D. De Ridder, *Stress-related functional connectivity changes between auditory cortex and cingulate in tinnitus*, Brain Connectivity, **5** (2015), 371–383.

[VD16] S. Vanneste and D. De Ridder, *Deafferentation-based pathophysiological differences in phantom sound: tinnitus with and without hearing loss*, Neuroimage, **129** (2016), 80-94.

[VJD12] S. Vanneste, K. Joos, and D. De Ridder, *Prefrontal cortex based sex differences in tinnitus perception: Same tinnitus intensity, same tinnitus distress, different mood*, PLoS One, **7** (2012), e31182.

[Van11] S. Vanneste, M. Plazier, E. van der Loo, P. Van de Heyning, and D. De Ridder, *The difference between uni- and bilateral auditory phantom percept*, Clinical Neurophysiology, **122** (2011), 578–587.

[VSD18] S. Vanneste, J. J. Song, and D. De Ridder, *Thalamocortical dysrhythmia detected by machine learning*, Nature Communications, **9** (2018), 1103.

[VTD19] S. Vanneste, WT. To, and D. De Ridder, *Tinnitus and neuropathic pain share a common neural substrate in the form of specific brain connectivity and microstate profiles*, Progress in Neuro Psychopharmacology & Biological Psychiatry, **88** (2019), 388–400.

[WCCL19] R. W. Y. Wang, W. L. Chang, S. W. Chuang, and I. N. Liu, *Posterior cingulate cortex can be a regulatory modulator of the default mode network in task-negative state*, Scientific Reports, **9** (2019), 7565.

[Was13] L. Wasserman, *All of statistics: A concise course in statistical inference*, New York, NY: Springer Science & Business Media (2013).

[Wei18] V. A. Weilnhammer, H. Stuke, P. Sterzer, and K. Schmack, *The neural correlates of hierarchical predictions for perceptual decisions*, The Journal of Neuroscience, **38** (2013), 5008–5021.

[WS16] A. M. Wikenheiser and G. Schoenbaum, *Over the river, through the woods: Cognitive maps in the hippocampus and orbitofrontal cortex*, Nature Reviews. Neuroscience, **17** (2016), 513–523

[Wu15] B. Wu, et al., *Tinnitus prevalence in New Zealand*, The New Zealand Medical Journal (Online), **128**(2015), no.1423, 24.

[XYL16] X. Xu, H. Yuan, and X. Lei, *Activation and connectivity within the default mode network contribute independently to future-oriented thought*, Scientific Reports, **6** (2016), 21001.

[Ake14] O. Akeju, M. L. Loggia, C. Catana, K. J. Pavone, R. Vazquez, J. Rhee, et al., *Disruption of thalamic functional connectivity is a neural correlate of dexmedetomidine-induced unconsciousness*, eLife 3:e04499 (2014), doi: 10.7554/eLife.04499

[And10] J. R. Andrews-Hanna, J. S. Reidler, J. Sepulcre, R. Poulin, and R. L. Buckner, *Functional-anatomic fractionation of the brain's default network*, Neuron, **65** (2010), 550–562.

[BML03] D. E. Bamiou, F. E. Musiek, and L. M. Luxon, *The insula (Island of Reil) and its role in auditory processing*, Literature review. Brain Res. Brain Res. Rev., **42** (2003), 143–154.

[Bin99] J. R. Binder, J. A. Frost, T. A. Hammeke, P. S. Bellgowan, S. M. Rao, and R. W. Cox, *Conceptual processing during the conscious resting state*, A functional MRI study. J. Cogn. Neurosci., **11** (1999), 80–95.

[Bol04] M. Boly, M. E. Faymonville, P. Peigneux, B. Lambermont, P. Damas, G. Del Fiore, et al., *Auditory processing in severely brain injured patients:*

Differences between the minimally conscious state and the persistent vegetative state, Arch. Neurol., **61** (2004), 233–238.

[Bol05] M. Boly, M. E. Faymonville, P. Peigneux, B. Lambermont, F. Damas, A. Luxen, et al., *Cerebral processing of auditory and noxious stimuli in severely brain injured patients: Differences between VS and MCS*, Neuropsychol. Rehabil., **15** (2005), 283–289.

[Bol08] M. Boly, C. Phillips, E. Balteau, C. Schnakers, C. Degueldre, G. Moonen, et al., *Consciousness and cerebral baseline activity fluctuations*, Hum. Brain Mapp., **29** (2008), 868–874.

[Buc08] R. L. Buckner, J. R. Andrews-Hanna and D. L. Schacter, *The brain's default network: anatomy, function, and relevance to disease*, Annals of the new York Academy of Sciences, **1124** (2008), 1-38.

[Cha10] J. K. Chau, et al., *Systematic review of the evidence for the etiology of adult sudden sensorineural hearing loss*, The Laryngoscope, **120** (2010), no. 5, 1011-1021.

[Che20] S. Cheng, G. Xu, J. Zhou, Y. Qu, Z. Li, Z. He, et al., *A multimodal meta-analysis of structural and functional changes in the brain of tinnitus*, Front. Hum. Neurosci., **14**:28 (2020).

[Chr16] K. Christoff, et al., *Mind-wandering as spontaneous thought: a dynamic framework*, Nature Reviews Neuroscience, **17** (2016), 718-731.

[Cim20] P. Ciminelli, S. Machado, M. Palmeira, E. S. F. Coutinho, D. Sender, and A. E. Nardi, *Dorsomedial Prefrontal cortex repetitive transcranial magnetic stimulation for tinnitus: Promising results of a blinded*, Randomized, Sham-Controlled Study. Ear. Hear., **42**, 12–19.

[Col14] M. W. Cole, G. Repovš and A. Anticevic, *The frontoparietal control system: a central role in mental health*, The Neuroscientist, **20** (2014), no. 6, 652-664.

[CP07] A. E. Conlin and L. S. Parnes, *Treatment of sudden sensorineural hearing loss: I. A systematic review*, Archives of otolaryngology–head & neck surgery, **133** (2007), no. 6, 573-581.

[DeR21a] D. De Ridder, D. Adhia and S. Vanneste, *The anatomy of pain and suffering in the brain and its clinical implications*, Neuroscience & Biobehavioral Reviews, **130** (2021), 125-146.

[DeR21b] D. De Ridder, et al., *Tinnitus and tinnitus disorder: Theoretical and operational definitions (an international multidisciplinary proposal)*, Progress in brain research, **260** (2021), 1-25.

[DV21] D. De Ridderm and S. Vanneste, *The Bayesian brain in imbalance: Medial, lateral and descending pathways in tinnitus and pain: A perspective*, Progress in Brain Research, **262** (2021), 309-334.

[DeR14a] D. De Ridder, K. Joos, and S. Vanneste, *The enigma of the tinnitus free dream state in a Bayesian world*, Neural Plast. (2014), 612147.

[DeR14b] D. De Ridder, S. Vanneste and W. Freeman, *The Bayesian brain: phantom percepts resolve sensory uncertainty*, Neuroscience & Biobehavioral Reviews, **44** (2014), 4-15.

[DeR14c] D. De Ridder, et al., *An integrative model of auditory phantom perception: tinnitus as a unified percept of interacting separable subnetworks*, Neuroscience & Biobehavioral Reviews, **44** (2014), 16-32.

[DeR15] D. De Ridder, et al., *Thalamocortical dysrhythmia: a theoretical update in tinnitus*, Frontiers in neurology, **6** (2015), 124.

[DeR12] D. De Ridder, S. Vanneste, T. Menovsky, and B. Langguth, *Surgical brain modulation for tinnitus: The past, present and future*, J. Neurosurg. Sci., **56** (2012), 323–340.

[DeR22] D. De Ridder, S. Vanneste, J. J. Song, and D. Adhia, *Tinnitus and the Triple network model: A perspective*, Clin. Exp. Otorhinolaryngol., **15** (2022), 205–212.

[DeR05] D. De Ridder, E. Verstraeten, K. Van der Kelen, G. De Mulder, S. Sunaert, J. Verlooy, et al., *Transcranial magnetic stimulation for tinnitus: Influence of tinnitus duration on stimulation parameter choice and maximal tinnitus suppression*, Otol. Neurotol., **26** (2005), 616–619.

[Dem12] A. Demertzi, A. Soddu, and S. Laureys, *nsciousness supporting networks*, Curr. Opin. Neurobiol., **23** (2012), 239–244.

[Din18] X. Ding, X. Zhang, Z. Huang, and X. Feng, *The Characteristic and short-term prognosis of tinnitus associated with sudden Sensorineural hearing loss*, Neural Plast. (2018), 6059697.

[Egg15] J. J. Eggermont, *Neural substrates of tinnitus in animal and human cortex*, HNO, **63** (2015), 298-301.

[ER04] J. J. Eggermont and L. E. Roberts, *The neuroscience of tinnitus*, Trends in neurosciences, **27** (2004), 676-682.

[Fic21] L. Ficco, L. Mancuso, J. Manuello, A. Teneggi, D. Liloia, S. Duca, et al., *Disentangling predictive processing in the brain: A Meta-analytic study in favour of a predictive network*, Sci. Rep., **11** (2021), 16258.

[Fox05] M. D. Fox, et al., *The human brain is intrinsically organized into dynamic, anticorrelated functional networks*, Proceedings of the National Academy of Sciences, **102** (2005), no. 27, 9673-9678.

[FM08] P. Fransson and G. Marrelec, *The precuneus/posterior cingulate cortex plays a pivotal role in the default mode network: Evidence from a partial correlation network analysis*, Neuroimage, **42** (2008), 1178–1184.

[Fri10] K. Friston, *The free-energy principle: a unified brain theory?*, Nature reviews neuroscience, **11** (2010), 127-138.

[Fri14] K. J. Friston, et al., *Computational psychiatry: the brain as a phantastic organ*, The Lancet Psychiatry, **1** (2014), no. 2, 148-158.

[Fuc02] M. Fuchs, J. Kastner, M. Wagner, S. Hawes, and J. S. Ebersole, *A standardized boundary element method volume conductor model*, Clin. Neurophysiol., **113** (2002), 702–712.

[Gib13] P. C. Gibrin, J. J. Melo, and L. L. Marchiori, *Prevalence of tinnitus complaints and probable association with hearing loss, diabetes mellitus and hypertension in elderly*, Codas, **25** (2013), 176–180.

[Gou14] N. Goulden, et al., *The salience network is responsible for switching between the default mode network and the central executive network: replication from DCM*, Neuroimage, **99** (2014), 180-190.

[Gro17] J. K. Grooms, G. J. Thompson, W. J. Pan, J. Billings, E. H. Schumacher, C. M. Epstein, et al., *Infraslow Electroencephalographic and dynamic resting state network activity*, Brain Connect., **7** (2017), 265–280.

[Hen05] J. A. Henry, K. C. Dennis and M. A. Schechter, *General review of tinnitus: Prevalence, mechanisms, effects, and management*, J. Speech Lang Hear. Res., **48** (2005), 1204–1235.

[Hu17] M. -L. Hu, X. -F. Zong, J. J. Mann, J. -J. Zheng, Y. -H. Liao, Z. -C. Li, et al., *A review of the functional and anatomical default mode network in schizophrenia*, Neurosci. Bull., **33** (2107), 73–84.

[Ish19] Y. Ishishita, N. Kunii, S. Shimada, K. Ibayashi, M. Tada, K. Kirihara, et al., *Deviance detection is the dominant component of auditory contextual processing in the lateral superior temporal gyrus: A human ECoG study*, Hum. Brain Mapp., **40** (2019), 1184–1194.

[Jas90] P. J. Jastreboff, *Phantom auditory perception (tinnitus): Mechanisms of generation and perception*, Neurosci. Res., **8** (1990), 221–254.

[Joo14] K. Joos, D. De Ridder, P. Van de Heyning, and S. Vanneste, *Polarity specific suppression effects of transcranial direct current stimulation for tinnitus*, Neural Plast. (2014), 930860.

[Jur07] V. Jurcak, D. Tsuzuki, and I. Dan, *10/20, 10/10, and 10/5 systems revisited: Their validity as relative head-surface-based positioning systems*, Neuroimage, **34** (2007), 1600–1611.

[KY11] S. Kanaya and K. Yokosawa, *Perceptual congruency of audio-visual speech affects ventriloquism with bilateral visual stimuli*, Psychon. Bull. Rev., **18** (2011), 123–128.

[Kim16] S. H. Kim, J. H. Jang, S. Y. Lee, J. J. Han, J. W. Koo, S. Vanneste, et al., *Neural substrates predicting short-term improvement of tinnitus loudness and distress after modified tinnitus retraining therapy*, Sci Rep, **6** (2016), 29140.

[KP04] D. C. Knill and A. Pouget, *The Bayesian brain: the role of uncertainty in neural coding and computation*, TRENDS in Neurosciences, **27** (2004), 712-719.

[KS07] E. Koechlin and C. Summerfield, *An information theoretical approach to prefrontal executive function*, Trends Cogn. Sci., **11** (2007), 229–235.

[Kor16] O. Korucuoglu, T. E. Gladwin, and R. W. Wiers, *The effect of acute alcohol on motor-related EEG asymmetries during preparation of approach or avoid alcohol responses*, Biol. Psychol., **114** (2016), 81–92.

[Lai09] A. R. Laird, S. B. Eickhoff, K. Li, D. A. Robin, D. C. Glahn, and P. T. Fox, *Investigating the functional heterogeneity of the default mode network using coordinate-based meta-analytic modeling*, J Neurosci, **29** (2009), 14496–14505.

[Lau04] S. Laureys, F. Perrin, M. E. Faymonville, C. Schnakers, M. Boly, V. Bartsch, et al., *Cerebral processing in the minimally conscious state*, Neurology, **63** (2004), 916–918.

[Lee21] S-Y. Lee, et al., *Is the posterior cingulate cortex an on-off switch for tinnitus?: A comparison between hearing loss subjects with and without tinnitus*, Hearing Research, **411** (2021), 108356.

[LeeJ21] J. M. Lee, et al., *Auditory experience, for a certain duration, is a prerequisite for tinnitus: lessons from subjects with unilateral tinnitus in the better-hearing ear*, Progress in Brain Research, **260**, 223-233.

[Mas07] M. F. Mason, et al., *Wandering minds: the default network and stimulus-independent thought*, Science, **315** (2007) 393-395.

[Men11] V. Menin, *Large-scale brain networks and psychopathology: a unifying triple network model*, Trends in cognitive sciences, **15** (2011), no. 10, 483-506.

[Men18] V. Menon, *The triple network model, insight, and large-scale brain organization in autism*, Biological psychiatry, **84** (2018), no. 4, 236-238.

[Mir00] F. Mirz, *Cortical networks subserving the perception of tinnitus-a PET study*, Acta Otolaryngol., **120** (2000), 241–243.

[Moh18] A. Mohan, et al., *Distress-dependent temporal variability of regions encoding domain-specific and domain-general behavioral manifestations of phantom percepts*, European Journal of Neuroscience, **48** (2018), 1743-1764.

[Muh06] M. Műhlau, J. Rauschecker, E. Oestreicher, C. Gaser, M. Rőttinger, A. Wohlschlăger, et al., *Structural brain changes in tinnitus*, Cereb. Cortex, **16** (2006), 1283–1288.

[Mul06] N. G. Műller and R. T. Knight, *The functional neuroanatomy of working memory: Contributions of human brain lesion studies*, Neuroscience, **139** (2006), 51–58.

[NE05] A. J. Noreña and J. J. Eggermont, *Enriched acoustic environment after noise trauma reduces hearing loss and prevents cortical map reorganization*, J. Neurosci., **25** (2005), 699–705.

[Ols07] I. R. Olson, A. Plotzker, and Y. Ezzyat, *The Enigmatic temporal pole: A review of findings on social and emotional processing*, Brain, **130**(Pt 7) (2007), 1718–1731.

[Pan13] W. J. Pan, G. J. Thompson, M. E. Magnuson, D. Jaeger and S. Keilholz, *Infraslow LFP correlates to resting-state fMRI BOLD signals*, Neuroimage, **74** (2013), 288–297.

[Pas02] R. D. Pascual-Marqui, *Standardized low-resolution brain electromagnetic tomography (sLORETA): Technical details*, Methods Find Exp. Clin. Pharmacol., **24**(Suppl. D) (2002), 5–12.

[Pez21] G. Pezzulo, M. Zorzi and M. Corbetta, *The secret life of predictive brains: What's spontaneous activity for?*, Trends Cogn. Sci., **25** (2021), 730–743.

[Rau10] J. P. Rauschecker, A. M. Leaver and M. Műhlau, *Tuning out the noise: Limbic-auditory interactions in tinnitus*, Neuron, **66** (2010), 819–826.

[Roh19] T. Rohe, A. C. Ehlis, and U. Noppeney, *The neural dynamics of hierarchical Bayesian causal inference in multisensory perception*, Nat. Commun., **10** (2019), 1907.

[Sad09] S. Sadaghiani, G. Hesselmann, and A. Kleinschmidt, *Distributed and antagonistic contributions of ongoing activity fluctuations to auditory stimulus detection*, J. Neurosci., **29** (2009), 13410–13417.

[Sch18] A. Schaefer, R. Kong, E. M. Gordon, T. O. Laumann, X. N. Zuo, A. J. Holmes, et al., *Local-Global parcellation of the human cerebral cortex from intrinsic functional connectivity MRI*, Cereb. Cortex, **28** (2018), 3095–3114.

[Sed16] W. Sedley, et al., *An integrative tinnitus model based on sensory precision*, Trends in neurosciences, **39**, 799-812.

[Seg13] M. L. Seghier, *The angular gyrus: Multiple functions and multiple subdivisions*, Neuroscientist, **19** (2013), 43–61.

[Sha19] Z. Sha, T. D. Wager, A. Mechelli, and Y. He, *Common Dysfunction of large-scale neurocognitive networks across psychiatric disorders*, Biol. Psychiatry, **85** (2019), 379–388.

[SK02] M. Siepmann and W. Kirch, *Effects of caffeine on topographic quantitative EEG*, Neuropsychobiology, **45** (2002), 161–166.

[Son21] J-J. Song, et al., *The balance between Bayesian inference and default mode determines the generation of tinnitus from decreased auditory input: A volume entropy-based study*, Human Brain Mapping, **42** (2021), 4059-4073.

[Son15] J. J. Song, S. Vanneste, and D. De Ridder, *Dysfunctional noise cancelling of the rostral anterior cingulate cortex in tinnitus patients*, PLoS One, **10** (2015), e0123538.

[Stu21] V. E. Sturm, A. R. K. Roy, S. Datta, C. Wang, I. J. Sible, S. R. Holley, S. R., et al., *Enhanced visceromotor emotional reactivity in dyslexia and its relation to salience network connectivity*, Cortex, **134** (2021), 278–295.

[Tho14] G. J. Thompson, W. J. Pan, M. E. Magnuson, D. Jaeger, and S. D. Keilholz, *Quasi-periodic patterns (QPP): Large-scale dynamics in resting state fMRI that correlate with local infraslow electrical activity*, Neuroimage, **84** (2014), 1018–1031.

[VD11] S. Vanneste and D. De Ridder, *Bifrontal transcranial direct current stimulation modulates tinnitus intensity and tinnitus-distress-related brain activity*, Eur. J. Neurosci., **34** (2011), 605–614.

[VD12b] S. Vanneste and D. De Ridder, *The auditory and non-auditory brain areas involved in tinnitus. An emergent property of multiple parallel overlapping subnetworks*, Front. Syst. Neurosci., **6** (2012), 31.

[VD16] S. Vanneste and D. De Ridder, *Deafferentation-based pathophysiological differences in phantom sound: tinnitus with and without hearing loss*, Neuroimage, **129** (2016), 80-94.

[Vin08] J. L. Vincent, et al., *Evidence for a frontoparietal control system revealed by intrinsic functional connectivity*, Journal of neurophysiology, **100** (2008), no. 6, 3328-3342.

[Whi10] T. P. White, V. Joseph, S. T. Francis, and P. F. Liddle, *Aberrant salience network (bilateral insula and anterior cingulate cortex) connectivity during information processing in schizophrenia*, Schizophr. Res., **123** (2010), 105–115.

[Whi17] J. R. Whitlock, *Posterior parietal cortex*, Curr. Biol., **27** (2017), R691–R695.

[Lun03] B. Iung, G. Baron, E. G. Butchart, et al., *A prospective survey of patients with valvular heart disease in Europe: The Euro Heart Survey on Valvular Heart Disease*, Eur Heart J., **24** (2003). 1231–1243.

[Nko06] V. T. Nkomo, J. M. Gardin, T. N. Skelton, J. S. Gottdiener, C. G. Scott, M. Enriquez-Sarano, *Burden of valvular heart diseases: a population based study*, Lancet., **368** (2006), 1005–1011.

[Bau17] H. Baumgartner, V. Falk, J. J. Bax, et al., *2017 ESC/EACTS guidelines for the management of valvular heart disease*, Eur Heart J., **38** (2017), 2739–2791.

[Wri21] M. Writing Committee, C. M. Otto, R. A. Nishimura, et al., *2020 ACC/AHA guideline for the management of patients with valvular heart disease: executive summary: a report of the American College of Cardiology/American Heart Association Joint Committee on Clinical Practice Guidelines*, J Am Coll Cardiol., **77** (2021), 450–500.

[Lum13] P. Y. Lum, G. Singh, A. Lehman, et al., *Extracting insights from the shape of complex data using topology*, Sci Rep., **3** (2013)m 1236.

[PB18] S. Pai and G. D. Bader, *Patient Similarity Networks for Precision Medicine*, J Mol Biol., **380** (2018), 2924–2938.

[LeeH17] H. Lee, H. Kang, M. K. Chung, S. Lim, B. N. Kim, D. S. Lee, *Integrated multimodal network approach to PET and MRI based on multidimensional persistent homology*, Hum Brain Mapp., **38** (2017), 1387–1402.

[Ha20] S. Ha, H. Lee, Y. Choi, et al., *Maturational delay and asymmetric information flow of brain connectivity in SHR model of ADHD revealed by topological analysis of metabolic networks*, Sci Rep., **10** (2020), 3197.

[NLC11] M. Nicolau, A. J. Levine, G. Carlsson, *Topology based data analysis identifies a subgroup of breast cancers with a unique mutational profile and excellent survival*, Proc Natl Acad Sci U S A., **108** (2011), 7265–7270.

[Li15] L. Li, W. Y. Cheng, B. S. Glicksberg, et al., *Identification of type 2 diabetes subgroups through topological analysis of patient similarity*, Sci Transl Med., **7** (2015), 311ra174.

[Cas19] G. Casaclang-Verzosa, S. Shrestha, M. J. Khalil, et al., *Network Tomography for Understanding Phenotypic Presentations in Aortic Stenosis*, J Am Coll Cardiol Img., **12** (2019), 236–248.

[Cho20] J. S. Cho, S. Shrestha, N. Kagiyama, et al., *A network-based "phenomics" approach for discovering patient subtypes from highthroughput cardiac imaging data*, J Am Coll Cardiol Img., **13** (2020), 1655–1670.

[Hwa21] D. Hwang, H. J. Kim, S. P. Lee, et al., *Topological data analysis of coronary plaques demonstrates the natural history of coronary atherosclerosis*, J Am Coll Cardiol Img., **14** (2021), 1410–1421.

[Ama20] M. Amano, C. Izumi, Y. J. Kim, et al., *Changes of echocardiographic parameters in primary mitral regurgitation and determinants of symptom: an assessment from the Asian Valve Registry data*, Heart Vessels., **35** (2020), 555–563.

[Lan15] R. M. Lang,L. P. Badano, V. Mor-Avi, et al., *Recommendations for cardiac chamber quantification by echocardiography in adults: an update from the American Society of Echocardiography and the European Association of Cardiovascular Imaging*, J Am Soc Echocardiogr., **28** (2015), 1–39.e14.

[Nag16] S. F. Nagueh, O. A. Smiseth, C. P. Appleton, et al., *Recommendations for the evaluation of left ventricular diastolic function by echocardiography: an update from the American Society of Echocardiography and the European Association of Cardiovascular Imaging*, J Am Soc Echocardiogr., **29** (2016), 277–314.

[Rud10] L. G. Rudski, W. W. Lai, J. Afilalo, et al., *Guidelines for the echocardiographic assessment of the right heart in adults: a report from the American Society of Echocardiography endorsed by the European Association of Echocardiography, a registered branch of the European Society of Cardiology, and the Canadian Society of Echocardiography*, Am Soc Echocardiogr., **23** (2010), 685–713. quiz 786-788.

[Zog17] W. A. Zoghbi, D. Adams, R. O. Bonow, et al., *Recommendations for noninvasive evaluation of native valvular regurgitation: a report from the American Society of Echocardiography Developed in Collaboration with the Society for Cardiovascular Magnetic Resonance*, J Am Soc Echocardiogr., **30** (2017), 303–371.

[SMC07] G. Singh, F. Mémoli, and G. E. Carlsson, *Topological methods for the analysis of high dimensional data sets and 3D object recognition*, Eurographics Symposium on Point-Based Graphics, **2** (2007).

[Car09] G. E. Carlsson, *Topology and data*, Bulletin of the American Mathematical Society, **46** (2009), 255–308.

[Gri18] F. Grigioni, M. A. Clavel, J. L. Vanoverschelde, et al., *The MIDA Mortality Risk Score: development and external validation of a prognostic model for early and late death in degenerative mitral regurgitation*, Eur Heart J., **39** (2018), 1281–1291.

[GM18] L. D. Gillam and L. Marcoff, *Hemodynamics in primary mitral regurgitation: support for and challenges to the conventional wisdom*, Circ Cardiovasc Imaging., **11** (2018), e007471.

[Cor91] W. J. Corin, T. Murakami, E. S. Monrad, O. M. Hess, and H. P. Krayenbuehl, *Left ventricular passive diastolic properties in chronic mitral regurgitation*, Circulation, **83** (1991), 797–807.

[Con95] C. H. Conrad, W. W. Brooks, J. A. Hayes, S. Sen, K. G. Robinson, and O. H. Bing, *Myocardial fibrosis and stiffness with hypertrophy and heart failure in the spontaneously hypertensive rat*, Circulation, **91** (1995), 161–170.

[Zan07] A. Zanchetti, C. Cuspidi, L. Comarella, et al., *Left ventricular diastolic dysfunction in elderly hypertensives: results of the APROS-diadys study*, J Hypertens., **25** (2007), 2158–2167.

[Wes08] D. Westermann, M. Kasner, P. Steendijk, et al., *Role of left ventricular stiffness in heart failure with normal ejection fraction*, Circulation, **117** (2008), 2051–2060.

[Ros01] A. Rossi, M. Cicoira, G. Golia, M. Anselmi, and P. Zardini, *Mitral regurgitation and left ventricular diastolic dysfunction similarly affect mitral and pulmonary vein flow Doppler parameters: the advantage of end-diastolic markers*, J Am Soc Echocardiogr., **14** (2001), 562–568.

[War63] J. H. Ward Jr, *Hierarchical grouping to optimize an objective function*, J Am Stat Assoc, **58** (1963), 236-244.

[BGLL08] V. D. Blondel, J-L. Guillaume, R. Lambiotte, E. Lefebvre, *Fast unfolding of communities in large networks*, J Stat Mech, (2008), P10008.

[LDB08] R. Lambiotte, J-C. Delvenne, M. Barahona, *Laplacian dynamics and multiscale modular structure in networks*, preprint arXiv 2008;0812.1770.

[AGMS21] J. An, L. Guan, A. Marnat, and R. Shi, *Divergent trajectories on products of homogeneous spaces*, Advances in Mathematics, **390** (2021), 107910.

[CC16] Y. Cheung and N. Chevallier, *Hausdorff dimension of singular vectors*, Duke Math. J., **165** (2016), 2273–2329.

[Che11] Y. Cheung, *Hausdorff dimension of the set of singular pairs*, Ann. of Math., **173** (2011), 127–167.

[DFSU] T. Das, L. Fishman, D. Simmons and M. Urbański, *A variational principle in the parametric geometry of numbers*, arXiv:1901.06602.

[GS20] L. Guan and R. Shi, *Hausdorff dimension of divergent trajectories on homogeneous spaces*, Compositio Math., **156** (2020), no. 2, 340–359.

[KKLM17] S. Kadyrov, D. Kleinbock, E. Lindenstrauss, and G. A. Margulis, *Singular systems of linear forms and non-escape of mass in the space of lattices*, J. Anal. Math., **133** (2017), 253—277.

[KP22] T. Kim and J. Park, *On a lower bound of Hausdorff dimension of weighted singular vectors*, arXiv preprint arXiv:2207.07944.

[LSST20] L. Liao, R. Shi, O. N. Solan, and N. Tamam, *Hausdorff dimension of weighted singular vectors in* $\mathbb{R}^2$, J. Eur. Math. Soc., **22** (2020), 833-875.

[Sol] O. N. Solan, *Parametric geometry of numbers for a general flow*, arXiv:2106.01707.

국문초록

거리그래프의 측지선 공간에는 거리 그래프의 기하학적, 동역학적 및 확률론적 특징을 반영하는 측지적 류에 대한 세 가지 중요한 불변측도가 있다. 측도는 동역학적 불변량과 범피복나무의 경계에서 정의된 측도류에 의해 구축된다. 본 학위논문에서는 동역학적 불변량과 경계 측도류를 결정하는 거리그래프의 구조에 집중한다.

먼저 다양체의 경우와 유사하게 퍼텐셜함수를 이용해 비지빌리티 측도, 패터슨-설리반 측도, 하모닉 측도, 총 세 가지 경측도를 공식화한다. 이러한 경측도류 중 두 개가 동치일 필요충분조건이 특정한 간선 길이에 대한 조건으로 나타남을 보인다 (정리 3.4.2, 정리 3.4.3, 정리 3.4.4).

다음은 동역학적 불변량과 경계 측도를 활용한 뇌 네트워크 연구이다. 뇌 네트워크를 거리그래프로 간주하여 부피 엔트로피와 패터슨-설리반 측도를 수치적으로 계산한다. 이명 집단과 비이명 집단에서 이 값들을 비교하여 베이지안 가설에 기반해 이명 증상의 원인을 해석한다.

또한 의료수학에서 위상수학적 데이터 분석에 대한 결과를 소개한다. 매퍼 알고리즘을 이용해 데이터 공간을 거리그래프로 나타내고 거리그래프의 구조에 기반한 그룹화 방법을 제안한다. 이러한 방법론에 기반해 승모판막 협착증 환자들의 새로운 하위 유형을 찾는다.

마지막으로 디오판틴 근사 분야의 결과를 향상시킨 결과를 소개한다. 나무의 구조와 균질 동역학의 투영 성질을 이용해 무게 특이 벡터들 안에 속하는 프랙탈 집합을 만든다. 격자점 셈을 통해 나무를 관찰해 무게 특이 벡터들의 하우스도르프 차원의 하계를 얻는다 (정리 1.5.1).

주요어휘: 거리그래프, 동역학적 불변량, 불변측도, 뇌 네트워크, 위상수학적 데이터 분석, 디오판틴 근사

학번: 2017-21999

감사의 글

가장 먼저 학위 과정 동안 저를 지도해주신 임선희 교수님께 감사의 말씀을 드립니다. 대학원 생활 초창기부터 연구 지도뿐만 아니라 연구자로서의 마음가짐, 경력을 쌓기 위한 방향성, 진로 계획 등 다양한 부분에서 교수님의 세심한 지도 덕분에 무사히 학위 과정을 마치고 졸업을 할 수 있게 되었습니다. 교수님께 지도받을 수 있어 영광이었고 다시 한번 감사드립니다.

본 학위 논문을 심사해주신 국웅 교수님, Otto van Koert 교수님, 이계선 교수님, 권상훈 교수님께도 감사드립니다.이 공동연구를 통해 만나 뵈었던 송재진 교수님과 이승표 교수님께도 감사의 인사를 드리고 싶습니다. 저에게는 생소한 의학 분야임에도 무사히 공동연구 성과를 낼 수 있어서 독특한 경력을 쌓을 수 있었습니다. 그리고 공동연구를 진행하며 함께 고생했던 태형이형, 정호형, 태진이, 재린이, 현우, 현영이에게도 고마움을 전하고 싶습니다.

함께 있는 동안 즐거운 추억을 많이 쌓은 연구실 동료들인 지영누나, 순기형, 슬비누나, 덕원이형, 재린이, 태형이형, 진호, 우연이, 국영씨, 명씨, 재영씨에게 고마움을 전합니다. 또한 기쁜 일을 함께해준 대학원 동료들인 호식이, 종흔이형, 원희, 필립이, 경이에게도 고마움을 전합니다.

학위 과정 동안 뒤에서 묵묵히 응원해주신 부모님과 동생에게도 늘 고맙습니다. 졸업 후에 떳떳한 모습으로 자랑스러운 아들이 되도록 노력하겠습니다.

마지막으로 항상 저에게 큰 힘과 위로가 되어주는 아내 윤희에게 가장 큰 고마움을 전합니다.